POLITECHNIKA GDAŃSKA

Imię i nazwisko autora rozprawy: Krystian Lankauf

Dyscyplina naukowa: Automatyka, Elektronika, Elektrotechnika i Technologie Kosmiczne

ROZPRAWA DOKTORSKA

Tytuł rozprawy w języku polskim: Nanokrystaliczne tlenki metali jako katalizatory reakcji wydzielania tlenu w środowisku zasadowym

Tytuł rozprawy w języku angielskim: Nanocrystalline metal oxides as catalysts for oxygen evolution reaction in alkaline media

Promotor   *podpis*
dr hab. inż. Sebastian Molin

Gdańsk, 2024 r.

POLITECHNIKA GDAŃSKA

OŚWIADCZENIE

Autor rozprawy doktorskiej: Krystian Lankauf

Ja, niżej podpisany(a), oświadczam, iż jestem świadomy(a), że zgodnie z przepisem art. 27 ust. 1 i 2 ustawy z dnia 4 lutego 1994 r. o prawie autorskim i prawach pokrewnych (t.j. Dz.U. z 2021 poz. 1062), uczelnia może korzystać z mojej rozprawy doktorskiej zatytułowanej:

> Nanokrystaliczne tlenki metali jako katalizatory reakcji wydzielania tlenu w środowisku zasadowym

do prowadzenia badań naukowych lub w celach dydaktycznych.[1]

Świadomy(a) odpowiedzialności karnej z tytułu naruszenia przepisów ustawy z dnia 4 lutego 1994 r. o prawie autorskim i prawach pokrewnych i konsekwencji dyscyplinarnych określonych w ustawie Prawo o szkolnictwie wyższym i nauce (Dz.U.2021.478 t.j.), a także odpowiedzialności cywilno-prawnej oświadczam, że przedkładana rozprawa doktorska została napisana przeze mnie samodzielnie.

Oświadczam, że treść rozprawy opracowana została na podstawie wyników badań prowadzonych pod kierunkiem i w ścisłej współpracy z promotorem dr. hab. inż. Sebastianem Molinem.

Niniejsza rozprawa doktorska nie była wcześniej podstawą żadnej innej urzędowej procedury związanej z nadaniem stopnia doktora.

Wszystkie informacje umieszczone w ww. rozprawie uzyskane ze źródeł pisanych i elektronicznych, zostały udokumentowane w wykazie literatury odpowiednimi odnośnikami, zgodnie z przepisem art. 34 ustawy o prawie autorskim i prawach pokrewnych.

Potwierdzam zgodność niniejszej wersji pracy doktorskiej z załączoną wersją elektroniczną.

Gdańsk, dnia ……. ……

podpis doktoranta

Ja, niżej podpisany(a), wyrażam zgodę/nie wyrażam zgody* na umieszczenie ww. rozprawy doktorskiej w wersji elektronicznej w otwartym, cyfrowym repozytorium instytucjonalnym Politechniki Gdańskiej.

Gdańsk, dnia ……. ……

podpis doktoranta

[1] Art. 27. 1. Instytucje oświatowe oraz podmioty, o których mowa w art. 7 ust. 1 pkt 1, 2 i 4–8 ustawy z dnia 20 lipca 2018 r. – Prawo o szkolnictwie wyższym i nauce, mogą na potrzeby zilustrowania treści przekazywanych w celach dydaktycznych lub w celu prowadzenia działalności naukowej korzystać z rozpowszechnionych utworów w oryginale i w tłumaczeniu oraz zwielokrotniać w tym celu rozpowszechnione drobne utwory lub fragmenty większych utworów.
2. W przypadku publicznego udostępniania utworów w taki sposób, aby każdy mógł mieć do nich dostęp w miejscu i czasie przez siebie wybranym korzystanie, o którym mowa w ust. 1, jest dozwolone wyłącznie dla ograniczonego kręgu osób uczących się, nauczających lub prowadzących badania naukowe, zidentyfikowanych przez podmioty wymienione w ust. 1.

POLITECHNIKA GDAŃSKA

OPIS ROZPRAWY DOKTORSKIEJ

Autor rozprawy doktorskiej: Krystian Lankauf

Tytuł rozprawy doktorskiej w języku polskim: Nanokrystaliczne tlenki metali jako katalizatory reakcji wydzielania tlenu w środowisku zasadowym

Tytuł rozprawy w języku angielskim: Nanocrystalline metal oxides as catalysts for oxygen evolution reaction in alkaline media

Język rozprawy doktorskiej: polski

Promotor rozprawy doktorskiej: Sebastian Molin

Data obrony:

Słowa kluczowe rozprawy doktorskiej w języku polskim: elektroliza wody; spinele; perowskity; elektrokatalizatory

Słowa kluczowe rozprawy doktorskiej w języku angielskim: water electrolysis; spinels; perovskites; electrocatalysts

Streszczenie rozprawy w języku polskim: W pracy poruszona została tematyka opracowania oraz zastosowania nanokrystalicznych tlenków metali jako katalizatorów reakcji wydzielania tlenu w elektrolicie zasadowym, tj. jednej z reakcji zachodzących podczas elektrolizy wody. Szczególną uwagę poświęcono tlenkom o strukturze spinelu i perowskitu, które znane są z wyjątkowych właściwości elektrycznych, magnetycznych, optycznych oraz katalitycznych. Materiały zostały przygotowane za pomocą metody zol żel lub wysokotemperaturowej syntezy w fazie stałej. Podjęte zostały próby modyfikacji materiałów poprzez wprowadzenie nowych pierwiastków do struktury krystalicznej czy zastosowanie dodatkowej obróbki cieplnej (wyżarzanie) lub mechanicznej (mielenie) w celu poprawy parametrów pracy katalizatora. Przeprowadzone zostały badania strukturalne za pomocą technik mikroskopowych i spektroskopowych, natomiast aktywność elektrokatalityczna była analizowana korzystając z pomiarów elektrochemicznych takich jak woltamperometria cykliczna czy elektrochemiczna spektroskopia impedancyjna. Dla najbardziej obiecujących materiałów przeprowadzono badania stabilności parametrów pracy w układzie laboratoryjnego elektrolizera. Uzyskane wyniki wskazują na możliwość poprawy parametrów materiałów poprzez odpowiedni dobór metod modyfikacji chemicznej oraz obróbki mechanicznej. Wyniki badań zostały opublikowane w międzynarodowych czasopismach naukowych i stanowią część niniejszej rozprawy.

Streszczenie rozprawy w języku angielskim: The topic of the synthesis and application of nanocrystalline metal oxides as catalysts for the oxygen evolution reaction in alkaline electrolyte, i.e., one of the reactions occurring during water electrolysis, was addressed in this work. Special attention was given to spinel and perovskite oxides, which are known for their exceptional electrical, magnetic, optical, and catalytic properties. The materials were prepared using the sol--gel method or high-temperature solid-state synthesis. Attempts were made to modify the materials by introducing new elements into the crystal structure or applying

additional thermal or mechanical treatment to improve the catalyst's performance parameters. Structural studies were conducted using microscopy and spectroscopy techniques, while the electrocatalytic activity was evaluated using electrochemical measurements such as cyclic voltammetry and electrochemical impedance spectroscopy. For the most promising materials, stability studies of the performance parameters were conducted in a laboratory electrolyzer setup. The obtained results indicate the possibility of improving material parameters through the appropriate selection of chemical modification methods and mechanical processing. The research results were published in international scientific journals and are part of this dissertation.

Rozprawa Doktorska

Nanokrystaliczne tlenki metali jako katalizatory reakcji wydzielania tlenu w środowisku zasadowym

mgr inż. Krystian Lankauf

Promotor: dr hab. inż. Sebastian Molin

„Praca wykonana przy wsparciu grantu Fundacji na rzecz Nauki Polskiej – POIR.04.04.00-00-42E9/17-00”

FNP Fundacja na rzecz Nauki Polskiej

SPIS TREŚCI

WYKAZ WAŻNIEJSZYCH OZNACZEŃ I SKRÓTÓW

AWE – alkaline water electrolyzer (elektrolizer alkaliczny)

CCM – catalyst-coated membrane (membrana pokryta katalizatorem)

CCS – catalyst-coated substrate (elektroda pokryta katalizatorem)

CE – counter electrode (elektroda pomocnicza)

CPE – constant phase element

CV – cyclic voltammetry (woltamperometria cykliczna)

CVD – chemical vapour deposition (chemiczne osadzanie z fazy gazowej)

ECSA – electrochemically active surface area (powierzchnia elektrochemicznie aktywna)

EDS – energy dispersive spectroscopy (spektroskopia dyspersji energii)

EDTA - ethylenediaminetetraacetic acid (kwas wersenowy)

EIS – electrochemical impedance spectroscopy (elektrochemiczna spektroskopia impedancyjna)

FCC - face-cantered cubic (komórka ściennie centrowana)

FTIR – fourier transform infrared (spektroskopia fourierowska w podczerwieni)

GD – glassy carbon (węgiel szklisty)

GDL – gas diffusion layer (warstwa gazodyfuzyjna)

HER – hydrogen evolution reaction (reakcja wydzielania wodoru)

ICP-OES - inductively coupled plasma optical emission spectroscopy (spektroskopia emisyjna z wzbudzeniem plazmowym)

LSM – lanthanum strontium manganite (manganian lantanowo strontowy)

LSV – linear sweep voltammetry (woltamperometria liniowa)

MEA – membrane electrode assembly (zespół elektrody-membrana)

MOF – metal-organic framework (szkielet metalo-organiczny)

NEXAFS – near edge x-ray absorption fine structure (blisko krawędziowa subtelna struktura absorpcyjna)

OCV – open circuit voltage (napięcie obwodu otwartego)

OER – oxygen evolution reaction (reakcja wydzielania tlenu)

OZE – odnawialne źródła energii

PEME – polymer electrolyte membrane water electrolyzer (elektrolizer z polimerową membraną elektrolityczną)

PLD – pulsed laser deposition (osadzanie laserem impulsowym)

RDE – rotating disk electrode (wirująca elektroda dyskowa)

RE – reference electrode (elektroda odniesienia)

RHE – reversible hydrogen electrode (odwracalna elektroda wodorowa)

SEM – scanning electron microscopy (skaningowa mikroskopia elektronowa)

SCR – soft chemistry route (synteza metodami mokrymi)

SLA – stereolithography (stereolitografia)

SSR – solid state reaction (synteza w fazie stałej)

SOEC – solid oxide electrolyzer cell (elektrolizer tlenkowy)

TEM – transmission electron microscopy (transmisyjna mikroskopia elektronowa)

TEY – total electron yield (pomiar prądu próbki)

TGA – thermogravimetric analysis (termograwimetria)

WE – working electrode (elektroda pracująca)

XAS – x-ray absorption spectroscopy (absorpcyjna spektroskopia promieni X)

XPS – x-ray photoelectron spectroscopy (rentgenowska spektroskopia fotoelektronów)

YSZ – yttrium stabilized zirconia (tlenek cyrkonu stabilizowany itrem)

a – punkt przecięcia z osią rzędnych

b – nachylenie krzywej Tafela

C_{DL} – double layer capacitance (pojemność warstwy podwójnej)

C_S – specific capacitance (pojemność właściwa)

E – rzeczywisty potencjał elektrody

E_0 – amplituda sygnału

E_a – energia aktywacji przewodnictwa

$E(t)$ – sygnał wzbudzający (potencjał w czasie)

$E°$ - napięcie równowagowe

E_{RHE} – zmierzony potencjał elektrody pracującej w odniesieniu do potencjału równowagowego RHE

F – stała Faradaya

h – grubość próbki

i – natężenie prądu

$I(t)$ – odpowiedź prądowa (natężenie prądu w czasie)

I_0 – amplituda odpowiedzi

j – gęstość prądu

k – stała Boltzmanna

K – stała związana z kształtem refleksów

n – liczba moli elektronów biorących udział w reakcji

R – rezystancja

T – temperatura

v – prędkość skanu (zmian potencjału)

Z – impedancja

Z_0 – moduł impedancji

β – szerokość refleksu zależna od wielkości krystalitów

ΔG - zmiana energii swobodnej Gibbsa

η – nadpotencjał

θ – kąt Bragga

λ – długość fali promieniowania

σ – przewodność próbki

σ_o – czynnik przedwykładniczy

τ – średni rozmiar krystalitów

φ – przesunięcie fazowe

ω – pulsacja

1. WSTĘP

Dynamicznemu rozwojowi cywilizacji od zawsze towarzyszy zwiększające się zapotrzebowanie na energię. Obecnie ok. 80% światowego zapotrzebowania energetycznego jest zaspokajane poprzez produkcję energii opartą na paliwach kopalnych [1]. Eksploatacja paliw kopalnych jako źródła energii powoduje emisję zanieczyszczeń do atmosfery w postaci dymów, gazów i pyłów. Ponadto, przy założeniu rosnącej konsumpcji, szacunki wskazują, że rezerwy paliw kopalnych są następujące: ropa naftowa - 30 lat, gaz ziemny - 40 lat, węgiel - 70 lat [2]. W związku z powyższym panuje konsensus, że nieodzowne jest poszukiwanie nowych, zrównoważonych, czystych i odnawialnych źródeł energii (OZE). Sezonowość oraz podatność na zmiany pogody ograniczają możliwość odnawialnych źródeł energii do zapewnienia ciągłości dostaw energii, dlatego konieczne jest magazynowania energii w momencie gdy jej produkcja przeważa nad zużyciem. Spośród wielu metod magazynowania energii (elektrownie szczytowo-pompowe, akumulatory elektryczne, koła zamachowe) wodór uznawany jest za przyszłościowy nośnik energii [3–5].

Wodór jest najprostszym i najczęściej występującym pierwiastkiem we Wszechświecie. W temperaturze pokojowej ma postać cząsteczkową H_2 jako bezwonny i bezbarwny gaz. Na Ziemi wodór nigdy nie występuje w prostej formie cząsteczkowej, a w postaci substancji złożonej tj. wody lub związków organicznych. W związku z tym wodoru nie można traktować jako źródła energii ale jako jej nośnik, który może zostać wyprodukowany przy pomocy innych źródeł energii, takich jak paliwa kopalne, energia jądrowa czy odnawialne źródła energii. Ponadto wodór znajduje szerokie zastosowanie w przemyśle chemicznym, metalurgicznym i spożywczym [6,7]. Aby wyróżnić wpływ metod produkcji wodoru na środowisko wprowadzono nomenklaturę bazującą na „kolorze wodoru” [3]. M.in. wyróżnia się: wodór szary – pochodzący z paliw kopalnych, wodór niebieski – również pochodzący z paliw kopalnych, ale w procesie produkcji zastosowano metody wychwytu dwutlenku węgla, wodór turkusowy otrzymany w procesie pirolizy metanu lub w wyniku przetwarzania odpadowych tworzyw sztucznych, wodór różowy/czerwony/purpurowy produkowany w procesie elektrolizy zasilanej energią jądrową, wodór żółty wytwarzany w procesie elektrolizy z bezpośrednim wykorzystaniem energii słonecznej oraz wodór zielony – wytwarzany w procesie elektrolizy wody zasilanym z OZE.

Wyróżnia się m.in. następujące metody produkcji wodoru:

-termiczne, np. reforming parowy gazu ziemnego,

-biologiczne np. procesy wykorzystujące fotosyntezę lub fermentację

-elektrochemiczne np. elektroliza wody [8].

Roczna produkcja wodoru wynosi ok. 50 milionów ton, z czego 96% pochodzi z reformingu węglowodorów, 4% z elektrolizy wody, natomiast pozostałe metody produkcji pozostają w sferze badań i rozwoju (B+R) [4,5]. Ze względu na nadzieje pokładane w wodorze jako przyszłościowym nośniku energii kluczowa jest zmiana tego trendu, tak, aby największy udział miały technologie oparte na elektrolizie. W dalszej części pracy przedstawione są

perspektywy oraz ograniczenia związane z elektrochemicznym rozkładem wody oraz opis prac nad rozwojem tej metody, które zostały wykonane w ramach dysertacji.

Na rysunku 1 przedstawiono schematyczny koncept systemu zarządzania energią, w którym elektroliza wody odgrywa ważną rolę w produkcji wodoru jako paliwa gazowego oraz nośnika energii. W momencie, gdy produkcja energii elektrycznej z OZE przewyższa zapotrzebowanie, nadmiar energii wykorzystywany jest do produkcji wodoru w procesie elektrolizy. W sytuacji odwrotnej zmagazynowany wodór może być wykorzystany bezpośrednio jako paliwo gazowe lub do wytwarzania energii elektrycznej w ogniwie paliwowym, która następnie trafia do sieci.

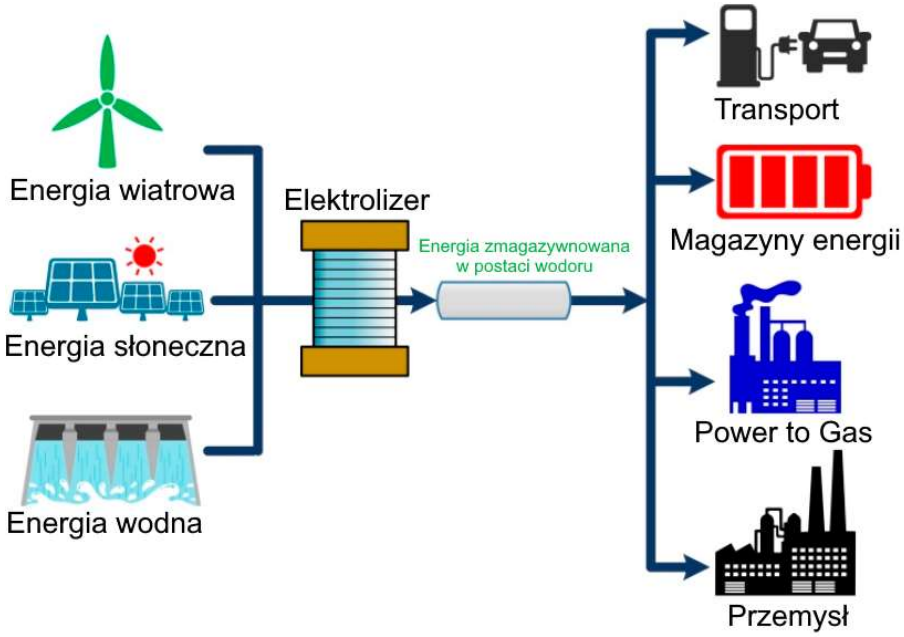

Rys. 1 Schematyczny koncept systemu zarządzania energią z wykorzystaniem elektrolizy wody [9]

W niniejszej pracy przedstawiono elektrolizę wody jako obiecującą metodę produkcji zielonego wodoru. Omówione zostały zachodzące procesy elektrochemiczne, aktualnie stosowane typy elektrolizerów, wady, zalety i perspektywy rozwoju materiałów wykorzystywanych do konstrukcji elektrolizerów. Badania własne skoncentrowane były na niezwykle istotnym zagadnienia tj. reakcji utleniania tlenu (OER – oxygen evolution reaction), jednej z dwóch reakcji zachodzących podczas elektrolizy. Ze względu na 4-elektronowy charakter tej reakcji jest ona obarczona wysokimi nadpotencjałami, więc ma znaczący wpływ na całościowy proces elektrolizy wody. Dlatego niezwykle istotne jest znalezienie materiałów elektrokatalitycznych, które pozwolą na redukcję nadpotencjału reakcji OER.

Za pomocą syntezy zol-żel oraz wysokotemperaturowej syntezy w fazie stałej przygotowano nanokrystaliczne materiały tlenkowe o strukturze krystalicznej spinelu i perowskitu. Jako materiały nanokrystaliczne definiuje się materiały zbudowane z elementów (krystalitów, ziaren, warstw, włókien etc.), których rozmiar nie przekracza 100 nm w przynajmniej jednym wymiarze [10]. Sprawdzona została aktywność elektrokatalityczna oraz stabilność tych

materiałów w środowisku zasadowym. Ponadto wskazano posyntezową obróbkę cieplną lub mechaniczną jako metody modyfikacji właściwości fizykochemicznych tych materiałów mających wpływ na ich wydajność. Zaproponowane elektrokatalizatory stanowią alternatywę dla dotychczas stosowanych materiałów elektrodowych.

1.1. Elektroliza wody

Elektrolizą wody nazywamy elektrochemiczną reakcję rozkładu wody w wyniku czego powstaje wodór i tlen, zgodnie z równaniem (1) i przedstawione na rys. 2:

$$2H_2O \rightarrow 2H_2 + O_2 \quad (1)$$

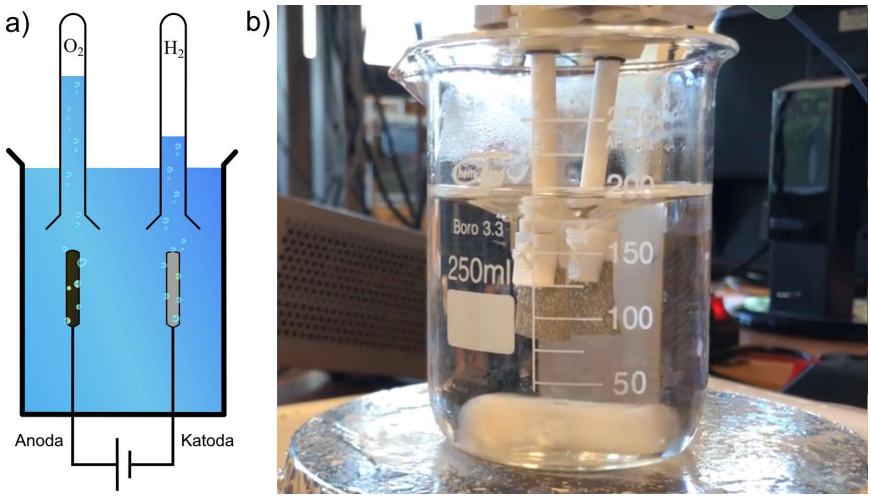

Rys. 2 (a) Schemat układu do elektrolizy wody [11] oraz (b) prosty dwuelektrodowy układ laboratoryjny

Podczas elektrolizy wody na elektrodach zachodzą dwie reakcje:

- Katoda: reakcja wydzielania wodoru (HER – hydrogen evolution reaction)
- Anoda: reakcja wydzielania tlenu (OER – oxygen evolution reaction)

Rozkład wody, w warunkach idealnych (odwracalnych) powinien nastąpić przy napięciu 1,23 V pomiędzy katodą i anodą. W praktyce ze względu na występowanie strat w rzeczywistych układach, którymi obarczone są reakcje elektrodowe, do utrzymania procesu wymagane są wyższe wartości napięcia; różnicę pomiędzy wartościami napięć określa się nadpotencjałami.

Kinetyka procesu elektrolizy wody zależy od wielu czynników, m.in.: materiału elektrod, mikrostruktury elektrod, np. stanu ich powierzchni (gładkie, porowate itp.) oraz parametrów zewnętrznych (temperatura i ciśnienie) [12]. Uzyskiwany wodór wykazuje wysoką czystość (99,9%, a nawet 99,999%)[13–15], co jest wielką zaletą w porównaniu do produkcji opartej na paliwach kopalnych i biomasie. Ponadto przy założeniu zasilania elektrolizera z OZE otrzymuje się zeroemisyjny - zielony wodór.

W celu zapewnienia wysokiej przewodności jonowej pomiędzy elektrodami stosuje się silne kwasy lub zasady jako elektrolity, w których zachodzą reakcje elektrolizy wody. W zależności od pH roztworu nośnikami ładunku elektrycznego są protony lub jony wodorotlenkowe.

Sumaryczna reakcja elektrolizy nie jest zależna od pH zastosowanego elektrolitu natomiast różne mogą być mechanizmy poszczególnych reakcji elektrodowych co jest przedstawione poniżej.

1.1.1. Reakcja wydzielania wodoru – HER

Reakcja wydzielania wodoru zachodzi na katodzie zgodnie z poniższymi równaniami:

Roztwór	Reakcja całkowita	Poszczególne etapy	
Kwaśny (pH<7)	$2H^+ + 2e^- \rightarrow H_2$	$H^+ + e^- \rightarrow H_{ads}$ (Volmer)	(2)
		$H^+ + e^- + H_{ads} \rightarrow H_2$ (Heyrovsky)	(3)
		lub	
		$2H_{ads} \rightarrow H_2$ (Tafel)	(4)
Zasadowy (pH>7)	$2H_2O + 2e^- \rightarrow H_2 + 2OH^-$	$H_2O + e^- \rightarrow H_{ads} + OH^-$(Volmer)	(5)
		$H_2O + e^- + H_{ads} \rightarrow H_2 + OH^-$(Heyrovsky)	(6)
		lub	
		$2H_{ads} \rightarrow H_2$(Tafel)	(7)

W pierwszym etapie, w roztworze kwaśnym, w wyniku transferu protonu z elektrolitu i jego rekombinacji z elektronem dostarczonym przez elektrodę następuje adsorpcja atomu wodoru (H_{ads}) na powierzchni elektrody. W roztworze zasadowym dodatkowo zachodzi dysocjacja cząsteczki wody. Ten krok nosi nazwę reakcji Volmera. W następnym kroku są dwie możliwości, reakcja Heyrovsky'ego, w której zaadsorbowany atom wodoru łączy się z elektronem przeniesionym z powierzchni elektrody i protonem z elektrolitu tworząc jedną cząsteczkę wodoru; druga to reakcja Tafela, w której dwa sąsiadujące, zaadsorbowane atomy wodoru łączą się tworząc jedną cząsteczkę wodoru [12,16].

1.1.2. Reakcja wydzielania tlenu – OER

Poniżej przedstawione są ogólnie przyjęte przebiegi reakcji wydzielania tlenu w roztworach kwaśnych i zasadowych, obejmujące przeniesienie czterech elektronów. W roztworach kwaśnych wydzielanie tlenu zachodzi poprzez bezpośrednie utlenianie cząsteczki wody, natomiast w roztworach zasadowych następuje przeniesienie ładunku i adsorpcja rodnika OH [12,16].

Roztwór	Reakcja całkowita	Poszczególne etapy	
Kwasowy (pH<7)	$2H_2O \rightarrow O_2 + 4H^+ + 4e^-$	$H_2O \rightarrow OH_{ads} + H^+ + e^-$	(8)
		$OH_{ads} \rightarrow O_{ads} + H^+ + e^-$	(9)
		$O_{ads} + H_2O \rightarrow OOH_{ads} + H^+ + e^-$	(10)
		$OOH_{ads} \rightarrow O_{2\,ads} + H^+ + e^-$	(11)
		$O_{2\,ads} \rightarrow O_2$	(12)

		$OH^- \rightarrow OH_{ads} + e^-$	(13)
Zasadowy	$4OH^- \rightarrow O_2 + 2H_2O + 4e^-$	$OH_{ads} + OH^- \rightarrow H_2O + O_{ads} + e^-$	(14)
(pH>7)		$O_{ads} + OH^- \rightarrow OOH_{ads} + e^-$	(15)
		$OOH_{ads} + OH^- \rightarrow O_{2\,ads} + e^-$	(16)
		$O_{2\,ads} \rightarrow O_2$	(17)

1.1.3. Elektrolizer wody jako obwód elektryczny

Zanim zajdzie całościowy proces elektrolizy wody musi zostać pokonany szereg barier, do których zaliczyć można np.:

- energie aktywacji reakcji elektrochemicznych zachodzących na powierzchniach elektrod,
- dostępność powierzchni elektrod ograniczona przez częściowe pokrycie powstającymi pęcherzykami gazów,
- opór elektryczny elektrolitu,
- opór elektryczny obwodu.

Rezystancje związane z reakcjami elektrodowymi wynikają z nadpotencjałów wymaganych do pokonania energii aktywacji wydzielania tlenu i wodoru na powierzchniach anody i katody. Pozostałe rezystancje związane są z transportem reagentów w elektrolicie jak i ograniczonym kontaktem pomiędzy elektrodami a elektrolitem wynikającym z pokrycia powierzchni elektrod produktami reakcji tj. pęcherzykami gazów O_2 i H_2. Na opór elektryczny obwodu składają się rezystancje związane z okablowaniem i kontaktem elektrycznym elektrod. Są one obliczane z prawa Ohma i wynikają z przewodności właściwiej i przekroju poprzecznego przewodników.

1.1.4. Napięcie elektrolizera

Aby wyprodukować wodór (i tlen) z wody poprzez jej elektrolizę należy przyłożyć napięcie o wartości przewyższającej napięcie równowagowe E°. Teoretyczne napięcie potrzebne aby doszło do rozkładu wody w warunkach standardowych wynosi 1,23 V. Korzystając z wartości napięcia równowagowego można obliczyć zmianę energii swobodnej Gibbsa ΔG:

$$\Delta G = nFE^o \tag{18}$$

, gdzie *n* – liczba moli elektronów biorących udział w reakcji, *F* – stała Faradaya [C mol^{-1}], *E*°- napięcie równowagowe [V]. Jest to minimalna energia potrzebna do produkcji jednego mola wodoru i w warunkach standardowych wynosi 237,2 kJ mol^{-1}.

W praktyce przyłożenie napięcia równego potencjałowi równowagowemu jest niewystarczające do przebiegu reakcji rozkładu wody. Wartość przyłożonego napięcia należy powiększyć o pewną wartość nazywaną nadpotencjałem (nadnapięciem) η. Wartość nadpotencjału wynika z występowania przedstawionego powyżej szeregu rezystancji w celce

elektrochemicznej. Całkowite napięcie potrzebne do przeprowadzenia procesu elektrolizy wyznacza się ze wzoru:

$$E = E_{anody} - E_{katody} + \sum|\eta| + iR \tag{19}$$

, gdzie: E – napięcie przyłożone do elektrolizera [V], E_{anody} i E_{katody} – potencjały anody i katody, $\sum|\eta|$ - suma nadpotencjałów reakcji elektrodowych [V], i – natężenie prądu przepływającego przez elektrolizer [A], R – suma rezystancji omowych pochodzących od elektrolitu i konstrukcji elektrolizera [Ω].

1.1.5. Sprawność elektrolizera

Z elektrochemicznego punktu widzenia napięciową sprawność elektrolizera można obliczyć z następującego równania:

$$\text{Sprawność napięciowa} = \frac{(E_{anody} - E_{katody}) \cdot 100\%}{E} \tag{20}$$

Fizyczne znaczenie tej definicji sprowadza się do stosunku efektywnego napięcia rozpadu wody do całkowitego napięcia przyłożonego do elektrolizera.

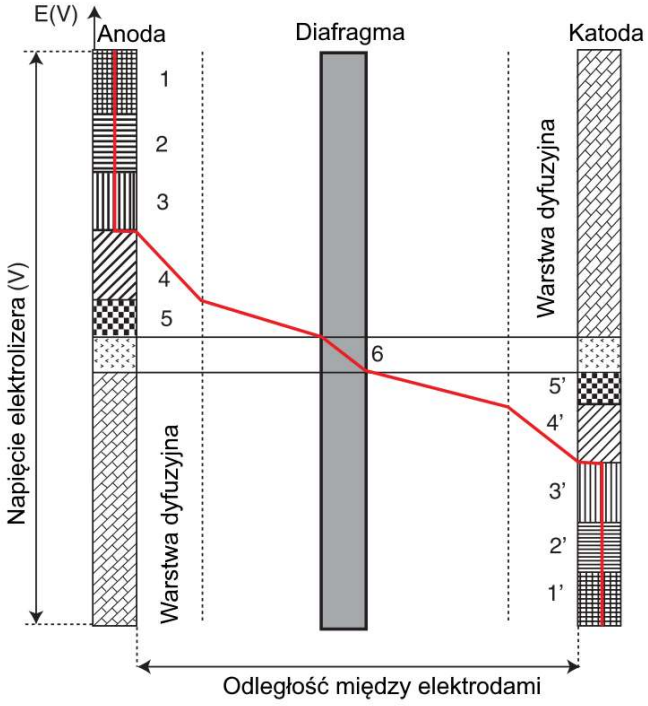

Rys. 3 Schemat rozkładu potencjału w elektrolizerze [4]

Największa część energii elektrycznej dostarczanej do elektrolizera (> 60%) wykorzystywana jest do zmiany energii swobodnej Gibbsa związanej z zachodzącą reakcją endoenergetyczną [4]. Istnieje jednak kilka miejsc, w których następuje rozpraszanie energii w postaci ciepła. Ich lokalizacja oraz znaczenie zależą od zastosowanej konstrukcji elektrolizera. Na rysunku 3 przedstawiono przekrój poprzeczny elektrolizera z ciekłym elektrolitem i występujące w nim spadki potencjału. Spadki te występują: w całej objętości elektrod (1, 1') ze

względu na ich wewnętrzną rezystancję; na warstwach elektrokatalitycznych (2, 2'), które nie zawsze są dobrymi przewodnikami prądu elektrycznego; na powierzchniach na których zachodzą procesy przeniesienia ładunku (3, 3'); w roztworze przez warstwy dyfuzyjne blisko powierzchni elektrod, gdzie występują zjawiska transportu masy lub tworzą się formy gazowe (4, 4'); w objętości elektrolitu w wyniku transportu jonów; oraz w diafragmie (separatorze) półogniw elektrolizera.

Na rysunku 4 przedstawiony jest kształt krzywej polaryzacyjnej elektrolizera wody pracującego w warunkach standardowych. Jak już wspomniano napięcie równowagowe wynosi 1,23 V. Powyżej tej wartości przez elektrolizer zaczyna przepływać prąd elektryczny. Natomiast przy napięciu 1,48 V nazywanym napięciem termoneutralnym dostarczana energia jest wystarczająca zarówno do napędzenia reakcji elektrochemicznej jak i utrzymaniu stałej temperatury. Powyżej napięcia termoneutralnego dodatkowa energia jest wykorzystywana do pokonania wewnętrznych rezystancji i rozpraszana w postaci ciepła do otoczenia. Przy małych gęstościach prądu omowe spadki napięcia są małe przy czym te związane z przeniesieniem ładunku są maksymalne. Logarytmiczny kształt krzywej polaryzacyjnej wynika właśnie ze zjawisk przeniesienia ładunku na anodzie i katodzie. W przypadku elektrolizy wody nadpotencjał reakcji anodowej (OER) jest wyraźnie wyższy niż reakcji katodowej (HER), ze względu na wolniejszą kinetykę reakcji OER. Wraz ze wzrostem gęstości prądu maleje rezystancja przeniesienia ładunku a krzywa polaryzacyjna przyjmuje charakter liniowy. Świadczy to o omowym charakterze elektrolizera (suma rezystancji elektronowej i jonowej). Pasożytnicze straty omowe są szczególnie widoczne w przemysłowych układach do elektrolizy wody o dużej powierzchni i odpowiadają za zwiększone zużycie energii i zmniejszoną sprawność konwersji energii.

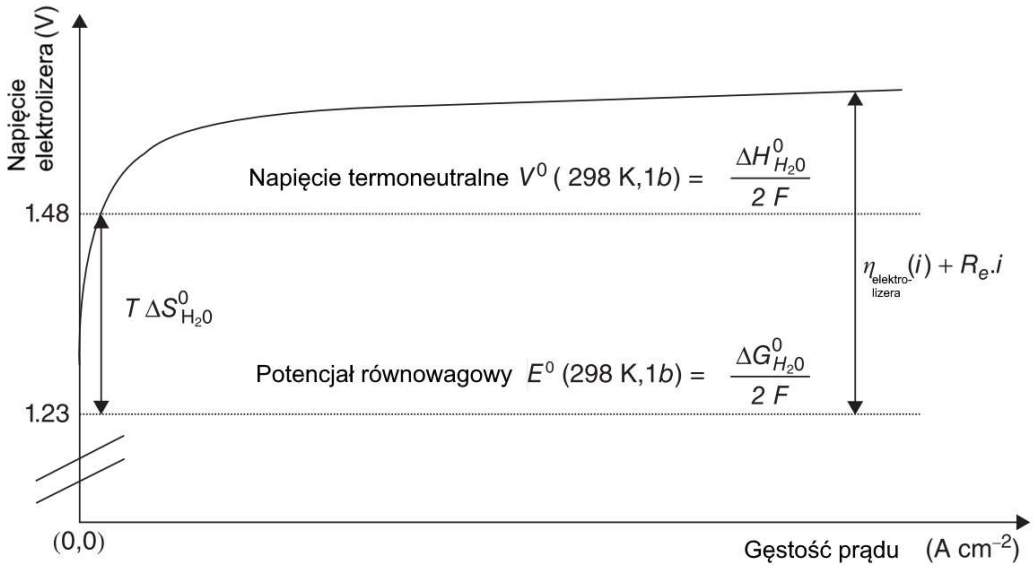

Rys. 4 Schematyczna krzywa polaryzacyjna elektrolizy wody [17]

Ilość gazów powstających w trakcie elektrolizy jest wprost proporcjonalna do prądu przepływającego przez obwód elektryczny co wynika z prawa Faradaya. Za każdym razem gdy

przez obwód przepływają 4 elektrony powstaje jedna cząsteczka tlenu i dwie cząsteczki wodoru (w przypadku idealnym).

1.2. Rodzaje elektrolizerów

Technologie elektrolizy wody klasyfikuje się na podstawie zastosowanego elektrolitu, oddzielającego dwie reakcje połówkowe przebiegające na anodzie (OER) oraz katodzie (HER). Poniżej przedstawiono budowę głównych typów elektrolizerów wody:

1.2.1. Elektrolizery z polimerową membraną elektrolityczną

Tak jak wskazuje nazwa elektrolizery z polimerową membraną elektrolityczną (ang. polimer electrolyte membrane water electrolyser – PEMWE) składają się z anody i katody odseparowanych od siebie za pomocą polimerowej membrany elektrolitycznej (rys.5).

Na poszczególnych elektrodach zachodzą następujące reakcje elektrodowe:

$$2\mathrm{H}^+ + 2\mathrm{e}^- \rightarrow \mathrm{H}_2 \text{ (katoda)} \quad (21)$$

$$\mathrm{H}_2\mathrm{O} \rightarrow \frac{1}{2}\mathrm{O}_2 + 2\mathrm{H}^+ + 2\mathrm{e}^- \text{ (anoda)} \quad (22)$$

Membrana PEM (np. Nafion™) powinna wykazywać wysokie przewodnictwo protonowe. Ponadto zastosowanie membrany pozwala na odseparowanie produktów gazowych oraz pracę przy wysokim ciśnieniu, do 100 barów, zmniejszając objętość powstających pęcherzy gazowych, a zatem rezystancji omowej. Kluczowym aspektem jest zastosowanie katalizatorów HER oraz OER, które oprócz aktywności katalitycznej wykazują stabilność w środowisku pracy elektrolizera PEME, tj. środowisku kwasowym. Aktualny stan wiedzy wskazuje odpowiednio tlenek irydu oraz platynę jako materiały spełniające powyższe wymagania, jednak ich ograniczone zasoby, a więc wysoki koszt, ograniczają możliwość zastosowania ich w skali przemysłowej [18].

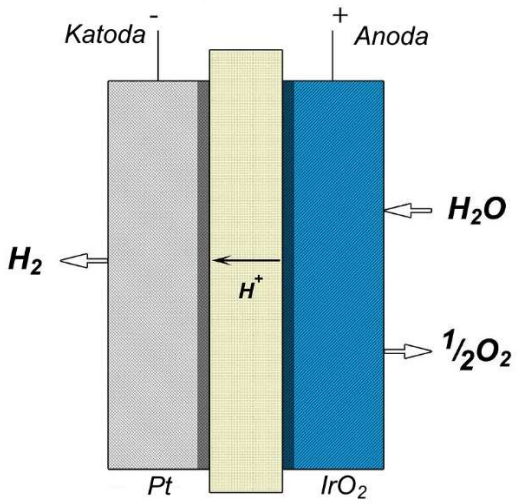

Rys. 5 Schemat elektrolizera z polimerową membraną elektrolityczną [19]

1.2.2. Elektrolizery alkaliczne

W elektrolizerach alkalicznych (AWE – ang. alkaline water electrolyzer) elektrody zanurzone są w elektrolicie o odczynie zasadowym, najczęściej 20 - 30% wodorotlenku potasu. Elektrolizery te pracują w temperaturach nieco poniżej 100°C i ciśnieniu atmosferycznym. Przedstawione na rys. 6 elektrody są odseparowane diafragmą przewodzącą jony wodorotlenkowe OH^-, co ma na celu odseparowanie i zapobieganie rekombinacji powstających cząsteczek wodoru i tlenu. Poniżej przedstawione są reakcje zachodzące na elektrodach:

$$2H_2O + 2e^- \rightarrow H_2 + 2OH^- \text{(katoda)} \quad (23)$$

$$2OH^- \rightarrow \frac{1}{2}O_2 + H_2O + 2e^- \text{ (anoda)} \quad (24)$$

Spośród wyróżnianych typów elektrolizerów to elektrolizery AWE stanowią najbardziej rozwiniętą technologię dostępną komercyjnie. Konstrukcję pierwszego przemysłowego elektrolizera alkalicznego przypisuje się Dmitrowi Lachinov i datuje na koniec XIX wieku [20]. Pomimo długiej historii technologia ta wciąż jest obarczona pewnymi wadami, np. zastosowanie diafragmy prowadzi do wysokich strat omowych i ogranicza maksymalną uzyskiwaną gęstość prądu. Wykorzystywane diafragmy nie są przystosowane do pracy przy wysokim ciśnieniu, ponieważ może dochodzić do mieszania produktów gazowych, wodoru i tlenu. Największą zaletą jest brak potrzeby stosowania kosztownych katalizatorów z grupy platynowców, gdyż dużo tańsze alternatywny, np. nikiel, wykazują wysoką aktywność katalityczną przy jednoczesnej odporności na korozję w środowisku zasadowym pozwalającej na czas pracy wynoszący 20-30 lat [21].

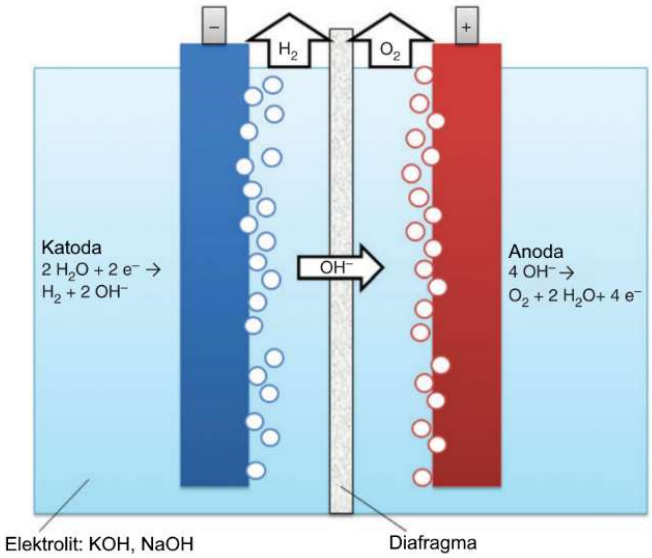

Rys. 6. Schemat elektrolizera alkalicznego [22]

1.2.3. Ogniwa fotoelektrochemiczne

W ogniwach fotoelektrochemicznych energia promieniowania jest przekształcana w energię chemiczną. Tak jak przedstawiono na rys. 7 powstająca para elektron-dziura oddziałuje z elektrolitem w wyniku czego powstaje wodór i tlen. Elektron i dziura generowane są poprzez

foton zaabsorbowany w półprzewodniku typu n. Na fotoanodzie powstaje tlen w wyniku utleniania wody przez dziurę, natomiast na fotokatodzie elektron redukuje wodę i powstaje wodór [23]. Ze względu na specyfikę pracy wyróżnia się trzy podstawowe rodzaje ogniw fotoelektrochemicznych tj. fotoelektrolizery, fotoelektrolizery wspomagane oraz elektrolizery fotowoltaiczne [24].

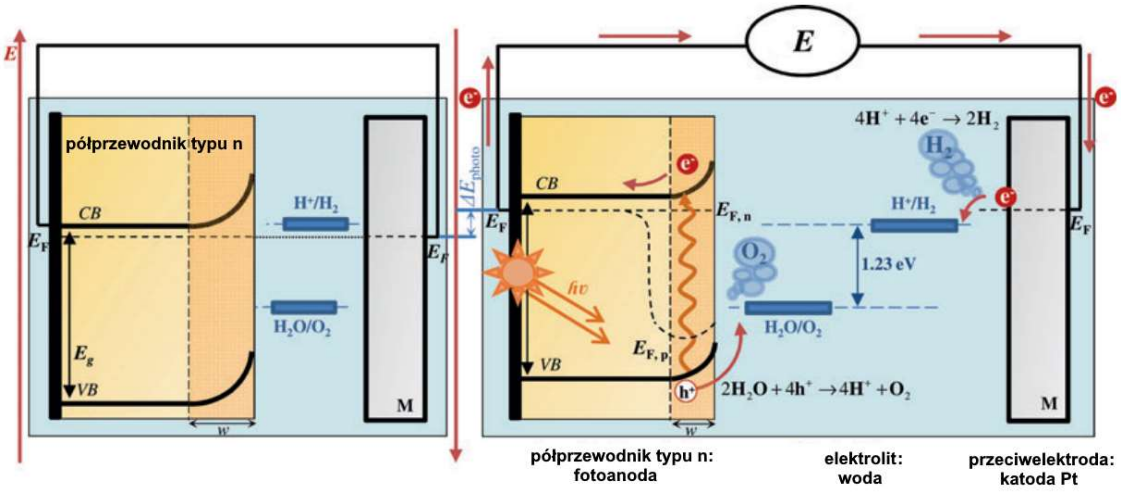

Rys. 7. Diagram energetyczny ogniwa fotoelektrochemicznego [25]

1.2.4. Elektrolizery tlenkowe

Elektrolizery tlenkowe (ang. solid oxide electrolyzer cell – SOEC) zbudowane są z katody i anody odseparowanych stałym, przewodzącym jony O^{2-} elektrolitem (rys. 8). Typowy SOEC składa się z elektrolitu w postaci tlenku cyrkonu stabilizowanego itrem (YSZ), cermetowej katody Ni/YSZ (elektroda wodorowa), oraz anody z kompozytu manganianu lantanowo strontowego (LSM)/YSZ (elektroda powietrzna). Na elektrodach zachodzą następujące reakcje:

$$H_2O + 2e^- \rightarrow H_2 + O^{2-} \text{(katoda)} \quad (25)$$

$$O^{2-} \rightarrow \frac{1}{2}O_2 + 2e^- \text{ (anoda)} \quad (26)$$

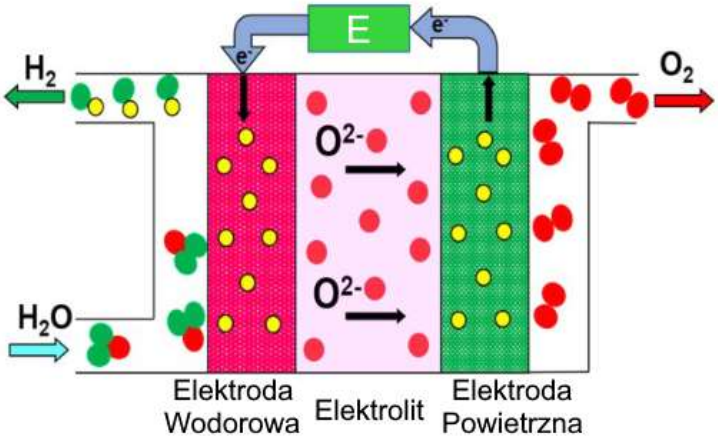

Rys. 8. Elektrolizer tlenkowy [26]

Cechą wyróżniającą ten rodzaj elektrolizera w porównaniu do poprzednich jest wysoka temperatura pracy w zakresie 700°C – 900°C, wynikająca ze słabego przewodzenia O^{2-} w niższych temperaturach. Elektrolizery tlenkowe odznaczają się wysoką wydajnością faradajowską produkcji wodoru sięgającą 100%. Wysoka wydajność wynika z poprawionej kinetyki reakcji oraz wykorzystaniu dostarczonego ciepła. Z drugiej strony wysoka temperatura pracy wpływa na szybszą degradację materiałów składowych, szczególnie anody [5].

1.3. Szczegółowa charakterystyka elektrolizerów alkalicznych

Jak już wspomniano największą zaletą elektrolizerów alkalicznych jest możliwość zastosowania stosunkowo tanich materiałów elektrodowych (stopy żelaza i niklu) do produkcji wodoru i tlenu. Elektrody zanurzone są w stężonym elektrolicie zasadowym, np. 6 M KOH, i są odseparowane diafragmą lub membraną przenoszącą jony hydroksylowe (OH^-) jednocześnie stanowiącą barierę dla powstających cząsteczek H_2 i O_2. Zastosowanie separatora przeciwdziała mieszaniu się powstających gazów i zapobiega powstaniu mieszanki wybuchowej.

1.3.1. Elektrolit

Objętość elektrolitu zapełniająca celkę elektrochemiczną wynika z odległość pomiędzy elektrodami. W typowych układach odległość ta mieści się w zakresie od milimetrów do centymetrów. Rezystancje omowe wewnątrz elektrolizera rosną wraz z odległością między elektrodami, jednak gdy odległość jest zbyt mała, co za tym idzie mała objętość elektrolitu wypełnia wnętrze celki, stężenie substratów dynamicznie zmienia się w okolicach elektrod powodując spadek wydajności układu.

Podstawowym kryterium wyboru elektrolitu jest jego przewodność elektryczna. Na rys. 9 przedstawione są zmiany przewodności roztworów KOH oraz NaOH. Na podstawie tej charakterystyki często stosowanym elektrolitem jest 30% KOH (6,9 M KOH).

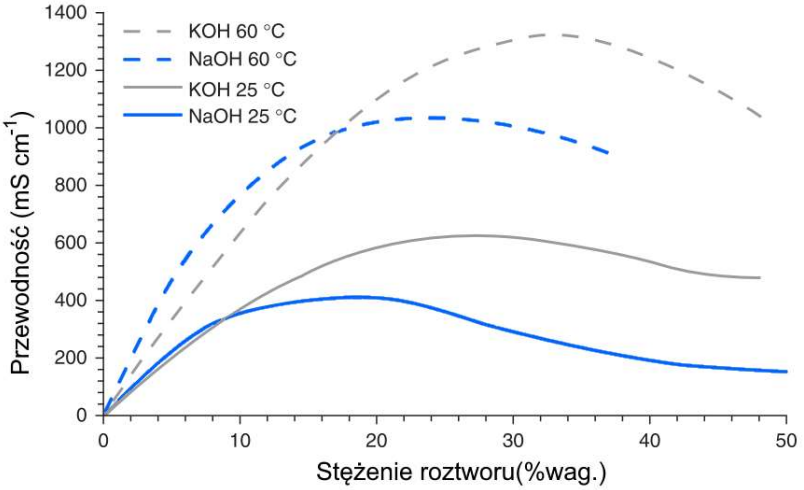

Rys. 9 Przewodność elektryczna roztworów KOH i NaOH [4]

1.3.2. Materiały elektrodowe

Materiały, z których wykonane są elektrody układu alkalicznego elektrolizera muszą spełniać szereg wymagań podyktowanych przez specyfikę warunków pracy. Przede wszystkim są to: dobra odporność korozyjna, wysoka przewodność elektryczna i dobre właściwości katalityczne reakcji wydzielania wodoru/tlenu. Kinetyka przebiegu reakcji HER i OER silnie zależy od doboru materiału z jakiego wykonano elektrody, ale nie jest to jedyny parametr. Ponadto wyraźny wpływ mają zastosowana obróbka (np. historia termiczna) oraz mikrostruktura i morfologia elektrod.

Najbardziej aktywnym materiałem katodowym jest platyna oraz pozostałe metale z grupy platynowców. Jednak ze względu na ich zaporowe ceny zwykle wybieraną alternatywą są stale nierdzewne oraz stopy niklu [22]. W celu poprawy stabilności i aktywności elektrod na bazie niklu stosowane są powłoki z bardziej aktywnych lub stabilniejszych materiałów np. kobaltu, glinu czy żelaza. Innym podejściem jest zastosowanie dodatków stopowych np. siarki w celu poprawy mikrostruktury powierzchni stopu. Ma to szczególne znaczenie w związku z powierzchniowym charakterem reakcji HER.

Ze względu na wysokie nadpotencjały reakcji OER, wartość potencjału procesu anodowego wydzielania tlenu jest zawsze dodatnia, niezależnie od zastosowanego katalizatora. W związku z tym powierzchnia anody zawsze pokrywa się warstwą tlenkową. Co więcej, w dłuższym czasie, wysoki nadpotencjał prowadzi do korozji zarówno katalizatora jak i przewodzącego rdzenia anody. Jest to jedna z głównych przeszkód występujących przy zwiększaniu żywotności katalizatora OER. Oprócz aktywności w kierunku OER oraz długoterminowej stabilności materiały anodowe muszą cechować się niską ceną i łatwą dostępnością, a metody ich wytwarzania powinny być proste i łatwe do skalowania do rozmiarów przemysłowych. Podobnie jak w przypadku katalizatorów katodowych dobrymi właściwościami katalizy OER wyróżniają się pierwiastki z grupy platynowców, tj. platyna, iryd, ruten i pallad oraz nikiel i jego stopy. Ponadto wyraźną aktywnością katalityczną wyróżniają się nanokrystaliczne materiały tlenkowe o strukturze spinelu lub perowskitu, które są szczegółowo opisane w dalszej części pracy.

1.3.3. Separatory

Zastosowanie separatorów w konstrukcji elektrolizera zapobiega mieszaniu się powstających gazów pomimo bliskiego sąsiedztwa elektrod. Właściwości separatorów muszą być tak dobrane, żeby jednocześnie przewodziły jony OH^- oraz stanowiły barierę dla gazowego tlenu i wodoru. Ponadto muszą wykazywać dobrą odporność korozyjną w silnie zasadowym środowisku o pH 14. Na rynku dostępnych jest wiele rodzajów separatorów, które w ogólności można podzielić na dwie grupy, tj. mikroporowate diafragmy i membrany jonowymienne. Mikroporowata budowa diafragmy hamuje transport cząsteczek o rozmiarach większych niż średnica porów natomiast membrany przewodzą jonowo jony OH^-. Separator spełniający swoją rolę musi utrzymywać czystość produkowanych gazów na poziomie 99,5%. Dodatek tlenu

w wodorze już powyżej 4% stanowi mieszaninę wybuchową [27]. Dodatkowo musi mieć niską rezystancję jonową poniżej 0,5 Ω cm^2.

Porowate diafragmy można uznać za klasyczną technologię rozwijaną od dziesięcioleci. Prąd jonowy przepływa przez ciekły elektrolit wypełniający pory diafragmy. Dlatego przewodność zależy od stopnia porowatości i krętości porów oraz przewodności właściwej samego elektrolitu. Aby zmaksymalizować przewodność jonową materiały, z których zbudowane są diafragmy powinny wykazywać się hydrofilowością. Pierwszym komercyjnym separatorem była diafragma azbestowa stosowana już w roku 1890 [28]. Jednak diafragmy azbestowe nie są odporne na korozję w silnie zasadowym środowisku w podwyższonych temperaturach oraz są klasyfikowane jako silnie rakotwórcze. Jako alternatywę zaproponowano kompozyty cermetowe w postaci ceramiki (np. YSZ, $NiTiO_3/NiO$, $BaTiO_3/ZrO_2/K_2Ti_6O_{13}$) osadzonej na metalowym szkielecie. Takie rozwiązanie okazało się nie być skalowalnym ze względu na wysokie koszty produkcji. Z drugiej strony materiały organiczne takie jak polisulfon, siarczek polifenylenu czy politetrafluoroetylen nie są wystarczająco hydrofilowe. Dobrym rozwiązaniem okazują się kompozyty składające się z hydrofobowego polimerowego spoiwa zmieszanego z hydrofilową ceramiką, łącząc wysoką stabilność chemiczną, wytrzymałość mechaniczną i zdolność do wypełniania porów elektrolitem.

Spośród nowych projektów diafragm szeroko stosowana jest diafragma Zirfon® (AGFA) zbudowana z tlenku cyrkonu (ZrO_2) osadzonego w polisulfonowym szkielecie (rys. 10). Zirfon® charakteryzuje się doskonałą separacją gazów (99.9%), długoterminową stabilnością i rezystancją na poziomie 0,3 Ω cm^2 (30°C, 30% KOH) dla diafragmy o grubości 0,5 mm [29].

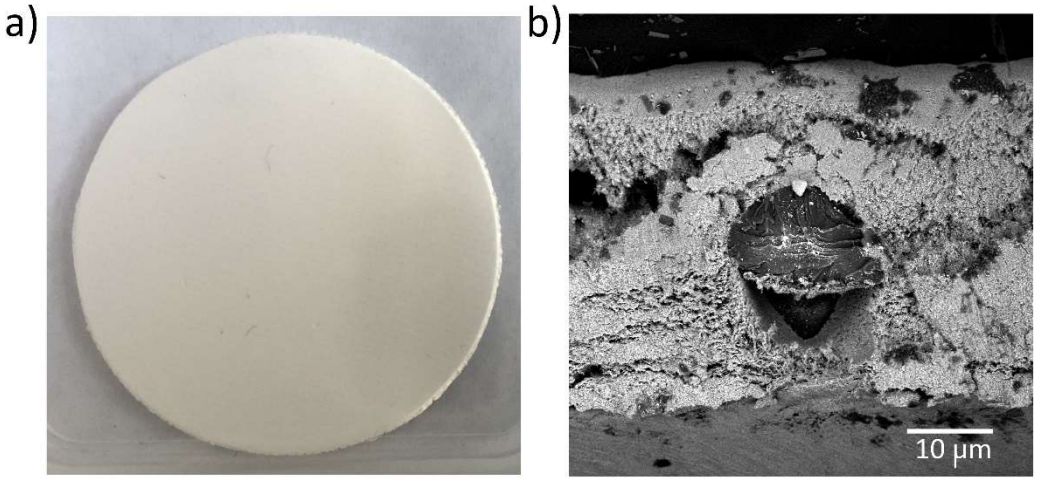

Rys. 10 Diafragma Zirfon® (a) widok z góry oraz (b) przekrój poprzeczny.

Membrany anionowymienne umożliwiają konstrukcję bardziej kompaktowych elektrolizerów o mniejszych stratach omowych. Składają się z polimerowego szkieletu (np. polistyren, tlenek polifenylynu, polisulfon) połączonego z jonowymi grupami funkcyjnymi np. ($-NH_3^+$, $-RN_2H^+$, $=R_2N^{2+}$, $-R_3P^+$, $-R_2S^+$). W tabeli 1.1. przedstawiono właściwości wybranych komercyjnych membran anionowymiennych.

Tabela 1.1. Charakterystyka komercyjnych membran jonowymiennych [30]

Nazwa handlowa	Producent	Materiał	Grubość [μm]	Przewodność jonowa [mS cm^{-1}]
Sustainion®	Dioxide Material (USA)	Sfunkcjonalizowany polistyren	50	70 – 80
Aemion™	Ionomer Innovation Co. (Canada)	HMT-PMBI (Heksametylo-p-terfenylopoli(benzimidazol))	50	80
Orion™	Orion Polymer (USA)	Poli(p-fenylen)	30	60

Przykładem membrany znajdującej szerokie zastosowanie w elektrolizie wody i elektrolizie dwutlenku węgla jest membrana anionowymienna Sustainion® (Dioxide Material). Membrana ta bazuje na tanim, powszechnym i przede wszystkim stabilnym w środowisku zasadowym szkielecie polistyrenowym. W celu nadania docelowych właściwości polimer jest sfunkcjonalizowany 1,2,4,5-tetrametylimidazolem [31]. Liu i inni przetestowali membranę Sustainion® do konstrukcji alkalicznego elektrolizera wody. Badania wykazały stabilność przez 2000 h podczas pracy w 1 M KOH przy przepływie 1 A cm^{-2} przy napięciu 1,9 V [32].

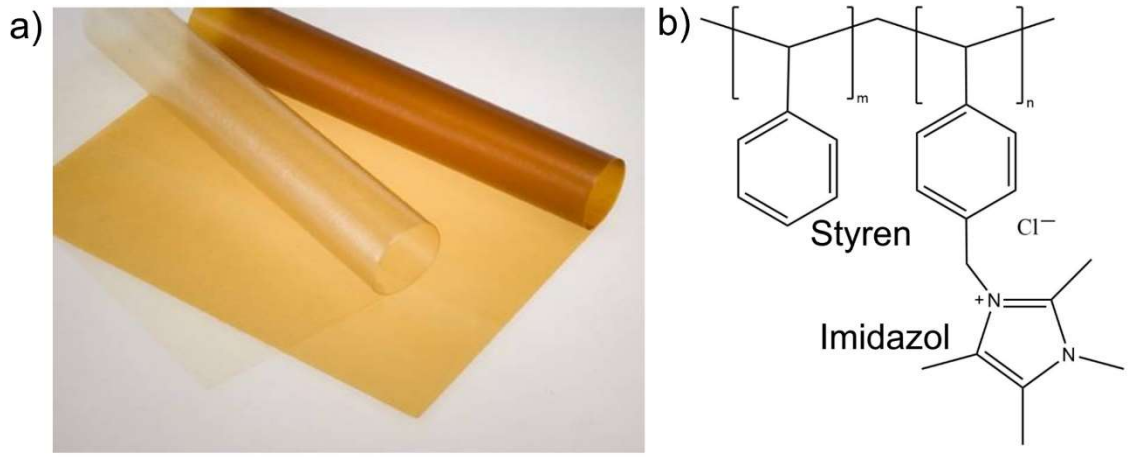

Rys. 11 (a) Membrana Sustainion oraz (b) jej wzór strukturalny [33,34]

1.3.4 Konstrukcja elektrolizera

Elektrolizery alkaliczne występują w dwóch podstawowych konfiguracjach, jedno i dwubiegunowych (rys. 12). W układzie jednobiegunowym obydwie elektrody są bezpośrednio połączone ze źródłem napięcia, przez co celki w stosie są połączone równolegle. Napięcie całego stosu ma taką samą wartość jak pojedynczej celki, a na każdej elektrodzie zachodzi reakcja

redukcji lub utleniania. W układzie dwubiegunowym tylko dwie zewnętrzne elektrody podłączone są do zasilacza. W tej konfiguracji prąd przepływa przez szeregowo połączone celki polaryzując każdą elektrodę w taki sposób, że na jednej stronie elektrody zachodzi reakcja utleniania, a na drugiej stronie reakcja redukcji. W takim wypadku każda elektroda pracuje zarówno jako anoda i katoda.

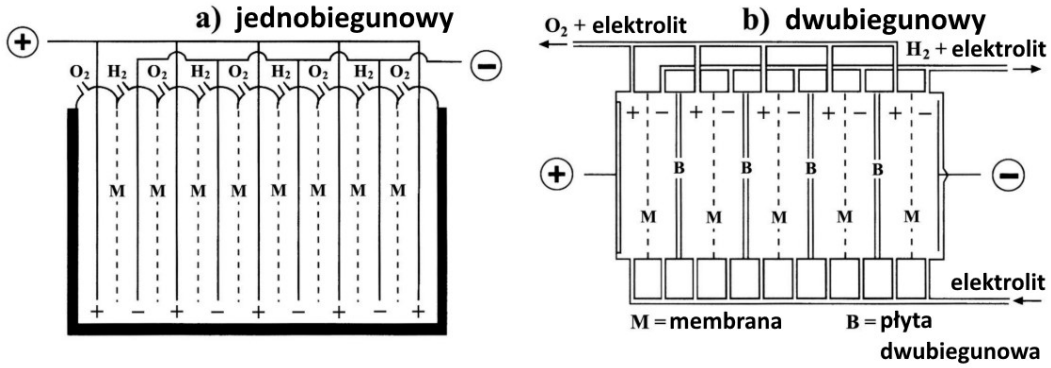

Rys. 12 Konfiguracja elektrolizera (a) jednobiegunowa i (b) dwubiegunowa [35]

Typowa wartość napięcia zasilającego układ jednobiegunowy to 2 V. Odpowiednio w układzie dwubiegunowym będzie to 2x(n-1), gdzie n to liczba elektrod, więc na jedną celkę przypada ~2 V. Wynika z tego, że aby zapewnić taką samą moc układu, korzystając z zależności P = UI, w układzie jednobiegunowym generowane są znacznie wyższe wartości prądu wprowadzające wysokie straty omowe [27].

W klasycznej wersji pojedynczego ogniwa elektrolitycznego pomiędzy powierzchnią elektrod oraz separatorem występuje przestrzeń wypełniona elektrolitem (rys.13a). Pęcherzyki gazu powstające na powierzchniach elektrod częściowo wypełniają objętość elektrolitu i w ten sposób stanowią opór dla przemieszczających się jonów wodorotlenkowych, obniżając sprawność ogniwa. Elektrolit również stanowi opór dla przemieszczających się jonów, który można zredukować poprzez minimalizację przestrzeni pomiędzy elektrodami ogniwa a membraną. Odległość ta może wynosić nawet zero w konstrukcji „zero gap", czyli z zerową przestrzenią pomiędzy separatorem i elektrodami [36]. Tak jak pokazano na rys. 13b w tej konfiguracji porowate elektrody są rozsunięte tylko o grubość separatora gazów. Kompaktowa struktura i porowate elektrody niejako wymuszają uwalnianie pęcherzyków gazów po tej stronie elektrody, która nie jest w kontakcie z separatorem, co ułatwia usuwanie pęcherzyków przez przepływający elektrolit i zmniejsza straty omowe [37]. Na rys. 14 przedstawiony jest prototyp elektrolizera „zero gap" wykonany w technologii druku 3D SLA (stereolitografia). Korpus wykonany z żywicy polimerowej ma przewidziane kanały zapewniające równomierny przepływ elektrolitu wewnątrz ogniwa. Elektrody stanowią pianki niklowe a jako separator wykorzystano membranę anionowymienną Sustainion X37-50 RT. Szczelność układu zapewniają silikonowe uszczelki oraz stalowe płytki odpowiadające za sztywność oraz ścisk.

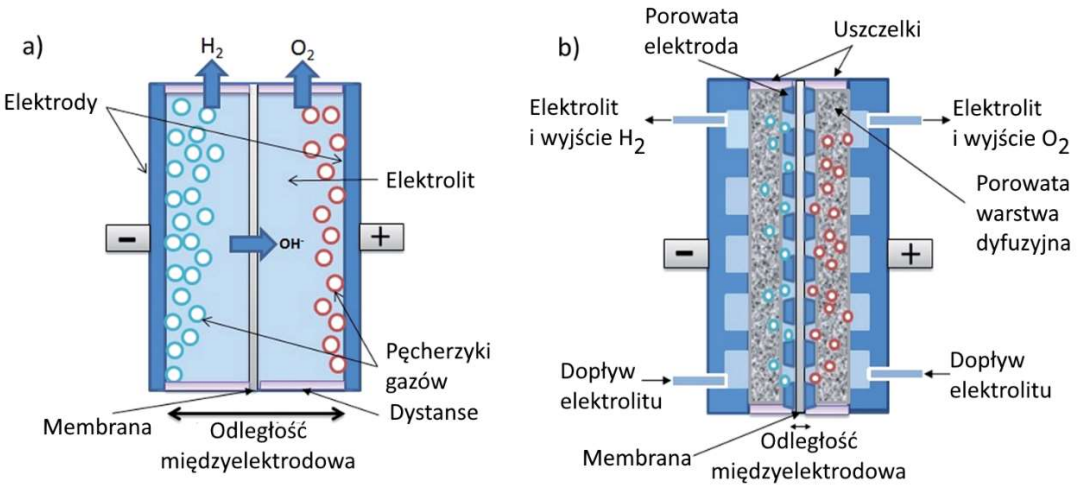

Rys. 13 Ogniwo elektrolizera (a) klasyczne i (b) z zerową przestrzenią [37]

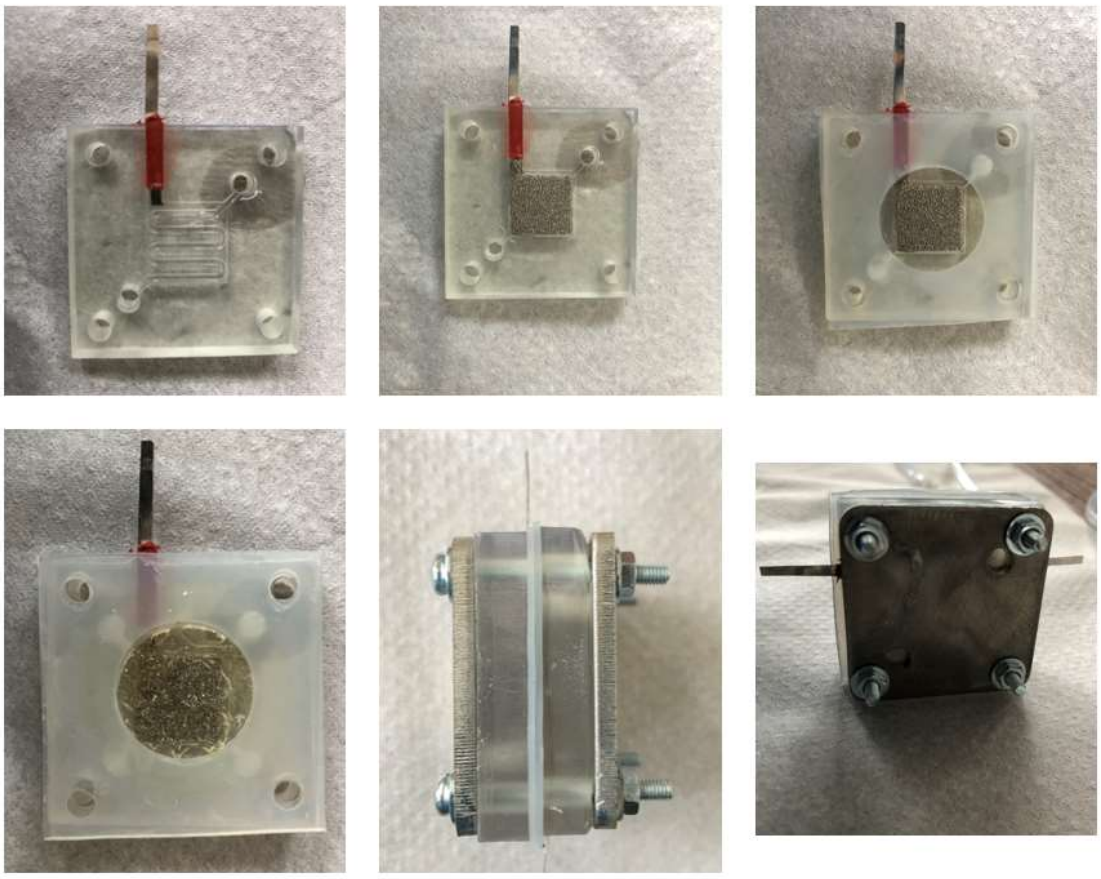

Rys. 14 Prototyp elektrolizera „zero gap" wykonany w technologii druku 3D SLA

W centralnej części elektrolizera „zero gap" znajduje się zespół elektrody-separator (MEA – membrane electrode assembly). Ze względu na sposób przygotowania tego zespołu wyróżnia się dwa podstawowe typy przedstawione na rys. 15, w których katalizatorem pokryte są elektrody (CCS – catalyst-coated substrate) lub bezpośrednio separator (CCM – catalyst-coated membrane). W konfiguracji CCS warstwa elektrokatalitycznie aktywnego materiału jest

nanoszona bezpośrednio na porowate podłoże. Podłoże to pełni rolę zarówno elektrody jak i warstwy gazodyfuzyjnej (GDL – gas diffusion layer). Materiały stosowane na elektrody CCS to najczęściej stalowe lub niklowe siatki i pianki oraz różnorodne materiały węglowe np. tkaniny lub papier [38–40]. W przypadku konfiguracji CCM katalizator w postaci nanocząstek jest mieszany z lepiszczem oraz rozpuszczalnikiem i w formie atramentu nanoszony na każdą stronę separatora. Porowate warstwy GDL ściśnięte z membraną stanowią kontakt elektryczny oraz ścieżki umożliwiające uwalnianie produkowanych gazów.

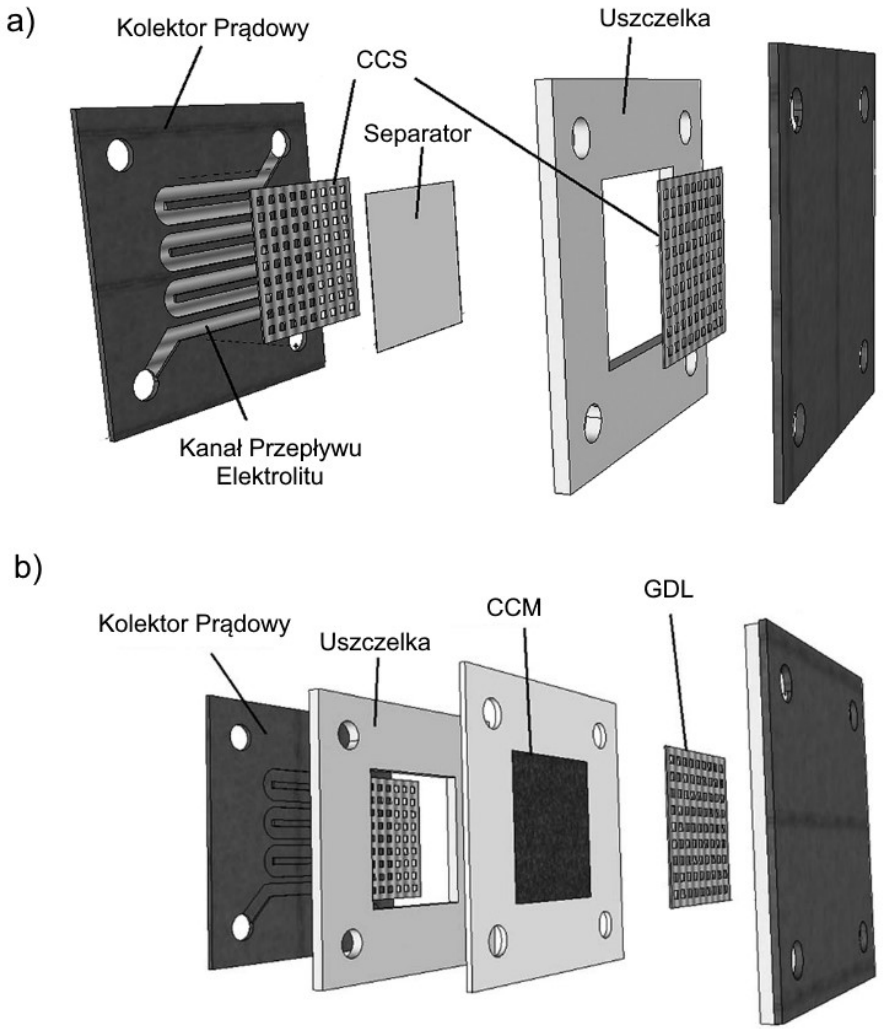

Rys. 15 Zespół elektrody-separator (MEA) typu (a) CCS oraz (b) CCM [37]

1.4. Wybrane materiały elektrokatalityczne

Tak jak zauważono w poprzednich sekcjach reakcje HER i OER obarczone są nadpotencjałami zmniejszającymi wydajność procesu elektrolizy wody. Reakcja utleniania tlenu (OER) jest tą bardziej złożoną, co wynika z 4-elektronowego charakteru, więc ma główny wpływ na całościową sprawność procesu. W związku z tym duży nacisk kładziony jest na poszukiwanie materiałów elektrokatalitycznych pozwalających na obniżenie wspomnianych nadpotencjałów. Wydajny katalizator OER musi:

- odznaczać się stabilnością pracy w szerokim zakresie pH,
- odznaczać się niskimi nadpotencjałami przy wysokich gęstościach prądu,
- być wyprodukowany z szeroko dostępnych materiałów,
- być wyprodukowany za pomocą prostych, dostępnych i niedrogich metod.

Ponadto, optymalny materiał elektrokatalityczny musi posiadać dużą powierzchnię właściwą, tak aby zminimalizować jego ilość potrzebną do przeprowadzenia reakcji. Podstawowym rozwiązaniem jest synteza porowatych lub nanometrycznych struktur. Innym aspektem jest zwilżalność elektrod wyprodukowanych przy użyciu danego materiału. W związku z powstawaniem cząsteczek tlenu i wodoru w trakcie elektrolizy wody na powierzchni elektrod powstają pęcherze gazu. Dopóki pęcherze nie osiągną krytycznej wielkości dopóty pozostają przyczepione do powierzchni elektrod, znacznie zwiększając rezystancję omową układu. Na fragmentach powierzchni, które są pokryte pęcherzami, tymczasowo blokowany jest transfer elektronów, więc w tych miejscach nie zachodzą procesy elektrokatalityczne. Powoduje to wzrost lokalnej gęstości prądu w miejscach nie pokrytych, co może wpływać na stabilność katalizatora. Jedną z możliwości na ułatwienie odrywania pęcherzy gazowych jest zastosowanie wymuszonego przepływu elektrolitu. Innym sposobem, bezpośrednio związanym z materiałem elektrodowym, jest redukcja napięcia powierzchniowego pomiędzy elektrolitem a elektrodą. Można to osiągnąć poprzez zastosowanie dodatkowych substancji w elektrolicie lub poprawiając zwilżalność elektrody. Zwiększając hydrofilowość katalizatora elektrolit może łatwiej zastąpić małe pęcherze gazu na powierzchni elektrod [41].

Materiałem, który jest najczęściej stosowany jako anoda w alkalicznych elektrolizerach jest nikiel. Metal ten wykazuje wysoką odporność korozyjną w zasadowym środowisku oraz zadowalającą aktywność elektrokatalityczną przy zachowaniu rozsądnej ceny w porównaniu do aktywniejszych, ale zarazem bardziej kosztownych platyny, irydu oraz rutenu [4]. W celu zwiększenia elektrochemicznie aktywnej powierzchni właściwej elektrody, produkowane są elektrody o złożonej morfologii (rys. 16). Zastosowanie elektrod o różnej morfologii wpływa na opór omowy pojedynczego ogniwa elektrolizera. Wynika to z różnic w średniej odległości przewodzenia jonów przez elektrolit [42]. Z drugiej strony, podczas pracy przy wysokich gęstościach prądu, drobno oczkowe elektrody, które wykazują niską rezystancję omową, mogą zapychać się bąblami generowanego gazu, co powoduje nagły wzrost rezystancji ogniwa.

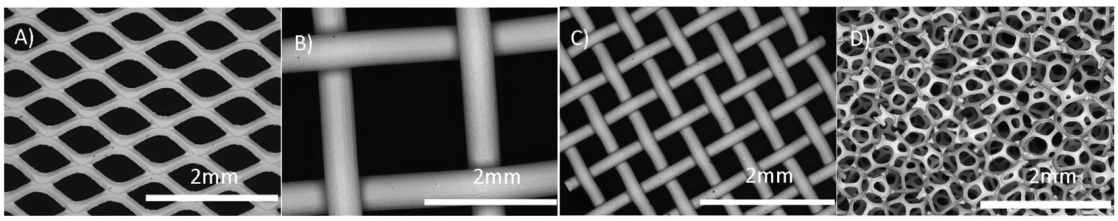

Rys. 16 Zdjęcia SEM typowych elektrod niklowych o złożonej morfologii: (a) siatka ekspandowana, (b) grubo i (c) drobno oczkowa siatka pleciona oraz (d) pianka [42].

Innym cieszącym się popularnością rozwiązaniem jest przygotowanie porowatych elektrod niklowych, nazywanych niklem Raney'a. Nazwa pochodzi od opatentowanego w 1925 roku, przez Murray'a Raney'a, procesu syntezy proszków niklu o dużej powierzchni właściwej [43]. W metodzie tej nikiel oraz krzem lub glin są mieszane i topione tworząc stop o proporcji niklu do drugiego metalu w zakresie od 10 do 80%. Stop jest następnie ługowany wodorotlenkiem sodu powodując powstawanie rozpuszczalnych w wodzie związków krzemu/glinu. Po ich usunięciu pozostaje wysoce porowaty czysty nikiel.

Ponadto inne zdobywające popularność materiały stosowane jako elektrokatalizatory OER w środowisku zasadowym to tlenki, selenki, fosforki, węgliki oraz hydrotalkity [44]. Ze względu na termodynamiczną stabilność przy potencjałach utleniających to tlenki są najbardziej atrakcyjną grupą. Z racji niskiej przewodności elektrycznej tlenki metali nie są stosowane do produkcji samonośnych elektrod. W związku z tym powszechnym rozwiązaniem jest synteza nanokrystalicznych proszków o wysoce rozwiniętej powierzchni właściwej, które następnie nanoszone są na przewodzące podłoża, np. elektrody niklowe [45]. W celu poprawienia przewodnictwa elektrycznego materiałów elektrodowych, proszki katalizatorów miesza się z węglem przewodzącym. Inną możliwością jest bezpośredni wzrost tlenkowych nanowarstw na powierzchni przewodzącej elektrody [46]. Typowo elektrokatalizatory tlenkowe dzieli się na dwie grupy na podstawie ich struktury krystalicznej, tj. spinele oraz perowskity.

1.4.1. Spinele

Spinele jest to grupa minerałów o typowej kompozycji AB_2O_4, w której A i B są to jony metali. W strukturze spinelu może występować jeden lub więcej pierwiastków. Jest to obszerna grupa materiałów obejmująca niemal wszystkie metale przejściowe. Ze względu na szerokie spektrum pierwiastków tworzących spinele, w wyniku różnorodnych konfiguracji elektronowych, ta grupa materiałowa wykazuje niezwykłe właściwości katalityczne, optyczne, magnetyczne i elektryczne [47–51]. Dotychczas spinele zostały zastosowane jako katalizatory w reakcjach redukcji NO_x, utlenianiu CO, redukcji CO_2, reakcjach HER, ORR, OER, utlenianiu NH_3, utlenianiu formaldehydu, spalaniu metanu, dekompozycji H_2O_2, utlenianiu glukozy, utlenianiu alkoholi i wielu innych [52,53].

Struktura spinelu została odkryta przez Bragga i Nishikawę w 1915 roku i została sklasyfikowana jako regularna należąca do grupy przestrzennej $Fd\bar{3}m$ [54,55]. Komórka elementarna spinelu składa się z ośmiu komórek ściennie centrowanych (FCC - face-centered cubic), których węzły zajęte są przez aniony tlenu O^{2-}. Ponadto 64 pozycje są skoordynowane tetraedrycznie oraz 32 oktaedrycznie, z których kolejno 8 i 16 jest zajmowanych przez kationy metali. Zwyczajowo pozycje tetraedrycznie oznaczane są literą A, natomiast oktaedryczne literą B.

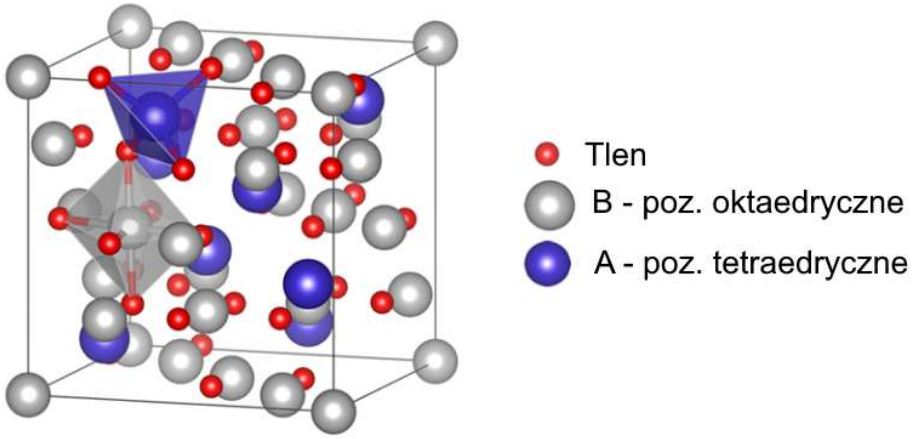

Rys. 17 Struktura regularna spinelu (w celu zwiększenia przejrzystości przedstawiona jest połowa komórki elementarnej) [56]

W niektórych specyficznych przypadkach spinele krystalizują w strukturze tetragonalnej o grupie przestrzennej I41/amd. Przykładowo spinel $MgMn_2O_4$ podlega odkształceniu Jahna-Tellera ze względu na występowanie jonów Mn^{3+}, co powoduje powstanie fazy tetragonalnej zamiast regularnej [57]. W artykule opublikowanym w ramach tej rozprawy również zaobserwowano występowanie struktury tetragonalnej spinelu. W serii $Mn_xCo_{3-x}O_4$ syntezowanych materiałów wykryto fazę regularną dla stechiometrii Co_3O_4, $Mn_{0.5}Co_{2.5}O_4$ i $MnCo_2O_4$, fazę mieszaną dla $Mn_{1.5}Co_{1.5}O_4$ (85% regularna i 15% tetragonalna) oraz wyłącznie fazę tetragonalną dla Mn_2CoO_4 [58].

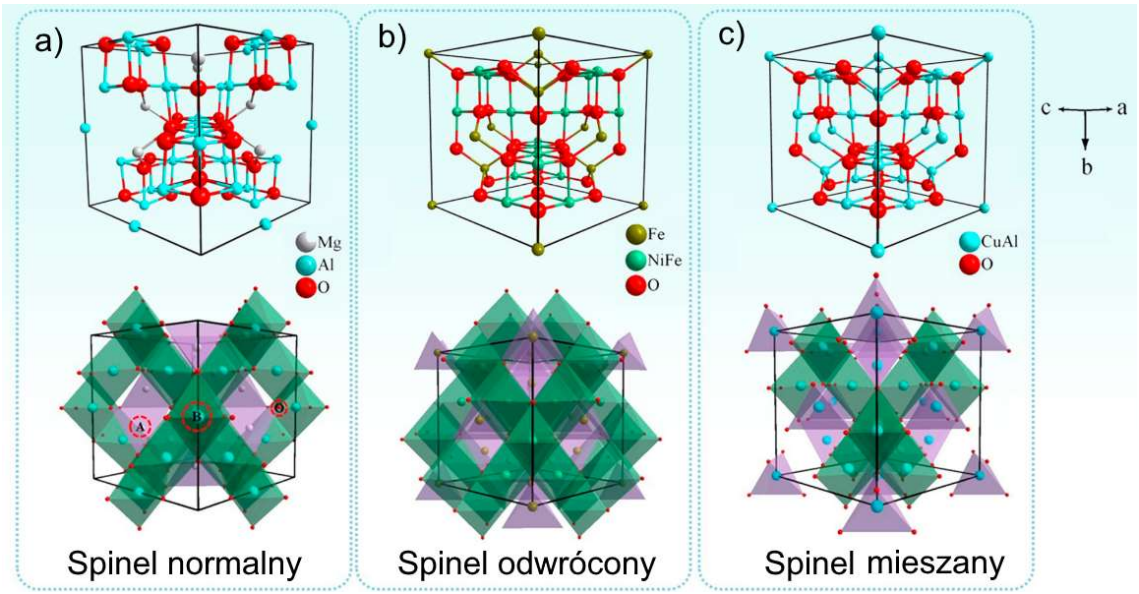

Rys. 18 Reprezentatywne struktury spinelu: (a) spinel normalny – $MgAl_2O_4$, (b) spinel odwrócony – $NiFe_2O_4$ oraz (c) spinel mieszany - $CuAl_2O_4$ [52]

W zależności od składu pierwiastkowego spinelu może on przyjmować różne typy struktury tj. normalną, złożoną i odwróconą. Aby dobrze zobrazować z jakim przypadkiem mamy do czynienia prawidłowym zapisem jest $A_{1-\lambda}B_{\lambda}(A_{\lambda}B_{1-\lambda})O_4$. Kationy zapisane przed nawiasem są

zlokalizowane w pozycjach tetraedrycznych, natomiast te zapisane w nawiasie w pozycjach oktaedrycznych. Jeżeli $\lambda = 0$, to spinel traktujemy jako normalny, jeżeli $\lambda = 1$ to spinel jest odwrotny, natomiast w przypadku kiedy $0 < \lambda < 1$ to spinel ma strukturę mieszaną (rys. 18).

To jakie jest rozmieszczenie kationów w strukturze spinelu zależy od kilku czynników, tj. promienia jonowego danych kationów, oddziaływań kulombowskich pomiędzy kationami i energią stabilizacyjną pola krystalicznego z której wynika preferencyjność zajmowania pozycji skoordynowanych oktaedrycznie przez dany kation.

1.4.2. Perowskity

Perowskity zostały odkryte w 1839 roku na Uralu przez niemieckiego mineraloga Gustawa Rosa i nazwane na cześć rosyjskiego mineraloga Lwa Pierowskiego. Wzór ogólny tych minerałów to ABO_3, gdzie mniejsze jony metali zajmują pozycje B w oktaedrach o koordynacji 6, natomiast większe kationy zajmują pozycje A o 12-krotnej koordynacji (rys. 19). W pozycjach A najczęściej znajdują się metale alkaliczne lub ziem rzadkich, natomiast w pozycjach B metale przejściowe. Perowskity krystalizują we wszystkich możliwych symetriach, przykłady niektórych struktur to:

- regularna,
- tetragonalna,
- rombowa,
- jednoskośna,
- trójskośna.

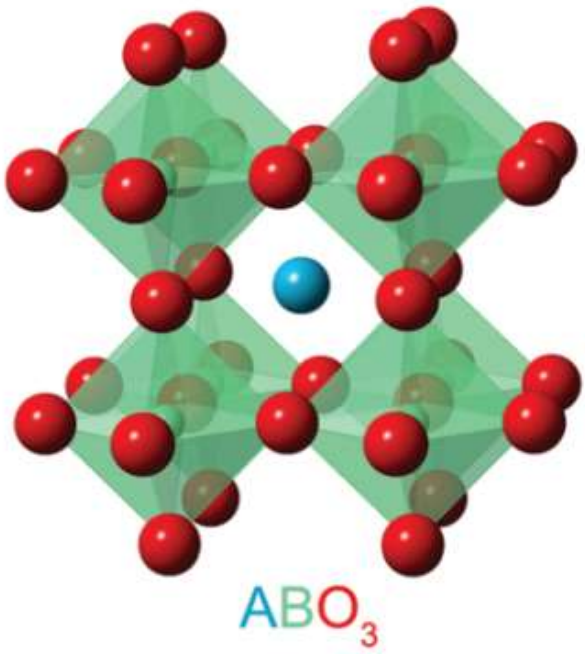

Rys. 19 Struktura regularna perowskitu [59]

Perowskity otrzymywane w laboratorium mają szeroki wachlarz kompozycji chemicznych, a co za tym idzie, wiele ciekawych właściwości i zastosowań. Właściwości te ściśle zależą od wartościowości kationów, struktury krystalicznej i metody syntezy. Najważniejsze, które należy wymienić to: wysokie przewodnictwo (jonowe, elektronowe lub mieszane), właściwości katalityczne, piezoelektryczność, właściwości magnetyczne i nadprzewodzące [60,61].

1.5. Metody otrzymywania materiałów elektrokatalitycznych

Materiały tlenkowe stosowane jako elektrokatalizatory reakcji utleniania tlenu mogą być wytwarzane wieloma metodami, w zależności od planowanego składu chemicznego i właściwości fizykochemicznych. Generalny podział tych metod to:

- synteza w fazie stałej (SSR – solid state reaction),
- synteza metodami mokrymi (SCR – soft chemistry route),
- osadzanie z fazy gazowej (CVD/PVD – chemical/physical vapor deposition).

Pierwsze dwie metody służą do syntezy proszków ceramicznych, natomiast metoda CVD umożliwia otrzymywanie warstw ceramicznych na podłożach/nośnikach.

1.5.1 Synteza w fazie stałej

Do metod syntezy w fazie stałej zalicza się **syntezę wysokotemperaturową** (rys.20). W metodzie tej prekursory zawierające metale (czyste metale, tlenki, halogenki, siarczki, wodorotlenki i/lub węgliki) są mieszane w odpowiednich proporcjach i poddane wysokim temperaturom zapewniającym procesy dyfuzyjne i powstanie nowych materiałów. Niewątpliwą zaletą tej metody jest możliwość zastosowania na dużą skalę. Jednak jak wspomniano, inicjacja procesów dyfuzyjnych wymaga stosowania wysokich temperatur, co generuje dodatkowe koszty oraz jest czasochłonne.

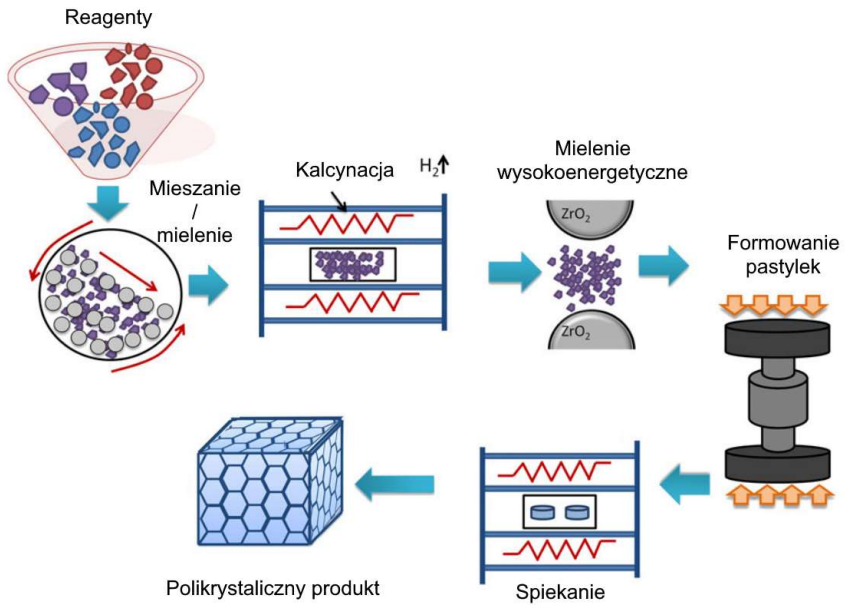

Rys. 20 Schemat przebiegu wysokotemperaturowej syntezy w fazie stałej [62]

Aby zmienić stan rzeczy stosowana jest dodatkowa obróbka przed obróbką termiczną tj. mechaniczne rozdrabnianie za pomocą młynów kulowych lub planetarnych. Wysokoenergetyczne mielenie powoduje rozdrabnianie cząstek reaktantów zapewniając szybszą kinetykę reakcji oraz wpływając na pożądane rozdrobnienie finalnego produktu. Ponadto generowane wysokie naprężenia w mielonym materiale mogą powodować powstawanie wakansów tlenowych modyfikujących właściwości wytwarzanego materiału.

Kolejną metodą jest **spalanie w fazie stałej**, podczas którego zachodząca reakcja egzotermiczna przyspiesza proces syntezy nowego materiału. Przykładem metody spaleniowej jest wykorzystanie sproszkowanego żelaza zarówno jako paliwa jak i reagenta do syntezy spineli żelazowych (ferrytów) [52].

Metodą pozwalającą na syntezę nanocząstek jest **rozkład termiczny.** W przeciwieństwie do spalania w fazie stałej, w którym źródłem energii jest reakcja termitowa, w tej metodzie azotany pełnią rolę utleniacza i źródła metali, a związki organiczne takie jak mocznik, glicyna, celuloza lub kwas cytrynowy pełnią rolę paliwa.

Innowacyjną metodą jest **otrzymywanie tlenków metali ze szkieletów metalo-organicznych** (MOF – metal-organic framework). Kalcynacja szkieletów metalo-organicznych w kontrolowanych warunkach umożliwia otrzymywanie złożonych struktur o wysoce rozwiniętej powierzchni właściwej np. porowatych nanoklatek.

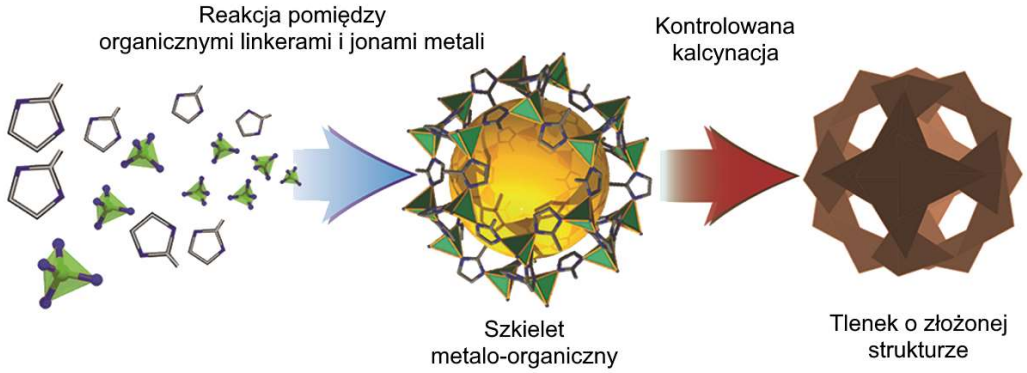

Rys. 21 Otrzymywanie tlenków metali ze szkieletów metalo-organicznych [63]

Cienkie warstwy katalizatorów mogą być wytwarzane za pomocą **osadzania laserem impulsowym** (PLD – pulsed laser deposition). Fotony lasera wysokiej mocy bombardują cel wykonany z docelowego materiału powodując wybijanie jego atomów. Następnie uwolnione atomy osadzają się na wybranym podłożu tworząc cienką warstwę. Morfologia otrzymywanych warstw może być modyfikowana poprzez zmianę parametrów PLD np. moc impulsu, prędkość przepływu gazów oraz temperaturę podłoża.

1.5.2. Synteza metodami mokrymi

Poniżej przedstawiono kilka wybranych mokrych metod syntezy materiałów.

Powszechnie stosowaną metodą zaliczaną do metod mokrych jest metoda **zol-żel**. Sole metali są używane jako prekursory, a kwasy organiczne są substancjami chelatującymi.

Reagenty po rozpuszczeniu w wodzie są mieszane do uzyskania jednorodnego zolu. Wraz z odparowaniem rozpuszczalnika w trakcie ogrzewania zol stopniowo zamienia się w żel. W wyniku kalcynacji żelu otrzymywany jest materiał w postaci tlenku. Za pomocą zmian temperatury kalcynacji można kontrolować powstawanie defektów w materiale. Dobór odpowiednich reagentów wpływa na morfologię końcowego produktu.

Odmianą syntezy zol-żel jest metoda **Pechiniego,** w której wybrane kwasy α-hydroksylowe tworzą związki kompleksowe z kationami metali. Następnie kompleksy te ulegają reakcji estryfikacji po dodaniu wielohydroksyalkoholi, a w kolejnym etapie po podwyższeniu temperatury zachodzi polimeryzacja. Kalcynacja powstałego żelu prowadzi do powstania nanokrystalicznego produktu w postaci proszku lub cienkich warstw. W porównaniu do innych metod klasyfikowanych jako metody zol-żel metoda Pechiniego wyróżnia się większą homogenicznością otrzymanych produktów.

Rys. 22 Schemat przebiegu syntezy metodą Pechiniego [64]

W syntezie **hydrotermalnej** reakcje pomiędzy rozpuszczalnikiem a reagentami zachodzą w warunkach wysokiego ciśnienia (>20 bar) oraz podwyższonej temperatury (~300°C). Syntezowane materiały powstają na drodze hydrolizy lub rekrystalizacji reagentów. Dzięki kontroli wzrostu krystalitów wyeliminowane jest zjawisko aglomeracji. W przypadku materiałów wrażliwych na wodę stosowana jest odmiana tej techniki tj. metoda **solwotermalna**, w której stosowane są rozpuszczalniki bezwodne, np. etanol, glikol etylenowy, izopropanol, dimetyloformamid itp. Co ciekawe morfologia ostatecznego produktu może być modyfikowana poprzez odpowiedni dobór proporcji różnych rozpuszczalników.

W metodzie **strącania** z roztworu sól metalu jest rozpuszczona w wodzie, a kationy mają postać hydratów (np. $Fe(H_2O)_6^{3+}$). Hydraty są zobojętniane poprzez dodanie zasady, a produktem zobojętnienia jest uwodniony tlenek lub wodorotlenek metalu. Strącony osad jest przemywany, filtrowany oraz suszony, a następnie poddany kalcynacji. Ostatecznie własności fizykochemiczne otrzymanego materiału zależą od zastosowanego odczynnika strącającego, pH roztworu, czy temperatury kalcynacji.

Metoda mikroemulsji, zwana również metodą odwróconych miceli polega na przygotowaniu emulsji, w których krople wodnych roztworów prekursorów stabilizowanych za pomocą surfaktantów są rozproszone w oleju. Wewnątrz kropli zachodzą reakcje hydrolizy oraz redukcji, prowadzące do powstania nanocząstek jako produktu. Można powiedzieć, że krople te stanowią rolę reaktorów, w których powstają cząstki o kontrolowanych rozmiarach, ograniczonych przez wielkość kropli.

Elektrochemiczne metody syntezy katalizatorów tlenkowych można podzielić na dwie kategorie, **elektroosadzanie** oraz **elektroprzędzenie**. Elektroosadzanie jest stosunkowo tanią i szybką metodą pozwalającą na otrzymanie tlenkowych produktów. Typowa celka do elektroosadzania składa się z klasycznego układu trójelektrodowego. Proces polega na osadzaniu na podłożu materiału z roztworów elektrolitów w wyniku zachodzenia reakcji utleniania i redukcji. Proces elektroosadzania jest wspomagany poprzez przyłożenie zewnętrznego źródła prądu elektrycznego. Sterowanie parametrami procesu takimi jak: temperatura elektrolitu, gęstość prądu, skład elektrolitu, prędkość mieszania i rodzaj podłoża, pozwala otrzymać powłoki o pożądanych właściwościach fizycznych.

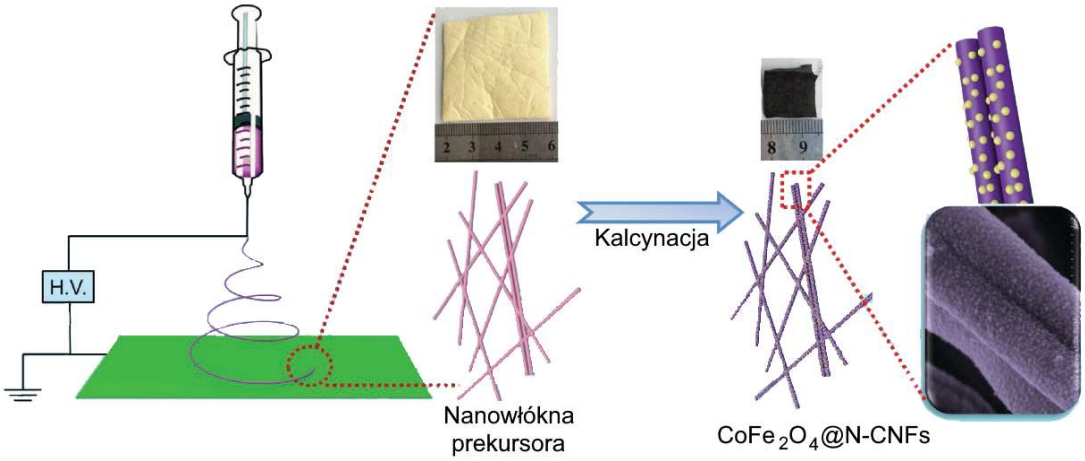

Rys. 23 Schemat elektroprzędzenia nanowłókien zintegrowanych z nanocząstkami spinelu $CoFe_2O_4$ [65]

Metoda **elektroprzędzenia** polega na przędzeniu z wykorzystaniem siły elektrostatycznej do wyciągania cienkich włókien z ciekłego roztworu lub stopionego polimeru. Dodatkowo, aby otrzymać włókna kompozytowe ze zintegrowanymi nanocząstkami tlenku metalu, w roztworze rozpuszczane są sole metali. Otrzymane nanowłókna prekursora poddawane są dodatkowej obróbce cieplnej w określonej atmosferze. Metoda elektroprzędzenia jest procesem skalowalnym, w związku z czym otrzymywanie włókien można przeprowadzać w skali zarówno laboratoryjnej jak i przemysłowej.

1.5.3. Osadzanie z fazy gazowej

Chemiczne osadzanie z fazy gazowej (CVD – chemical vapour deposition) polega na wytwarzaniu warstw, proszku lub monokryształu ze składników atmosfery gazowej na przygotowanym, podgrzewanym podłożu. Zmieniając warunki eksperymentalne, w tym materiał podłoża, jego temperaturę, skład mieszaniny gazów reakcyjnych, przepływ tych gazów itp. otrzymuje się materiały o szerokim zakresie właściwości fizycznych i chemicznych. Cechą charakterystyczną procesu CVD jest możliwość wytwarzania powłok o jednolitej grubości, niskiej porowatości i powtarzalnych właściwościach na podłożach o złożonym kształcie. Metoda CVD jest wykorzystywana w wielu zastosowaniach np. do produkcji cienkich warstw dielektrycznych, przewodzących, pasywacyjnych, powłok żaroodpornych oraz warstw elektrokatalitycznych [66].

Piroliza aerozolowa jest to technika, w której cienkie warstwy nakładane są przy użyciu roztworu prekursora, dyszy napylającej oraz podgrzewanego podłoża. Roztwór jest atomizowany za pomocą dyszy napylającej do postaci aerozolu, następnie rozproszone krople są transferowane do docelowego podłoża, na którym zachodzi wzrost powłoki. Powstała warstwa cechuje się wysoką jednorodnością przy jednoczesnej możliwości pokrywania dużych powierzchni. Morfologia finalnej powłoki zależy od parametrów procesu takich jak stężenie roztworu prekursora, ciśnienie gazu nośnego, temperatura podłoża. Piroliza aerozolowa jest metodą wydajną, a do jej stosowania nie jest wymagany wysoce specjalistyczny sprzęt, co czyni ją metodą stosunkowo niedrogą [67].

Rozpylanie magnetronowe (magnetron sputtering) jest metodą klasyfikowaną jako fizyczne osadzanie z fazy gazowej, wykorzystującą magnetron czyli układ diodowy z zimną katodą. Silne pole elektryczne jonizuje gaz roboczy, którego jony bombardują target, który jest ujemnie spolaryzowaną elektrodą. W trakcie bombardowania jony przekazują swoją energię atomom targetu i powodują ich wybijanie. W ten sposób powstaje strumień par metalu, który jest przenoszony w kierunku podłoża, na którym kondensuje i tworzy warstwę. Metoda ta jest wykorzystywana do osadzania warstw zabezpieczających, dielektrycznych, elektrokatalitycznych oraz dekoracyjnych [68].

2. CELE I TEZY PRACY

Technologia alkalicznej elektrolizy wody do wytwarzania wodoru i tlenu znana jest już od ponad 100 lat, jednak wciąż nie wynaleziono atrakcyjnych materiałów elektrodowych mogących zastąpić kosztowne i trudno dostępne elektrody platynowe, irydowe i rutenowe. Celem pracy i przeprowadzonych badań było opracowanie aktywnych materiałów nanokrystalicznych działających jako elektrokatalziatory jednej z reakcji zachodzących podczas elektrolizy wody, tj. reakcji wydzielania tlenu (OER). Ponadto zwrócono uwagę, aby materiały były wytwarzane metodami syntezy dostępnymi w typowym laboratorium chemicznym z możliwością skalowania do warunków przemysłowych. Na podstawie doniesień literaturowych, spośród różnych alternatywnych grup materiałowych, wytypowano tlenki o strukturze krystalicznej spinelu i perowskitu jako materiały potencjalnie mogące zastąpić te z grupy platynowców. Tlenki te wykazują szereg wyjątkowych właściwości fizykochemicznych, a ze względu na szeroką gamę pierwiastków mogących budować ich strukturę otrzymuje się niezliczone możliwości modyfikowania tych właściwości.

Na podstawie obecnego stanu wiedzy zauważono, że wciąż brakuje elektrokatalizatorów składających się z łatwo dostępnych pierwiastków, które oferują niskie nadpotencjały reakcji i stabilność parametrów pracy w środowisku zasadowym. Jedną z możliwych dróg do opracowania takiego materiału jest modyfikacja znanej struktury poprzez włączenie w nią dodatkowego pierwiastka, a zatem modyfikację struktury krystalicznej, co może wpłynąć na zmianę właściwości fizykochemicznych i poprawę aktywności elektrokatalitycznej. Przedstawiony kierunek rozwoju badań dotyczących elektrokatalizatorów OER umożliwił sformułowanie następującej tezy:

1. Możliwe jest zwiększenie aktywności elektrokatalitycznej spinelu $MnCo_2O_4$ oraz perowskitu $SrTiO_{3-d}$ w kierunku wydzielania tlenu z zachowaniem stabilności chemicznej poprzez wprowadzenie żelaza do struktury krystalicznej.

Ponadto właściwości materiałów elektrokatalitycznych mogą być modulowane bez zmian składu chemicznego. Na postawie analizy literatury wytypowano obróbkę mechaniczną lub cieplną jako metody wpływu na zarówno morfologię wytworzonych proszków jaki i stopnie utlenienia kationów metali w zewnętrznych warstwach atomowych. Do tej pory nieznany był rezultat takich modyfikacji poczynionych na spinelach o stechiometriach $MnCo_2O_4$ oraz $MnCo_{1,5}Fe_{0,5}O_4$. W związku z powyższym sformułowano drugą tezę:

2. Możliwe jest poprawienie aktywności elektrokatalitycznej spineli $MnCo_2O_4$ oraz $MnCo_{1,5}Fe_{0,5}O_4$ w kierunku reakcji wydzielania tlenu poprzez zastosowanie posyntezowej obróbki cieplnej lub mechanicznej.

Badania udowodniające powyższe tezy zostały opublikowane w czasopismach naukowych znajdujących się na liście Journal Citation Reports (JCR) i są przedstawione w rozdziale 4.

3. SYNTEZA MATERIAŁÓW I METODY POMIAROWE

3.1. Synteza materiałów

Przegląd metod wytwarzania materiałów elektrokatalitycznych został przedstawiony w pierwszym rozdziale niniejszej pracy. W tej sekcji szczegółowo omówione zostaną procesy wytwarzania materiałów spinelowych i perowskitowych wykorzystane podczas realizacji badań w ramach studiów doktoranckich.

3.1.1. Synteza spineli metodą zol-żel

Proszki elektrokatalizatorów o strukturze spinelu otrzymane zostały za pomocą syntezy zol-żel (rys. 24). Jako źródło jonów metali wybrano sole kwasu azotowego (azotany), natomiast substancjami chelatującymi były kwas cytrynowy oraz kwas wersenowy (EDTA - ethylenediaminetetraacetic acid*)*. Substancje te były rozpuszczane w wodzie dejonizowanej korzystając z mieszadła magnetycznego. W trakcie przygotowywania zolu pH roztworu było kontrolowane i modyfikowane poprzez dodatek wody amoniakalnej w celu zapobiegania wytrąceniu wodorotlenków metali. W niektórych przypadkach do roztworu dodawany był glikol etylenowy w celu wywołania reakcji poliestryfikacji i utworzenia sieci polimerowej. Podczas syntezy manganianu kobaltu, $MnCo_2O_4$, zaobserwowano krystalizację dwufazowej mieszaniny (~70% $Mn_{1.4}Co_{1.6}O_4$ oraz ~30% Co_3O_4) jedynie w sytuacji, gdy zastosowano dodatek glikolu etylenowego, dlatego w dalszych pracach zaniechano dodawania glikolu. Przygotowane zole były podgrzewane do 80°C na płycie grzewczej i utrzymywane w tej temperaturze przez ok. 12 h w celu odparowania rozpuszczalnika i utworzenia żelu. Następnie żele umieszczano w suszarce laboratoryjnej w temperaturze 180°C, aby odparować wodę pozostałą w objętości żelu. Kolejno żel był rozdrabniany w moździerzu laboratoryjnym i poddawany spalaniu w piecu komorowym w odpowiedniej temperaturze zapewniającej krystalizację fazy regularnej bądź tetragonalnej spinelu. Minimalna temperatura potrzebna do samospalenia organicznego szkieletu została wyznaczona za pomocą analizy termograwimetrycznej i jest przedstawiona na rys. 25. Ostatnim etapem było mechaniczne mielenie otrzymanych proszków za pomocą medium mielącego, tj. kulek wytworzonych z tlenku cyrkonu stabilizowanego itrem (YSZ – yttria-stabilised zirconia). Kulki wraz z mielonym proszkiem były umieszczane w szklanych fiolkach i zalewane izopropanolem. Tak przygotowane naczynie było umieszczane na wytrząsarce rolkowej i obracane przez określony czas. Celem mielenia było rozbicie aglomeratów krystalitów, w związku z tym, zwiększenie powierzchni materiału dostępnej dla zachodzących reakcji elektrokatalitycznych. Zaobserwowano wyraźny wpływ czasu mielenia na wzrost aktywność elektrokatalityczną materiałów, a wyniki badań zostały szczegółowo opisane w jednym z artykułów wchodzących w skład tej rozprawy.

Rys. 24 Przebieg syntezy zol-żel

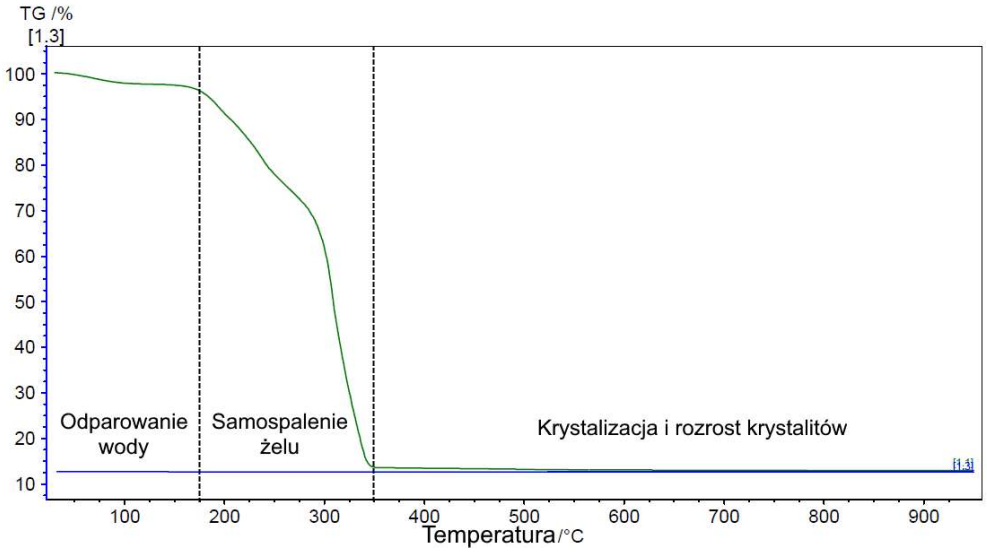

Rys. 25 Wykres analizy termograwimetrycznej prekursora żelowego wykorzystanego do otrzymania spinelu MnCoFeO4

3.2.1. Synteza w fazie stałej

Perowskity $SrTi_{1-x}Fe_xO_{3-d}$ (STFx) zostały przygotowane za pomocą wysokotemperaturowej syntezy w fazie stałej. Prekursorami były węglan strontu ($SrCO_3$), tlenek żelaza(III) (Fe_2O_3) oraz dwutlenek tytanu (TiO_2). Reagenty były wymieszane za pomocą mielenia w młynie planetarnym. Następnie z uzyskanego proszku sprasowano pastylki, które poddano kalcynacji w odpowiedniej temperaturze w zależności od spiekalności danego materiału. Pastylki ponownie rozdrobniono, sprasowano i kalcynowano. Końcowy proszek został wygrzany w temperaturze 600°C w powietrzu w celu uzyskania stechiometrycznych perowskitów.

3.2. Badania strukturalne

3.2.1. Dyfraktometria rentgenowska - XRD

Dyfraktometria rentgenowska (XRD – x-ray diffraction) jest podstawową techniką badań strukturalnych pozwalającą na określenie składu fazowego badanego materiału oraz wyznaczenie stałych sieci krystalicznej. W tej metodzie wiązka monochromatycznego promieniowania X kierowana jest w kierunku próbki, na której zachodzi zjawisko dyfrakcji i wiązka jest odbijana od płaszczyzn krystalicznych. W przypadku, gdy wiązka promieniowania pada pod kątem spełniającym prawo Bragga (rys. 26) zachodzi interferencja konstruktywna odbitych promieni i trafiają one do detektora. Wyniki badania przedstawiane są w postaci dyfraktogramu, czyli liczby zaliczeń detektora w zależności od kąta padania wiązki promieniowania. Porównanie dyfraktogramu z danymi literaturowymi i dyfraktogramami wygenerowanymi komputerowo na podstawie modeli struktur krystalicznych pozwala na identyfikację faz w polikrysztale.

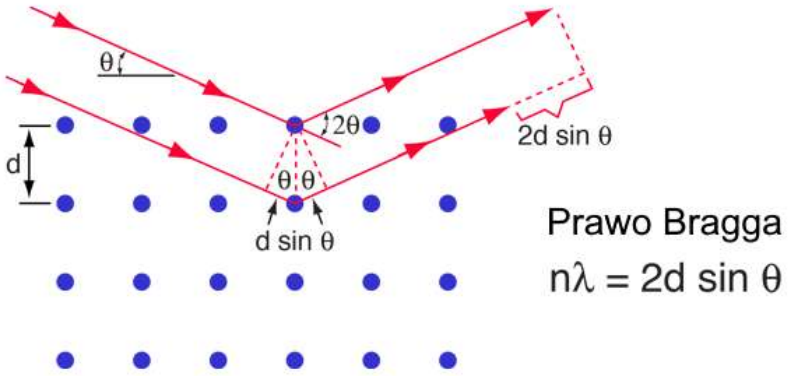

Rys. 26 Prawo Bragga

W ramach tej pracy dyfraktogramy rentgenowskie próbek zostały wykonane za pomocą dyfraktometru Bruker D2 Phaser wyposażonego w detektor Lynxeye XE-T. Pomiary zostały przeprowadzone w zakresie kątowym od 5 do 110° w temperaturze pokojowej. Rozmiar komórki elementarnej oraz skład fazowy został obliczony za pomocą oprogramowania FullProf Suite lub GSAS-II. Korzystając z równania Scherrera obliczono średni rozmiar krystalitów:

$$\tau = \frac{K\lambda}{\beta cos\theta}, \tag{27}$$

, gdzie τ – średni rozmiar krystalitów [nm], K – stała związana z kształtem refleksów (K=0,9), λ – długość fali promieniowania [nm], β – szerokość refleksu zależna od wielkości krystalitów, θ – kąt Bragga [º].

3.2.2. Skaningowa i transmisyjna mikroskopia elektronowa – SEM i TEM

Skaningowa mikroskopia elektronowa polega na skanowaniu powierzchni próbki za pomocą nanometrowej wiązki elektronów uformowanej przez układ elektromagnetycznych

soczewek (rys. 27). Sygnałem z powierzchni próbki, który dociera do detektora są elektrony wtórne lub wstecznie rozproszone. W porównaniu do mikroskopii optycznej, mikroskopia SEM pozwala uzyskać znacznie wyższe powiększenia z zachowaniem wysokiej rozdzielczości. Mikroskopia ta pozwala na precyzyjną obserwację topografii powierzchni z możliwością rozróżnienia obiektów o średnicach poniżej 1 nm. Stosowana jest do analizy morfologicznej tj. oceny kształtu, wielkości i rozmieszczenia ziaren, wtrąceń oraz faz w badanym materiale.

Nieco inną odmianą mikroskopii elektronowej jest transmisyjna mikroskopia elektronowa. W tym przypadku wiązka elektronów jest transmitowana przez cienką próbkę (5 – 100 nm). Obraz powstający na ekranie ma ciemniejsze obszary w miejscach, w których doszło do rozproszenia elektronów. Techniki transmisyjnej mikroskopii elektronowej umożliwiają uzyskiwanie obrazów z rozdzielczością rzędu 0,1 – 0,05 nm.

Obserwacje mikroskopowe przygotowanych proszków, elektrod oraz pastylek były realizowane za pomocą mikroskopów FEI Quanta 250 FEG, Thermo Fisher Phenom XL oraz Titan Cubed G2 60-300. Badania przeprowadzono we współpracy z Międzynarodowym Centrum Mikroskopii Elektronowej dla Inżynierii Materiałowej (Akademia Górniczo-Hutnicza im. Stanisława Staszica w Krakowie).

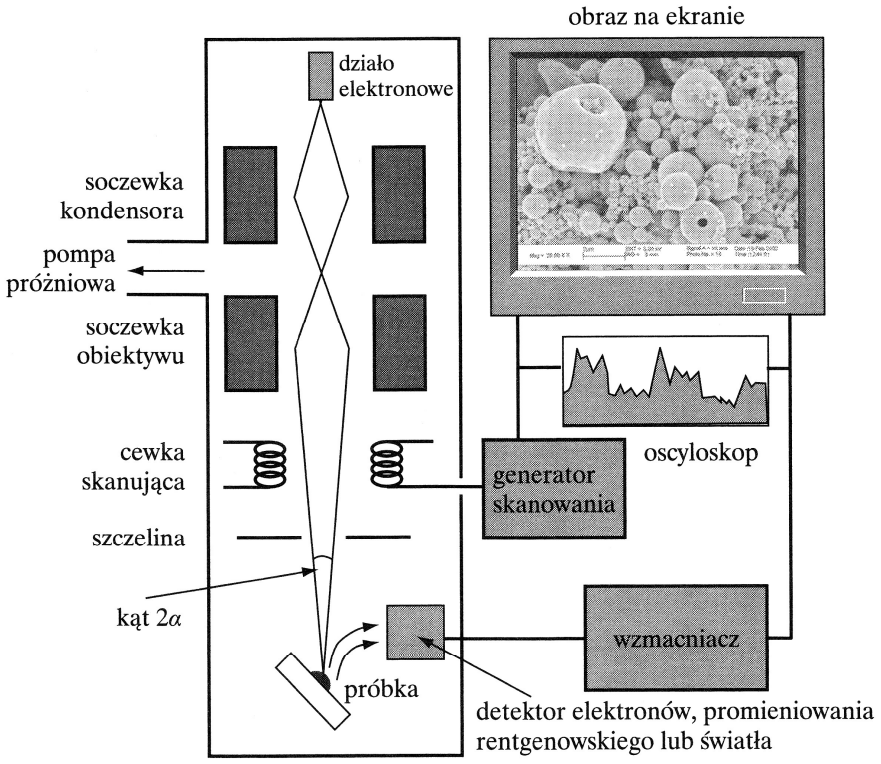

Rys. 27 Uproszczony schemat budowy mikroskopu SEM [69]

3.2.3. Spektroskopia dyspersji energii – EDS

Spektroskopia dyspersji energii EDS (energy disspersive spectroscopy), zwana inaczej mikroanalizą rentgenowską, jest to metoda analityczna stosowana w skaningowych mikroskopach elektronowych pozwalająca wyznaczyć lokalny skład chemiczny próbki. Tak samo

jak w mikroskopii SEM badany materiał jest naświetlany zogniskowaną wiązką elektronów. Wiązka ta może wybijać elektrony z powłok atomów, a więc je jonizować. Luki powstałe na powłokach elektronowych są uzupełniane poprzez elektrony z zewnętrznych powłok danego atomu. Przy takim przejściu elektronu emitowany jest kwant promieniowania rentgenowskiego o dyskretnych wartościach charakterystycznych dla pierwiastków wchodzących w skład próbki. Fotony promieniowania X są zbierane przez detektor umieszczony nad próbką. Dokładne pomiary EDS umożliwiają wykrywanie pierwiastków o zawartości 0,1% atomowego. Technika ta umożliwia analizę rozmieszczenia pierwiastków na powierzchni próbki w trybie punktowym, liniowym lub obszarowym (mapa). Gdy detektor EDS jest używany w połączeniu z mikroskopem TEM, to uzyskuje się większą rozdzielczość przestrzenną co wynika z małej grubości próbki.

Za pomocą tej metody określano skład chemiczny przygotowanych materiałów oraz badano stabilność wybranych materiałów w środowisku zasadowym poprzez obserwację zmian składu chemicznego po ekspozycji próbki w elektrolicie.

3.2.4. Izoterma adsorpcji BET

Jednym z kluczowych parametrów materiału elektrokatalitycznego jest powierzchnia właściwa, wyrażona w $m^2 g^{-1}$, która mówi o liczbie aktywnych katalitycznie miejsc przypadających na daną masę próbki. Podstawową metodą wyznaczania powierzchni właściwej jest pomiar objętości gazu zaadsorbowanego w określonej masie próbki w funkcji prężności gazu lub w funkcji względnej prężności gazu. Taki pomiar nazywamy izotermą adsorpcji. Odważona próbka badanego materiału jest odgazowywana w próżni i schładzana do niskiej temperatury. Następnie przeprowadzana jest kontrolowana adsorpcja fizyczna gazu (np. helu lub azotu). Otrzymana izoterma adsorpcji ma charakterystyczny kształt, który zależy od właściwości fizycznych substancji adsorbującej i substancji adsorbowanej. Analiza takiej krzywej polega na dopasowaniu do odpowiedniego modelu teoretycznego.

W ramach tej pracy zastosowano izotermę BET (Brunauera, Emmetta i Tellera), czyli prosty model adsorpcji wielowarstwowej. Model ten zakłada, że cząsteczki adsorbatu adsorbują w sposób zlokalizowany, tj. nie mogą się przemieszczać po powierzchni adsorbentu ze względu na silne oddziaływania adsorbent-adsorbat. Ponadto model ten zakłada, że na powierzchni próbki znajdują się centra adsorpcyjne, które adsorbują cząstki gazu tworząc monowarstwy jak i kolejne warstwy, gdzie centrami adsorpcyjnymi stają się już zaadsorbowane cząsteczki. Kolejnymi założeniami są brak oddziaływania pomiędzy cząstkami zaadsorbowanymi wzdłuż powierzchni adsorbentu, zależności ilości zaadsorbowanych cząstek od ciśnienia pary nasyconej, oraz różne wartości ciepła adsorpcji pierwszej i kolejnych warstw adsorbatu.

Do pomiaru powierzchni właściwej wytworzonych proszków elektrokatalizatorów wykorzystano urządzenia Quantachrome Instruments Autosorb iQ oraz Nova-Touch LX1.

3.2.5. Rentgenowska spektroskopia fotoelektronów - XPS

Rentgenowska spektroskopia fotoelektronów (XPS – x-ray photoelectron spectroscopy) jest to metoda badawcza stosowana w badaniach powierzchni materiałów. W technice XPS

próbka jest wzbudzana za pomocą wiązki monochromatycznego promieniowania X o niskiej energii. Z atomów ulokowanych na powierzchni próbki następuje emisja fotoelektronów, a energia tych fotoelektronów jest mierzona przez analizator. Do analizy wykorzystywane są elektrony o energii od 10 do 2000 eV. Każdy atom posiada elektrony rdzenia atomowego, które nie tworzą bezpośrednio wiązań chemicznych, mimo to, energia wiązania takiego elektronu zależy od chemicznego otoczenia atomu. Wartość energii wiązania elektronu rdzenia jest wartością charakterystyczną dla danego atomu oraz orbitalu do którego należy ten elektron. W związku ze znajomością energii padających fotonów, zmierzona wartość energii kinetycznej fotoelektronów jest przypisywana odpowiedniej energii wiązania. Na typowym widmie XPS widoczne są piki od fotoelektronów, natomiast tło pochodzi od fotoelektronów rozproszonych niesprężyście. Dzięki stabelaryzowanym wartościom energii wiązania charakterystycznych pików fotoelektronowych w łatwy sposób można przeprowadzić jakościową analizę składu chemicznego próbki. Ponadto, jeżeli orbitale atomów tego samego pierwiastka znajdują się w różnym otoczeniu chemicznym, to wykazują różnice w energii wiązania. Takie przesunięcie energii wiązania wynika z oddziaływania otoczenia chemicznego atomu, jego stopnia utlenienia i liczby koordynacyjnej.

Badania XPS zostały przeprowadzone za pomocą spektrometrów Axis Supra Kratos Analytical oraz Omicron Nanotechnology.

3.2.6. Absorpcyjna spektroskopia promieni X – XAS

Badania absorpcji promieniowania rentgenowskiego wykonuje się korzystając ze źródeł promieniowania synchrotronowego. Promieniowanie generowane przez synchrotrony jest charakteryzowane dużą intensywnością wiązki i stabilnością długości fali. Spektroskopia absorpcyjna polega na jonizacji atomów poprzez wysokoenergetyczną wiązkę fotonów. Padające fotony przekazują energię elektronom, które następnie przechodzą do pustego pasma przewodnictwa. Początek absorpcji promieniowania zachodzi dla długości fali charakterystycznej dla danej powłoki pierwiastka. W metodzie XAS mierzona jest zmiana współczynnika absorpcji w funkcji energii padającego promieniowania.

W ramach charakteryzacji struktury wytworzonych elektrokatalizatorów zastosowano spektroskopię XAS w zakresie miękkiego promieniowania rentgenowskiego (250-1800 eV), określaną jako spektroskopię subtelnej struktury w pobliżu krawędzi absorpcji promieniowania rentgenowskiego NEXAFS (near edge x-ray absorption fine structure). Metodą tą otrzymuje się informacje o stanie chemicznym i lokalnej strukturze materiału z pierwiastkową selektywnością. Badania przeprowadzono na linii pomiarowej PIRX Narodowego Centrum Promieniowania Synchrotronowego SOLARIS w Krakowie (rys. 28). Pomiary wykonano przy pomocy pomiaru prądu próbki (TEY– - total electron yield). Wyniki analizowano za pomocą dedykowanego oprogramowania PyMCA oraz Bessy.

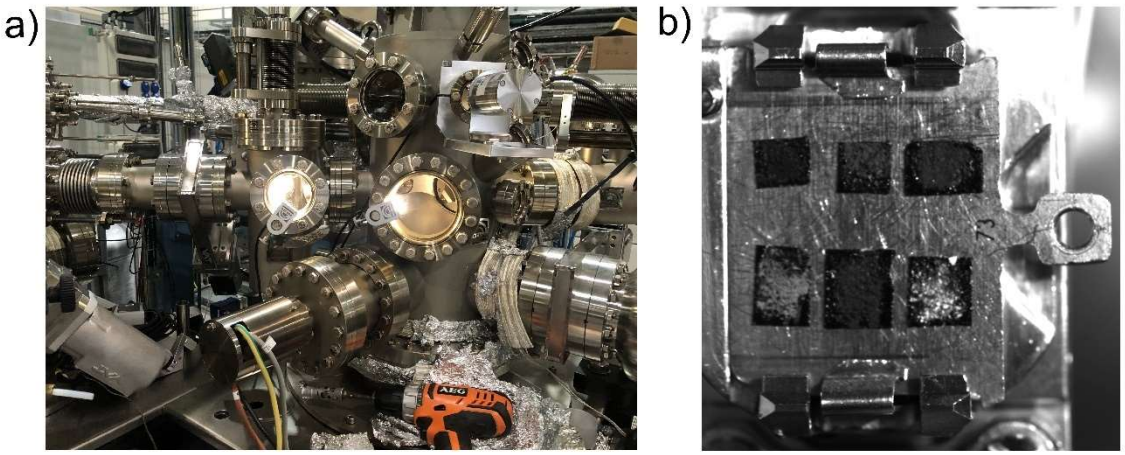

Rys. 28 (a) Stacja końcowa linii pomiarowej PIRX Narodowego Centrum Promieniowania Synchrotronowego SOLARIS oraz (b) płytka typu Omicron z nałożonymi proszkami badanych materiałów

3.2.7. FTIR

Fale podczerwone (IR – infrared) mają energie wywołujące oscylacje większości cząsteczek. Ze względu na to możliwe jest wywołanie i zaobserwowanie tych oscylacji poprzez naświetlanie próbki falami o długości w zakresie od 2 do 16 μm.

W spektrometrii FTIR (fourier transform infrared) wiązka wytworzona przez źródło promieniowania jest rozdzielana na dwie wiązki. Jedna z nich jest odbita od próbki lub przez nią przechodzi, zaś druga pełni rolę wiązki referencyjnej. Wiązka, która oddziałuje z próbką interferuje z pierwotną wiązką. Transformata Fouriera powstałego obrazu interferencyjnego daje zależność intensywności promieniowania w funkcji długości fali. W momencie gdy cząsteczka jest wzbudzona na dany stan oscylacyjny to pochłania energię fali o określonej częstotliwości, więc następuje zmniejszenie intensywności wiązki przechodzącej w stosunku do pierwotnej. Grupy funkcyjne znajdujące się w cząsteczce różnią się częstotliwością oscylacji wynikających z rozciągania lub zginania wiązań chemicznych. W związku z tym można zidentyfikować poszczególne grupy funkcyjne.

Pomiary FTIR zostały wykonane na Wydziale Inżynierii Materiałowej i Ceramiki Akademii Górniczo-Hutniczej im. Stanisława Staszica w Krakowie za pomocą spektrometru Bruker Vertex 70v w warunkach próżni i trybie transmisji.

3.2.8. Termograwimetria – TGA

Termograwimetria (TGA – thermogravimetric analysis) jest to instrumentalna metoda analityczna, w której rejestrowana jest zmiana masy próbki przy zmianie temperatury według kontrolowanego programu. Wyniki analizy przedstawiane są graficznie w formie termogramu. Urządzeniem wykorzystywanym do przeprowadzenia termograwimetrii jest termowaga. Najczęściej stosowane jest badanie dynamiczne, które przebiega w warunkach liniowego wzrostu lub spadku temperatury. W wyniku otrzymywana jest krzywa termograwimetryczna, gdzie przedstawiana jest zmiana masy próbki w funkcji czasu lub temperatury. Techniką tą

charakteryzuje się materiały, których zmiana masy może wynikać z powodu rozkładu, utleniania lub przebiegu innych reakcji chemicznych.

Pomiary TGA zostały przeprowadzone za pomocą termowagi Netzsch TG 209 F3.

3.2.9. ICP-OES

ICP-OES (inductively coupled plasma optical emission spectroscopy) jest to spektroskopowa metoda analityczna wykorzystywana do analizy składu chemicznego próbek. Podstawowym elementem tej techniki jest indukcyjnie sprzężona plazma generowana przez podgrzanie gazów, np. argonu, w cewce indukcyjnej. Próbka w postaci stałej lub ciekłej jest rozpylana i w formie drobnych kropel wprowadzana do generowanej plazmy, gdzie dochodzi do jonizacji pierwiastków zawartych w próbce. Powstające jonu pierwiastków przechodzą do stanów wzbudzonych energetycznie, a następnie powracają do stanów podstawowych emitując energię w postaci promieniowania elektromagnetycznego o charakterystycznych dla siebie długościach (widmo emisyjne). Promieniowanie to jest rejestrowane przez spektrometr optyczny. Na podstawie intensywności emisji można określić zawartość pierwiastków w próbce.

Badania ICP-OES zostały zlecone zewnętrznie akredytowanemu laboratorium badawczemu.

3.3. Pomiary elektryczne i elektrochemiczne

W tej części przedstawione zostaną wykonane pomiary elektryczne i elektrochemiczne. Hasłem pomiary elektrochemiczne określone są badania wchodzące w protokół pomiarowy służący do ewaluacji aktywności elektrokatalitycznej katalizatora.

Badania te były przeprowadzane za pomocą bipotencjostatu w typowym układzie trójelektrodowym przedstawionym na rysunku 29. Elektroda pracująca (WE – working electrode) jest to elektroda na powierzchni której zachodzi reakcja utleniania lub redukcji. Elektroda odniesienia (RE – reference electrode) jest to półogniwo o znanym potencjale, który nie zależy od stężenia analitu ani żadnego jonu obecnego w elektrolicie pomiarowym. Elektroda pomocnicza/przeciwelektroda (CE – counter electrode) jest to elektroda, która przyjmuje prąd płynący przez elektrodę pracującą. Po zamknięciu obwodu elektrycznego prąd przepływa między elektrodą pracującą i pomocniczą. W badaniach opublikowanych w artykułach w ramach rozprawy jako elektrody pracujące stosowano piankę niklową lub wirującą elektrodę dyskową z rdzeniem z węgla szklistego (RDE-GC – rotating disk electrode– - glassy carbon), jako elektrodę odniesienia elektrodę tlenkowo-rtęciową (Hg/HgO), chlorosrebrową (Ag/AgCl) lub odwracalną elektrodę wodorową (RHE – reversible hydrogen electrode), natomiast jako elektrodę pomocniczą platynową blaszkę lub drut. Pianka niklowa przedstawiona na rys. 30 w dobry sposób odwzorowuje elektrodę CCS przedstawioną w rozdziale 1.3.4, która potencjalnie może być stosowana w elektrolizerze „zero gap”. Natomiast w badaniach podstawowych główny nacisk kładziony jest na wnikliwe poznanie cech fizykochemicznych konkretnego materiału, a jeszcze nie jego zastosowanie w rozbudowanych układach elektrolizerów. W tym przypadku popularniejszym rozwiązaniem jest wykorzystanie obrotowych elektrod RDE. Ich przewagą jest

ściśle zdefiniowana powierzchnia, tj. powierzchnia przewodzącego rdzenia (0,196 cm^2), co pozwala na precyzyjne, ilościowe wyznaczenie właściwej aktywności elektrokatalitycznej materiału. Ponadto obroty elektrody w trakcie eksperymentu wspomagają usuwanie produktów reakcji w postaci pęcherzyków gazowych.

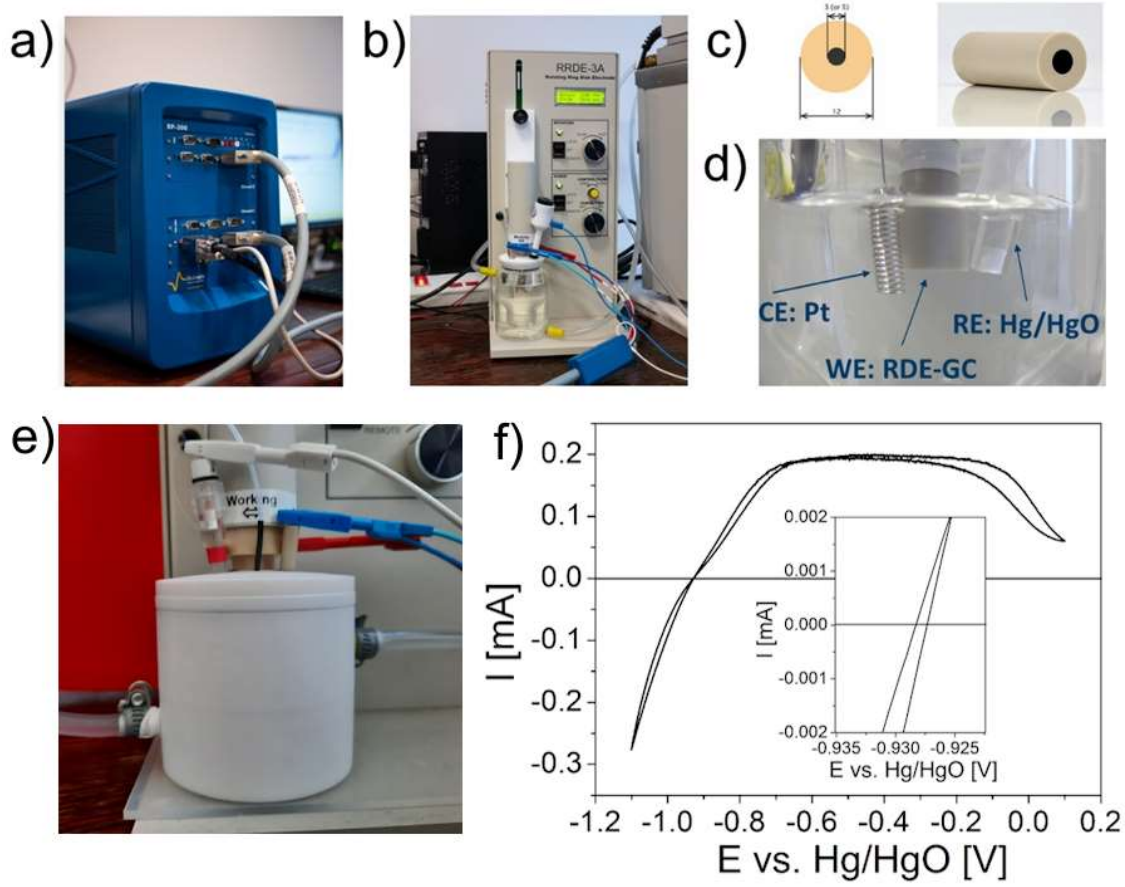

Rys. 29 Układ pomiarowy wykorzystywany do ewaluacji elektrokatalizatorów: (a) bipotencjostat BP-300, (b) układ elektrody wirującej ALS RRDE-3A, (c) wirująca elektroda dyskowa z rdzeniem z węgla szklistego, (d) trójelektrodowy układ pomiarowy, (e) teflonowe naczynko pomiarowe oraz (f) krzywa kalibracyjna elektrody Hg/HgO w nasyconym H_2 roztworze 0.1 M KOH

Pomiary były wykonywane w teflonowym naczynku pomiarowym, w roztworze wodorotlenku potasu o temperaturze 25°C utrzymywanej przez zewnętrzny termostat. Naczynie to zostało specjalnie zaprojektowane i wytoczone z teflonowego wałka na potrzeby niniejszej pracy. Niezależnie od wyboru elektrody odniesienia mierzony potencjał elektrody pracującej zawsze przedstawiany był względem RHE. W przypadku użycia elektrod Ag/AgCl oraz Hg/HgO wymagało to przeprowadzenia eksperymentalnej kalibracji w celu przeliczenia ich potencjałów równowagowych względem RHE [70,71].

Katalizator był nakładany na powierzchnię elektrody roboczej w postaci zawiesiny za pomocą pipety. Zawiesina składała się z proszku katalizatora, fazy ciągłej (etanolu lub izopropanolu) oraz dodatku jonomeru Nafion, który pełnił funkcję dyspersanta w zawiesinie, a po wyschnięciu działał jako lepiszcze sklejające cząstki katalizatora z podłożem. Na rys. 31 przedstawiona jest interakcja pomiędzy Nafionem a cząstkami katalizatora w zależności od ich

wzajemnego stosunku. Brak dodatku jonomeru skutkuje organizacją cząstek katalizatora w aglomeraty, odpowiednio dobrana ilość poprawia dyspersję cząstek, przy czym zbyt duża ilość powoduje ponowne formowanie aglomeratów [72]. Ponadto, żeby zapewnić równomierne rozłożenie cząstek katalizatora na powierzchni elektrody, zawiesinę nakładano na RDE-GC w trakcie wirowania [73].

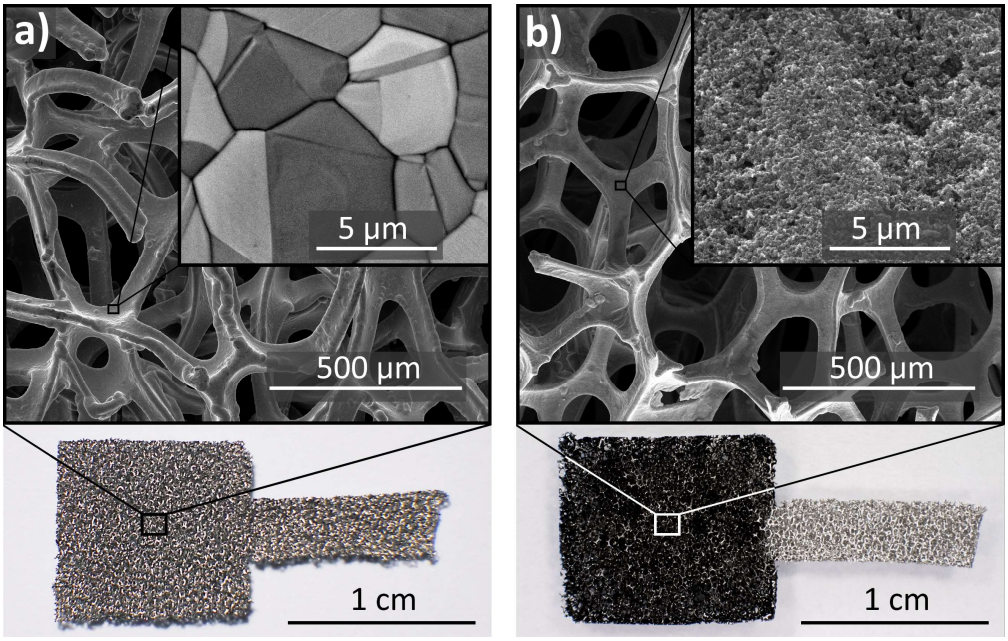

Rys. 30 Piankowa elektroda niklowa (a) przed modyfikacją oraz (b) pokryta ceramicznym katalizatorem.

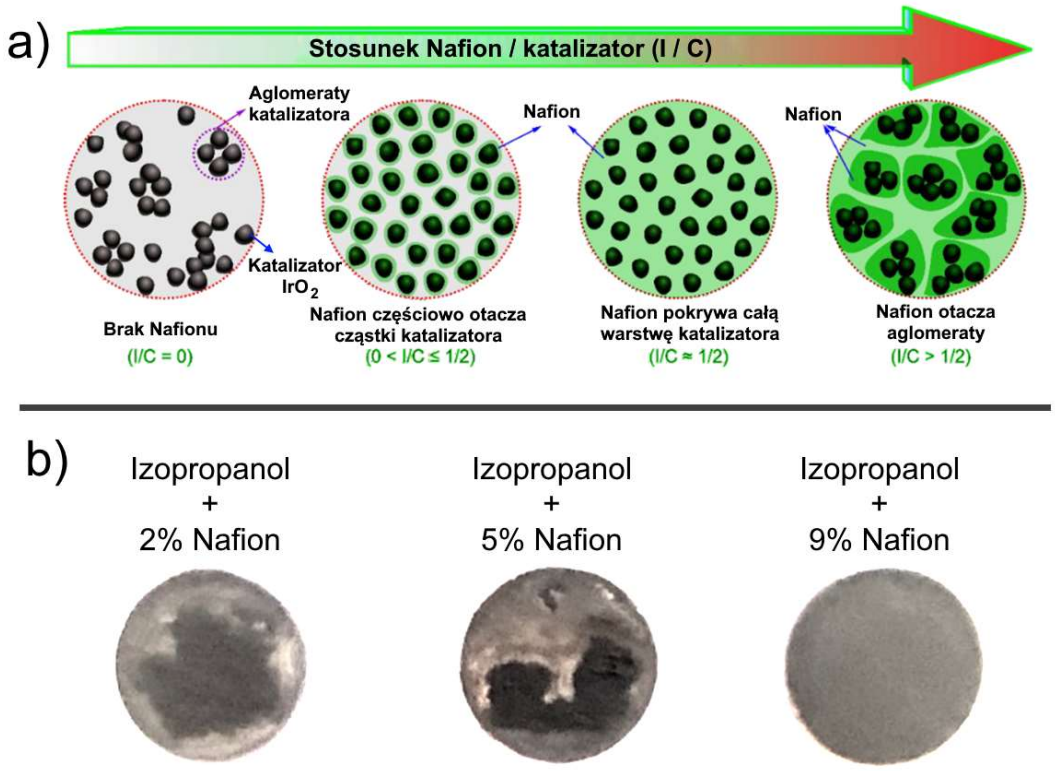

Rys. 31 (a) Schematyczny wpływ dodatku Nafionu na formowanie warstwy katalizatora [72] oraz (b) obserwacje eksperymentalne

Poniżej, na rys. 32, przedstawiono przykładowy protokół pomiarowy do ewaluacji aktywności katalizatorów w układzie wirującej elektrody dyskowej RDE. Pierwszym etapem jest polaryzacja elektrody pracującej w niskim zakresie potencjałów utleniających (aktywacja/kondycjonowanie) w celu otrzymania stabilnej odpowiedzi. Następnie wyznaczana jest powierzchnia elektrody za pomocą woltamperometrii cyklicznej. Aby wyznaczyć wartość strat omowych wynikających z konfiguracji układu pomiarowego, w głównej mierze odległości między elektrodami, wyznacza się rezystancję elektrolitu za pomocą elektrochemicznej spektroskopii impedancyjnej (EIS – electrochemical impedance spectroscopy). Kolejnym krokiem jest woltamperometria cykliczna w szerszym zakresie potencjałów niż w przypadku kondycjonowania. Z otrzymanych krzywych polaryzacyjnych wyznacza się wskaźniki aktywności elektrokatalitycznej tj. nadpotencjał reakcji OER oraz nachylenie krzywej Tafela. W ostatnim kroku rezystancja przeniesienia ładunku w trakcie reakcji OER wyznaczana jest za pomocą EIS przy zadanym potencjale.

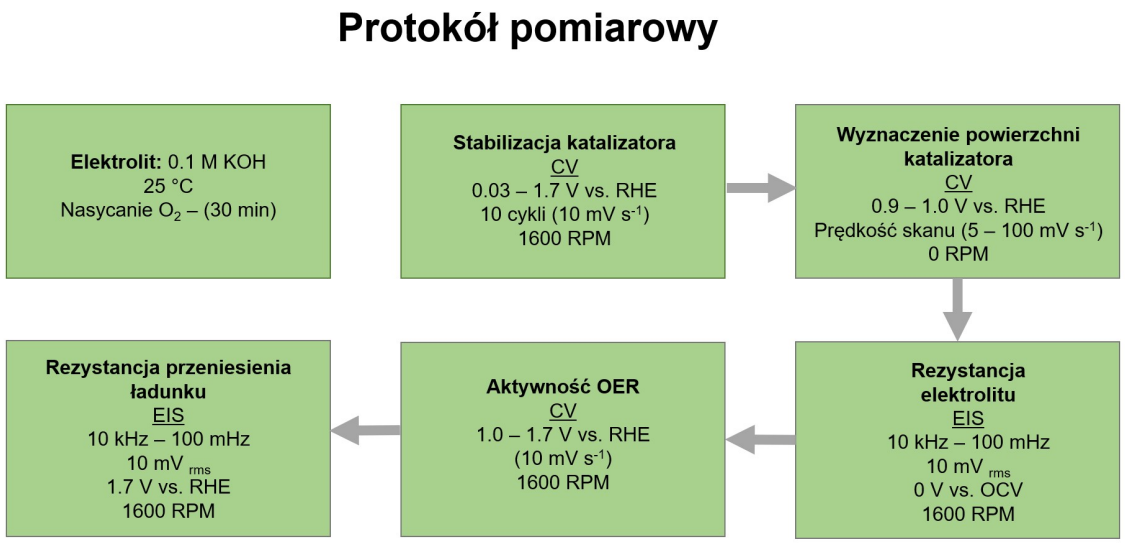

Rys. 32 Podstawowy protokół pomiarowy do ewaluacji aktywności elektrokatalitycznej katalizatora w układzie obrotowej elektrody dyskowej RDE

W przypadku wybranych katalizatorów protokół pomiarowy został rozszerzony o testy stabilności pracy materiału jako katalizatora OER. W tym celu wykorzystano komercyjny układ laboratoryjnego elektrolizera Micro Flow firmy ElectroCell, który jest przedstawiony na rys. 33. W układzie tym proszek katalizatora nakładany jest na powierzchnię elektrody pracującej (np. papier węglowy) w postaci zawiesiny tak samo jak w przypadku RDE. W elektrolizerze Micro Flow powierzchnia elektrody pracującej wynosi 10 cm^2, dużo więcej niż elektrody RDE (0,196 cm^2), więc lepiej odwzorowuje skalę rzeczywistego elektrolizera alkalicznego w warunkach laboratoryjnych.

W dalszej części przedstawione są elektrochemiczne i elektryczne techniki pomiarowe wykorzystywane w opublikowanych pracach.

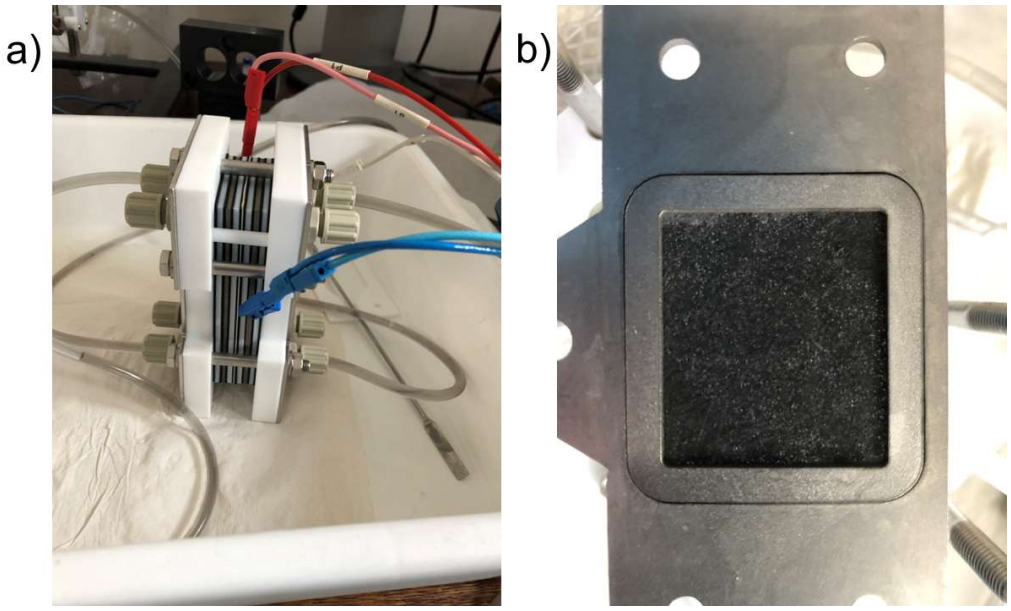

Rys. 33 (a) Elektrolizer Micro Flow oraz (b) elektroda pracująca w postaci papieru węglowego pokrytego proszkowym elektrokatalizatorem

3.3.1. Woltamperometria

Woltamperometria jest to elektrochemiczna technika, która polega na pomiarze natężenia prądy przepływającego przez elektrodę w funkcji przyłożonego potencjału. Jeżeli elektrodą pracującą, na której zachodzi reakcja elektrochemiczna jest elektroda o stałej powierzchni to obowiązuje określenie woltamperometria. Jeżeli wykorzystywana jest elektroda ciekła z powierzchnią odnawiającą się to określamy tę technikę polarografią. Zależność rejestrowanego natężenia prądu w funkcji potencjału elektrody przedstawiana jest na wykresie nazywanym woltamperogramem.

Jeżeli do elektrody pracującej przykładany jest liniowo zmieniający się potencjał to technikę tę nazywamy woltamperometrią liniową (LSV – linear sweep voltammetry). Natomiast, jeżeli do elektrody jest przykładany potencjał liniowo zmieniający się od wartości początkowej do wartości końcowej i zmiany potencjału są okresowo odtwarzane (rys.34), tak długo jak to konieczne, to technika nosi nazwę woltamperometrii cyklicznej (CV – cyclic voltammetry).

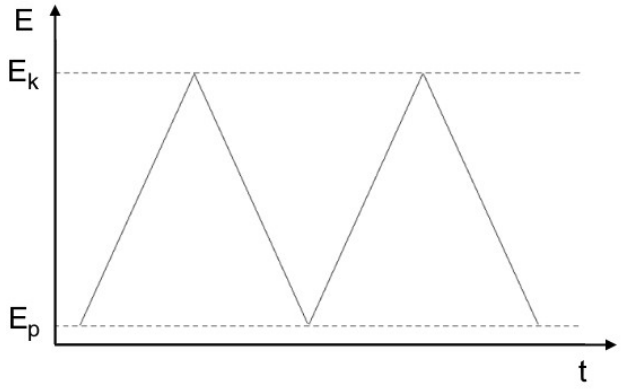

Rys. 34 Woltamperometria cykliczna – przebieg zmian potencjału

Technika woltamperometrii cyklicznej wykorzystywana była do określania elektrochemicznie aktywnej powierzchni (ECSA – electrochemically active surface area) badanych elektrokatalizatorów. W tym celu przeprowadzano elektrochemiczny pomiar pojemności elektrycznej warstwy podwójnej. Elektryczna warstwa podwójna powstaje na granicy faz elektroda/elektrolit i w uproszczeniu może być przedstawiona jako kondensator o przeciwnie naładowanych okładkach, gdzie jedną okładką jest powierzchnia elektrody, a drugą nieruchoma warstwa jonów przylegająca do elektrody od strony roztworu. Aby wyznaczyć pojemność warstwy podwójnej wyznaczane są cykliczne krzywe woltamperometryczne w zakresie potencjałów niefaradajowskich (w tym zakresie nie zachodzą procesy obejmujące transfer elektronów pomiędzy elektrodą a elektrolitem). W efekcie zmian potencjału elektrody następuje ładowanie warstwy podwójnej. Pojemność warstwy podwójnej oblicza się z zależności:

$$C_{DL} = v \cdot i \tag{28}$$

, gdzie: C_{DL} – pojemność warstwy podwójnej (double layer capacitance) [mF], v – prędkość skanu (zmian potencjału) [V s^{-1}], i – prąd pojemnościowy [mA].

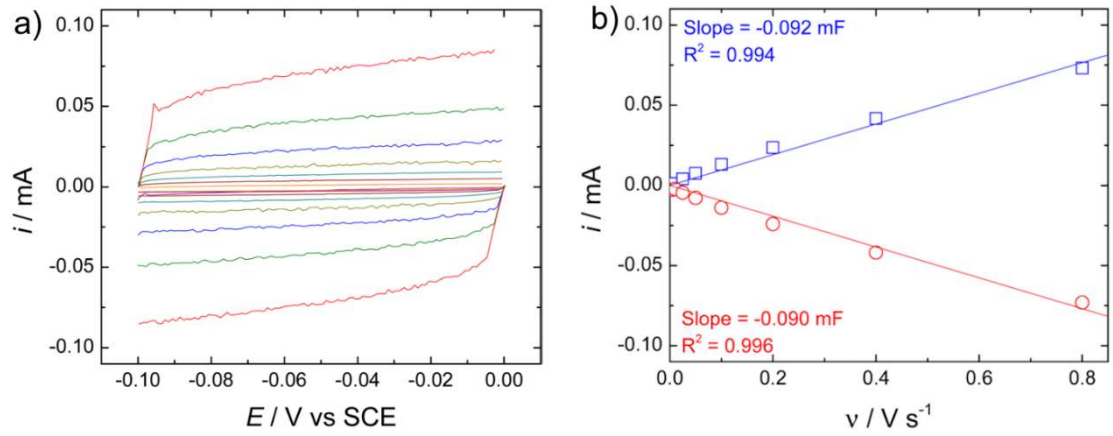

Rys. 35 (a) Pomiary pojemności warstwy podwójnej elektoosadzonej warstwy NiO_x przy różnych prędkościach skanu woltamperometrii cyklicznej oraz (b) wartości katodowego i anodowego prądu pojemnościowego w funkcji prędkości skanu [74].

Tak jak pokazano na rys. 35 krzywe woltamperometryczne wyznaczane są przy różnych prędkościach zmian potencjału. Następnie wykreśla się wartości prądu katodowego i anodowego (wartości odczytane przy potencjale w połowie mierzonego zakresu) w funkcji prędkości skanu. Nachylenie prostej otrzymanej za pomocą dopasowania krzywej regresji liniowej odpowiada pojemności warstwy podwójnej, a ostateczna wartość to średnia wyznaczona dla prądów katodowych i anodowych.

Następnie wartość ECSA danego katalizatora można wyznaczyć z zależności:

$$ECSA = \frac{C_{DL}}{C_S} \tag{29}$$

, gdzie: *ECSA* – powierzchnia elektrochemicznie aktywna [cm^2], C_{DL} – pojemność warstwy podwójnej [F], C_S – pojemność właściwa [F cm^{-2}].

Pojemność właściwa jest to wielkość ściśle związana z właściwościami danego materiału i elektrolitu, w którym jest wyznaczona. Dla katalizatorów tlenkowych literaturowo przyjmuje się wartość 0,040 mF cm^{-2} w 1.0 M NaOH [74].

Aktywność w kierunku elektrokatalizy OER była wyznaczana za pomocą woltamperometrii cyklicznej w zakresie dodatnich potencjałów obejmujących wydzielanie tlenu na elektrodzie pracującej. W przypadku, gdy pomiary wykonywano na wirującej elektrodzie RDE, to prędkość obrotowa elektrody była ustawiona na 1600 obrotów na minutę. Zastosowana prędkość skanu to 10 mV s^{-1}. Przy tak niskiej prędkości skanu zachowany jest stan ustalony na powierzchni elektrody, natomiast obroty pomagają w usuwaniu produktu i tworzeniu pęcherzyków tlenu na powierzchni elektrody. Zebrane dane poddawane są obróbce mającej na celu wyznaczenie rzeczywistych krzywych OER z pominięciem wpływu rezystancji elektrolitu czy ładowaniem elektrody. Tak jak przedstawiono na rys. 36 woltamperogramem zbierany jest w pełnym zakresie potencjałów, tj. w kierunku rosnącym i malejącym, a następnie wyznaczana jest średnia arytmetyczna reprezentująca krzywą OER z pominięciem prądów pojemnościowych. Żeby wyznaczyć rzeczywisty potencjał elektrody pracującej kluczowe jest wyeliminowanie wpływu strat omowych szczególnie wynikających z rezystancji elektrolitu pomiędzy elektrodą pracującą i referencyjną oraz wszelkich rezystancji kontaktowych. Zmierzony potencjał poddawany jest korekcie spadku omowego zgodnie z poniższą zależnością:

$$E = E_{RHE} - iR \tag{29}$$

, gdzie E – rzeczywisty potencjał elektrody, E_{RHE} – zmierzony potencjał elektrody pracującej w odniesieniu do potencjału równowagowego RHE [V], i – zmierzone natężenie prądu [A], R – rezystancja elektrolitu [Ω].

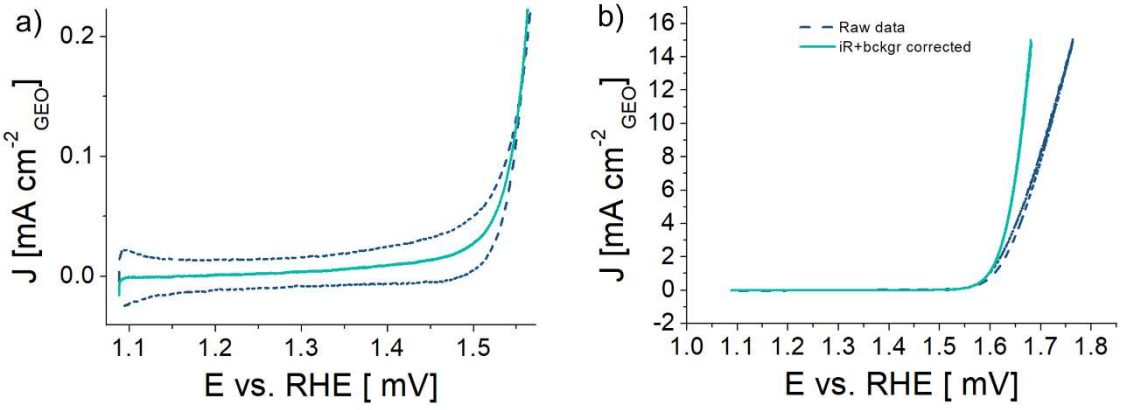

Rys. 36 Krzywa polaryzacyjna OER po korekcie pojemnościowej oraz (b) po korekcie iR.

Aby w prosty sposób porównać aktywność badanego materiału z wynikami literaturowymi, niezależnie od rodzaju wykorzystywanej elektrody, zmierzony prąd jest normalizowany. Znormalizowana gęstość prądu wyznaczana jest poprzez podzielenie zmierzonego natężenia prądu przez geometryczną powierzchnię elektrody, elektrochemicznie aktywną powierzchnię katalizatora ECSA, powierzchnię właściwą katalizatora wyznaczoną z izotermy adsorpcji lub przez masę katalizatora znajdującego się na elektrodzie pracującej.

Typowym parametrem wyznaczanym do oceny aktywności elektrokatalizatora OER jest nadpotencjał η_{10}, czyli różnica pomiędzy potencjałem potrzebnym do osiągnięcia gęstości prądu o wartości 10 mA cm^{-2}_{GEO}(normalizacja geometryczna) a potencjałem równowagowym OER (1,23 V względem RHE).

Drugim podstawowym kryterium oceny jest nachylenie krzywej Tafela, które pokazuje zależność pomiędzy nadpotencjałem a gęstością prądu elektrokatalizy. Jest to ważny wskaźnik kinetyki zachodzącej reakcji, który wyznaczany jest z równania Tafela:

$$\eta = a + b \log\ j \tag{30}$$

, gdzie η – nadpotencjał reakcji [mV], a – punkt przecięcia z osią rzędnych, b – nachylenie krzywej Tafela [mV dec^{-1}], j – gęstość prądu [mA cm^{-2}]. Eksperymentalnie wyznacza się je po wykreśleniu wykresu Tafela, tj. nadpotencjału w funkcji logarytmu gęstości prądu i dopasowaniu prostej w prostoliniowym regionie grafu. W przypadku reakcji wieloelektronowych, takich jak OER, nachylenie krzywej Tafela dostarcza informacji na temat mechanizmu reakcji, ponieważ wartość nachylenia zależy od współczynnika przenoszenia ładunku i liczby przenoszonych elektronów. Nachylenie krzywej Tafela podaje również bezpośrednią korelację między zmianami prądu a przyłożonym napięciem. Mniejsza wartość nachylenia krzywej Tafela wskazuje na szybszy wzrost prądu katalitycznego po przyłożeniu wyższego napięcia, więc niska wartość jest cechą pożądaną dla idealnego katalizatora OER.

3.3.2. Elektrochemiczna Spektroskopia Impedancyjna

Elektrochemiczna spektroskopia impedancyjna (EIS – electrochemical impedance spectroscopy) jest to szeroko stosowana metoda badawcza polegająca na przyłożeniu napięcia przemiennego (AC – alternating current) do układu elektrochemicznego i pomiarze odpowiedzi prądowej. Technika ta umożliwia badanie układów o dużym stopniu skomplikowania. Możliwe jest zbadanie oddzielnych elementów i zjawisk zachodzących w układzie np. oporu elektrolitu lub warstwy pasywnej, wyznaczenie pojemności warstwy podwójnej, zbadanie reakcji przeniesienia ładunku i procesów dyfuzyjnych. Odpowiedź układu elektrochemicznego po naruszeniu jego równowagi poprzez zmiennoprądowy sygnał o danym potencjale i częstotliwości, przyjmuje formę prądową o amplitudzie pomniejszonej o opór badanego materiału i przesuniętą w fazie względem wzbudzenia. Impedancję układu wyznacza się z poniższych zależności:

$$E(t) = E_0 \cos\left(\omega t\right) \tag{31}$$

$$I(t) = I_0 \cos\left(\omega t + \varphi\right) \tag{32}$$

$$Z = \frac{E(t)}{I(t)} = Z_0 \frac{\cos\left(\omega t\right)}{\cos\left(\omega t + \varphi\right)} \tag{33}$$

, gdzie $E(t)$ – sygnał wzbudzający (potencjał w czasie) [V], E_0 – amplituda sygnału [V], ω – pulsacja [Hz], $I(t)$ – odpowiedź prądowa (natężenie prądu w czasie) [A], I_0 – amplituda odpowiedzi [A], φ – przesunięcie fazowe, Z – impedancja [Ω], Z_0 – moduł impedancji [Ω].

Dane zebrane podczas pomiaru EIS są najczęściej prezentowane w postaci wykresów Nyquista lub Bodego. Na wykresie Nyquista widma impedancyjne przedstawione są na

płaszczyźnie zmiennej zespolonej, gdzie na osi rzędnych umieszczona jest część urojona impedancji (*Z''*), a na osi odciętych część rzeczywista impedancji (*Z'*). Wykres Bodego przedstawia moduł impedancji (Z_0) oraz przesunięcie fazowe (φ) w funkcji częstotliwości.

W ramach tej pracy pomiary EIS były wykonywane w tym samym trójelektrodowym układzie co pozostałe techniki. Widma EIS były zbierane w zakresie malejących częstotliwości od 100 kHz do 100 mHz przy napięciu 0 V względem OCV (open circuit voltage – napięcie obwodu otwartego) oraz 1,7 V względem RHE. Widma były interpretowane na wykresach Nyquista. Dane eksperymentalne były dopasowywane do układu zastępczego za pomocą programu EC-Lab. Wybranym modelem był zmodyfikowany układ Randlesa (rys. 37), w którym *Rs* to rezystancja elektrolitu, *Rct* to rezystancja przeniesienia ładunku (z ang. charge transfer resistance), a element stałofazowy (CPE – constant phase element) Q jest interpretowany jako pojemność warstw podwójnej. Na wykresie Nyquista rezystancja elektrolitu może zostać odczytana jako przecięcie z osią odciętych przy wysokich częstotliwościach, natomiast rezystancja przeniesienia ładunku to szerokość wykreślonego półokręgu.

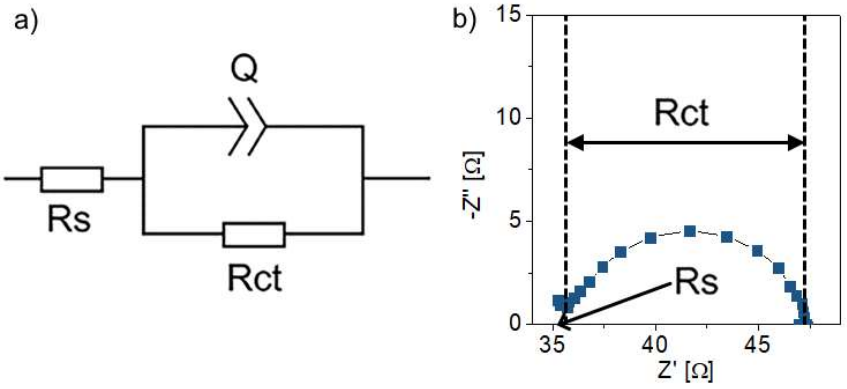

Rys. 37 (a) Zmodyfikowany układ zastępczy Randlesa oraz (b) przykładowy wykres Nyquista otrzymany dla próbki $MnCo_{1,5}Fe_{0,5}O_4$.

3.3.3. Chronopotencjometria

Chronopotencjometria jest to metoda galwanostatyczna, w której ustala się stałe natężenie prądu, natomiast mierzone są zmiany napięcia w czasie. Technika ta jest wykorzystywana do badania stabilności pracy elektrokatalizatorów OER.

Ze względu na odrywanie się warstwy katalitycznej od powierzchni elektrody RDE wraz z powstawaniem pęcherzy tlenu, pomiary chronopotencjometryczne zostały przeprowadzone w układzie laboratoryjnego elektrolizera Micro Flow. Mierzona była stabilność sygnału w postaci napięcia potrzebnego do utrzymania przepływu prądu o gęstości 10 mA cm^{-2} w czasie 48 h.

3.3.4. Pomiar przewodności metodą Van der Pauwa

Metoda Van der Pauwa służy do pomiaru przewodności elektrycznej płaskich próbek przewodzących o dowolnym kształcie [75]. W ramach pracy nad perowskitami $SrTi_{1-x}Fe_xO_{3-d}$, próbki zostały przygotowane w formie pastylek o określonej średnicy oraz grubości. Cztery kontakty elektryczne zostały przygotowane ze srebrnej pasty i umiejscowione na obrzeżach

pastylki, tak jak jest to przedstawione na rys. 38. W trakcie badania wywoływano przepływ prądu elektrycznego pomiędzy kontaktami A(C) i B(D) i jednocześnie mierzono napięcie pomiędzy kontaktami C(D) i D(B). Przewodność badanego materiału wyznacza się z zależności:

$$\sigma = \frac{ln2}{\pi h}\frac{2}{R_{AB,CD} + R_{CA,DB}} \tag{34}$$

, gdzie: σ – przewodność próbki [S cm^{-1}], h – grubość próbki [m], R – rezystancja wyznaczona z wyników pomiaru metodą Van der Pauwa [Ω].

Ponadto korzystając z równania Arrheniusa wyznaczono energię aktywacji przewodnictwa:

$$ln\sigma = \frac{E_a}{k} \times \frac{1}{T} + ln\sigma_0 \tag{35}$$

, gdzie E_a – energia aktywacji przewodnictwa [eV], T – temperatura [K], k – stała Boltzmanna [J K^{-1}], σ_o – czynnik przedwykładniczy.

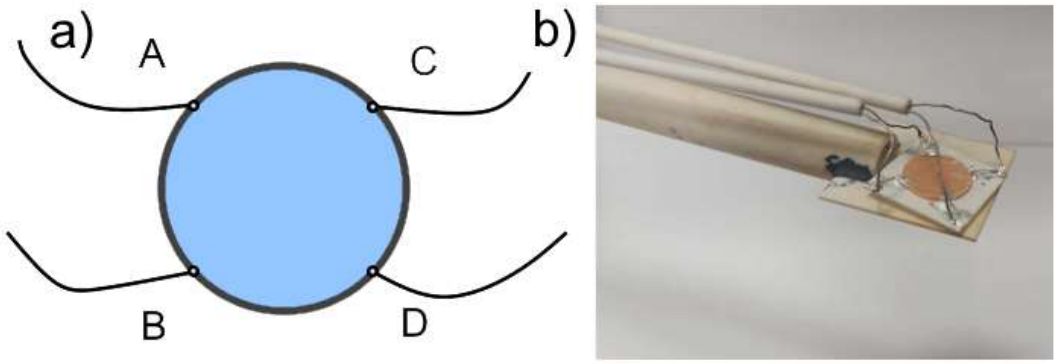

Rys. 38 (a) Schemat pastylki na której mierzono przewodność wytworzonych materiałów oraz (b) zdjęcie układu pomiarowego

Pomiary zostały wykonane w atmosferze syntetycznego powietrza (20% O_2) w zakresie temperatur od 200°C do temperatury pokojowej. Dane zostały zebrane za pomocą automatycznego systemu logującego.

4. WYKAZ PUBLIKACJI WCHODZĄCYCH DO ZBIORU ARTYKUŁÓW

W tym rozdziale zawarte są artykuły publikacji naukowych opracowanych i opublikowanych w ramach studiów doktoranckich. Każda publikacja poprzedzona jest streszczeniem w języku polskim oraz oświadczeniami autorów stanowiącymi o ich wkładzie w powstanie pracy.

W pozycji nr 1 wytypowana została stechiometria materiału wykazująca największą aktywność elektrokatalityczną; praca to stanowi swoiste wprowadzenie do tematu spineli manganowo-kobaltowych jako elektrokatalizatorów OER. Natomiast praca nr 2 skupia się na metodach modyfikacji właściwości fizykochemicznych struktury spinelu $MnCo_2O_4$ poprzez wprowadzenie żelaza do struktury krystalicznej w celu polepszenia jego aktywności. Publikacja nr 3 zwraca uwagę na możliwość zastosowania alternatywnych elektrokatalizatorów o strukturze perowskitu, w których skład wchodzą stosunkowo niedrogie i bezpieczne dla środowiska pierwiastki, tj. Sr, Ti oraz Fe. Szczególną uwagę poświęcono wpływowi obecności żelaza w strukturze perowskitu na jego aktywność elektrokatalityczną oraz równie ważną stabilność chemiczną w zasadowym elektrolicie. Ostatnie dwie publikacje pokazują, że właściwości materiałów elektrokatalitycznych mogą być modulowane bez zmian składu chemicznego. W pracach opisany został wpływ obróbki mechanicznej lub cieplnej na zarówno morfologię wytworzonych proszków jaki i stopnie utlenienia kationów metali w zewnętrznych warstwach atomowych.

W skład rozprawy wchodzą następujące publikacje:

Wprowadzenie do tematu spineli manganowo-kobaltowych jako elektrokatalizatorów OER:

1. Lankauf K, Cysewska K, Karczewski J, Mielewczyk-Gryń A, Górnicka K, Cempura G, Chen M, Jasiński P, Molin S. *$Mn_xCo_{3-x}O_4$ spinel oxides as efficient oxygen evolution reaction catalysts in alkaline media.* Int J Hydrogen Energy 2020;5., IF: 7,139, Liczba punktów ministerialnych: 140, liczba cytowań[2]: 34.

Publikacje związane z wykazaniem tezy 1:

1. Możliwe jest zwiększenie aktywności elektrokatalitycznej spinelu $MnCo_2O_4$ oraz perowskitu $SrTiO_{3-d}$ w kierunku wydzielania tlenu z zachowaniem stabilności chemicznej poprzez wprowadzenie żelaza do struktury krystalicznej:

2. Lankauf K, Górnicka K, Błaszczak P, Karczewski J, Ryl J, Cempura G, Zając M, Bik M, Sitarz M, Jasiński P, Molin S. *Tuning of e_g electron occupancy of $MnCo_2O_4$ spinel for oxygen evolution reaction by partial substitution of Co by Fe at octahedral sites*. Int J Hydrogen Energy 2023;48:8854–66., IF: 7,139, Liczba punktów ministerialnych: 140, liczba cytowań[2:] 6

[2] Według Scopus na dzień 26.01.2024

3. Lankauf K, Mroziński A, Błaszczak P, Górnicka K, Ignaczak J, Łapiński M, Karczewski J, Cempura G, Jasiński P, Molin S. *The effect of Fe on chemical stability and oxygen evolution performance of high surface area $SrTi_{x-1}Fe_xO_{3-d}$ mixed ionic-electronic conductors in alkaline media* 2021;6. IF: 7,139, Liczba punktów ministerialnych: 140, liczba cytowań[3]: 14.

Publikacje związane z wykazaniem tezy 2:

2. Możliwe jest poprawienie aktywności elektrokatalitycznej spineli $MnCo_2O_4$ oraz $MnCo_{1,5}Fe_{0,5}O_4$ w kierunku reakcji wydzielania tlenu poprzez zastosowanie posyntezowej obróbki cieplnej lub mechanicznej:

4. Pawłowska S, Lankauf K, Błaszczak P, Karczewski J, Górnicka K, Cempura G, Jasiński P, Molin S. *Tailoring a Low-Energy Ball Milled $MnCo_2O_4$ Spinel Catalyst to Boost Oxygen Evolution Reaction Performance*. SSRN Electron J 2022;619., IF: 6.86, Liczba punktów ministerialnych: 140, liczba cytowań[3]: 4.
5. Lankauf K, Lemieszek B, Górnicka K, Błaszczak P, Zając M, Jasiński P, Molin S. *Enhanced Electrochemical Performance of $MnCo_{1.5}Fe_{0.5}O_4$ Spinel for Oxygen Evolution Reaction through Heat Treatment*. Energy & Fuels, IF: 5.3, Liczba punktów ministerialnych: 100, liczba cytowań[3]: 0

[3] Według Scopus na dzień 26.01.2024

4.1 $Mn_xCo_{3-x}O_4$ spinel oxides as efficient oxygen evolution reaction catalysts in alkaline media

W tej pracy za pomocą syntezy zol-żel przygotowano serię tlenków manganowo-kobaltowych o strukturze spinelu $Mn_xCo_{3-x}O_4$ (x = 0, 0,5, 1, 1,5, 2) i zbadano ich właściwości pod kątem aktywności elektrokatalitycznej reakcji utleniania tlenu w środowisku zasadowym. Przygotowany prekursor był kalcynowany w temperaturze 400°C, a następnie 600°C. W kolejnym kroku w celu rozdrobnienia ziaren, a zatem zwiększania powierzchni właściwej, proszki spineli były mielone przy użyciu kulek mielących (φ = 3 mm) wykonanych z YSZ. Za pomocą dyfraktometrii rentgenowskiej zbadano, że w zależności od stosunku składowych pierwiastków metalicznych spinel $Mn_xCo_{3-x}O_4$ krystalizuje w strukturze regularnej lub tetragonalnej. Ponadto w przypadku stechiometrii $MnCo_2O_4$ badania wykazały uzyskanie dwufazowej mieszaniny tlenków $Mn_{1.4}Co_{1.6}O_4$ oraz Co_3O_4 w stosunku 7:3. Analizując obrazy wykonane za pomocą mikroskopii TEM można wyodrębnić dwie grupy nanokryształów, tj. o średnicach ziaren poniżej 50 nm oraz powyżej 100 nm. Analizy EDS pokazują segregację pierwiastków pomiędzy poszczególnymi ziarnami, co dodatkowo potwierdza utworzenie mieszaniny dwóch faz.

Seria przygotowanych materiałów została zbadana pod kątem elektrokatalizy reakcji utleniania tlenu w 1 M KOH. Proszki tlenków spineli w postaci roztworów z dodatkiem Nafionu i węgla przewodzącego były nanoszone za pomocą pipety na podłoże z pianki niklowej i w takiej formie wykorzystywane jako elektrody pracujące (anody) podczas elektrolizy wody. Wykazano, że dodatek Mn (maksymalnie do poziomu $x \leq 1$) do struktury regularnej Co_3O_4 polepsza właściwości elektrokatalityczne tej grupy materiałów. Najniższy nadpotencjał reakcji OER o wartości 327 mV został osiągnięty przez dwufazową strukturę $Mn_{1.4}Co_{1.6}O_4$ oraz Co_3O_4. Za pomocą pomiarów chronopotencjometrycznych zbadano stabilność pracy katalizatorów. Badania wykazały dobrą stabilność, porównywalną z referencyjnym dwutlenkiem irydu, dla wszystkich materiałów poza dwufazowym $MnCo_2O_4$.

Do oryginalnych wyników zaliczam syntezę zol-żel serii spineli manganowo-kobaltowych dla celów elektrokatalizy reakcji OER. Łącząc kompleksowe badania strukturalne i elektrochemiczne wykazałem, że największą aktywność elektrokatalityczną posiada hybrydowa dwufazowa mieszanina $Mn_{1.4}Co_{1.6}O_4$ oraz Co_3O_4 otrzymana podczas syntezy związku o stechiometrii $MnCo_2O_4$. Co więcej, aktywność ta jest obserwowana tylko dla ściśle określonej mieszaniny, a nie dla poszczególnych faz.

W przedstawionej publikacji samodzielne przeprowadziłem syntezę materiałów oraz przygotowałem elektrody niklowe z naniesionym katalizatorem. W dalszej kolejności przeprowadziłem część pomiarów elektrochemicznych. Ponadto odpowiadałem za analizę otrzymanych wyników, przygotowanie rysunków oraz napisanie manuskryptu. Jako autor korespondencyjny zgłosiłem artykuł do publikacji w czasopiśmie oraz przygotowałem poprawki w odpowiedzi na recenzje.

Oświadczenie współautorów o wkładzie w powstanie publikacji: „$Mn_xCo_{3-x}O_4$ spinel oxides as efficient oxygen evolution reaction catalysts in alkaline media"

Imię i nazwisko autora	Wkład w powstanie pracy	Podpis
Krystian Lankauf	Konceptualizacja, metodologia, badania, pisanie – oryginalna wersja robocza, wizualizacja	
Karolina Cysewska	Konceptualizacja, analiza formalna, badania (pomiary elektrochemiczne), pisanie – recenzja i redakcja	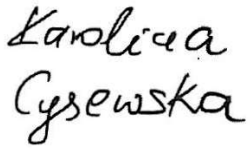
Jakub Karczewski	Badania (SEM), pisanie – recenzja i redakcja	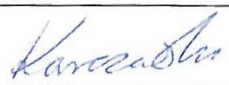
Aleksandra Mielewczyk-Gryń	Badania (BET), pisanie – recenzja i redakcja	
Karolina Górnicka	Badania (XRD), pisanie – recenzja i redakcja	
Grzegorz Cempura	Badania (TEM), pisanie – recenzja i redakcja	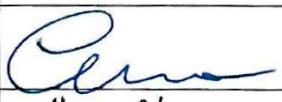
Ming Chen	Badania (diagram fazowy), pisanie – recenzja i redakcja	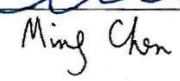
Piotr Jasiński	Pisanie – recenzja i redakcja, nadzór, zasoby	
Sebastian Molin	Konceptualizacja, pisanie – recenzja i redakcja, nadzór, zasoby, pozyskiwanie funduszy	

INTERNATIONAL JOURNAL OF HYDROGEN ENERGY 45 (2020) 14867–14879

Available online at www.sciencedirect.com

ScienceDirect

journal homepage: www.elsevier.com/locate/he

$Mn_xCo_{3-x}O_4$ spinel oxides as efficient oxygen evolution reaction catalysts in alkaline media

K. Lankauf [a,*], *K. Cysewska* [a], *J. Karczewski* [b], *A. Mielewczyk-Gryń* [b], *K. Górnicka* [b], *G. Cempura* [c], *M. Chen* [d], *P. Jasiński* [a], *S. Molin* [a]

[a] *Faculty of Electronics, Telecommunications and Informatics, Gdańsk University of Technology, ul. G. Narutowicza 11/12, 80-233 Gdańsk, Poland*

[b] *Faculty of Applied Physics and Mathematics, Gdańsk University of Technology, ul. G. Narutowicza 11/12, 80-233 Gdańsk, Poland*

[c] *International Centre of Electron Microscopy for Materials Science, AGH University of Science and Technology, al. A. Mickiewicza 30, 30-059 Kraków, Poland*

[d] *Department of Energy Conversion and Storage, Technical University of Denmark, Frederiksborgvej 399, 4000, Roskilde, Denmark*

HIGHLIGHTS

- $Mn_xCo_{3-x}O_4$ spinel oxides were synthesised via a soft chemistry method.
- The effect of Mn addition on structural and physicochemical properties was investigated.
- Synthesised oxides powders were examined as OER catalysts in alkaline medium.
- Synergistic effect of dual phase $MnCo_2O_4$ improves the OER catalytic activity.

GRAPHICAL ABSTRACT

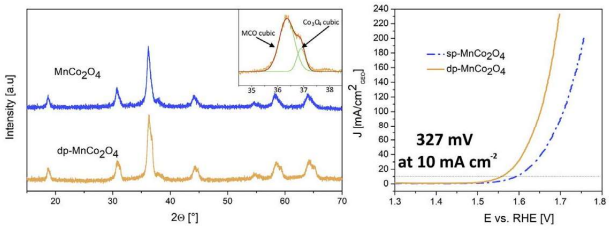

ARTICLE INFO

Article history:
Received 10 February 2020
Received in revised form
20 March 2020
Accepted 26 March 2020
Available online 23 April 2020

Keywords:
Manganese cobaltite
Oxygen evolution reaction

ABSTRACT

The design of efficient electrocatalysts for oxygen evolution reaction (OER) is an essential task in developing sustainable water splitting technology for the production of hydrogen. In this work, manganese cobalt spinel oxides with a general formula of $Mn_xCo_{3-x}O_4$ ($x = 0, 0.5, 1, 1.5, 2$) were synthesised via a soft chemistry method. Non-equilibrium mixed powder compositions were produced, resulting in high electrocatalytic activity. The oxygen evolution reaction was evaluated in an alkaline medium (1 M KOH). It was shown that the addition of Mn (up to $x \leq 1$) to the cubic Co_3O_4 phase results in an increase of the electrocatalytic performance. The lowest overpotential was obtained for the composition designated as $MnCo_2O_4$, which exhibited a dual-phase structure (~30% Co_3O_4 + 70% $Mn_{1.4}Co_{1.6}O_4$): the benchmark current density of 10 mA cm^{-2} was achieved at the relatively low overpotential of 327 mV. The corresponding Tafel slope was determined to be ~79 mV dec^{-1}.

* *Corresponding author.*
E-mail address: krystian.lankauf@pg.edu.pl (K. Lankauf).

https://doi.org/10.1016/j.ijhydene.2020.03.188

Spinel oxides
Water splitting

Stabilities of the electrodes were tested for 25 h, showing degradation of the $MnCo_2O_4$ powder, but no degradation, or even a slight activation for other spinels.

Introduction

Among different hydrogen production methods, water electrolysis seems to be a viable process to provide clean hydrogen [1,2], especially when coupled with renewable electricity production. The key point impeding the electrolysis process is the sluggish oxygen evolution reaction (OER) kinetics of the multi-electron charge transfer reaction resulting in high reaction overpotentials [3,4]. For this reason, effective electrocatalysts may be applied to accelerate the reaction and reduce the overpotential. The most active catalysts for water splitting reactions, hydrogen and oxygen evolution, are based on precious elements: Pt and IrO_2, respectively. Their low abundance in the Earth's crust coupled with high costs significantly limits those elements' application for water splitting electrodes.

Recently, researchers have shown an increased interest in 3d transition-metals OER electrocatalysts, especially in oxides with perovskite [5–7] and spinel structures [8–14], layered double hydroxides (LDH) [15–17] and carbides [18–20]. For example, She et al. reported an $Sr(Co_{0.8}Fe_{0.2})_{0.7}B_{0.3}O_{3-\delta}$ (SCFB-0.3) perovskite realising ultrafast oxygen evolution with overpotential (η) at 10 mA cm^{-2} of 240 mV in 1.0 M KOH aqueous electrolyte [21]. Cubic structure Co_3O_4 spinel nanoparticles with average diameters of 5.9 nm were synthesised by Esswein et al. and demonstrated η of 328 mV at 10 mA cm^{-2} in 1.0 M KOH [22]. One of the promising spinel group materials is mixed-valent $Mn_xCo_{3-x}O_4$ due to the possibility of tuning the cation distribution by changing the synthesis parameters and composition. Mn-Co spinels have interesting flexible properties and have been reported both for oxygen reduction [23] and evolution processes. Han et al. fabricated mixed phases of Co- and Mn-based oxides which for OER demonstrated η of 450 mV at 10 mA cm^{-2} in 1.0 M KOH with a low Tafel slope of 35.8 mV dec^{-1} [24]. The hybrid nanostructure of manganese cobaltite/nitrogen-doped multi-walled carbon nanotubes ($Mn_xCo_{3-x}O_4$@NCNTs) was proposed by Zhao et al. and exhibited an overpotential of 470 mV at 10 mA cm^{-2} in 0.1 M KOH [25].

The physicochemical properties of the spinels can be tailored by manipulating different cations and also by altering their preparation methods. Spinels can be synthesised by different approaches, including physical and preferably chemical processes: hard-template [26], wet-chemical [27], hydrothermal [28,29], solvothermal [30], spray pyrolysis [31], co-precipitation [32], and sol-gel [22,33–35]. Depending on the thermal history, the cation distribution may vary resulting in data scattering and uncertainties.

In this work, series of $Mn_xCo_{3-x}O_4$ (x = 0, 0.5, 1, 1.5, 2) spinels were prepared by an ethylenediamine tetra acetic acid - citric acid - ethylene glycol (EDTA-CA-EG) process, and were tested as OER catalysts in an alkaline media (1M KOH). The purpose of this study was to explore the relationship between the Mn content in the Co-based spinel structure and its electrocatalytic activity.

Experimental section

Powder synthesis

The spinel powders evaluated in this work were synthesised via a sol-gel EDTA-citric acid-ethylene glycol method. The initial compounds with thermogravimetrically standardised cation content: $Mn(NO_3)_2 \cdot 4H_2O$ and $Co(NO_3)_2 \cdot 6H_2O$ (analytical grade) were dissolved in deionised water and added to a mixture of CA and EDTA. The solution was stirred for 10 min on a magnetic stirrer at room temperature. In order to avoid the risk of citrate protonation or metal hydroxide precipitation, the pH of the solution was sustained at a level of 6 by the addition of ammonia solution (25% solution, POCH, Poland). Ethylene glycol (EG, Aldrich) was added and the temperature of the solution was increased up to 80 °C in order to initiate the transesterification reaction, and was kept overnight until all solvents evaporated, leaving a semi-solid gel. The specific molar ratio of the reagents was maintained, i.e. TMI:CA:EDTA:EG = 1:2:1:2 (*TMI -Total Metal Ions*). The obtained gel was heated in a muffle furnace first at 130 °C to ensure the evaporation of residual solvents. Subsequently, the gel was pre-calcined at 400 °C, ground in an agate mortar and calcined at a final temperature of 600 °C. The calcined powders were ball-milled in isopropanol with yttria-stabilised zirconia (YSZ) spherical grinding media (φ3 mm) for the purpose of agglomerate defragmentation with the intention of improving electrocatalytic performance [4]. After milling, powders were dried in a laboratory drier at 100 °C in the air.

Powder analysis

Crystalline phases were identified by powder X-ray diffraction (pXRD), conducted at room temperature on a Bruker D2 Phaser diffractometer with CuK_α radiation (λ = 1.5404 Å) and a LynxEye XE-T detector. The results were analysed by Rietveld refinement using the Fullprof software package [36]. The.cif files required to perform the analyses were downloaded from the Crystallography Open Database [37,38]. Calculation of MnOx-CoOx phase diagram in air was done utilising the Thermo-Calc software [39] with the thermodynamic description of Co-Mn-O developed by Weiland [40]. FEI Quanta 250 FEG, and Thermo Fisher Phenom XL scanning Electron

Microscopes (SEM), and a C_s-corrected Titan Cubed G2 60-300 (FEI) Scanning Transmission Electron Microscope (S/TEM) were used to investigate the morphologies and chemical composition (using the ChemiSTEM EDX system based on 4 windowless Silicon Drift Detectors (Super X) of the as-prepared powders). The powders for TEM investigations were prepared traditionally: a drop of a water suspension containing the powder was placed onto a copper grid followed by vacuum drying. The specific surface areas were determined by means of the 10-point Brunauer–Emmett–Teller (BET) method: the N_2 adsorption isotherms were measured by a Quantachrome Instruments Autosorb iQ analyser. Assuming a spherical geometry, the mean sizes of the powders' particles were calculated by the following equation:

$$d = \frac{6000}{A_{BET}\rho} \quad (1)$$

where d is particle diameter, A_{BET} is the BET specific surface area, and ρ is the theoretical density calculated based on data obtained from Rietveld.

Preparation of electrodes for OER

Highly porous Ni foam (1.6 mm thick, 110 ppi, Shanghai Tankii Alloy Material Co. Ltd., China) was cut into smaller samples in the shape of a square with a working (active) area of 1 cm^2 with an additional holding/electrical connection part. Before the deposition of the catalyst inks, the nickel was cleaned in deionised water and, subsequently in acetone for 5 min in an ultrasonic bath. Then, the Ni foam was dried in a laboratory drier at 100 °C in the air for at least 1 h. The electrocatalyst inks were prepared by mixing 100 mg of the prepared spinel powders, 100 mg Timcal Super C45 Conductive Carbon Black (Imerys, Belgium), and 6 ml of Ethyl Alcohol Absolut 99.8% Pure (POCH, Poland). The prepared mixture was ball-milled for 24 h. Afterwards, the milling balls were rinsed with 4 ml of ethanol and the powder drying step was skipped to avoid re-agglomeration. After the milling step, 1 ml of 5% Nafion 117 solution was added to the mixture as an ink dispersant and a catalyst binder [41,42]. At the end, the ink was sonicated in a water bath for 30 min to obtain a homogeneous colloid. The catalyst ink was pipetted onto the cleaned Ni foam to achieve a mass loading of 1.3 mg, and dried overnight in ambient conditions.

For comparison, reference IrO_2 (PK Catalyst, FuelCellStore, USA) electrodes were prepared in the same manner as the other ones.

Electrochemical tests

The electrochemical measurements were performed in a three-electrode glass cell system in 1.0 M KOH aqueous solution. A HydroFlex reversible hydrogen reference electrode (RHE) (Gaskatel, Germany), a Pt sheet, and a coated Ni foam were used as the reference (RE), counter (CE), and working (WE) electrodes, respectively. The electrochemical tests were performed using an Ametek VersaSTAT 4 potentiostat/galvanostat/impedance meter. All measurements were carried out at 25 °C, maintained by a Julabo F12 thermostat. Before each measurement, the electrolyte was purged with high purity argon for 20 min. After purging, the working electrode was cycled between 1.1 V and 1.6 V vs. RHE at a scan rate of 100 mV s^{-1} for 40 (example of activation procedure is shown Fig. S1). This treatment reduces the activity of the electrodes but allows to achieve stable performance and reproducible results. Cycling voltammetry (CV) scans were performed in the non-faradaic potential region from 1.15 V to 1.25 V (vs. RHE) at scan rates of 10, 20, 40, 60, 80, 100 mV s^{-1} in order to estimate the double-layer capacitance (C_{dl}). Then, the values of C_{dl} were used to assess the electrochemical active surface area (ECSA) of the material [21,43]. To obtain the surface area values from the specific capacitances, a reference capacitance value of 40 μF cm^{-2} was assumed [44]. Linear sweep voltammetry (LSV) data were collected from 1.1 to 2.0 V (vs. RHE) at a scan rate of 5 mV s^{-1}. Electrochemical impedance spectroscopy (EIS) measurements were carried out to investigate the electrical properties of the materials, i.e. the charge transfer resistance R_{ct}. Measurements were performed in the frequency range from 10 kHz to 0.1 Hz at 1.7 V vs. RHE with an amplitude of 10 mV. For the quantitative analysis, a fitting to a modified Randles equivalent circuit was carried out using the Zview software. To evaluate the temporal stability of the electrodes, chronopotentiometry was performed at 10 mA cm^{-2} for 25 h.

All potential values were iR-corrected to remove the effect of solution resistance according to the equation $E_{iR\text{-}corrected} = E_{applied} - iR_{un}$, where i is the current, and R_{un} is an uncompensated ohmic electrolyte resistance. The overpotential (η) for the oxygen evolution reaction was calculated by the following equation: $\eta = E\ (10\ mA \cdot cm^{-2}) - 1.23$ V (vs. RHE). The current density was normalised by the geometrical surface area of the working electrode (1 cm^2). The catalyst mass activity at specific overpotential values was calculated by current normalisation by the catalyst oxide loading (~1.3 mg).

Results and discussion

Catalyst characterisation

$Mn_xCo_{3-x}O_4$ (x = 0, 0.5, 1, 1.5, 2) spinel powders were synthesised by a EDTA-CA-EG process. Utilisation of the soft-chemistry based synthesis method leads to powders with a small particle size and high specific surface area, which is beneficial for the catalysis. The powders' morphologies, observed by SEM, are presented in Fig. 1. Submicron particles were obtained for all compositions. It was observed that the introduction of Mn into the Co-based spinel results in finer particles (enlarged images are shown in Fig. S2). This observation is confirmed by specific surface area (SSA-BET) measurements. The specific surface area of the powders increases on the addition of Mn with x = 0.5, and then decreases for a higher Mn content. The $Mn_{0.5}Co_{2.5}O_4$ powder has the highest specific area of 32.9 m^2 g^{-1}. Interestingly, for the Mn-rich Mn_2CoO_4 composition, the SSA is similar to the pure Co_3O_4 spinel, indicating a complex influence of the Mn on the particle size. Based on the SSA, particle sizes were calculated, and the values are presented in Table 1. The obtained values are consistent with the SEM images, denoting submicrometric grains, with particles in the 30–100 nm range.

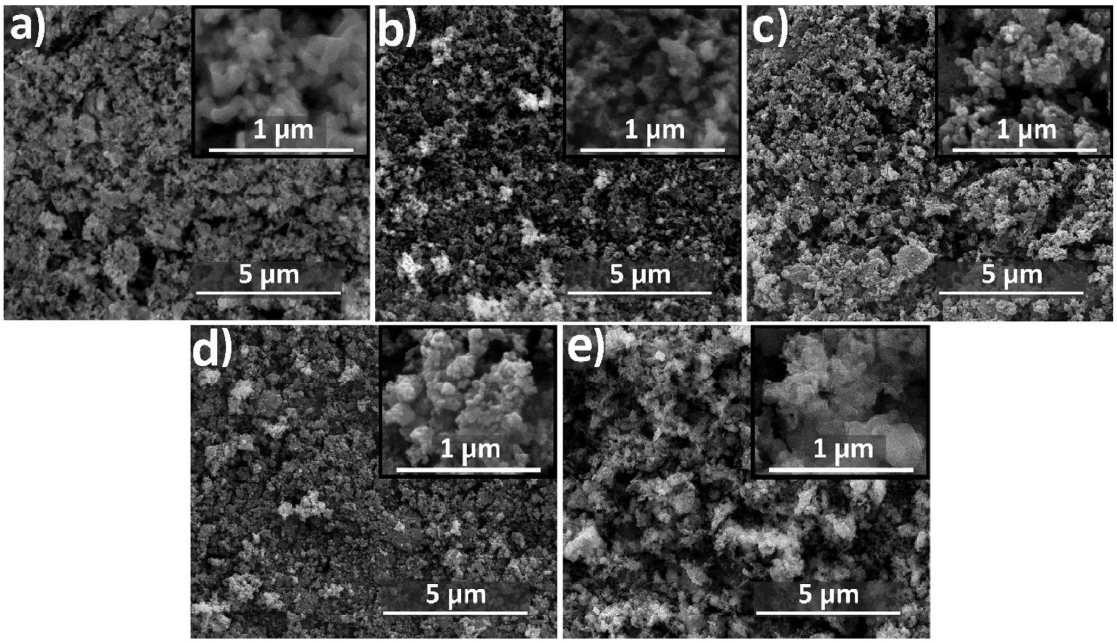

Fig. 1 – SEM images of synthesised $Mn_xCo_{3-x}O_4$ powders (a) x = 0, (b) x = 0.5, (c) x = 1, (d) x = 1.5 and x = 2.

Table 1 – Properties of the prepared $MnxCo_3$-xO_4 powders (EDS and BET analyses results).

Material	Theoretical ratio Mn:Co	EDS analysis results			Corresponding composition	Surface area [$m^2 g^{-1}$]	Particle diameter [nm]
		Mn [at. %]	Co [at. %]	Mn:Co			
Co_3O_4	–	–	100	–	Co_3O_4	9.6	103
$Mn_{0.5}Co_{2.5}O_4$	0.2	18.2	81.8	0.22	$Mn_{0.55}Co_{2.45}O_4$	32.9	30
$MnCo_2O_4$	0.5	32.3	67.7	0.48	$Mn_{0.97}Co_{2.03}O_4$	17.6	59
$Mn_{1.5}Co_{1.5}O_4$	1	46.9	53.1	0.89	$Mn_{1.41}Co_{1.59}O_4$	20.0	56
Mn_2CoO_4	2	65.4	34.6	1.88	$Mn_{1.96}Co_{1.04}O_4$	9.5	124

In order to evaluate the chemical compositions of the synthesised powders, EDS analyses were performed (quantitative results are included in Table 1 and the obtained EDS spectra are shown in Fig. S3). The Mn:Co ratios in the synthesised powders were close to the desired ones.

In order to determine the crystallographic structure and phase purity of the synthesised $Mn_xCo_{3-x}O_4$ powders, X-ray diffraction (pXRD) characterisation was performed, followed by Rietveld refinement of the unit cell parameters. The pXRD patterns are shown in Fig. 2, and the obtained results are summarised in Table 2. For the Mn_2CoO_4 compound, all of the diffraction peaks correspond to the tetragonal crystal structure (space group I41/amd), whereas all reflections for the Co_3O_4 and $Mn_{0.5}Co_{2.5}O_4$ compounds are indexed in the cubic spinel phase (space group Fd3m). In the case of $Mn_{0.5}Co_{2.5}O_4$, the peaks are broader, indicating a smaller crystallite size. Similar phenomena was observed by Zhang et al. for $MnCo_2O_4$ [45].

The powder designated as $MnCo_2O_4$, which was expected to crystallise in a single cubic phase, shows the presence of two phases. Analysis of the peaks reveals the formation of two phases with similar structure (with the same space group). The phases differ by cation composition and thus a shift of the peaks is visible in the spectra. One of the phases (based on lattice constant value) is similar to the pure Co_3O_4 phase, and the other must contain the Mn and Co. The elemental content, i.e. the Mn:Co ratio in the powder, has been confirmed by EDS, as presented in Table 1. For this particular cation ratio, a single cubic phase is expected as presented in the literature [46–48]. By rough analysis of the peaks' intensity, the amount of Co_3O_4 phase in the mixed powder is estimated to be ~30 vol%. Assuming that some of the Co atoms were consumed to form the pure Co_3O_4 phase, the rough calculation of the stoichiometry of the second phase is $Mn_{1.4}Co_{1.6}O_4$.

In order to verify the result, the synthesis of the spinel was repeated, and the same result was obtained. In order to exclude possible influence of a too-short annealing step, an additional thermal annealing step was carried out. The powders were subjected to a second heat treatment of 600 °C for 2 h, yielding the same mixed structure (Fig. S4). Therefore the

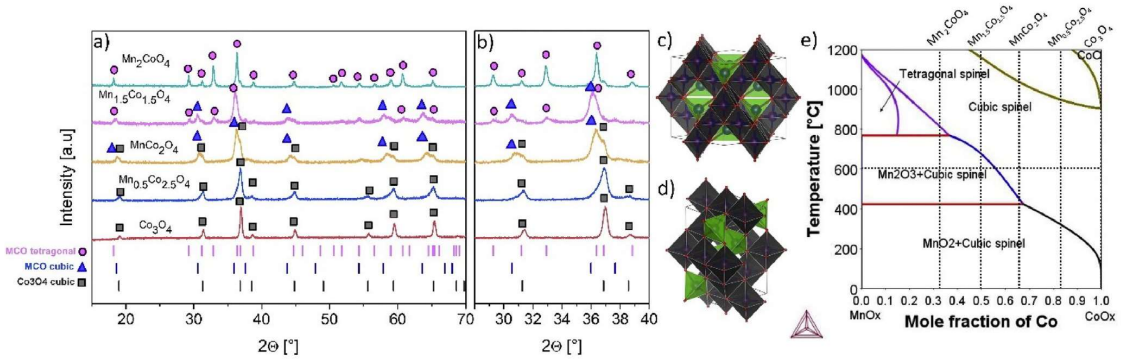

Fig. 2 – XRD patterns of synthesised $Mn_xCo_{3-x}O_4$ powders (a) and partially enlarged patterns (b), cubic (c) and tetragonal (d) spinel unit cells, e) calculated MnOx-CoOx phase diagram in air based on the thermodynamic description in the literature [40].

Table 2 – Rietveld analysis results. Cubic/tetragonal phase contribution (weight fraction(%)) and unit cell parameters.

Material	Cubic phase (Fd3m)	Tetragonal phase (I41/amd)	a_C [Å]	$a_T = b_T$ [Å]	c_T [Å]
Co_3O_4	100%	–	8.086(1)	–	–
$Mn_{0.5}Co_{2.5}O_4$	100%	–	8.1246(3)	–	–
$MnCo_2O_4$	100%	–	8.1926(4) ($Mn_{1.4}Co_{1.6}O_4$)	–	–
	~70% $Mn_{1.4}Co_{1.6}O_4$ ~30?% Co_3O_4		8.0812(4) (Co_3O_4)		
$Mn_{1.5}Co_{1.5}O_4$	85%	15%	8.2669(5)	5.7426(4)	9.2583(5)
Mn_2CoO_4	–	100%	–	5.7270(2)	9.2797(4)

structure of the spinel is reproducible. For the spinel initially designated as $MnCo_2O_4$, to highlight the phase composition of the powder, the name "dual-phase $MnCo_2O_4$" spinel will be used in the remainder of the work.

We postulate, that the mixed-phase composition of the dual-phase $MnCo_2O_4$ spinel (Co_3O_4+$Mn_{1.4}Co_{1.6}O_4$) results from the use of a modified EDTA-CA-EG powder synthesis method. When utilising a pure EDTA-CA synthesis method (with no EG), only a single cubic spinel was produced (results included in Fig. S5, full results will be reported elsewhere). Interestingly, the single phase $MnCo_2O_4$ powder revealed much lower performance towards OER than the dual phase powder. Apparently, due to the different binding/chelating powers of the acids/EG, different powders were produced.

The powder with the intended stoichiometry of $Mn_{1.5}Co_{1.5}O_4$ consisted of two phases: cubic (85%) and tetragonal (15%), while the Mn_2CoO_4 was entirely tetragonal. These powders have structures according to the reported ones.

Calculation of MnO_x – CoO_x phase diagram in the air was performed in order to compare structures of prepared powders with theoretical data. According to Fig. 2e, Mn has four different oxides, from low to high temperature, MnO_2, Mn_2O_3, tetragonal Mn_3O_4 spinel and cubic Mn_3O_4 spinel, while Co has two stable oxides, cubic Co_3O_4 spinel and CoO. Tetragonal Mn_3O_4 spinel has limited Co solubility, while the two cubic spinels are mutually soluble. In general, the phase diagram does not predict the existence of a single phase only material at room temperatures (other than pure Co_3O_4 spinel). For the mixed Mn-Co compositions at room temperature, a mixed phase system composed of tetragonal MnO_2-cubic Mn-Co spinel are predicted.

For comparison, Brylewski et al. have synthesised and analysed $Mn_{1+x}Co_{2-x}O_4$ with x = 0, 0.25, 0.5, 0.75, 1.0, and 1.5 by EDTA-gel processes [49]. In their work, the $Mn_{1.5}Co_{1.5}O_4$ powders were composed of mostly the tetragonal phase (~68%) and the remaining, cubic phase (~32%). For the $MnCo_2O_4$ and $Mn_{1.25}Co_{1.75}O_4$, only a cubic phase was detected. The lattice constant for the latter spinel was reported to be 8.31 Å, while for the $Mn_{1.15}Co_{1.85}O_4$ spinel reported in this work, a = 8.19 Å. Talic et al. performed the characterisation on sintered pellets, which can give different results to powder analysis [50]. In other work, Bobruk et al. have analysed $Mn_{1.2}Co_{1.8}O_4$ powders synthesised by different soft-chemistry methods [51]. The cation composition is thus quite similar to the one obtained for the Mn-containing phase in the $MnCo_2O_4$ designated sample. For XRD, the powders were calcined at 800 °C. Interestingly, depending on the precipitation agent used, either single or double phase materials were obtained. This highlights the complex nature of the spinels, and the possible effects on their structure. For the case where the pure cubic spinel phase was obtained (using EDTA as the precipitation/chelating agent), the lattice parameter was ~8.20 Å, so comparable with the one obtained in our study.

In order to further characterise the catalyst with the nominal composition of $MnCo_2O_4$, transmission electron microscopy (TEM) analyses were performed. Fig. 3 (and Fig. S6)

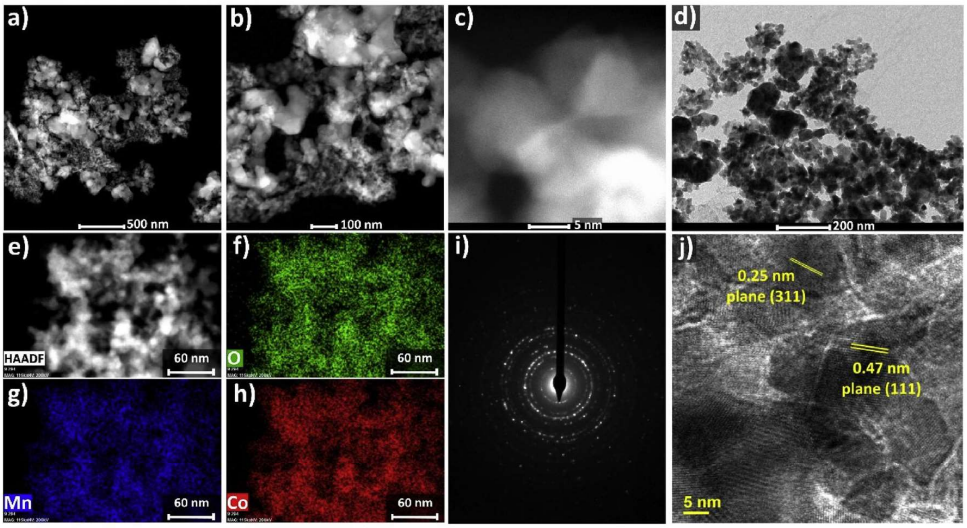

Fig. 3 – HAADF-(S)TEM images (a–d) and corresponding SAED (i) and HRTEM (j) patterns of the dual-phase $MnCo_2O_4$ powder. TEM-EDS elemental maps (e–h) of oxygen (f), manganese (g), and cobalt (h).

presents high-angle annular dark-field (HAADF) images, a TEM-EDS elemental analysis, and selected area electron diffraction (SAED) patterns. From the TEM images, it can be observed (Fig. 3a and b) that the synthesised material consists of nanocrystals in two size ranges i.e. < 50 nm and >100 nm. EDS mapping shows that Co and Mn are mutually well dispersed in the powder volume in the case of the small particles (Fig. 3e). Additionally, the HRTEM image (Fig. 3j) reveals the lattice fringes with an inter-planar spacing of 0.25 nm, corresponding to the <311> plane, and 0.47 nm, corresponding to the <111> plane of the $Mn_{1.4}Co_{1.6}O_4$ phase. The SAED patterns confirm the well-defined polycrystalline structure of $MnCo_2O_4$. TEM/EDS analysis of the larger particles confirms that the larger particles are composed of mostly pure Co oxide, as previously discussed, based on the XRD results. The smaller particles contain more Co than Mn. The $MnCo_2O_4$ powders thus consist of very fine (<30 nm diameter) $Mn_{1.4}Co_{1.6}O_4$ particles and larger (>100 nm diameter) Co_3O_4 particles.

For the electrochemical study, the produced spinel oxides were deposited on highly porous nickel foam substrates (porosity > 95%). For the determination of the coating quality, i.e. the homogeneity of catalyst distribution, scanning

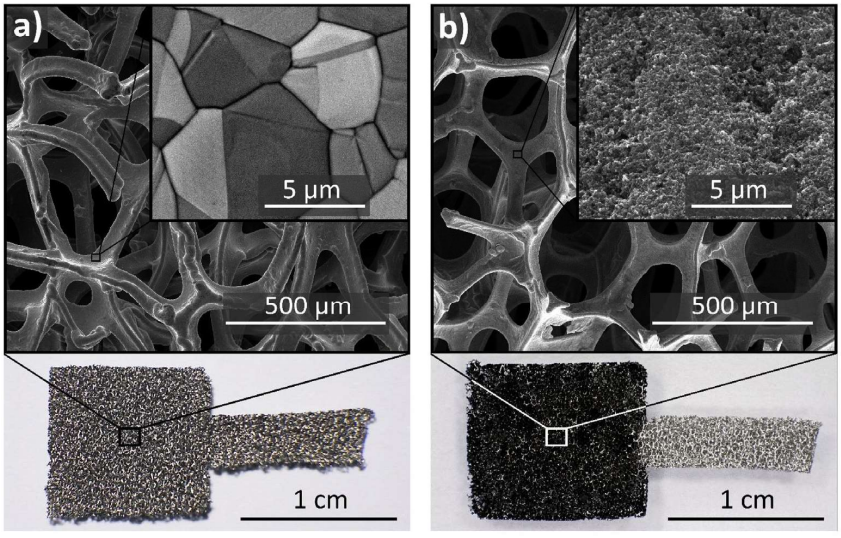

Fig. 4 – Electrodes used in electrochemical tests: (a) bare Ni foam, (b) Ni foam coated with dual-phase $MnCo_2O_4$ catalyst.

Table 3 – Comparison of OER activity data for examined catalysts.

Electrode material	η at J = 10 mA cm^{-2} [mV]	Tafel slope [mV dec^{-1}]	R_{ct} [Ω cm^2]	$ECSA_{(abs)}$ [cm^2]	$ECSA_{(g)}$ [m^2 g^{-1}]
Ni foam	388	73.1	2.23	43	3.3
Co_3O_4	368	75.5	0.98	75	5.8
$Mn_{0.5}Co_{2.5}O_4$	345	74.3	0.78	78	6.0
dual-phase $MnCo_2O_4$	327	78.9	0.69	143	11.0
$Mn_{1.5}Co_{1.5}O_4$	371	79.9	1.06	85	6.5
Mn_2CoO_4	399	78.9	1.52	53	4.1
IrO_2	289	82.2	1.29	115	8.8

electron and visible light microscopy analyses were performed. Images of the Ni foam before the catalyst deposition and after the catalyst deposition are presented in Fig. 4. The nickel foam had visible grains within a size range of 5–20 μm. The prepared catalyst ink was distributed evenly over the active area of the porous foam, the surface coverage being very uniform. The total amount of the catalyst spinel powder was ~1.3 mg. SEM images confirm the uniform microstructure of the catalyst, with no agglomerates visible.

Evaluation of electrocatalytic activity for OER

The electrocatalytic OER performance of the $Mn_xCo_{3-x}O_4$ spinels was investigated in 1.0 M KOH solution. For comparison, pure Ni foam and Ni foam coated with commercial IrO_2 catalyst were also examined. Based on the LSV polarisation curves presented in Fig. 5a, it can be observed that all of the spinel catalysts outperformed the pure Ni foam electrode. Among the spinels, the lowest performance was determined for the tetragonal Mn_2CoO_4, whereas the best performance was found for the dual-phase $MnCo_2O_4$ material (Co_3O_4/$Mn_{1.4}Co_{1.6}O_4$).

The electrode overpotential determined at 10 mA cm^{-2}, Tafel slope, R_{ct}, and ECSA are the most common parameters determined and used to assess the catalytic performance of an electrode towards OER. These values obtained for the studied materials are summarised in Table 3. The results indicate that the lowest overpotential (η) at 10 mA cm^{-2} of 289 mV was exhibited by IrO_2 but its performance weakened at higher overpotentials compared to the other synthesised spinels. Pure tetragonal Mn_2CoO_4 spinel showed very low catalytic activity, the overpotential was even slightly higher than the overpotential obtained for the pure nickel. Therefore, this phase can be considered inactive towards OER. The activity obtained for the pure Co_3O_4 spinel was slightly better in comparison to the nickel foam. For the $Mn_{1.5}Co_{1.5}O_4$, which was a mixture of the tetragonal and cubic phases, the performance was comparable to the Co_3O_4 catalyst.

The dual-phase $MnCo_2O_4$ exhibited the lowest η of 327 mV. Since it was a mixture of Co_3O_4 (~30 vol%) and $Mn_{1.4}Co_{1.6}O_4$ (~70 vol%), with the former being only a mediocre catalyst (LSV curves obtained for dp-$MnCo_2O_4$ and sp-$MnCo_2O_4$ are compared in Fig. S7), either the latter has very high activity or there exist some synergistic interaction between the two phases. Also, as based on the TEM analyses, the Mn-Co phase in the mixed catalyst had a much finer structure, preferable for the surface-driven OER. In any case, the dual-phase spinel designated as $MnCo_2O_4$ is an interesting alternative to the state-of-the-art IrO_2 in the role of OER catalyst.

From Fig. 5b, it can be seen that the Tafel slopes for all measured spinels are very similar (70–80 mV dec^{-1}) and are slightly lower compared to IrO_2. The results indicate that the

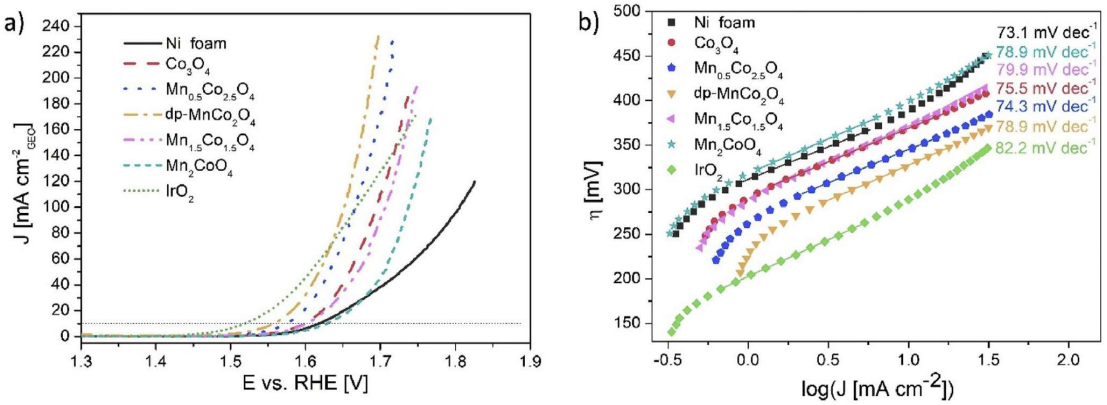

Fig. 5 – (a) Polarisation curves, (b) Tafel plots. All tests were performed in 1.0 M KOH electrolyte.

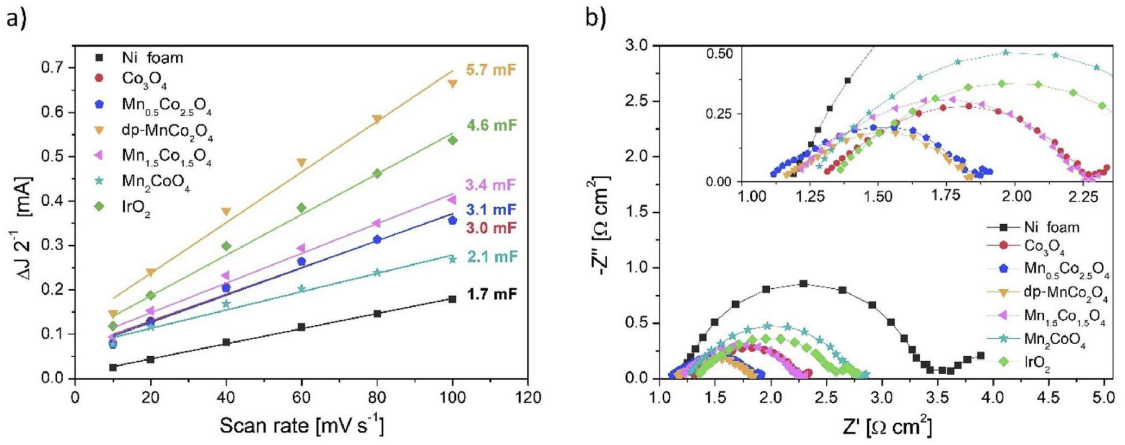

Fig. 6 – (a) Double layer capacitance, (b) EIS spectra at potential of 1.7 V vs. RHE. All tests were performed in 1.0 M KOH electrolyte.

OER mechanism for all of the spinels is similar. The values of the Tafel slopes are characteristic for the limiting process of the electrochemical reaction. The value of 120 mV dec^{-1} represents the limiting process of the first electron transfer step, the slope of 60 mV dec^{-1} is caused by the chemical step, and finally, the value of 40 mV dec^{-1} is representative of the second electron transfer step [52–54]. The values obtained in this work point to a possible mixed mechanism, with a strong influence of the chemical step.

Fig. 6a presents the relationship between the current density and scan rate obtained from cycling voltammetry (CV curves are shown in Fig. S8). Double layer capacitances were used for the calculation of the electrochemically active surface areas (ECSAs) of the catalysts. The collected data was used to calculate C_{dl}, and consecutively ECSA (Table 3). The ECSA increases with the addition of Mn in the $Mn_xCo_{3-x}O_4$ spinel structure for $x \leq 1$, but then the trend reverses. The ECSA demonstrates that the dual-phase $MnCo_2O_4$ has the highest number of active sites, which may be an explanation for its superior OER activity among the prepared spinels. It is important to note that ECSA of $Mn_{0.5}Co_{2.5}O_4$ and Co_3O_4 are almost the same, while the BET specific surface area of $Mn_{0.5}Co_{2.5}O_4$ is 3 times higher than that of Co_3O_4. This indicates that the number of active sites does not correlate with the specific area of the material.

For example, Fe:Ni(OH_2)/NF integrated catalysts have an ECSA of 18.04 cm^2 (for 3 × 1 cm^2 nickel foam) [55]. Commercially available spinel nanoparticles of Co_3O_4 and Mn_3O_4 (Sigma Aldrich), have an ECSA of 0.19 and 0.49 $m^2\ g^{-1}$, respectively [56]. For comparison, Zhu et al. reported a $SrNb_{0.1}Co_{0.7}Fe_{0.2}O_{3-\delta}$ perovskite nanorod with a high ECSA of 175 $m^2\ g^{-1}$ [57].

Additionally, the EIS was employed in order to study the electrochemical properties of the material in more detail.

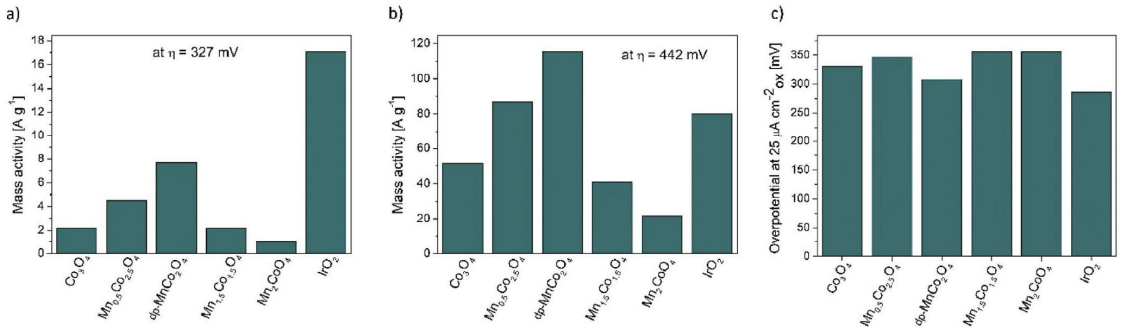

Fig. 7 – Mass and surface specific catalytic activity at η = 327 mV (a) and at η = 442 mV (b) and (c) specific surface activity of catalyst powders.

Nyquist plots obtained by EIS are shown in Fig. 6b. As might be predicted, the dual phase $MnCo_2O_4$ demonstrates the semicircle with the smallest diameter, which indicates the lowest charge transfer resistance among all of the spinels, and results in superior OER activity. The $R_s(CPE\text{-}R_p)$ equivalent circuit was chosen based on the literature reports [3,30,58]. The trend of R_{ct} (Table 3) correlates with the trend of η at 10 mA cm^{-2} i.e. the catalyst with a lower R_{ct} reveals higher OER performance (lower η) due to the faster charge transfer kinetics. The relation suggests that improved charge transfer may be one of the main factors determining OER performance in $Mn_xCo_{3-x}O_4$ spinels.

Based on the above discussion, it seems that the performance of the MnCo2O4 spinel, which is in reality a dual-phase compound consisting of Co_3O_4 and $Mn_{1.15}Co_{1.85}O_4$, is the highest one based on the metrics shown. In the following discussion, other performance metrics are shown, indicating the complex nature of catalyst benchmarking. Namely, the specific weight of the catalyst and its surface area (based on BET) are used.

Fig. 7a and b present the specific mass activities of the catalysts determined at the $\eta = 327$ mV and $\eta = 442$ mV (values of η for dual-phase $MnCo_2O_4$ needed to achieve a current density of 10 mA cm^{-2} and 150 mA cm^{-2}, respectively). In addition, the surface-specific activity was calculated based on the determined BET surface areas and the results are presented in Fig. 7c.

Dual-phase $MnCo_2O_4$ exhibits the highest mass activity among the $Mn_xCo_{3-x}O_4$ spinels and, more importantly, at higher potentials, the dual-phase $MnCo_2O_4$ performance significantly surpasses the performance of IrO_2. The mass activity of the dual-phase $MnCo_2O_4$ at $\eta = 442$ is 115 A g^{-1}, which is about 2.3 and 1.4 times higher than the values for Co_3O_4 and IrO_2, respectively. For instance, Wang et al. reported the mesoporous $MnCo_2O_4$ exhibiting a mass activity of 20.6 mA g^{-1} at 1.6 vs. RHE measured in 0.1 M KOH [59]. On the other hand, Chen et al. have reported mass activities of 1000–9000 A g^{-1} for amorphous BSCF [60]. These very high performances were obtained on 1 nm–20 nm thick films, so their scaling and thus direct comparison to the values with the powder-based catalysts are questionable.

When comparing the surface-specific (BET adjusted) catalyst performance, presented in Fig. 7c, the overpotential values determined at 25 μA cm^{-2} are quite similar, no large differences are noticed. The lowest overpotential values are obtained for the IrO_2 reference catalyst, followed by the $MnCo_2O_4$ catalyst. In this case, it would mean that the performance gain is caused by the extended specific surface area of the powders obtained for Mn-containing compounds. However, this is not entirely true, as the ECSA does not scale linearly with the BET area, and the comparisons are more complex and require further studies.

The catalysts' durability was evaluated by chronopotentiometry tests at a 10 mA cm^{-2} current density performed for 25 h. From the plots presented in Fig. 8 a) it can be seen that all electrodes exhibited an initial large increase of potential in the first 1–2 h. This can be possibly caused by the formation of sticking O_2 bubbles on the electrode surface, and thus decreasing the effective surface coverage. After a stationary state was achieved, the electrode degradation could be discussed.

Up to ~10 h, the spinel materials demonstrated quite stable behaviour. A segment of each plot corresponding to the last 5 h, where the degradation was relatively steady, has been used to estimate the degradation rate. The results plotted in Fig. 8 b) demonstrate a slight loss of performance with a rate of around 0.3–2.5 mV h^{-1}. $MnCo_2O_4$ appears to be the least stable spinel with a performance drop-rate of 2 mV h^{-1}. The reference IrO_2 catalyst shows the lowest initial overpotential and a slow, but visible degradation rate. Notably, the spinels exhibit better stability than the pure Ni foam electrode.

For a broader comparison with the data obtained in this study, results recently reported in the literature for spinels

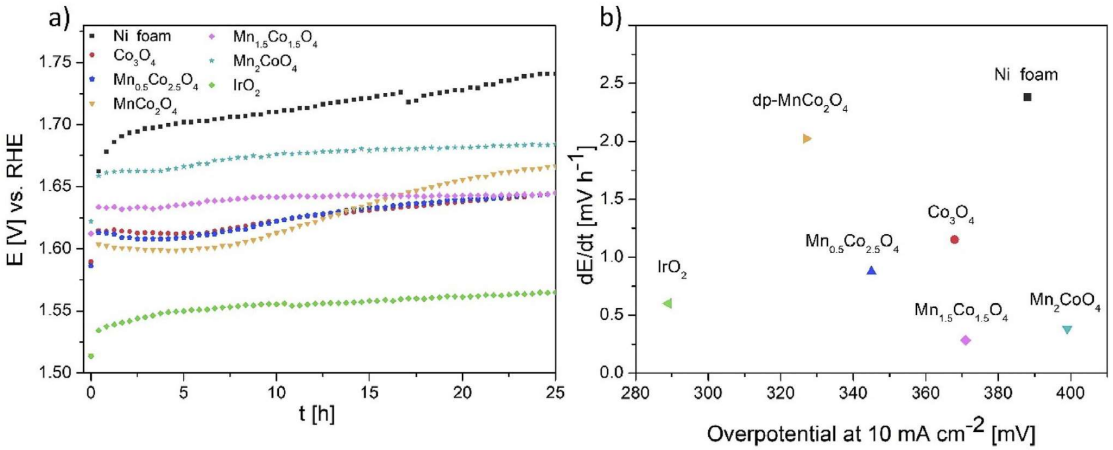

Fig. 8 – a) Potential profiles during chronopotentiometry at 10 mA cm^{-2} current density. b) Degradation rate estimated for the last 5 h of stability test.

Table 4 – Comparison of reported OER electrocatalysts, including Mn-Co spinels.

Catalyst	Electrolyte	Substrate	η at 10 mA cm^{-2} [mV]	Tafel slope [mV dec^{-1}]	Catalyst's loading [mg cm^{-2}]	Ref.
Co_3O_4	1M KOH	**Ni foam**	**368**	**75.5**	**1.30**	**This work**
$MnCo_2O_4$ (Co_3O_4 + $Mn_{1.4}Co_{1.6}O_4$)			**327**	**78.9**		
Co_3O_4 5.9 nm		Ni foam	328	–	1.00	[22]
Flower-like Co_3O_4 on Co foam		Co foam	273	61.8	–	[62]
$MnCo_2O_4$		Glassy Carbon (GC)	560	167	1.48	[64]
Ce-$MnCo_2O_4$-3%			390	120.0	1.48	[64]
$NiCo_2O_4$ nanoflowers with graphene			383	137	–	[63]
MnCo2O4@CoS nanosheets		Ni foam	270 (@20 mA cm-2)	132	–	[61]
rod bundle-like $NiCo_2O_4$			320	59.3	1.0	[65]
Co_3O_4	1M NaOH	Glassy Carbon – Rotating	500	60.9		[56]
$NiFe_2O_4$		Disk electrode (GC-RDE)	510	–		[56]
Mn_3O_4			430	60.9		[56]
$MnCo_2O_4$@NCNTs	0.1M KOH		470	106.0	0.28	[25]
Co_3O_4/$MnCo_2O_4$ nanocomposite			540	–	–	[66]
Co3O4/Ppy/RGO			300	105	~0.1	[67]
$MnCo_2O_4$ microspheres			510	55	0.051	[68]
Mn_2CoO_4 microspheres			600	64	0.051	[68]
mesoporous $MnCo_2O_4$			400	90.0	–	[59]
Mn_2O_3 porous nanoplates		Ni foam	420	81.0	–	[27]

and Mn/Co-based materials are summarised in Table 4. The presented data shows that the $MnCo_2O_4$ on nickel foam synthesised in this work by a EDTA-CA-EG method exhibit improved or comparable electrocatalytic performance to reported spinel-based electrocatalysts. The reached overpotential of 327 mV at 10 mA cm^{-2} can be considered one of the lowest reported for spinels. The lowest overpotential value of 270 (at 20 mA cm^{-2}) for a spinel/sulphide hybrid material in the form of nanosheet was reported by Du et al. [61]. The materials have however a somewhat higher Tafel slope of ~130 mV dec^{-1}. The very low overpotential of this hybrid structure shows the great potential of combining spinels with other materials for improved performance, also supported by other good results [61–63].

Wang et al. have reported a relatively similar well-dispersed nanocomposite of Co_3O_4–$MnCo_2O_4$. In 0.1M KOH it showed a moderate performance of $\eta = 540$ mV at 10 mA cm^{-2} [66]. The catalyst was obtained by separate nucleation and ageing steps (SNAS). Cheng et al. have studied room-temperature synthesised nanocrystalline spinels $M_xMn_{3-x}O_4$ (M = Co, Mg or Zn) for ORR/OER reactions in 0.1M KOH [69]. The authors described, that the low synthesis temperature provided higher electrocatalytic activity and that for OER, the tetragonal phase was more active than the cubic phase. Menezes et al. have compared Mn_2CoO_4 and $MnCo_2O_4$ in the form of microspheres for OER and ORR reactions in 0.1M KOH [68]. Interestingly, the Co-rich cubic compound outperformed the Mn-rich spinel in OER, but the trend was reversed in ORR. In addition, a study by Rios et al. reported that increasing the content of Co in $Mn_xCo_{3-x}O_4$ ($0 \leq x \leq 1$) improved the OER rate, which was related to the higher Co^{3+} content in the spinel structure [70]. In their case, the best performance was obtained for a pure Co_3O_4 spinel. As reported by Wei et al. [47], tetragonal spinel Mn_2CoO_4 could be expected to exhibit the highest OER catalytic activity, which was not the case in this study.

The differing and sometimes contradicting results obtained by different groups indicate the possible influence of the preparation of the catalyst and measurement procedures on determining the electrocatalytic properties. As pointed out by Wei et al. [47] (for the Mn-Co spinels), and Zhou et al. [71] (in the case of $MnFe_2O_4$), changes in the annealing temperature of the powders can result in oxidation of Mn^{2+} to Mn^{3+} and transfer from tetrahedral to octahedral sites in the lattice. Thus the comparison and discussion are altered by the preparation, thermal history and measurements methodology. More studies are required in order to clarify the observed differences.

The good catalytic properties of the heterogeneous hybrid structure of Co_3O_4 and $Mn_{1.4}Co_{1.6}O_4$ spinels (η of 327 mV at 10 mA cm^{-2}) can result from various factors. Firstly, the addition of Mn causes the powder's grain refinement with a mean particle diameter smaller than 100 nm (determined by BET). Based on TEM, the smaller particles attributable to the mixed Mn-Co phase are smaller than 50 nm. The grain refinement is directly related to the increase of the BET surface area. Esswein et al. determined that the overpotential for water oxidation at a constant current density of 10 mA cm^{-2} decreases by ~50 mV with the increase of catalyst's surface area by an order of magnitude [22]. The ECSA calculated from the electrode's double-layer capacitance is the highest for the electrode coated with dual-phase $MnCo_2O_4$ catalyst (143 cm^2). When recalculated per weight of the catalyst (~1.3 mg), the mass-specific ECSA of the dual-phase $MnCo_2O_4$ is ~11 m^2 g^{-1}. Compared to other reported catalysts, this value seems relatively high.

Additionally, dual-phase $MnCo_2O_4$ exhibits the lowest charge transfer resistance of 0.69 Ω cm^2, which indicates a much higher conductivity compared to other Co-Mn-O catalysts [24]. A combination of a dual-phase structure, relatively high specific surface area and the high conductivity of $MnCo_2O_4$ are the possible explanations of its remarkable activity compared to other stoichiometries [72].

Conclusions

$Mn_xCo_{3-x}O_4$ spinel powders were fabricated via a facile EDTA-CA-EG method. The powders were analysed for their surface area, chemical and phase composition, and their electrocatalytic properties towards oxygen evolution reaction.

The performed electrochemical studies indicated that the low content ($x \leq 1$) of Mn in $Mn_xCo_{3-x}O_4$ enhances its catalytic activity towards OER in an alkaline medium by increasing the number of active sites and lowering the charge transfer resistance. The highest initial performance has been reported for the spinel with the nominal $MnCo_2O_4$ designation, which has been revealed to consist of two cubic phases: Co_3O_4 (~30 vol%) and $Mn_{1.4}Co_{1.6}O_4$ (~70 vol%). This particular material shows very high activity, not explainable by simple additive properties of the two phases. The effects of BET and ECSA surface areas on the OER activity were investigated. Except for $MnCo_2O_4$, all prepared materials revealed relatively good stability with degradation rates similar to IrO_2. Future work will focus on further studies of the effects of the synthesis and microstructure of the spinels on their electrocatalytic activity. Studies of dual-phase materials seem a promising route for further lowering and understanding the complex OER phenomena.

Acknowledgements

The presented research is part of the "Nanocrystalline ceramic materials for efficient electrochemical energy conversion" project, carried out within the First TEAM programme of the Foundation for Polish Science (grant agreement nr. POIR.04.04.00-00-42E9/17-00), co-financed by the European Union under the European Regional Development Fund. Funding from Statutory Funds of WETI PG is also acknowledged.

Appendix A. Supplementary data

Supplementary data to this article can be found online at https://doi.org/10.1016/j.ijhydene.2020.03.188.

REFERENCES

[1] Schmidt O, Gambhir A, Staffell I, Hawkes A, Nelson J, Few S. Future cost and performance of water electrolysis: an expert elicitation study. Int J Hydrogen Energy 2017;42:30470–92. https://doi.org/10.1016/j.ijhydene.2017.10.045.

[2] da Silva FS, de Souza TM. Novel materials for solid oxide fuel cell technologies: a literature review. Int J Hydrogen Energy 2017;42:26020–36. https://doi.org/10.1016/J.IJHYDENE.2017.08.105.

[3] Mitra D, Trinh P, Malkhandi S, Mecklenburg M, Heald SM, Balasubramanian M, et al. An efficient and robust surface-modified iron electrode for oxygen evolution in alkaline water. Electrolysis 2018;165:392–400. https://doi.org/10.1149/2.1371805jes.

[4] Zhu Y, Zhou W, Chen ZG, Chen Y, Su C, Tadé MO, et al. SrNb0.1Co0.7Fe0.2O3-δ perovskite as a next-generation electrocatalyst for oxygen evolution in alkaline solution. Angew Chem Int Ed 2015;54:3897–901. https://doi.org/10.1002/anie.201408998.

[5] Adolphsen JQ, Sudireddy BR, Gil V, Chatzichristodoulou C. Oxygen evolution activity and chemical stability of Ni and Fe based perovskites in alkaline media. J Electrochem Soc 2018;165:F827–35. https://doi.org/10.1149/2.0911810jes.

[6] Zhang J, Cui Y, Jia L, He B, Zhang K, Zhao L. Engineering anion defect in LaFeO2.85Cl0.15 perovskite for boosting oxygen evolution reaction. Int J Hydrogen Energy 2019;44:24077–85. https://doi.org/10.1016/j.ijhydene.2019.07.162.

[7] Xu X, Pan Y, Zhou W, Chen Y, Zhang Z, Shao Z. Toward enhanced oxygen evolution on perovskite oxides synthesized from different approaches: a case study of Ba0.5Sr0.5Co0.8Fe0.2O3−δ. Electrochim Acta 2016;219:553–9. https://doi.org/10.1016/j.electacta.2016.10.031.

[8] Kordek K, Yin H, Rutkowski P, Zhao H. Cobalt-based composite films on electrochemically activated carbon cloth as high performance overall water splitting electrodes. Int J Hydrogen Energy 2019;44:23–33. https://doi.org/10.1016/j.ijhydene.2018.02.095.

[9] Singh RN, Mishra D, Anindita, Sinha ASK, Singh A. Novel electrocatalysts for generating oxygen from alkaline water electrolysis. Electrochem Commun 2007;9:1369–73. https://doi.org/10.1016/j.elecom.2007.01.044.

[10] Huang Y, Yang W, Yu Y, Hao S. Ordered mesoporous spinel CoFe 2 O 4 as efficient electrocatalyst for the oxygen evolution reaction. J Electroanal Chem 2019;840:409–14. https://doi.org/10.1016/j.jelechem.2019.04.010.

[11] Peng S, Gong F, Li L, Yu D, Ji D, Hu Z, et al. Necklace-like multi-shelled hollow spinel oxides with oxygen vacancies for efficient water electrolysis. J Am Chem Soc 2018;140. https://doi.org/10.1021/jacs.8b05134. jacs.8b05134.

[12] Ge X, Liu Y, Goh FWT, Hor TSA, Zong Y, Xiao P, et al. Dual-phase spinel $MnCo_2O_4$ and Spinel $MnCo_2O_4$/nanocarbon hybrids for electrocatalytic oxygen reduction and evolution. ACS Appl Mater Interfaces 2014;6:12684–91. https://doi.org/10.1021/am502675c.

[13] Béjar J, Álvarez-Contreras L, Ledesma-García J, Arjona N, Arriaga LG. Electrocatalytic evaluation of Co3O4 and NiCo2O4 rosettes-like hierarchical spinel as bifunctional materials for oxygen evolution (OER) and reduction (ORR) reactions in alkaline media. J Electroanal Chem 2019;847:113190. https://doi.org/10.1016/j.jelechem.2019.113190.

[14] Sivakumar P, Subramanian P, Maiyalagan T, Gedanken A, Schechter A. Ternary nickel–cobalt–manganese spinel oxide nanoparticles as heterogeneous electrocatalysts for oxygen evolution and oxygen reduction reaction. Mater Chem Phys 2019;229:190–6. https://doi.org/10.1016/j.matchemphys.2019.03.017.

[15] Si S, Hu HS, Liu RJ, Xu ZX, Wang CBin, Feng YY. Co–NiFe layered double hydroxide nanosheets as an efficient electrocatalyst for the electrochemical evolution of oxygen. Int J Hydrogen Energy 2020;45:9368–79. https://doi.org/10.1016/j.ijhydene.2020.01.241.

[16] Liang Z, Zhou P, Wang Z, Wang P, Liu Y, Qin X, et al. Electrodeposition of NiFe layered double hydroxide on Ni3S2 nanosheets for efficient electrocatalytic water oxidation. Int J Hydrogen Energy 2020;45:8659–66. https://doi.org/10.1016/j.ijhydene.2020.01.113.

[17] Yan Q, Kong L, Zhang X, Wei T, Yin J, Cheng K, et al. Vertical Nickel–Iron layered double hydroxide nanosheets grown on hills-like nickel framework for efficient water oxidation and splitting. Int J Hydrogen Energy 2020;45:3986–94. https://doi.org/10.1016/j.ijhydene.2019.12.088.

[18] Cui S, Mtukula AC, Bo X, Guo L. High-efficiency Co6W6C catalyst with three-dimensional ginger-like morphology for promoting the hydrogen and oxygen evolution reactions. Int J Hydrogen Energy 2020;45:6404–15. https://doi.org/10.1016/j.ijhydene.2019.12.160.
[19] Xu S, Wang M, Saranya G, Chen N, Zhang L, He Y, et al. Pressure-driven catalyst synthesis of Co-doped Fe3C@Carbon nano-onions for efficient oxygen evolution reaction. Appl Catal B Environ 2020;268:118385. https://doi.org/10.1016/j.apcatb.2019.118385.
[20] Zhang S, Gao G, Hao J, Wang M, Zhu H, Lu S, et al. Low-electronegativity vanadium substitution in cobalt carbide induced enhanced electron transfer for efficient overall water splitting. ACS Appl Mater Interfaces 2019;11:43261–9. https://doi.org/10.1021/acsami.9b16390.
[21] She S, Zhu Y, Chen Y, Lu Q, Zhou W, Shao Z. Realizing ultrafast oxygen evolution by introducing proton acceptor into perovskites. Adv Energy Mater 2019;1900429:1–6. https://doi.org/10.1002/aenm.201900429.
[22] Esswein AJ, Mcmurdo MJ, Ross PN, Bell AT, Tilley TD. Size-dependent activity of Co3O4 nanoparticle anodes for alkaline water electrolysis. J Phys Chem C 2009;113:15068–72. https://doi.org/10.1021/jp904022e.
[23] Lee E, Jang JH, Kwon YU. Composition effects of spinel MnxCo3-xO4 nanoparticles on their electrocatalytic properties in oxygen reduction reaction in alkaline media. J Power Sources 2015;273:735–41. https://doi.org/10.1016/j.jpowsour.2014.09.156.
[24] Han H, Mhin S. Oxygen evolution reaction of Co-Mn-O electrocatalyst prepared by solution combustion synthesis. https://doi.org/10.3390/catal9060564; 2019.
[25] Zhao T, Gadipelli S, He G, Ward MJ, Do D, Zhang P, et al. Tunable bifunctional activity of $Mn_xCo_{3-x}O_4Na_n$ocrystals decorated on carbon nanotubes for oxygen electrocatalysis. ChemSusChem 2018;11:1295–304. https://doi.org/10.1002/cssc.201800049.
[26] Ishihara T, Yokoe K, Miyano T, Kusaba H. Mesoporous MnCo2O4 spinel oxide for a highly active and stable air electrode for Zn-air rechargeable battery. Electrochim Acta 2019;300:455–60. https://doi.org/10.1016/J.ELECTACTA.2019.01.092.
[27] Sim H, Lee J, Yu T, Lim B. Manganese oxide with different composition and morphology as electrocatalyst for oxygen evolution reaction. Kor J Chem Eng 2018;35:257–62. https://doi.org/10.1007/s11814-017-0247-2.
[28] Sivakumar P, Subramanian P, Maiyalagan T, Gedanken A, Schechter A. Ternary nickel–cobalt–manganese spinel oxide nanoparticles as heterogeneous electrocatalysts for oxygen evolution and oxygen reduction reaction. Mater Chem Phys 2019;229:190–6. https://doi.org/10.1016/j.matchemphys.2019.03.017.
[29] Zhan Y, Xu C, Lu M, Liu Z, Lee JY. Mn and Co co-substituted Fe3O4nanoparticles on nitrogen-doped reduced graphene oxide for oxygen electrocatalysis in alkaline solution. J Mater Chem A 2014;2:16217–23. https://doi.org/10.1039/c4ta03472d.
[30] Wu S, Liu J, Cui B, Li Y, Liu Y, Hu B, et al. Fluorine-doped nickel cobalt oxide spinel as efficiently bifunctional catalyst for overall water splitting. Electrochim Acta 2019;299:231–44. https://doi.org/10.1016/j.electacta.2019.01.012.
[31] Talic B, Hendriksen PV, Wiik K, Lein HL. Thermal expansion and electrical conductivity of Fe and Cu doped MnCo2O4 spinel. Solid State Ionics 2018;326:90–9. https://doi.org/10.1016/j.ssi.2018.09.018.
[32] Kumar M, Awasthi R, Sinha ASK, Singh RN. New ternary Fe, Co, and Mo mixed oxide electrocatalysts for oxygen evolution. Int J Hydrogen Energy 2011;36:8831–8. https://doi.org/10.1016/j.ijhydene.2011.04.071.
[33] Singh NK, Yadav R, Yadav MK. Electrocatalytic activity of NixFe3-xO4 ($0 \leq x \leq 1.5$) obtained by natural egg ovalbumin for alkaline water electrolysis. J New Mater Electrochem Syst 2016;19:209–15.
[34] Maček J, Novosel B, Zupan K, Razpotnik T, Francetič V, Marinšek M. A polymer complex solution process for the synthesis and characterization of Ni–YSZ cermet material. Ceram Int 2007;34:1741–6. https://doi.org/10.1016/j.ceramint.2007.05.006.
[35] Wang HY, Hung SF, Chen HY, Chan TS, Chen HM, Liu B. In operando identification of geometrical-site-dependent water oxidation activity of spinel Co3O4. J Am Chem Soc 2016;138:36–9. https://doi.org/10.1021/jacs.5b10525.
[36] Rodriguez-Carvajal J. Recent advances in magnetic structure determination by neutron powder diffraction. Phys B 1993:55–69. https://doi.org/10.1016/0921-4526(93)90108-I.
[37] Bordeneuve H, Rousset A, Tenailleau C, Guillemet-Fritsch S. Cation distribution in manganese cobaltite spinels Co3-xMnxO4($0 \leq x \leq 1$) determined by thermal analysis. J Therm Anal Calorim 2010;101:137–42. https://doi.org/10.1007/s10973-009-0557-7.
[38] Habjanic J, Juric M, Popovic J, Molcanov K, Pajic D. A 3D oxalate-based network as a precursor for the CoMn2O4 spinel: synthesis and structural and magnetic studies. Inorg Chem 2014:9633–43. https://doi.org/10.1063/1.5087986.
[39] Andersson JO, Helander T, Höglund L, Shi P, Sundman B. Thermo-Calc & DICTRA, computational tools for materials science. Calphad Comput Coupling Phase Diagrams Thermochem 2002;26:273–312. https://doi.org/10.1016/S0364-5916(02)00037-8.
[40] Weiland R. Untersuchungen zur Thermodynamik oxidischer Lösungsphasen im System Co-Fe-Mn-O. Arbeit; 2002.
[41] Shukla S, Bhattacharjee S, Weber AZ, Secanell M. Experimental and theoretical analysis of ink dispersion stability for polymer electrolyte fuel cell applications. J Electrochem Soc 2017;164:F600–9. https://doi.org/10.1149/2.0961706jes.
[42] Li G, Yang D, Chuang P-Y. Defining Nafion ionomer roles for enhancing alkaline oxygen evolution electrocatalysis. ACS Catal 2018. https://doi.org/10.1021/acscatal.8b02217. acscatal.8b02217.
[43] Stelmachowski P, Monteverde Videla AHA, Ciura K, Specchia S. Oxygen evolution catalysis in alkaline conditions over hard templated nickel-cobalt based spinel oxides. Int J Hydrogen Energy 2017;42:27910–8. https://doi.org/10.1016/j.ijhydene.2017.06.034.
[44] McCrory CCL, Jung S, Peters JC, Jaramillo TF. Benchmarking heterogeneous electrocatalysts for the oxygen evolution reaction. J Am Chem Soc 2013;135:16977–87. https://doi.org/10.1021/ja407115p.
[45] Zhang S, Sun X, Zheng Z, Zhang L. Nanoscale center-hollowed hexagon MnCo2O4 spinel catalyzed aerobic oxidation of 5-hydroxymethylfurfural to 2,5-furandicarboxylic acid. Catal Commun 2018;113:19–22. https://doi.org/10.1016/j.catcom.2018.05.004.
[46] Lavela P, Tirado JL, Vidal-Abarca C. Sol–gel preparation of cobalt manganese mixed oxides for their use as electrode materials in lithium cells. Electrochim Acta 2007;52:7986–95. https://doi.org/10.1016/j.electacta.2007.06.066.
[47] Wei C, Feng Z, Scherer GG, Barber J, Shao-Horn Y, Xu ZJ. Cations in octahedral sites: a descriptor for oxygen electrocatalysis on transition-metal spinels. Adv Mater 2017;29. https://doi.org/10.1002/adma.201606800.
[48] Zhao Q, Yan Z, Chen C, Chen J. Spinels: controlled preparation, oxygen reduction/evolution reaction application, and beyond. Chem Rev 2017;117:10121–211. https://doi.org/10.1021/acs.chemrev.7b00051.

[49] Kruk A, Stygar M, Brylewski T. Mn-Co spinel protective-conductive coating on AL453 ferritic stainless steel for IT-SOFC interconnect applications. J Solid State Electrochem 2013;17:993–1003. https://doi.org/10.1007/s10008-012-1952-8.
[50] Talic B, Hendriksen PV, Wiik K, Lein HL. Thermal expansion and electrical conductivity of Fe and Cu doped MnCo2O4spinel. Solid State Ionics 2018;326:90–9. https://doi.org/10.1016/j.ssi.2018.09.018.
[51] Bobruk M, Brylewska K, Durczak K, Wojciechowski K, Adamczyk A, Brylewski T. Synthesis of manganese-cobalt spinel via wet chemistry methods and its properties. Ceram Int 2017;43:15597–609. https://doi.org/10.1016/j.ceramint.2017.08.116.
[52] Anantharaj S, Karthick K, Kundu S. Evolution of layered double hydroxides (LDH) as high performance water oxidation electrocatalysts: a review with insights on structure, activity and mechanism. Mater Today Energy 2017;6:1–26. https://doi.org/10.1016/j.mtener.2017.07.016.
[53] Browne MP, Nolan H, Duesberg GS, Colavita PE, Lyons MEG. Low-overpotential high-activity mixed manganese and ruthenium oxide electrocatalysts for oxygen evolution reaction in alkaline media. ACS Catal 2016;6:2408–15. https://doi.org/10.1021/acscatal.5b02069.
[54] Doyle RL, Godwin IJ, Brandon MP, Lyons MEG. Redox and electrochemical water splitting catalytic properties of hydrated metal oxide modified electrodes. Phys Chem Chem Phys 2013;15:13737–83. https://doi.org/10.1039/c3cp51213d.
[55] Zhang W, Qi J, Liu K, Cao R. A nickel-based integrated electrode from an autologous growth strategy for highly efficient water oxidation. Adv Energy Mater 2016;6:1502489. https://doi.org/10.1002/aenm.201502489.
[56] Jung S, McCrory CCL, Ferrer IM, Peters JC, Jaramillo TF. Benchmarking nanoparticulate metal oxide electrocatalysts for the alkaline water oxidation reaction. J Mater Chem A 2016;4:3068–76. https://doi.org/10.1039/c5ta07586f.
[57] Zhu Y, Zhou W, Zhong Y, Bu Y, Chen X, Zhong Q, et al. A perovskite nanorod as bifunctional electrocatalyst for overall water splitting. Adv Energy Mater 2017;7:10–7. https://doi.org/10.1002/aenm.201602122.
[58] Béjar J, Álvarez-Contreras L, Ledesma-García J, Arjona N, Arriaga LG. Electrocatalytic evaluation of Co3O4 and NiCo2O4 rosettes-like hierarchical spinel as bifunctional materials for oxygen evolution (OER) and reduction (ORR) reactions in alkaline media. J Electroanal Chem 2019. https://doi.org/10.1016/j.jelechem.2019.113190.
[59] Wang W, Kuai L, Cao W, Huttula M, Ollikkala S, Ahopelto T, et al. Mass-production of mesoporous MnCo2O4 spinels with manganese(IV)- and Cobalt(II)-rich surfaces for superior bifunctional oxygen electrocatalysis. Angew Chem Int Ed 2017;56:14977–81. https://doi.org/10.1002/anie.201708765.
[60] Chen G, Zhou W, Guan D, Sunarso J, Zhu Y, Hu X, et al. Two orders of magnitude enhancement in oxygen evolution reactivity on amorphous Ba0.5Sr0.5Co0.8Fe0.2O3−d nanofilms with tunable oxidation state. Sci Adv 2017;3:1–9. https://doi.org/10.1126/sciadv.1603206.
[61] Du X, Su H, Zhang X. 3D MnCo2O4@CoS nanoarrays with different morphologies as an electrocatalyst for oxygen evolution reaction. Int J Hydrogen Energy 2019;44:21637–50. https://doi.org/10.1016/j.ijhydene.2019.06.086.
[62] Zhang L, Liang Q, Yang P, Huang Y, Chen W, Deng X, et al. Flower-like Co3O4 microstrips embedded in Co foam as a binder-free electrocatalyst for oxygen evolution reaction. Int J Hydrogen Energy 2019;44:24209–17. https://doi.org/10.1016/j.ijhydene.2019.07.146.
[63] Li Z, Li B, Chen J, Pang Q, Shen P. Spinel NiCo2O4 3-D nanoflowers supported on graphene nanosheets as efficient electrocatalyst for oxygen evolution reaction. Int J Hydrogen Energy 2019;44:16120–31. https://doi.org/10.1016/j.ijhydene.2019.04.219.
[64] Huang X, Zheng H, Lu G, Wang P, Xing L, Wang J, et al. Enhanced water splitting electrocatalysis over $MnCo_2O_4$ via introduction of suitable Ce content. ACS Sustainable Chem Eng 2018. https://doi.org/10.1021/acssuschemeng.8b04814. acssuschemeng.8b04814.
[65] Li Z, Gu A, He X, Lv H, Wang L, Lou Z, et al. Rod bundle-like nickel cobaltate derived from bimetal-organic coordination complex as robust electrocatalyst for oxygen evolution reaction. Solid State Ionics 2019;331:37–42. https://doi.org/10.1016/j.ssi.2018.12.022.
[66] Wang D, Chen X, Evans DG, Yang W. Well-dispersed Co3O4/Co2MnO4 nanocomposites as a synergistic bifunctional catalyst for oxygen reduction and oxygen evolution reactions. Nanoscale 2013;5:5312. https://doi.org/10.1039/c3nr00444a.
[67] Jayaseelan SS, Bhuvanendran N, Xu Q, Su H. Co3O4 nanoparticles decorated Polypyrrole/carbon nanocomposite as efficient bi-functional electrocatalyst for electrochemical water splitting. Int J Hydrogen Energy 2020;45:4587–95. https://doi.org/10.1016/j.ijhydene.2019.12.085.
[68] Menezes PW, Indra A, Sahraie NR, Bergmann A, Strasser P, Driess M. Cobalt-manganese-based spinels as multifunctional materials that unify catalytic water oxidation and oxygen reduction reactions. ChemSusChem 2015;8:164–7. https://doi.org/10.1002/cssc.201402699.
[69] Cheng F, Shen J, Peng B, Pan Y, Tao Z, Chen J. Rapid room-temperature synthesis of nanocrystalline spinels as oxygen reduction and evolution electrocatalysts. Nat Chem 2011;3:79–84. https://doi.org/10.1038/nchem.931.
[70] Rios E, Chartier P, Gautier JL. Oxygen evolution electrocatalysis in alkaline medium at thin MnxCo3-xO4 ($0 \leq x \leq 1$) spinel films on glass/SnO2 : F prepared by spray pyrolysis. Solid State Sci 1999;1:267–77. https://doi.org/10.1016/S1293-2558(00)80081-3.
[71] Zhou Y, Du Y, Xi S, Xu ZJ. Spinel manganese ferrites for oxygen electrocatalysis: effect of Mn valency and occupation site. Electrocatalysis 2018;9:287–92. https://doi.org/10.1007/s12678-017-0429-z.
[72] Ma TY, Dai S, Jaroniec M, Qiao SZ. Synthesis of highly active and stable spinel-type oxygen evolution electrocatalysts by a rapid inorganic self-templating method. Chem - A Eur J 2014;20:12669–76. https://doi.org/10.1002/chem.201403946.

Supporting Information

$Mn_xCo_{3-x}O_4$ spinel oxides as efficient oxygen evolution reaction catalysts in alkaline media

K. Lankauf[1*], K. Cysewska[1], J.Karczewski[2], A. Mielewczyk-Gryń[2], K. Górnicka[2], G. Cempura[3], M. Chen[4], P. Jasiński[1], S. Molin[1]

[1] Faculty of Electronics, Telecommunications and Informatics, Gdańsk University of Technology, ul. G. Narutowicza 11/12, 80-233 Gdańsk, Poland

[2] Faculty of Applied Physics and Mathematics, Gdańsk University of Technology, ul. G. Narutowicza 11/12, 80-233 Gdańsk, Poland

[3] International Centre of Electron Microscopy for Materials Science, AGH University of Science and Technology, al. A. Mickiewicza 30, 30-059 Kraków, Poland

[4] Department of Energy Conversion and Storage, Technical University of Denmark, Frederiksborgvej 399, 4000, Roskilde, Denmark

*e-mail: krystian.lankauf@pg.edu.pl

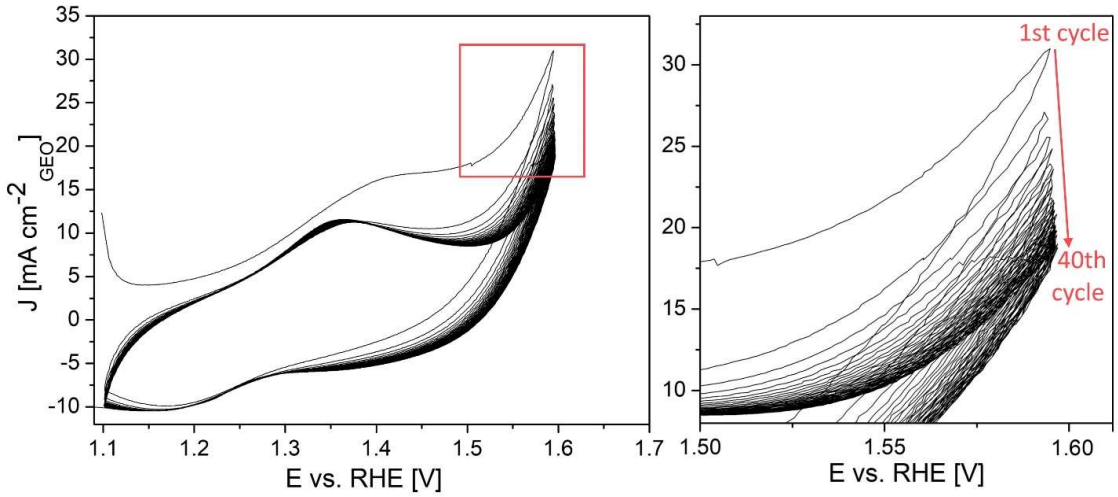

Fig. S1 – Electrochemical activation of dp-$MnCo_2O_4$ electrode by 40 CV scans between 1.1 to 1.6 V vs. RHE at scan rate of 100 mV s^{-1}.

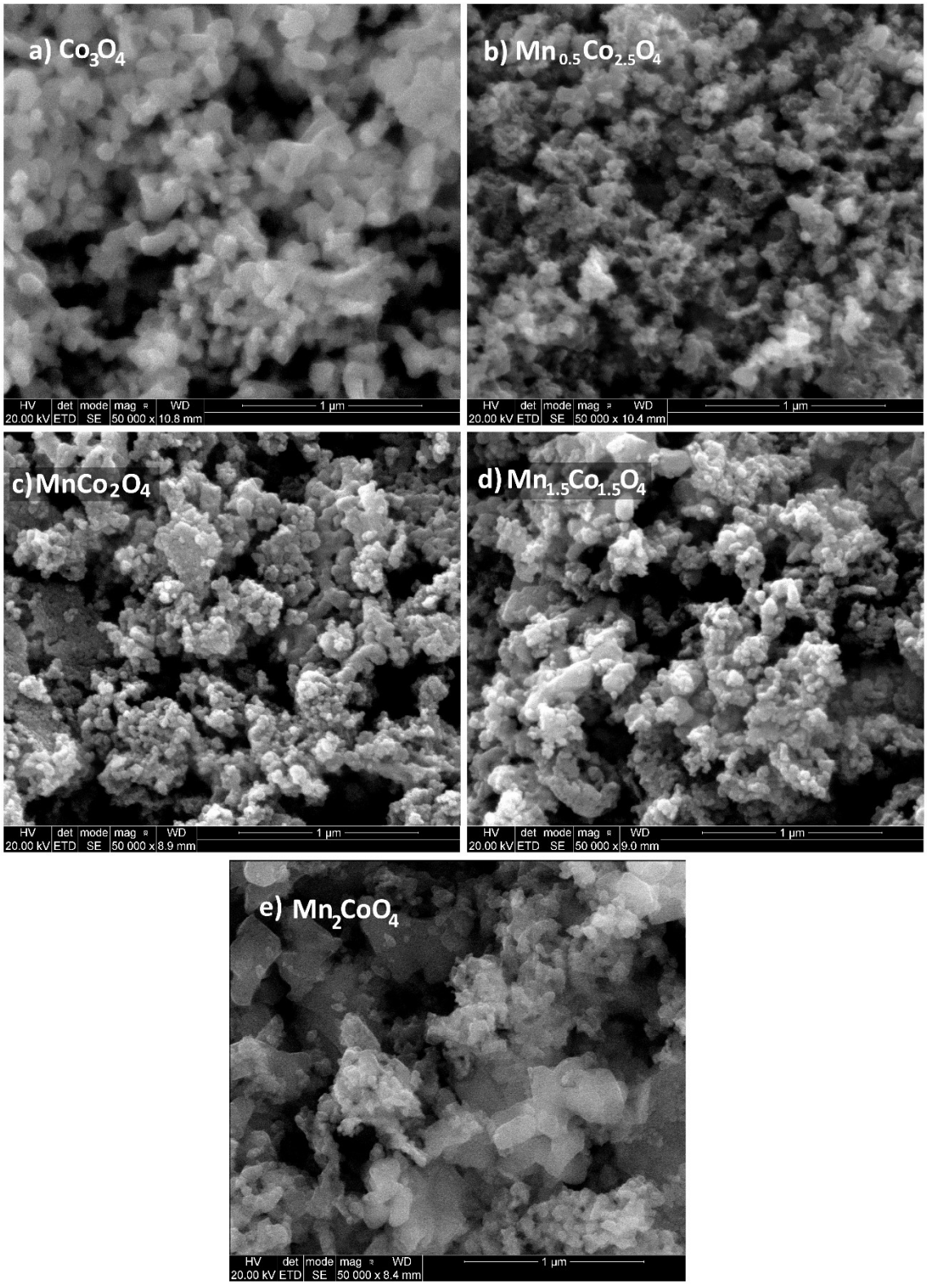

Fig. S2 – Enlarged SEM images of synthesised $Mn_xCo_{3-x}O_4$ powders. Magnitude 50 000x. a) x=0, b) x=0.5, c) x=1, d) x=1.5, e) x=2.0.

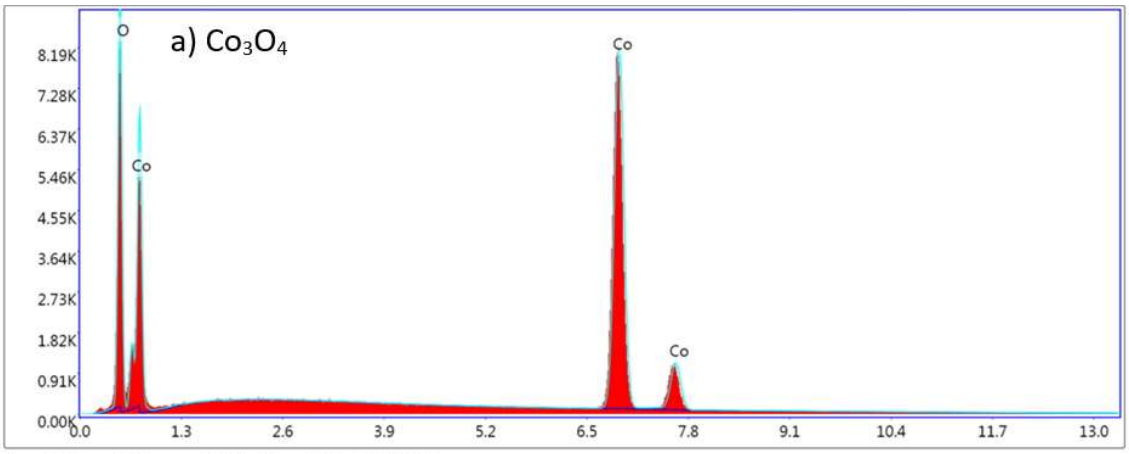

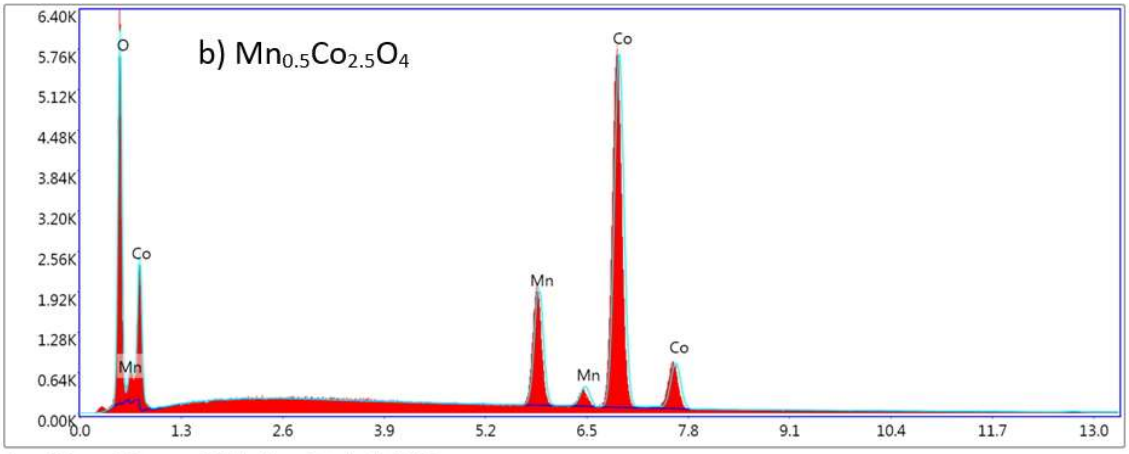

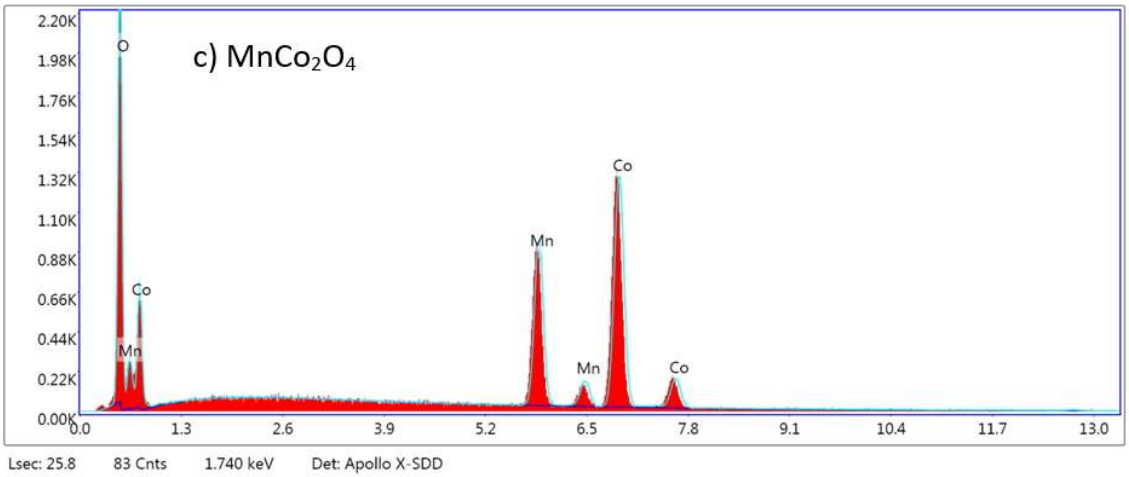

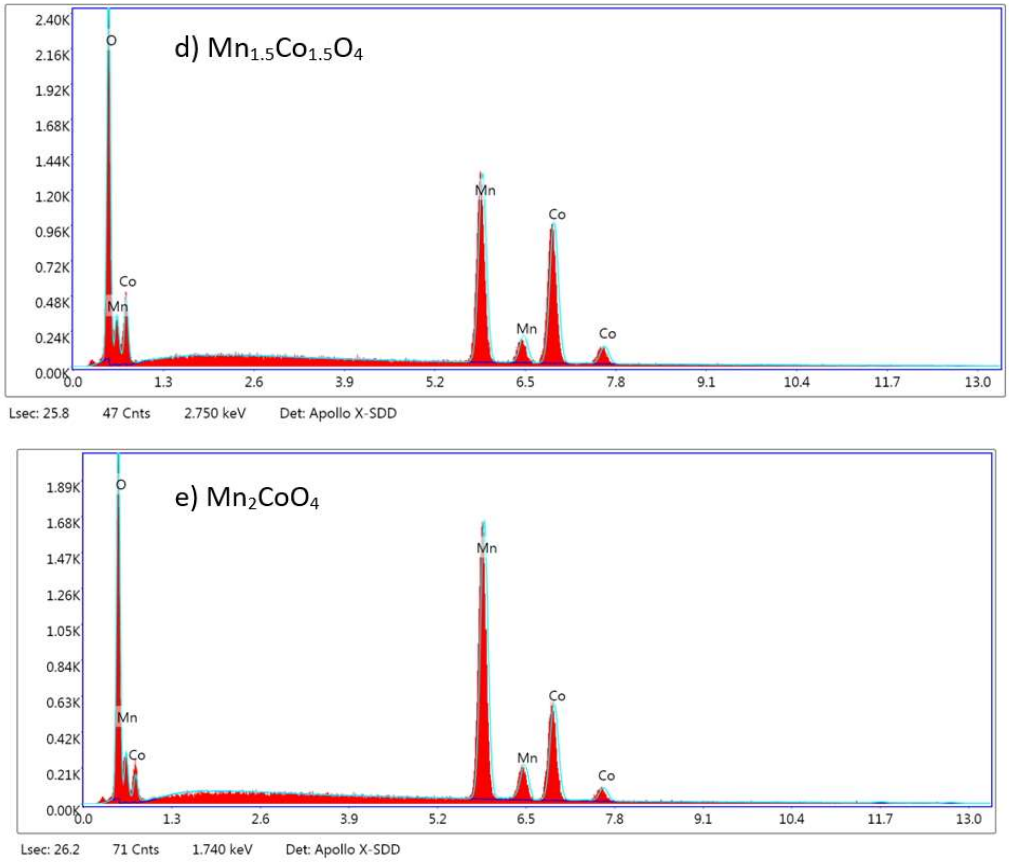

Fig. S3 – EDS spectra of synthesized MnxCo3-xO4 powders. A) x=0, b) x=0.5, c) x=1, d) x=1.5, e) x=2.0.

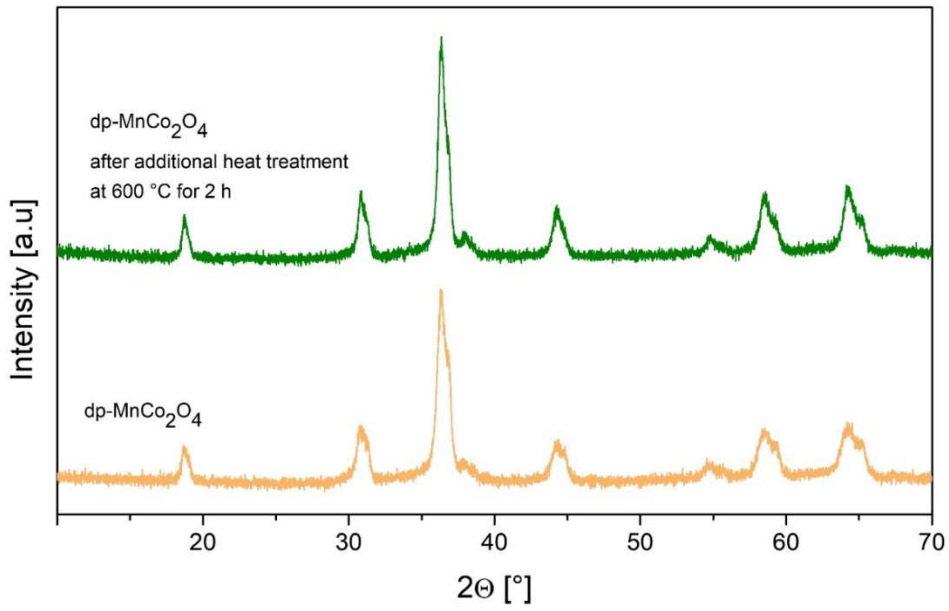

Fig. S4 – Comparison of XRD patterns of synthesised sp-$MnCo_2O_4$ before and after additional heat treatment.

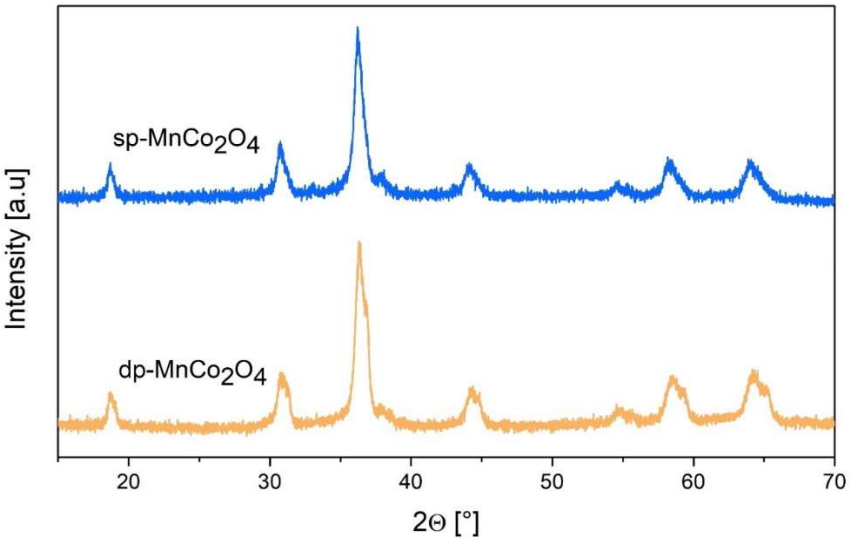

Fig. S5 – XRD patterns of synthesised sp-$MnCo_2O_4$ dp-$MnCo_2O_4$ powders synthesized by EDTA-CA and EDTA-CA-EG synthesis method, respectively.

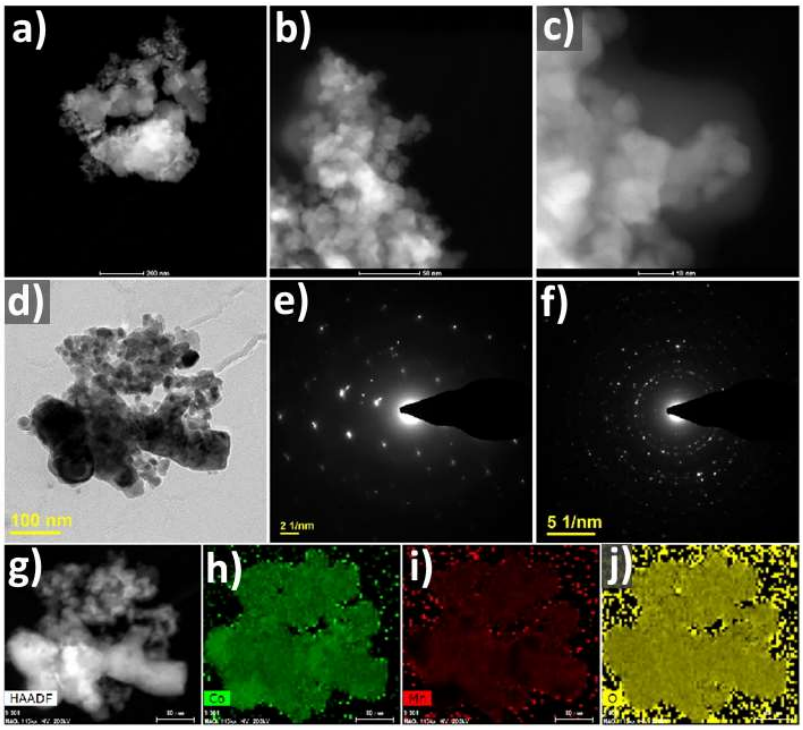

Fig. S6 – HAADF-(S)TEM images (a-d) and corresponding SAED (e,f) patterns of the dual-phase MnCo2O4 powder. TEM-EDS elemental maps (g-j) of cobalt (h), manganese (i), and oxygen (j).

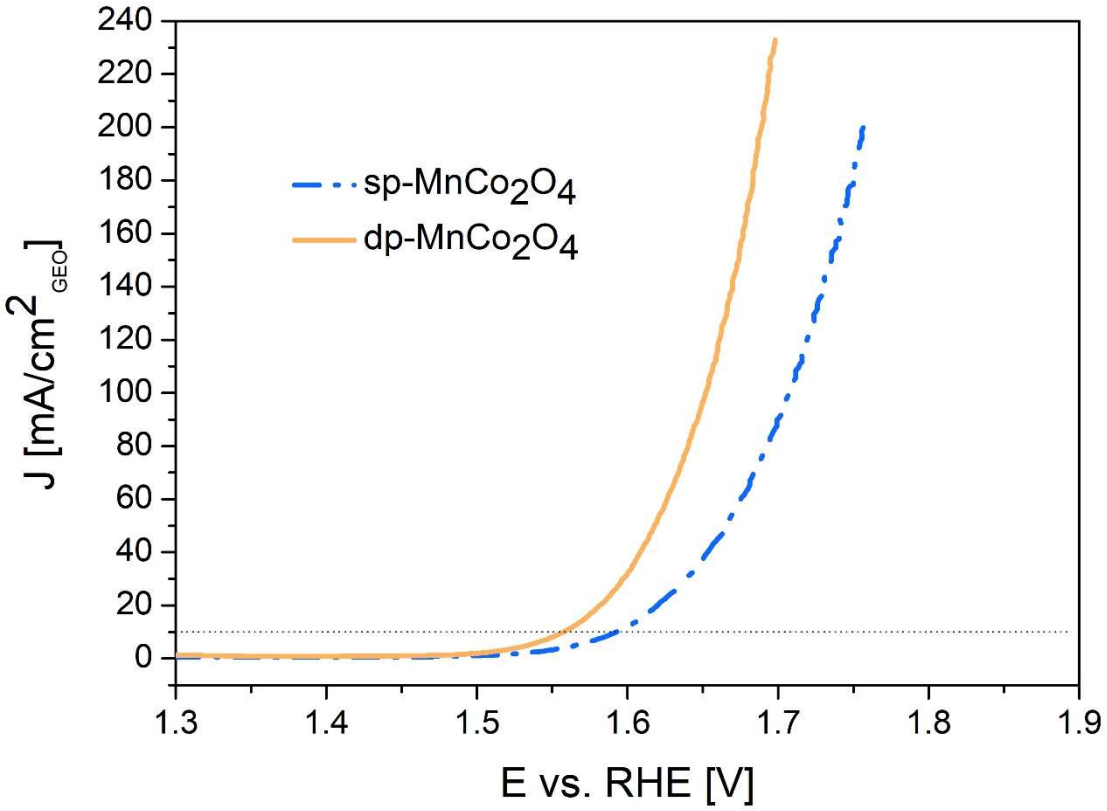

Fig. S7 –dp-$MnCo_2O_4$ and sp-$MnCo_2O_4$ LSV polarization curves comparison.

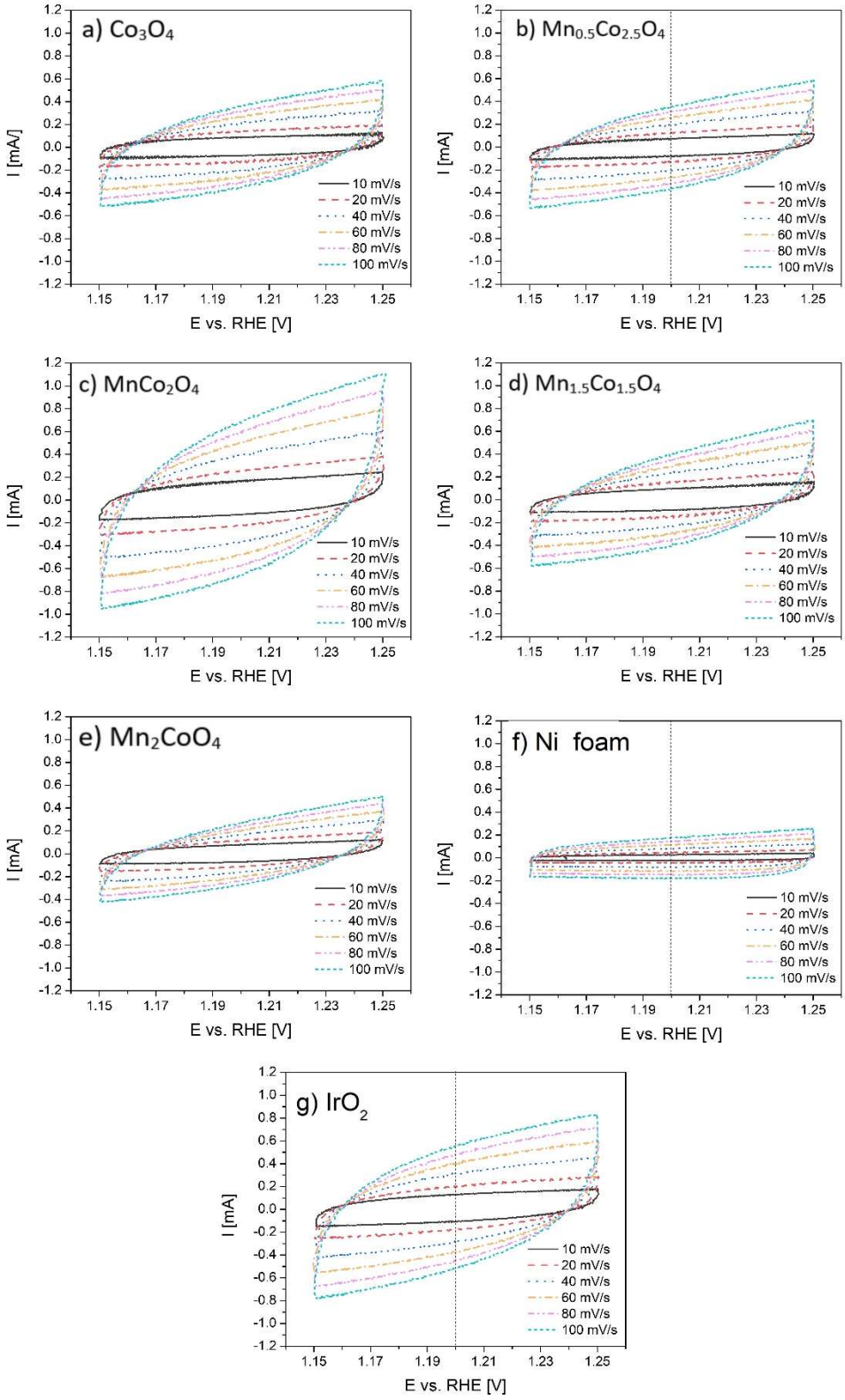

Fig. S8 – Cyclic voltammetry curves in a capacitive current region (1.15 – 1.25 V vs. RHE) at various scan rates (10, 20, 40, 60, 80 and 100 mV/s) of: a) Co_3O_4, b) $Mn_{0.5}Co_{2.5}O_4$, c) $MnCo_2O_4$, d) $Mn_{1.5}Co_{1.5}O_4$, e) Mn_2CoO_4, f) Ni foam, g) IrO_2

4.2 Tuning of e_g electron occupancy of $MnCo_2O_4$ spinel for oxygen evolution reaction by partial substitution of Co by Fe at octahedral sites

W przedstawionej publikacji kontynuowane były prace nad zastosowaniem i ulepszeniem spinelu $MnCo_2O_4$ jako katalizatora reakcji OER w środowisku zasadowym. Jako metodę modyfikacji materiału zbadano wpływ dodatku żelaza w strukturze krystalicznej spinelu na jego właściwości fizykochemiczne i aktywność elektrochemiczną. W tym celu za pomocą syntezy zol-żel wytworzono serię proszków $MnCo_{2-x}Fe_xO_4$ (x = 0,125; 0,250; 0,500; 0,750; 1,000), w których atomy kobaltu były podstawiane przez atomy żelaza.

Właściwości fizykochemiczne otrzymanych materiałów były badane za pomocą szeregu technik tj. dyfraktometrii proszkowej XRD, skaningowej i transmisyjnej mikroskopii elektronowej SEM i TEM, rentgenowskiej spektroskopii fotoelektronów XPS, rentgenowskiej spektroskopii absorpcyjnej XAS, spektrometrii FTIR oraz spektroskopii ICP-OES. Materiały o zawartości żelaza do x=0,5 odznaczały się czystością fazową, natomiast przy większych ilościach zaobserwowano występowanie niewielkich ilości zanieczyszczeń w postaci tlenków manganu i żelaza. Ziarna proszków po rozmieleniu za pomocą kulek z YSZ posiadały nieregularny kształt o średnicach mieszczących się w zakresie 50-200 nm. Za pomocą metod spektroskopowych zbadano, że na powierzchni proszków Mn przyjmuje głównie +3 stopień utlenienia, co sugeruje jego występowanie w pozycjach o koordynacji oktaedrycznej. Ważną obserwacją jest, że podstawianie żelaza w miejsce kobaltu, który domyślnie występuje na +2 i +3 stopniu utlenienia, następuje tylko dla kationów na +3 stopniu utlenienia. Sugeruje to, że żelazo podstawiane jest za kobalt tylko w pozycjach o koordynacji oktaedrycznej, natomiast w pozycjach skoordynowanych tetraedrycznie pozostaje wyłącznie kobalt.

Analiza aktywności elektrokatalitycznej została przeprowadzona za pomocą wirującej elektrody RDE-GC w elektrolicie 0,1 M KOH. Sprawdzono, że podstawianie żelaza do x = 0,5 skutkuje obniżeniem nadpotencjału oraz nachylenia krzywej Tafela. Dalsze zwiększanie dodatku żelaza powoduje nagłe pogorszenie aktywności elektrokatalitycznej OER. Korzystając z normalizacji gęstości prądu względem powierzchni właściwej każdego z materiałów zauważono, że rozkład aktywności elektrokatalitycznej w funkcji zawartości żelaza tworzy krzywą typu „volcano". Zależność tą można powiązać ze średnią liczbą elektronów na zdegenerowanym orbitalu e_g kationów w pozycjach oktaedrycznych, gdzie największą aktywność posiadają materiały, dla których liczba ta wynosi 1.

Dla materiału wykazującego najniższy nadpotencjał, tj. $MnCo_{1.5}Fe_{0.5}O_4$ przeprowadzono testy stabilności w układzie laboratoryjnego elektrolizera. Wykazano stabilność pracy w czasie minimum 48 h.

Moim osiągnięciem jest zwiększenie aktywności elektrokatalitycznej spinelu $MnCo_2O_4$, otrzymanego za pomocą metody zol-żel, poprzez modyfikację jego stechiometrii podstawiając żelazo w miejsce kobaltu. Badania, które wykonałem wykazały, że działanie takie wpływa na zmianę właściwości fizykochemicznych materiału z zachowaniem stabilności pracy.

W przedstawionym artykule samodzielnie przeprowadziłem syntezę materiałów oraz przygotowałem elektrody RDE z naniesionym katalizatorem. W dalszej kolejności przeprowadziłem pomiary elektrochemiczne. Przeprowadzałem również pomiary spektroskopowe w zakresie miękkiego promieniowania rentgenowskiego na linii badawczej PIRX w Narodowym Centrum Promieniowania Synchrotronowego SOLARIS. Ponadto odpowiadałem za analizę otrzymanych wyników, przygotowanie rysunków oraz napisanie manuskryptu. Jako autor korespondencyjny zgłosiłem artykuł do publikacji w czasopiśmie oraz przygotowałem poprawki w odpowiedzi na recenzje.

Oświadczenie współautorów o wkładzie w powstanie publikacji: „Tuning of e_g electron occupancy of $MnCo_2O_4$ spinel for oxygen evolution reaction by partial substitution of Co by Fe at octahedral sites"

Imię i nazwisko autora	Wkład w powstanie pracy	Podpis
Krystian Lankauf	Konceptualizacja, metodologia, badania, pisanie – oryginalna wersja robocza, wizualizacja	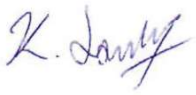
Karolina Górnicka	Badania (XRD), pisanie – recenzja i redakcja	
Patryk Błaszczak	Badania (BET), pisanie – recenzja i redakcja	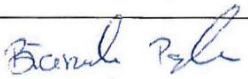
Jacek Ryl	Badania (XPS), pisanie – recenzja i redakcja	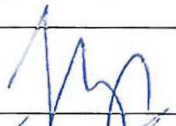
Jakub Karczewski	Badania (SEM), pisanie – recenzja i redakcja	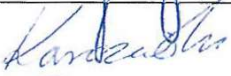
Grzegorz Cempura	Badania (TEM), pisanie – recenzja i redakcja	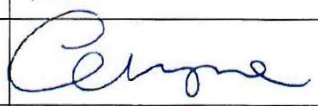
Marcin Zając	Badania (XAS), pisanie – recenzja i redakcja	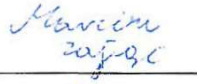
Maciej Bik	Badania (FTIR), pisanie – recenzja i redakcja	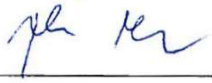
Maciej Sitarz	Badania (FTIR), pisanie – recenzja i redakcja	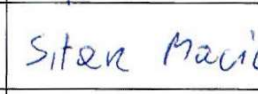
Piotr Jasiński	Pisanie – recenzja i redakcja, nadzór, zasoby	
Sebastian Molin	Konceptualizacja, pisanie – recenzja i redakcja, nadzór, zasoby, pozyskiwanie funduszy	

INTERNATIONAL JOURNAL OF HYDROGEN ENERGY 48 (2023) 8854–8866

Available online at www.sciencedirect.com

ScienceDirect

journal homepage: www.elsevier.com/locate/he

Tuning of e_g electron occupancy of $MnCo_2O_4$ spinel for oxygen evolution reaction by partial substitution of Co by Fe at octahedral sites

Krystian Lankauf [a,*], *Karolina Górnicka* [b], *Patryk Błaszczak* [b], *Jakub Karczewski* [b], *Jacek Ryl* [b], *Grzegorz Cempura* [c], *Marcin Zając* [d], *Maciej Bik* [e], *Maciej Sitarz* [e], *Piotr Jasiński* [a], *Sebastian Molin* [a]

[a] *Advanced Materials Center, Faculty of Electronics, Telecommunications and Informatics, Gdańsk University of Technology, ul. G. Narutowicza 11/12, 80-233 Gdańsk, Poland*

[b] *Advanced Materials Center, Faculty of Applied Physics and Mathematics, Gdańsk University of Technology, ul. G. Narutowicza 11/12, 80-233 Gdańsk, Poland*

[c] *Faculty of Metals Engineering and Industrial Computer Science, Centre of Electron Microscopy for Materials Science, AGH University of Science and Technology, al. A. Mickiewicza 30, 30-059 Kraków, Poland*

[d] *National Synchrotron Radiation Centre Solaris, Jagiellonian University, 30-392 Kraków, ul. Czerwone Maki 98 Poland*

[e] *AGH University of Science and Technology, Faculty of Materials Science and Ceramics, al. Mickiewicza 30, 30-059 Kraków, Poland*

HIGHLIGHTS

- A series of $MnCo_{2-x}Fe_xO_4$ powders (x = 0.125; 0.250; 0.500; 0.750; 1.000) were synthesized by a facile sol-gel method.
- Moderate Fe incorporation in $MnCo_2O_4$ spinel enhances the catalytic activity towards OER.
- The OER-specific activity exhibits a volcano-type shape as a function of the e_g occupancy at octahedral sites.

GRAPHICAL ABSTRACT

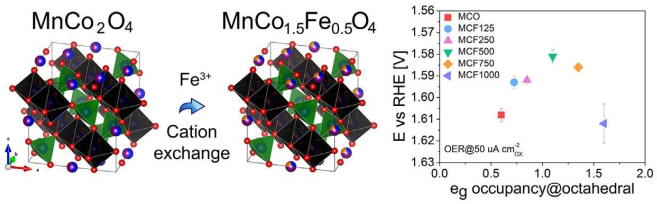

ARTICLE INFO

Article history:
Received 2 September 2022
Received in revised form
18 November 2022
Accepted 2 December 2022
Available online 22 December 2022

ABSTRACT

To study the effect of partial Co substitution by Fe in the B-site of $MnCo_2O_4$ spinel on its physicochemical and electrochemical properties, a series of $MnCo_{2-x}Fe_xO_4$ powders (x = 0.125; 0.250; 0.500; 0.750; 1.000) were synthesized by means of the sol-gel method. The produced powders were characterized by powder X-ray diffraction (pXRD), scanning and transmission electron microscopy (SEM & TEM) coupled with energy dispersive spectroscopy (EDS), X-ray photoelectron and absorption spectroscopy (XPS & XAS), Fourier transformed infrared spectroscopy (FTIR), and inductively coupled plasma optical emission

* *Corresponding author.*
E-mail address: krystian.lankauf@pg.edu.pl (K. Lankauf).

https://doi.org/10.1016/j.ijhydene.2022.12.013

Keywords:
Spinel
Oxygen evolution
Electrocatalysts
Water splitting
Element substitution

spectroscopy (ICP-OES). The electrocatalytic activity towards oxygen evolution reaction (OER) was evaluated in an alkaline environment (0.1 M KOH). From our findings, the activity increased with the addition of Fe up to x = 0.5, characterized by a decrease of overpotential at 10 mA cm^{-2}_{GEO} from 406 mV for $MnCo_2O_4$ to 376 mV for $MnCo_{1.5}Fe_{0.5}O_4$, with a corresponding 44 mV dec^{-1} Tafel slope. It was identified that the OER-specific activity exhibits a volcano-type shape as a function of the e_g occupancy at octahedral sites tuned by Co substitution with Fe.

Introduction

The development of highly efficient energy storage and conversion technologies is crucial to meet the growing energy needs and to reduce the human impact on the environment. Hydrogen is prominent as a clean and abundant sustainable energy carrier and fuel [1–3]. Electrochemical water splitting is a promising process due to the abundance of the reaction substrate and safety of the byproduct, i.e. water and molecular oxygen, respectively. The efficiency of electrocatalytic water splitting is limited by its high energy consumption related to the overpotentials needed to sustain the electrolysis half-reactions: the cathodic hydrogen evolution reaction (HER) and the anodic oxygen evolution reaction (OER). Among these two processes, the OER is more challenging due to the sluggish kinetics and is thermodynamically less favorable, which is associated with the four-electron/proton-coupled transfer reaction pathway [4,5]. Therefore, the development of low-cost, highly active OER catalysts is an important task to reduce the reaction overpotentials, and hence the energy consumption of water splitting systems [6,7].

Transition metal oxides with the formula AB_2O_4 (where A and B are transition metal ions), named spinels after the representative $MgAl_2O_4$, have found interest in energy conversion systems due to their exceptional electrocatalytic properties [8,9]. Spinel oxides are composed of A-O tetrahedrons and B–O octahedrons, where A and B can contain the same or a different metal element. The valence equilibrium is maintained if cation A is in the +2 or +4 oxidation state and cation B is in the +3 or +2 oxidation state. Knowing the crystal field stabilization energy (CFSE) and ionic radii of the elements, one can "design" the spinel structure, predicting the positions of its constituent elements, and hence the valence state and electronic structure [10,11]. Various compositions, morphologies, structures, and valence states can be obtained through the deliberate choice of the preparation method. In brief, spinel oxides can be prepared by solid-phase [12,13], solution-phase [14,15] and vapor-phase methods [16–18].

One of the spinels with flexible applications is the manganese cobaltite spinel: $MnCo_2O_4$, which can be fine-tuned by chemical modifications [9]. Commonly, $MnCo_2O_4$ is described as an inverse spinel with the Mn cations preferring to occupy the octahedral site. Depending on the preparation method and thermal history, its physicochemical properties can be modulated by induced cationic distribution changes. Wei et al. synthesized $MnCo_2O_4$ at 150, 300, 400, 500, 700, and 900 °C and observed that the average Mn valence state ranges from +3.2 to +3.7 depending on the synthesis temperature [19]. The OER studies exhibited a volcano shape of activity as a function of the Mn valence state with the peak of the trend around +3. Wang et al. employed the spray-pyrolysis route to prepare a mesoporous $MnCo_2O_4$ bifunctional oxygen electrocatalyst [20]. Both Mn_2O_3-like performance for oxygen reduction reaction (ORR) and Co_3O_4-like activity for OER were observed. The notable bifunctional activity resulted from the preferred Mn^{IV}- and Co^{II}-rich surface attained by the surface state engineering approach. A series of Fe-substituted $ZnFe_xCo_{2-x}O_4$ was prepared by Zhou et al. [21]. Fe substitution at 10–30 at.% facilitates the injection/extraction of electrons from oxygen. As a result, enlarged Co 3d and O 2p covalency occurred, associated with enhanced OER activity.

The ternary Mn–Co–Fe spinel oxides have already exhibited the promising properties for application in sustainable energy field. Liu et al. have synthesized the series of $MnCo_{2-x}Fe_xO_4$ (x = 0–0.7) spinel oxides by solid-state reaction for SOFC interconnect coatings. The Fe doping stabilized the cubic spinel structure and decreased the electrical conductivity obeying the small polaron hopping mechanism at 800 °C in air [22]. Elkholy et al. reported the ternary $MnCoFeO_4$ nanoparticles for high-performance supercapacitor application, exhibiting high energy and power densities with excellent long-term stability [23]. Kim et al. presented that the redox potential of $mnCoFeO_4$ differs than of mixture of component spinels (Co_3O_4, Fe_3O_4, Mn_3O_4) [24]. Furthermore, they demonstrated an economically viable approach for fabrication of high-performance MFC based anodes for lithium rechargeable batteries. However, to our knowledge, there is a lack of complex studies of ternary Mn–Co–Fe spinel oxides, with emphasis on optimal Co: Fe ratio, for OER electrocatalysis application.

Herein, we studied the effect of partial Co substitution by Fe in the B-site of $MnCo_2O_4$ on the physicochemical and electrochemical properties. A series of $MnCo_{2-x}Fe_xO_4$ powders (x = 0.125; 0.250; 0.500; 0.750; 1.000) were synthesized by a facile sol-gel method. All materials were examined for their structural properties and OER electrocatalytic activity in an alkaline electrolyte (0.1 M KOH).

Experimental section

Materials synthesis

Iron-substituted manganese cobaltite spinel oxides were prepared by a sol-gel EDTA-Citric Acid method similarly to in

previous work [25]. Analytical grade $Mn(NO_3)_2 \cdot 4H_2O$, $Co(NO_3)_2 \cdot 6H_2O$, and $Fe(NO_3)_3 \cdot 9H_2O$ were dissolved in a minimum amount of deionized water in the right proportions to obtain stoichiometric products. In parallel, citric acid (CA) and ethylenediaminetetraacetic acid (EDTA) were dissolved in deionized water with the addition of an ammonia solution to allow EDTA dissolution. The specific molar ratio of the reagents was maintained, i.e. TMI:CA:EDTA = 1:2:1 (TMI –Total Metal Ions). The prepared solutions were mixed together and stirred on a magnetic stirrer at room temperature for 10 min and ammonia solution was added to maintain a pH level of 6. The precursor solution was heated to 90 °C and maintained under magnetic stirring for ~5 h until a dark gel was formed. The gel was transferred to a laboratory drier and dried at 90° for 2 h, at 120 °C for 5 h, and at 180 °C for 5 h. The obtained dry powder was ground in an agate mortar, placed in an alumina crucible and calcined in a muffle furnace in air at 400 °C for 1 h, again ground in the agate mortar, and further heat-treated in air at 800 °C for 2 h. The calcined powders were ball-milled in ethanol for 144 h (Zoz Gmbh, Rollermill RM1) in 20 mm diameter glass vials using yttria-stabilized zirconia (YSZ) spherical grinding media (φ1 mm) with a rotation speed of 100 rpm for agglomerate defragmentation to improve the electrocatalytic performance.

Characterization

Powder X-ray diffraction (pXRD) was conducted at room temperature on a Bruker D2 Phaser diffractometer with CuKα radiation (λ = 1.5404 Å) and a Lynxeye XE-T detector in the range from 5 to 110° with 0.01° step size. Unit cell parameter calculation was performed by Le Bail refinement using the Fullprof software package [26]. Weight fractions of additional phases were estimated by Rietveld refinement performed using GSAS-II [27]. The *.cif files were downloaded from the Inorganic Crystal Structure Database and Crystallography Open Database [28,29].

The morphologies of the prepared powders were investigated using an FEI Quanta 250 FEG Scanning Electron Microscope (10 kV accelerating voltage, Everhart–Thornley detector) and a Cs-corrected Titan Cubed G2 60 300 (FEI) Scanning Transmission Electron Microscope (S/TEM). The chemical composition was examined using the ChemiSTEM EDX system based on four windowless Silicon Drift Detectors (Super X). The powders for TEM investigations were prepared by placing a drop of water suspension containing the powder onto a copper grid followed by vacuum drying.

The specific surface area of the powders was measured using the N_2 adsorption technique (Quantachrome, NovaTouch LX1) according to the BET isotherm model. The samples were degassed prior to sorption measurement at 300 °C for 3 h under vacuum.

X-ray photoelectron spectroscopy (XPS) measurements were performed using an Axis Supra spectrometer (Kratos Analytical) to investigate the valence states of the Mn and Co in the MnCo2O4 spinel. The spectroscope was equipped with an Al Kα source. The pass energy and the spot size diameter were 20 eV and 2 × 0.7 mm, respectively. Metallic gold and copper were used for the instrument calibration. The CasaXPS 2.3.18 software on a Shirley background was used to analyze the obtained spectra. The XPS binding energies were corrected using the C 1s peak at 284.6 eV.

X-ray absorption spectroscopy (XAS) measurements of the $MnCo_{2-x}Fe_xO4$ samples were performed at the 04BM PIRX (former PEEM/XAS) beamline of the SOLARIS National Synchrotron Radiation Centre for the $L_{2,3}$-edge spectra of Mn, Co, and Fe. The PIRX beamline uses a bending magnet (1.31 T) to provide a photon energy range from 100 to 2000 eV with an energy resolution no lower than $2.5 \cdot 10^{-4}$ [30]. The beam spot size at the sample was 250 μm × 40 μm (horizontal x vertical). Powder samples were applied to carbon tape and located on the Omicron-type plate sample holder. XANES spectra were recorded using total electron yield detection mode (TEY) which reflects an information depth of several nm. Measurements were performed in UHV and at ambient temperature. The obtained data were processed in the Bessy software. The data were first normalized to the measured incident photon flux I_0. Further data processing steps consisted of subtracting a straight line fitted to the L_3 pre-edge region, dividing by a polynomial function fitted to the L_2 post-edge region, and normalizing to a maximum intensity of 1.

Fourier Transformed Infrared Spectroscopy studies in the Middle (MIR) and Far Infrared Range (FIR) were performed on a Bruker Vertex 70v spectrometer under vacuum conditions using the transmission technique. For sample preparation, ca. 2 mg of thoroughly ground powder was mixed with a reference material (400 mg of KBr (Uvasol®, Merck) in MIR and 180 mg of polyethylene (Uvasol®, Merck) in FIR range) and pressed with a hydraulic press. To record the spectra, 256 scans and a resolution of 2 cm^{-1} were applied in the 4000–400 cm^{-1} (MIR) and 400–100 cm^{-1} (FIR) spectral ranges. The spectra were subsequently post-processed using the OPUS 7.2. Software. First, the MIR spectra were cut within the 1000–400 cm^{-1} range, as no important bands occurred within the remaining part. Afterwards, three representative spectra (MCO, MCF500, MCF1000) were deconvoluted using the Handke method [31] and the Levenberg-Marquardt algorithm. During the deconvolution process, a set of Gaussian-Lorentzian bands was used which resulted in an RMS error of 0.05. Finally, the positions of all bands were estimated using the Peak Picking function, both before and after the deconvolution process.

Electrode preparation and electrochemical measurements

Glassy carbon rotating disk electrodes (RDE-GCE, 0.196 cm^2, ALSCo., Ltd) were used as support electrodes for the powder catalysts. Before the deposition of the catalyst inks, the RDE-GCE were polished for 5 min using 9, 3, and 1 μm polishing diamond solutions, sonicated for 10 min in deionized water and isopropanol, respectively, then dried overnight under ambient conditions. The catalyst and Super P Li Conductive Carbon Black (CCB) (Imerys Graphite & Carbon) powders were separately ball-milled in ethanol for 144 h using φ1 mm YSZ grinding balls. The spinel powder and CCB suspensions were mixed with K+-exchanged Nafion solution in the appropriate proportion to obtain 1 mL of ink with a weight ratio of solids of 5:5:2 (Catalyst:CCB:Nafion). The K+-exchanged Nafion preparation has been described elsewhere [32]. Subsequently, the inks were sonicated in an ice-water bath for 30 min. Then 5 μL

of ink was drop-cast onto the RDE-GCE rotating at 700 rpm, achieving a catalyst mass loading of 45.5 μg. All electrochemical measurements were performed in a custom-made three-electrode Teflon cell system in 0.1 M KOH aqueous solution (prepared from 1 M KOH Titripur from Merck, diluted with DI water ~12 MΩ). A coated RDE-GCE, a Pt coil, and a Hg/HgO in 0.1 M KOH solution (ALS Co., Ltd, Japan) were used as the working (WE), counter (CE), and reference (RE) electrodes, respectively. The electrochemical tests were performed on BP-300 (BioLogic) bipotentiostat connected in a rotating disk electrode (RDE) configuration (RRDE-3A Rotating Ring Disk Electrode Apparatus Ver.2.0, ALS Co., Ltd). Before each experiment, the electrolyte was purged with 99.995% O_2 for 30 min, then the gas flow (50 mL min^{-1}) was maintained over the electrolyte to maintain the O_2/H_2O equilibrium. An electrolyte temperature of 25 °C was maintained by a Julabo F12 thermostat. All electrocatalytic experiments were performed using the same protocol. The disk electrode was conditioned by potential cycling 10 times in the range of 1.0–1.7 V vs RHE at a scan rate of 100 mV s^{-1}. Cycling voltammetry (CV) scans were performed in the non-faradaic potential region of 0.98–1.08 V vs RHE at scan rates of 10, 20, 40, 60, 80, 100 mV s^{-1} without RDE rotation for the double-layer capacitance (Cdl) estimation. The electrochemical active surface area (ECSA) was calculated assuming the reference capacitance value of 40 μF cm^{-2} for oxides [33]. The charge transfer resistance (R_{ct}) was calculated from the electrochemical impedance spectroscopy (EIS) measurements in the frequency range from 10 kHz to 0.1 Hz at 1.7 V vs RHE with an amplitude of 10 mV and a rotation speed of 1600 rpm. Fitting to the modified Randles equivalent circuit was performed with the EC-Lab® Software. CV scans for OER were performed in the range from 1.1 to 1.9 V vs RHE at a scan rate of 10 mV s^{-1} with a rotation speed of 1600 rpm. All measured potentials were converted to RHE by the experimental calibration of the Hg/HgO reference electrode against RHE (exemplary CV is shown in Fig. S1) [34]. The reference electrode was calibrated under experimental conditions weekly to exclude non-negligible electrode potential differences [35]. The value of E_{Offset} against RHE equals the measured equilibrium potential of hydrogen electrocatalysis (HER/HOR) and was determined to be in the range of $< -928; -920 >$ mV. For the OER polarization curves, the background correction was performed by averaging the positive and negative-going scans [34]. All potential values were iR-corrected to eliminate the solution resistance. The current density was normalized by the geometric surface area of the RDE-GCE (0.196 cm^2) (expressed in the unit mA cm^{-2}_{GEO}). The OER overpotential was calculated as the difference between the potential when the current density reached 10 mA cm^{-2}_{GEO} and the standard potential of oxygen electrocatalysis (1.23 V). The specific activity was determined by current normalization using the BET-specific surface area of each oxide catalyst (expressed in the unit μA cm^{-2}_{OX}). For each material, at least 3 separate samples were prepared and tested.

The durability tests (chronopotentiometry at 10 mA cm^{-2}) were performed with commercial electrolyzer cell (ElectroCell, Micro Flow Cell) in 0.1 M KOH. The electrolyser cell consisted of Ti cathode, Zirfon® Perl 500 UTP diaphragm (AGFA), and Sigracet 39 AA (SGL Carbon) carbon paper support as anode. The active geometrical area for both electrodes was 10 cm^{-2}. The anode potential was measured using leak-free LF-1 Ag/AgCl reference electrode (ElectroCell). Electrolyte circulation of 200 mL min^{-1} flow was forced using water pump (12V, 1.2 l min^{-1}, 1200 mA).

Results and discussion

Structure characterization

The powders, based on the general formula of $MnCo_{2-x}Fe_xO_4$, with $x = 0.125; 0.250; 0.500; 0.750; 1.000$, are labelled as MCO, MCF125, MCF250, MCF500, MCF750, and MCF1000.

The chemical composition of the synthesized powders was analyzed by EDS and ICP-OES, and the results are presented in Table S1. Good agreement between the planned stoichiometry and the resulting powder composition was obtained. The main impurities, as detected by ICP were Na, Si, K, Ca, not exceeding 0.05 at. %.

The phase composition of the powders was studied using X-ray diffractometry. As shown in Fig. 1b, the pXRD peaks of the ball-milled powders show the standard spinel $MnCo_2O_4$ cubic structure (space group Fd-3m, No. 227) [36]. The synthesized oxides were phase pure up to $x = 0.5$ composition. A slightly visible additional peak (33°) indicating the existence of Mn and/or Fe oxide was observed for the MCF750 (Fig. S2) and MCF1000 powders. Since the weight fraction of observed impurities calculated by Rietveld refinement was <3% (Fig. S3), the impurities are considered to be negligible in the terms of OER electrocatalysis.

In comparison to our previous work, the addition of ethylene glycol was omitted during the synthesis, which ensured crystallization of pure, single-phase material [25]. The calcination temperature was also increased from 600 °C to 800 °C. At the lower calcination temperature, Mn and Fe oxides were detected in the powders by pXRD (Fig. S4).

Fig. 1c shows the shift of the position of the characteristic peak (311) towards lower 2θ angles with the increasing Fe content, demonstrating the incorporation of iron into the structure and resulting in enlargement of the lattice size. For coordination number VI (the octahedral position), the ionic radius of Fe^{3+} (high spin) is 0.645 Å, whereas the radius of Co^{3+} (high spin) is 0.61 Å. The ball-milling process reduces the particle size and influences the average crystallite size, as determined by the broadening of the peaks (according to the Scherrer equation).

The Le Bail refinement results presented in Fig. 1d show that the lattice parameter scales almost linearly with the higher Fe substitution (data in Table S2). The dashed line presents Vegard's slope calculated based on unit cell data taken from the literature, i.e. $MnCo_2O_4$ (ICSD ID 291115) and $MnFe_2O_4$ (COD ID 2300585) [28,29].

Fig. 2a shows the SEM image of the morphology of the ball-milled MCF500 powder. The sample is composed of irregularly shaped grains with diameters in the range of 50–200 nm. All other $MnCo_{2-x}Fe_xO_4$ powders have similar morphology and grain size distribution (Fig. S5). The chemical compositions of the synthesized powders were evaluated by EDS/ICP

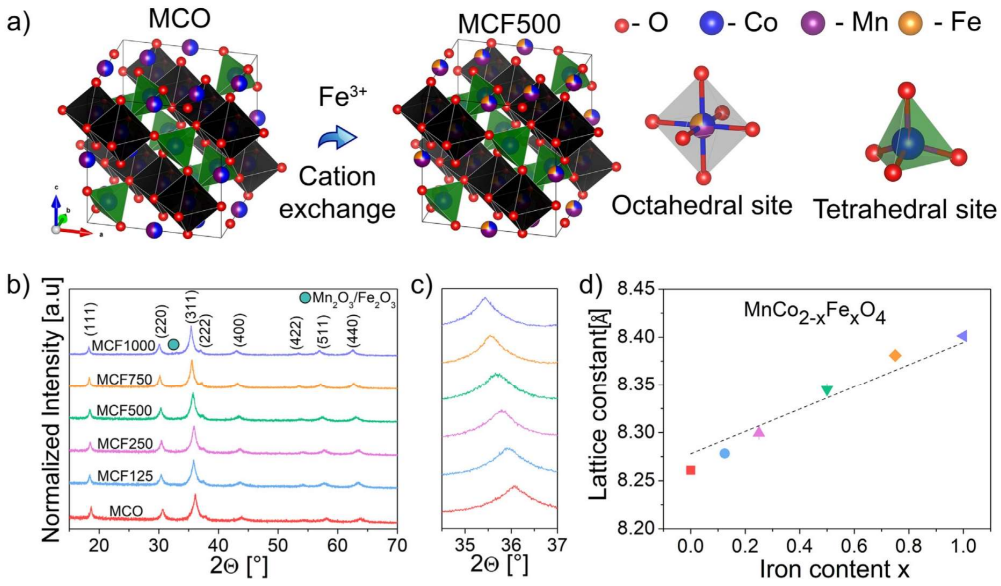

Fig. 1 – (a) Inverse cubic spinel structure (B [AB]O_4) with highlighted octahedrally and tetrahedrally coordinated transition metal cations. (b) pXRD patterns of ball-milled $MnCo_{2-x}Fe_xO_4$ powders, (c) zoom-in of the patterns showing the main reflection (311) shift, (d) and calculated lattice parameters.

analyses, which confirmed the desired stoichiometry (Table S1). The powders' specific surface area, measured with the N_2 adsorption technique presented in Table S2 shows that for all Fe-substituted materials, the specific surface area was ~23 $m^2 g^{-1}$, which corresponds to a characteristic particle size of ~50 nm.

The transmission emission electron microscopy image (TEM) in Fig. 2b further confirmed the grains' size and their irregular morphology, also demonstrating the plate-like structure of some grains, possibly resulting from the ball-milling process. As shown in Fig. 2c, the HRTEM image displays the lattice fringes with an interplanar distance of 0.483 nm, which corresponds to the (111) plane of $MnCo_{1.5}Fe_{0.5}O_4$ and is consistent with the d-spacing of the (111) plane derived by Le Bail refinement (0.482 nm). Furthermore, the selected area electron diffraction (SAED) patterns (Fig. S6) demonstrate the well-defined crystalline cubic structure of the Fd-3m space group. Dispersion of the

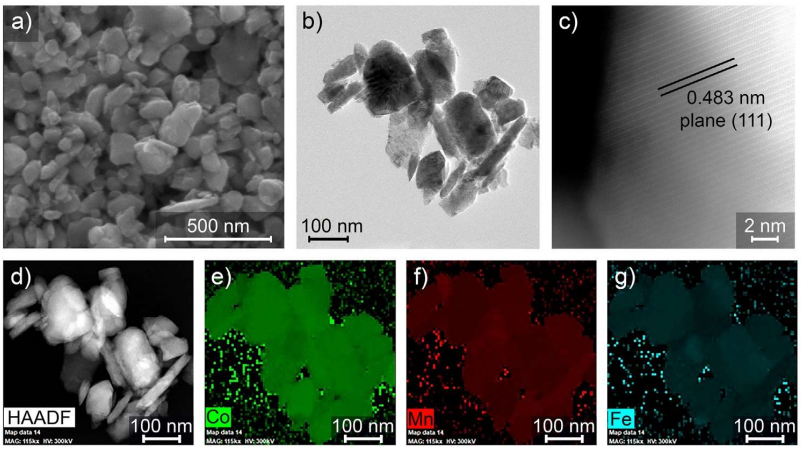

Fig. 2 – (a) SEM image (×100,000 magnification) of synthesized and ball-milled MCF500 powder, (b) BF-TEM image, (c) HRTEM image, (d) HAADF-STEM image, (e–g) and corresponding STEM-EDS elemental maps of (e) cobalt, (f) manganese, and (g) iron.

constituent elements (Mn, Co, Fe) was observed by TEM-EDS elemental analysis (Fig. 2e–g). However, segregation of Mn and Fe in some spots indicates the inherence of impurities in the form of Mn and Fe oxides in such a low amount that it was not observed earlier in the pXRD histograms.

Fig. 3 displays the XPS spectra of the MCFx (x = 0.125; 0.250; 0.500) samples. The Mn2p spectra are presented in Fig. 3a. Three oxidation states of manganese (II, III, IV), which are probable to co-exist in the inverse spinel structure, are characteristic because of the significant multiplet splitting observable in the XPS spectra, making a quantitative analysis challenging [37]. Due to the above, the collected spectra were fitted with respect to the most likely occurring Mn^{3+} species. Fitting parameters based on the Mn_2O_3 parameters provided by Biesinger et al. are presented in Table S3. For all samples, the main peak (Peak 2, ~641.9 eV) area is lower than that of the reference Mn_2O_3 (<44.5%), suggesting the observation of the influence of other Mn species on the collected spectra. In general, peaks at lower and higher binding energies have a higher area than the reference, indicating the existence of both Mn^{2+} and Mn^{4+}, respectively. For a detailed analysis of surface Mn valency, a more sophisticated method is necessary and is described in the next section. Co2p spectra are demonstrated in Fig. 3b. It is clearly visible that Co is, as expected, present in two forms: Co^{2+} and Co^{3+}. For samples the MCF250 and MCF500, additional slightly visible peaks are observed at ~779 eV, indicating the formation of new Co–O species, which may be related to the element segregation observed by the TEM studies. A quantitative analysis was omitted due to the influence of Auger signals from the Fe [38,39]. The Fe2p spectra presented in Fig. 3c are highly influenced by Co-LMM Auger peaks. However, a higher ratio of Fe^{3+} in the $MnCo_{2-x}Fe_xO_4$ with higher x is still observed.

X-ray absorption near-edge structure (XANES) spectra using total electron yield (TEY) were carried out to explore the impact of Fe substitution on the $MnCo_{2-x}Fe_xO_4$ spinels. L_3-edge XANES involves excitation of $2p_{3/2}$ electrons into unoccupied states of 3d character and was used to examine the valence of the Mn, Co and Fe. Additionally, reference samples, known for the stable and specified valence of their constituent transition metals cations, i.e. spinel oxides: Co^{2+} in $CoAl_2O_4$, Co^{3+} in $ZnCo_2O_4$, Co^{2+} and Co^{3+} in Co_3O_4, Fe^{3+} in $ZnFe_2O_4$, and oxides: Mn^{2+} in MnO, Mn^{3+} in Mn_2O_3, Mn^{4+} in MnO_2, were compared [40–43]. All observed Mn XANES spectra of the examined $MnCo_{2-x}Fe_xO_4$ spinels, as presented in Fig. 4a, were close to that of the Mn_2O_3 reference with the main peak at ~642.2 eV corresponding to Mn^{3+} in octahedral coordination. Slight shoulders observed at ~640.3 eV indicate a small share of Mn^{2+} in most of the examined spinels. Moreover, the samples exhibited a pronounced, higher energy shoulder at ~643.1 eV corresponding to Mn^{4+}. Unlike the other stoichiometries, changes in the Mn valence for MCF1000 were observed. The amount of Mn^{4+} decreased in favor of Mn^{2+}, which is indicated by the less pronounced peak at the higher energy of ~643 eV and the more pronounced one at the lower energy of ~640 eV. For most of the samples, the observed mixed Mn valence complies well with the inverse spinel model proposed by Bordeneuve [44].

The Co L_3-edge XANES of the basic $MnCo_2O_4$ (Fig. 4b) indicates a mixture of Co^{3+} and Co^{2+} with a high/low energy peak ratio of Co^{3+}/Co^{2+} close to 1, confirming the inverse spinel structure. It is important to highlight the fact that with higher Fe substitution, the observed Co L_3-edge high/low energy peak ratio systematically decreases, evidencing the incorporation of Fe ions in the octahedral sites. Besides this, after the main Co^{3+} peak, the high energy shoulder is observed around 782.5 eV, which may confirm the low spin state of trivalent cobalt ions [45].

The Fe-L_3 XANES spectra presented in Fig. 4c are similar to that of the $ZnFe_2O_4$ reference and are characterized by two distinct spectral features at 708.4 eV and 709.9 eV corresponding to t_2g and e_g sub-bands, respectively [46,47]. From these results, it is clear that Fe^{3+} species were successfully substituted in place of Co^{III}, and remained in the high spin 3 d^5 configuration.

According to group theory, four typical IR bands should be present for cubic II-III spinels. Two of them (ν_1 and ν_2, usually present in the MIR range) can be attributed to vibrations of octahedral units, and two others (ν_3 and ν_4, usually present in the FIR range) can be assigned to mixed octahedral and tetrahedral units within the spinels structure [48,49].

Fig. 5 illustrates the spectra within both the MIR (a) and FIR (b) spectral ranges. Multiple bands are present for all spectra below 700 cm^{-1}, including the ν_1 band (Fig. 5a) at the highest

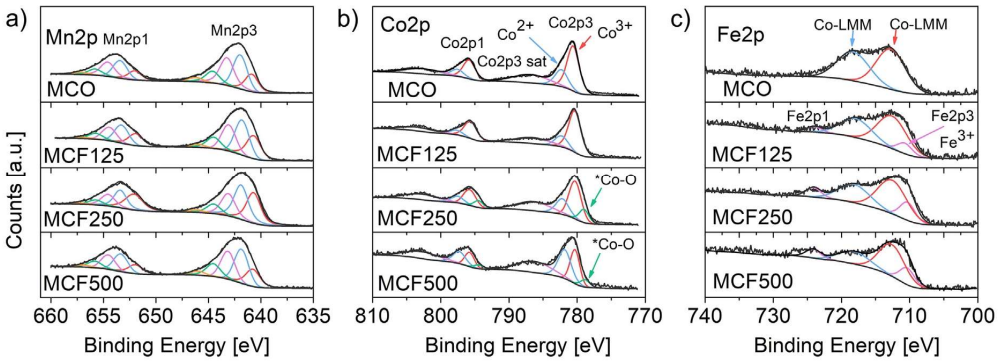

Fig. 3 – (a) Mn2p, (b) Co2p and (c) Fe2p X-ray photoelectron spectra of MCO, MCF125, MCF250, MCF500 powders.

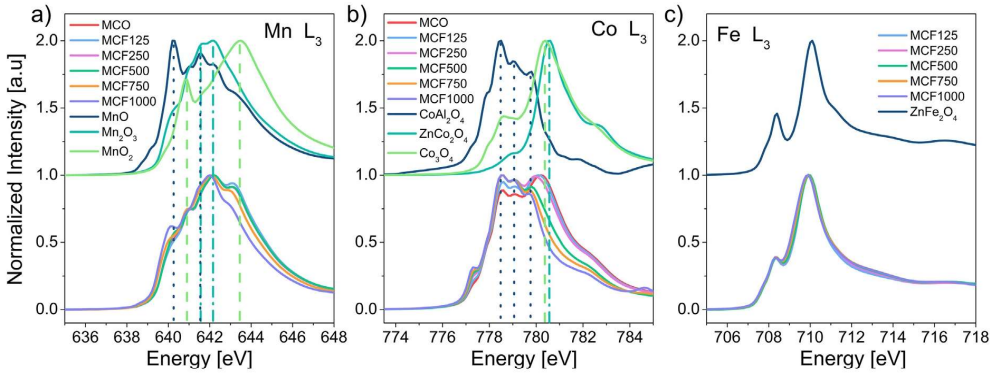

Fig. 4 – (a) Mn-L_3, (b) Co-L_3, and (c) Fe-L_3 XANES spectra of $MnCo_{2-x}Fe_xO_s$ powders and several reference materials.

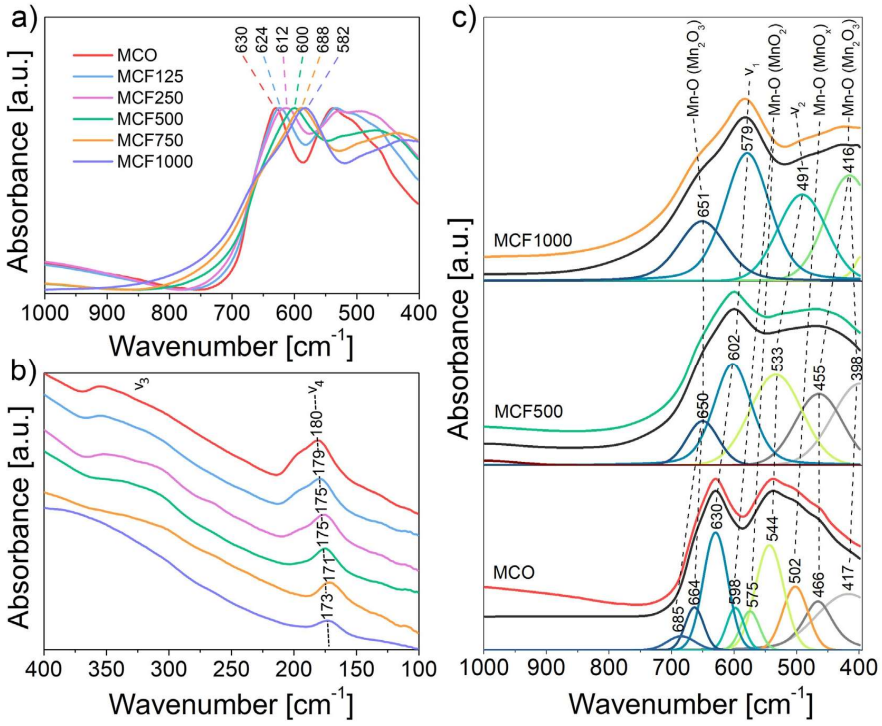

Fig. 5 – a) Middle Infrared Spectra with marked positions of spinel ν_1 band, b) Far Infrared Spectra with marked positions of spinel ν_4 band, and c) Middle Infrared Spectra after deconvolution process.

wavenumbers (630–582 cm^{-1}) and the ν_2 band which is noticeable for samples with either no (MCO) or the lowest Fe doping share (MCF125 and MCF250) in the ca. 540–530 cm^{-1} region. The higher the Fe content, the broader and less visible the ν_2 band becomes. A similar observation of the ν_2 band can be stated for the ν_3 band (Fig. 5b), which occurs at around the 360–350 cm^{-1} range. In the end, ν_4 can be found within the 180–171 cm^{-1} range [48].

The most important findings concern the shift of the ν_1 band which is responsible for structural vibrations of the condensed $Co^{3+}O_6$ octahedrons [48]. With the increasing share of introduced Fe, not only does this band shift towards lower wavenumbers, but the value of such a wavenumber shift also corresponds to the expected chemical composition. Taking the boundary examples (MCO and MCF1000) as a sort of scale, 48 cm^{-1} is the maximum shift. Then, during the first

doping (MCF125), 1/8 of the maximum doping was executed, which resulted in a shift of 6 cm^{-1}, being exactly 1/8 of 48 cm^{-1}. For the next specimens, this quantitative approach can also be applied with good accuracy (3/8 for MCF250, 5/8 for MCF500 and 7/8 for MCF750).

When it comes to qualitative interpretation, two factors have to be taken into consideration. Firstly, the broadening of bands occurred, which is due to the partial doping, hence the presence of two cations on the octahedral sites [48,49]. Secondly, based on [48], the direction of the band shift is connected with the M^{III}–O bonding force. The lower the wavenumber, the lower the bond energy. However, in this case, the simple bond energy cannot be applied as different valences and spin states should be taken into account. In Refs. [21,50], the authors used the term "covalency" estimated with the N–V parameter (N – number of the unpaired electrons for the metal cation; V – nominal valence state of the metal cation). The lower the N–V parameter (which describes the net ability of the octahedral cation to donate electrons to oxygen), the higher the covalency (in terms of dragging the electron density from oxygen towards the metal cation, thereby forming the stronger, more "covalent" bond). In the case of this work, we observe a decrease in the wavenumbers, which suggests a lower M^{III}–O bonding force expressed by the lower covalency, after the substitution of Co^{3+} cations by Fe^{3+} ones. It stays then in a good agreement with the scenario, in which the electron configuration of degenerated orbitals for Co changes towards the optimal one – assuming that the e_g electron orbital for cobalt cations after the introduction of Fe is free, the N–V parameter for Co is low (0–3 = −3 → high covalency), and for Fe is much higher (5-3 = 2 → low covalency).

In the case of the ν_2 band, also dependent on the trivalent cation nature [48], the shift towards lower wavenumbers can be seen, similar to the ν_1 band. However, all spectra have a very complicated shape in this range, therefore in the next paragraph, more details will be provided taking into account the deconvolution process. When it comes to the ν_3 and ν_4 bands, the former, responsible for complex vibrations of M^{II} and M^{III} [48], can be found along with numerous neighboring bands forming the very complicated contour of the spectrum within the 360–300 cm^{-1} range. Due to the fact that this band is the least informative about the spinels structure, spectra in the aforementioned range were not decomposed. The last evoked band (ν_4), dependent on the mass of tetrahedral cations, could be observed as well. In comparison to the previously described shift for the ν_1 band, this band changes its position in a nearly negligible way, which suggests that cobalt is being substituted by iron predominantly within the octahedral sites.

To provide more structural details, the MIR spectra for the MCO, MCF500 and MCF1000 samples were deconvoluted below 700 cm^{-1}. Fig. 5c demonstrates that apart from the previously described spinel bands, abundant modes are also contributing to the complicated contour of the spectra. Firstly, it is important to recognize that the positions for the ν_1 band are nearly the same as in the case of Fig. 5a (±3 cm^{-1}). Secondly, for the stoichiometric Mn–Co spinel, an additional four bands (598, 575, 502 and 466 cm^{-1}) assigned to MnO_2 and MnO_x oxides occurred and disappeared for the Fe-substituted specimens [51,52]. However, as such phases were not detected by the XRD method, and taking into account the much higher sensitivity and detection threshold of MIR compared to XRD, the share of Mn oxides can be treated as very small, which may actually come from some secondary phases after the synthesis. In contrast, two bands at ca. 660 and 410 cm^{-1} assigned to Mn_2O_3 [51] considerably increased in their intensities, especially for the sample with the highest share of iron, which is in good agreement with the XRD findings. The presence of Mn oxides was also revealed in the FIR range, where numerous bands attributed to the MnO_2 and MnO_x phases can usually be observed [51,52]. In this work, the clearly noticeable band at ca. 200 cm^{-1} decreased in intensity, which confirms the results described for the MIR deconvoluted spectra.

Electrocatalytic activity

The OER performance of the ball-milled catalyst powders was examined in an alkaline medium (0.1 M KOH). The electrochemical double-layer capacitance (C_{dl}) was analyzed using cyclic voltammetry to determine the electrochemically active surface area (Fig. 6a). A slight decrease of C_{dl} with Fe substitution up to x = 0.5 in the $MnCo_{2-x}Fe_xO_4$ spinels is noticeable (446 μF and 394 μF for the MCO and MCF500, respectively), whereas further iron incorporation resulted in a threefold C_{dl} decrease for the MCF1000 (146 μF). The obtained data is not consistent with the measured specific surface area. All iron-containing powders exhibited similar surface areas in the range from 22.7 to 23.9 $m^2\ g^{-1}$ indicating similar particle size distributions (further supported by the SEMobservations). This remark suggests that the number of active sites available for water oxidation decreases with the higher Fe content in the MCF spinel structure, from which it results that iron in the octahedral sites does not catalyze the oxygen evolution reaction as efficiently as cobalt.

To gain insight into the electrode reaction kinetics, electrochemical impedance spectroscopy (EIS) was performed during the OER at a fixed potential. The EIS spectra shown in Fig. 6b was fitted using Randles equivalent circuit (presented in Fig. S7) to calculate the charge transfer resistance (R_{ct}) between the catalyst and liquid junction during the electrochemical reaction. The lowest R_{ct} of 12.1 Ω was measured for the MCF500, whereas the high Fe content resulted in an increase of R_{ct} to 20.5 Ω and 39.0 Ω for the MCF750 and MCF1000, respectively. It is apparent that the partial Co substitution by Fe cations in the $MnCo_2O_4$ enhances the charge transfer kinetics (R_{ct}) by ~30%. This observation provides the basis for considering the optimally Fe-substituted $MnCo_2O_4$ as superior OER catalysts, despite the slight decrease in the number of active sites indicated by the ECSA studies (Table S4).

The oxygen evolution reaction geometric current densities of all $MnCo_{2-x}Fe_xO_4$ spinels are shown in Fig. 7a. The Glassy Carbon (GC) Rotating Disk Electrode was measured separately to exclude its possible contribution to oxygen electrocatalysis – as expected, negligible activity was observed. The OER electrocatalyst activity is typically characterized by the overpotential (η) needed to deliver the current density of 10 mA cm^{-2} (dashed horizontal line) [53]. The MCO demonstrates an overpotential of 406 mV, which can be reduced to

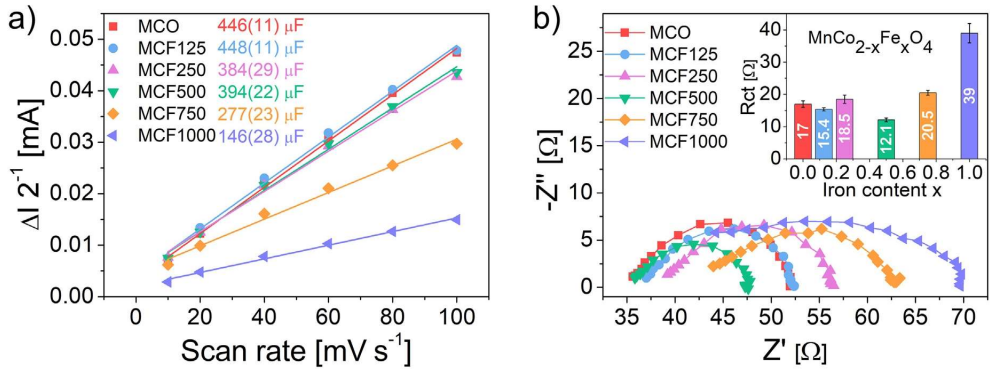

Fig. 6 – (a) Double-layer capacitance and (b) EIS Nyquist plots recorded at 1.7 V vs RHE. Inset demonstrates calculated charge transfer resistance. Electrochemical tests were performed in 0.1 M KOH electrolyte.

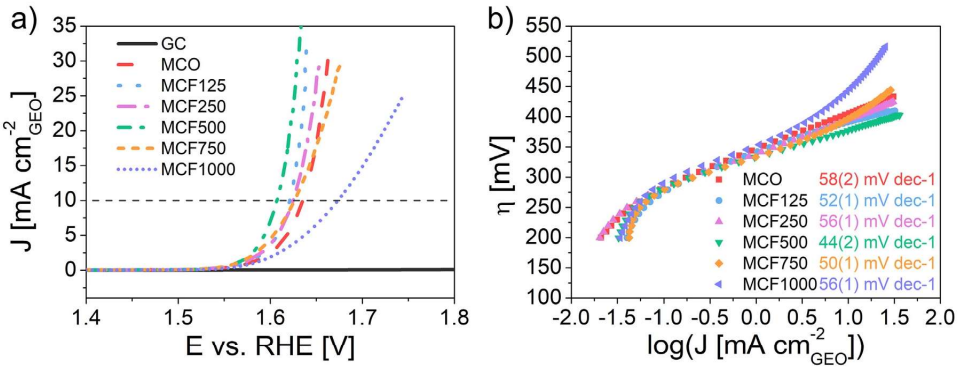

Fig. 7 – (a) Oxygen evolution polarization curves of $MnCo_{2-x}Fe_xO_4$ catalysts (b) and corresponding Tafel plots measured in O_2-saturated 0.1 M KOH at 10 mV s^{-1} with a rotation speed of 1600 rpm.

376 mV for the MCF500 by partial Fe/Co substitution in the spinel structure. Further Fe incorporation results in a sharp overpotential increase up to 447 mV for the MCF1000, implying that Fe cations are not active sites themselves, although an optimal amount can modulate the intrinsic activity of the $MnCo_2O_4$ spinel. The relationship between the octahedral occupation of Fe and OER activity can be seen in the extracted Tafel plots in Fig. 7b. The estimated Tafel slope of 44 mV dec^{-1} for the MCF500 is clearly smaller than the 58 mV dec^{-1} for the MCO, implying faster reaction kinetics. The Tafel slopes of the MCF750 and MCF1000 seem to be reduced if compared with the MCO and, from this standpoint, could be considered as more catalytically active, which does not agree with the calculated overpotentials. The explanation for that is the change of the Tafel slope of those two materials at higher overpotentials, i.e. 110 mV dec^{-1} and 180 mV dec^{-1} for the MCF750 and MCF1000, respectively. This observation indicates a possible change in the OER rate-determining step when Fe occupies more than 25% of the available octahedral sites. The lowest Tafel slope of the MCF500 suggests that the rate-determining step is at the ending part of the multiple-electron transfer oxygen evolution reaction, and it is an indicator of a promising electrocatalyst [54]. Huang et al. reported a similar 45 mV dec^{-1} Tafel slope using an advanced 2D Fe/Co oxide heterostructure. A lower Tafel slope than for single metal 2D structures (67 and 79 mV dec^{-1} for Co(oxides) nanosheets and Fe (oxides) nanochains, respectively) was attributed to the switch of the rate-determining step for OER. The authors propose the switch from $MOH_{ad} + OH^- \rightarrow MO^- + H_2O$ to the electron-proton reaction of $MOH_{ad} + OH^- \rightarrow MO + H_2O + e^-$ rate-determining step [55].

Further, the measured polarization curves have been normalized using the BET-specific surface area (Table S2) to exclude the surface area effect and to gain insight into the specific activity of the prepared catalysts. Due to the comparable specific area, the overall trend of increasing activity with moderate Fe substitution in $MnCo_{2-x}Fe_xO_4$ is unchanged, as is shown in Fig. 8a.

The reference $MnCo_2O_4$ cation distribution was based on Bordeneuve's report and established as $Co^{2+}_{0.965}Mn^{2+}_{0.035}[Mn^{3+}_{0.78}Mn^{4+}_{0.21}Co^{2+}_{0.21}Co^{III}_{0.8}]$, where Co^{III} means that trivalent cobalt ions are of low spin (LS, $t_{2g}^6e_g^0$) [44]. As is

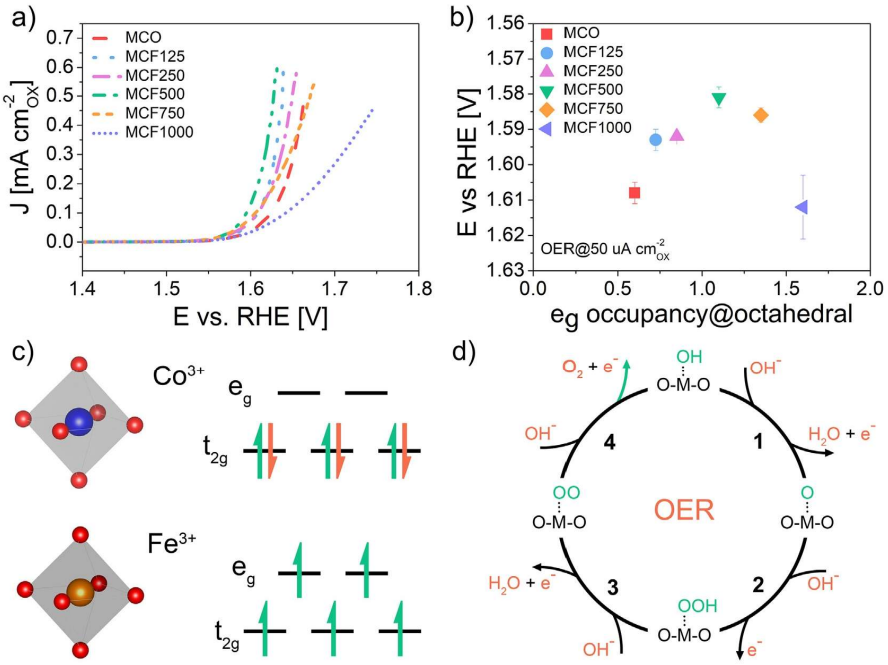

Fig. 8 – (a) Oxygen evolution polarization curves with current normalized by BET surface area, (b) correlation between OER potentials at 50 μA cm$^{-2}_{ox}$ and e_g occupancy at the octahedral site in $MnCo_{2-x}Fe_xO_4$, (c) e_g/t_{2g} electron assignment for Co and Fe octahedrally coordinated cations, and (d) proposed four-electron/proton-coupled oxygen evolution mechanism.

presented in Fig. 1a, iron (as Fe^{3+}) is considered to replace Co^{III} in octahedral sites [56]. This hypothesis was further confirmed by the XANES studies described in the previous part of the article and coincides well with Kim et al. who indicated, by first principle calculations, that in the $MnCoFeO_4$ spinel Co preferentially occupies tetrahedral while Mn and Fe octahedral sites [24].

To understand the possible origin of the enhanced activity, the activity descriptor based on the e_g occupancy at the octahedral sites in the spinel structure was adopted. The e_g filling of the 3d electron of the surface transition metal cations influencing the binding of OER intermediates to the perovskite oxide surface was proposed by Suntivich et al. and has proven to be a reliable perovskite OER activity descriptor [57–59]. The e_g orbital has a stronger spatial overlap with the oxygen-related adsorbate than the t_{2g} orbital; consequently, the electron transfer between the surface cation and adsorbed intermediate may be more directly promoted by the e_g orbital. Likewise, the e_g occupancy of the active site was proposed to be the activity descriptor for spinels [19,38,60]. Fig. 8b presents the e_g/t_{2g} electron assignment for Co and Fe octahedrally coordinated cations. The incorporation of octahedrally coordinated Fe cations ($t_{2g}^3e_g^2$) increases the overall number of e_g occupancy in the $MnCo_{2-x}Fe_xO_4$ spinel. As depicted in Fig. 8b, the potential required to maintain the current density of 50 μA cm$^{-2}_{OX}$ decreases with the e_g occupancy increase up to 1.1 for the MCF500. The observed volcano plot with the inflection point around unity points to the proposed four-electron/proton-coupled oxygen evolution mechanism presented in Fig. 8d. If the e_g occupancy is less than unity, the deprotonation of the oxyhydroxide group during step 3 (M^{m+}-$OOH^- + OH^- \rightarrow M^{(m+1)+}$-$O_2^{2-} + H_2O + e^-$) might be limited. On the contrary, too many electrons in e_g orbitals limits the formation of the O–O bond in the OOH adsorbate during step 2 ($M^{(m+1)+}$-$O^{2-} + OH^- \rightarrow M^{m+}$-$OOH^- + e^-$).

For comparison of our results with other literature reports, the OER performance data for recently studied spinel-based electrocatalysts is summarized in Table S5. After Fe incorporation into the $MnCo_2O_4$, the OER overpotential is reduced from 510 mV, as obtained by Menezes et al. for $MnCo_2O_4$ microspheres or from 406 mV for the $MnCo_2O_4$ powder examined in this study to 376 mV for $MnCo_{1.5}Fe_{0.5}O_4$ [61]. Moreover, $MnCo_{1.5}Fe_{0.5}O_4$ exhibits a distinctively low Tafel slope of 44 mV dec^{-1} if compared to 75 mV dec^{-1} for Te–Co_3O_4 or 58 mV dec^{-1} for $MnCo_2O_4$ [62].

A similar substitution with the Fe effect was observed by Zhou et al. in a series of $ZnFe_xCo_{2-x}O_4$ oxides [21]. Up to x = 0.4, the OER-specific activity increase was observed, followed by a systematic decrease to x = 2.0, creating a volcano-type dependency with respect to the amount of Fe substitution. The authors concluded that the origin of the observed phenomenon is related to the optimal active cation to oxygen covalency, in this case Co–O covalency, as predicted by the *N–V* parameter. Wei et al. investigated $MnCo_2O_4$ cubic

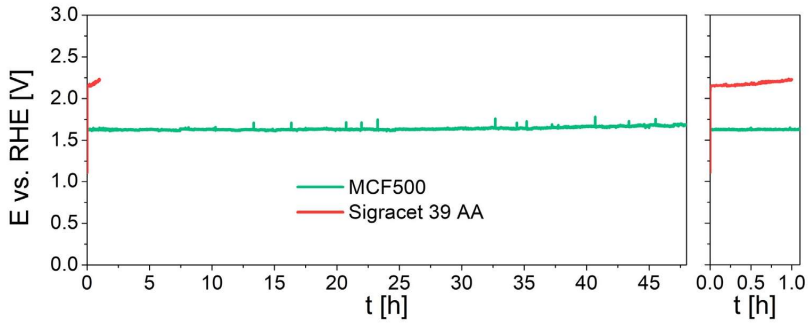

Fig. 9 – Chronopotentiometric durability test at 10 mA cm^{-2}

spinels synthesized by a solid-state chemistry method at different temperatures (150–900 °C) [19]. Varying heat treatment-induced changes in the Mn valence state. Knowing the valences and cation distribution quantified by EXAFS, the authors were able to estimate the e_g/t_{2g} assignment of the more active cation in the octahedrally coordinated sites, which correlated well with the spinels' OER activity, confirming the applicability of the e_g occupancy descriptor. Likewise, this descriptor is suitable to elucidate the enhanced activity of $MnCo_{2-x}Fe_xO_4$ with moderate Fe substitution.

The long-term electrolyzer stability test of $MnCo_{1.5}Fe_{0.5}O_4$ was performed at a current density of 10 mA cm^{-2} for 48 h (Fig. 9). During the test, the catalyst-coated electrode exhibited great stability up to 30 h, and then a slight (4%) increase in voltage was observed. We assume that the performance decrease is related to the degradation of supporting carbon paper. As is shown the test of pure Sigracet carbon paper ended rapidly after 1 h with degradation of the electrode (Fig. S8). Similar but slower and less pronounced degradation of catalyst-coated electrode was observed for $MnCo_{1.5}Fe_{0.5}O_4$ (Fig. S9).

Conclusions

The present research examined the effect of Fe ions at octahedral sites in $MnCo_2O_4$ spinel on the physicochemical properties and electrochemical activity. Spectroscopic studies (XAS and FTIR) confirmed the successful substitution of Co ions by Fe ions in octahedrally coordinated positions in $MnCo_{2-x}Fe_xO_4$ spinel powders synthesized using an EDTA-CA sol-gel method.

This study found that moderate Fe incorporation in $MnCo_2O_4$ spinel enhances the catalytic activity towards OER by lowering the charge transfer resistance and moderating the influence of the rate-determining steps during the oxidation cycle. We found that an optimal amount of incorporated Fe into the octahedral sites improves the OER performance by the 30 mV decrease of overpotential needed to achieve a 10 mA cm$^{-2}_{GEO}$ current density compared to the benchmark $MnCo_2O_4$. Tafel slope analysis indicates the possible change of the OER rate-determining step when Fe occupies more than 25% of the available octahedral sites. The OER-specific activity exhibits a volcano-type shape as a function of the e_g occupancy at octahedral sites. Overall, this work supports the idea that e_g occupancy at octahedral sites can be used as the activity descriptor for spinels. The strategy of tuning the optimal e_g configurations by transition metal substitution in the spinel's octahedral sites is a promising tool for the design of superior OER catalysts.

Declaration of competing interest

The authors declare that they have no known competing financial interests or personal relationships that could have appeared to influence the work reported in this paper.

Acknowledgments

The presented research is part of the "Nanocrystalline ceramic materials for efficient electrochemical energy conversion" project, carried out within the First TEAM programme of the Foundation for Polish Science (grant agreement nr. POIR.04.04.00-00-42E9/17-00), co-financed by the European Union under the European Regional Development Fund. Funding from Statutory Funds of WETI PG is also acknowledged.

Appendix A. Supplementary data

Supplementary data to this article can be found online at https://doi.org/10.1016/j.ijhydene.2022.12.013.

REFERENCES

[1] Farrukh S, Fan X, Mustafa K, Hussain A, Ayoub M, Younas M. Nanotechnology and the generation of sustainable hydrogen. 2021.

[2] Platzer MF, Sarigul-Klijn N. Conversion of hydrogen to electricity. Green energy sh. Concept renew. Energy from wind over water. Cham: Springer International Publishing; 2021. p. 99–101. https://doi.org/10.1007/978-3-030-58244-9_24.

[3] Klingmann J, Andersson M. Hydrogen and hydrogen-rich fuels: production and conversion to electricity. In: Gupta AK, De A, Aggarwal SK, Kushari A, Runchal A, editors. Innov. Sustain. Energy clean. Environ. Singapore: Springer Singapore; 2020. p. 219–33. https://doi.org/10.1007/978-981-13-9012-8_10.
[4] Fabbri E, Habereder A, Waltar K, Kötz R, Schmidt TJ. Developments and perspectives of oxide-based catalysts for the oxygen evolution reaction. Catal Sci Technol 2014;4:3800–21. https://doi.org/10.1039/c4cy00669k.
[5] Liu L, Xiao Y. Theoretical exploration electrocatalytic active of spinel M2CoO4 (M = Co, Fe and Ni) as efficient catalyst for water splitting. Comput Mater Sci 2021;187:110082. https://doi.org/10.1016/j.commatsci.2020.110082.
[6] Du J, Qian Y, Wang L, Yang H, Kang DJ. Facile synthesis of copper sulfides on copper foam as an efficient electrocatalyst for oxygen evolution reaction. Mater Today Commun 2020;25:101585. https://doi.org/10.1016/j.mtcomm.2020.101585.
[7] Li M, Wang L, Qian Y, Du J. Facile synthesis of MoS2/CuS nanoflakes as high performance electrocatalysts for hydrogen evolution reaction. Int J Hydrogen Energy 2022;47:5319–25. https://doi.org/10.1016/j.ijhydene.2021.11.182.
[8] Chen C, Tuo Y, Lu Q, Lu H, Zhang S, Zhou Y, et al. Hierarchical trimetallic Co-Ni-Fe oxides derived from core-shell structured metal-organic frameworks for highly efficient oxygen evolution reaction. Appl Catal B Environ 2021;287:119953. https://doi.org/10.1016/j.apcatb.2021.119953.
[9] Gonçalves JM, Silva MNT, Naik KK, Martins PR, Rocha DP, Nossol E, et al. Multifunctional spinel MnCo2O4based materials for energy storage and conversion: a review on emerging trends, recent developments and future perspectives. J Mater Chem 2021;9:3095–124. https://doi.org/10.1039/d0ta11129e.
[10] O'Neill HSC, Navrotsky A. Simple spinels: crystallographic parameters, cation radii, lattice energies, and cation distribution. Am Mineral 1983;68:181–94.
[11] Saito T. Chemistry of transition metals. Introd Chem Ser 1996:110–53.
[12] Yunasfi Mulyawan A, Mashadi Suyanti, Ari Adi W. Synthesis of NiCe Fe(2-)O4 (0 ≤ x ≤ 0.05) as microwave absorbing materials via solid-state reaction method. J Magn Magn Mater 2021;532:167985. https://doi.org/10.1016/j.jmmm.2021.167985.
[13] Xuan S, Wang X, Tian Y, Hao J. Properties of magnesium-aluminate spinel derived from bauxite and magnesia. Int J Appl Ceram Technol 2021:1–8. https://doi.org/10.1111/ijac.13740.
[14] Li C, Han X, Cheng F, Hu Y, Chen C, Chen J. Phase and composition controllable synthesis of cobalt manganese spinel nanoparticles towards efficient oxygen electrocatalysis. Nat Commun 2015;6:1–8. https://doi.org/10.1038/ncomms8345.
[15] Paul B, Bhanja P, Sharma S, Yamauchi Y, Alothman ZA, Wang ZL, et al. Morphologically controlled cobalt oxide nanoparticles for efficient oxygen evolution reaction. J Colloid Interface Sci 2021;582:322–32. https://doi.org/10.1016/j.jcis.2020.08.029.
[16] Waqas M, El Kasmi A, Wang Y, Mountapmbeme Kouotou P, Tian ZY. CVD synthesis of Cu-doped cobalt spinel thin film catalysts for kinetic study of propene oxidation. Colloids Surfaces A Physicochem Eng Asp 2018;556:195–200. https://doi.org/10.1016/j.colsurfa.2018.08.006.
[17] El Kasmi A, Waqas M, Mountapmbeme Koutou P, Tian Z. Cu-promoted cobalt oxide film catalyst for efficient gas emissions abatement. J Therm Sci 2018;28:225–31. https://doi.org/10.1007/s11630-019-1093-9.
[18] Sheil R, Butts D, Jungjohann K, Yoo J, Dunn B, Chang JP. Plasma enhanced atomic layer deposition of thin film Li 1+x Mn 2−x O 4 for realization of all solid-state 3D lithium-ion microbatteries. J Vac Sci Technol, A 2021;39:012408. https://doi.org/10.1116/6.0000644.
[19] Wei C, Feng Z, Scherer GG, Barber J, Shao-Horn Y, Xu ZJ. Cations in octahedral sites: a descriptor for oxygen electrocatalysis on transition-metal spinels. Adv Mater 2017;29:1–8. https://doi.org/10.1002/adma.201606800.
[20] Wang W, Kuai L, Cao W, Huttula M, Ollikkala S, Ahopelto T, et al. Mass-production of mesoporous MnCo2O4 spinels with manganese(IV)- and cobalt(II)-Rich surfaces for superior bifunctional oxygen electrocatalysis. Angew Chem Int Ed 2017;56:14977–81. https://doi.org/10.1002/anie.201708765.
[21] Zhou Y, Sun S, Song J, Xi S, Chen B, Du Y, et al. Enlarged CoO covalency in octahedral sites leading to highly efficient spinel oxides for oxygen evolution reaction. Adv Mater 2018;30:1–7. https://doi.org/10.1002/adma.201802912.
[22] Liu Y, Fergus JW, Wang K, Dela Cruz C. Crystal structure, chemical stabilities and electrical conductivity of Fe-doped manganese cobalt spinel oxides for SOFC interconnect coatings. J Electrochem Soc 2013;160:F1316–21. https://doi.org/10.1149/2.114311jes.
[23] Elkholy AE, El-Taib Heakal F, Allam NK. Nanostructured spinel manganese cobalt ferrite for high-performance supercapacitors. RSC Adv 2017;7:51888–95. https://doi.org/10.1039/c7ra11020k.
[24] Kim H, Seo DH, Kim H, Park I, Hong J, Park KY, et al. Multicomponent effects on the crystal structures and electrochemical properties of spinel-structured M 3O 4 (M = Fe, Mn, Co) anodes in lithium rechargeable batteries. Chem Mater 2012;24:720–5. https://doi.org/10.1021/cm2036794.
[25] Lankauf K, Cysewska K, Karczewski J, Mielewczyk-Gryń A, Górnicka K, Cempura G, et al. MnxCo3-xO4 spinel oxides as efficient oxygen evolution reaction catalysts in alkaline media. Int J Hydrogen Energy 2020;5. https://doi.org/10.1016/j.ijhydene.2020.03.188.
[26] Rodriguez-Carvajal J. Recent advances in magnetic structure determination by neutron powder diffraction. Phys Bull 1993;55–69. https://doi.org/doi.org/10.1016/0921-4526(93)90108-I.
[27] Toby BH, Von Dreele RB. GSAS-II: the genesis of a modern open-source all purpose crystallography software package. J Appl Crystallogr 2013;46:544–9. https://doi.org/10.1107/S0021889813003531.
[28] Meena PL, Kumar R, Sreenivas K. Rietveld refinement and spectroscopic analysis of Co3-xMnxO4 (0.1≤ x≤ 1.0) ceramic compositions. Int J Phys Chem Math Sci 2014;3:7.
[29] König U, Chol G. Röntgenbeugungs- und Neutronenbeugungsuntersuchungen an Ferriten der reihe MnxZn1−xFe2O4. J Appl Crystallogr 1968;1:124–6. https://doi.org/10.1107/s0021889868005145.
[30] Madej E, Pitala K, Kozio A, Sikora M, Spiridis N, Sl T, et al. B the first experimental results from the 04BM (PEEM/XAS) beamline at Solaris. Nucl Instrum Methods Phys Res 2021;492:43–8.
[31] Handke M, Mozgawa W, Nocuń M. Specific features of the IR spectra of silicate glasses. J Mol Struct 1994;325:129–36. https://doi.org/https://doi.org/10.1016/0022-2860(94)80028-6.
[32] Lankauf K, Mroziński A, Błaszczak P, Górnicka K, Ignaczak J, Łapiński M, et al. The effect of Fe on chemical stability and oxygen evolution performance of high surface area SrTix-1FexO3-δ mixed ionic-electronic conductors in alkaline media. Int J Hydrogen Energy 2021;46:28575–90. https://doi.org/https://doi.org/10.1016/j.ijhydene.2021.06.088.

[33] McCrory CCL, Jung S, Peters JC, Jaramillo TF. Benchmarking heterogeneous electrocatalysts for the oxygen evolution reaction. J Am Chem Soc 2013;135:16977–87. https://doi.org/10.1021/ja407115p.
[34] Wei C, Rao RR, Peng J, Huang B, Stephens IEL, Risch M, et al. Recommended practices and benchmark activity for hydrogen and oxygen electrocatalysis in water splitting and fuel cells. Adv Mater 2019;1806296:1–24. https://doi.org/10.1002/adma.201806296.
[35] Niu S, Li S, Du Y, Han X, Xu P. How to reliably report the overpotential of an electrocatalyst. ACS Energy Lett 2020;5:1083–7. https://doi.org/10.1021/acsenergylett.0c00321.
[36] Purwanto A, Fajar A, Mugirahardjo H, Fergus JW, Wang K. Cation distribution in spinel (Mn,Co,Cr)3O4 at room temperature. J Appl Crystallogr 2010;43:394–400. https://doi.org/10.1107/S0021889810008150.
[37] Biesinger MC, Payne BP, Grosvenor AP, Lau LWM, Gerson AR, Smart RSC. Resolving surface chemical states in XPS analysis of first row transition metals, oxides and hydroxides: Cr, Mn, Fe, Co and Ni. Appl Surf Sci 2011;257:2717–30. https://doi.org/10.1016/j.apsusc.2010.10.051.
[38] Gao X, Liu J, Sun Y, Wang X, Geng Z, Shi F, et al. Optimized Co2+(Td)-O-Fe3+(Oh) electronic states in a spinel electrocatalyst for highly efficient oxygen evolution reaction performance. Inorg Chem Front 2019;6:3295–301. https://doi.org/10.1039/c9qi00852g.
[39] Mountapmbeme Kouotou P, Vieker H, Tian ZY, Tchoua Ngamou PH, El Kasmi A, Beyer A, et al. Structure-activity relation of spinel-type Co-Fe oxides for low-temperature CO oxidation. Catal Sci Technol 2014;4:3359–67. https://doi.org/10.1039/c4cy00463a.
[40] Nikolic MV, Vasiljevic ZZ, Lukovic MD, Pavlovic VP, Krstic JB, Vujancevic J, et al. Investigation of ZnFe 2 O 4 spinel ferrite nanocrystalline screen-printed thick films for application in humidity sensing. Int J Appl Ceram Technol 2019;16:981–93. https://doi.org/10.1111/ijac.13190.
[41] Yu F, Yang J, Ma J, Du J, Zhou Y. Preparation of nanosized CoAl2O4 powders by sol-gel and sol-gel-hydrothermal methods. J Alloys Compd 2009;468:443–6. https://doi.org/10.1016/j.jallcom.2008.01.018.
[42] Kim TW, Woo MA, Regis M, Choi KS. Electrochemical synthesis of spinel type ZnCo2O4 electrodes for use as oxygen evolution reaction catalysts. J Phys Chem Lett 2014;5:2370–4. https://doi.org/10.1021/jz501077u.
[43] Wang HY, Hung SF, Chen HY, Chan TS, Chen HM, Liu B. In operando identification of geometrical-site-dependent water oxidation activity of spinel Co3O4. J Am Chem Soc 2016;138:36–9. https://doi.org/10.1021/jacs.5b10525.
[44] Bordeneuve H, Tenailleau C, Guillemet-Fritsch S, Smith R, Suard E, Rousset A. Structural variations and cation distributions in Mn3-xCoxO4 ($0 \leq x \leq 3$) dense ceramics using neutron diffraction data. Solid State Sci 2010;12:379–86. https://doi.org/10.1016/j.solidstatesciences.2009.11.018.
[45] Istomin SY, Tyablikov OA, Kazakov SM, Antipov EV, Kurbakov AI, Tsirlin AA, et al. An unusual high-spin ground state of Co3+ in octahedral coordination in brownmillerite-type cobalt oxide. Dalton Trans 2015;44:10708–13. https://doi.org/10.1039/c4dt03670k.
[46] Singh JP, Kaur B, Sharma A, Kim SH, Gautam S, Srivastava RC, et al. Mechanistic insights into the interaction between energetic oxygen ions and nanosized ZnFe2O4: XAS-XMCD investigations. Phys Chem Chem Phys 2018;20:12084–96. https://doi.org/10.1039/c8cp00368h.
[47] Kumar S, Kim YJ, Koo BH, Sharma SK, Vargas JM, Knobel M, et al. Structural and magnetic properties of chemically synthesized Fe doped ZnO. J Appl Phys 2009;105:1–4. https://doi.org/10.1063/1.3073933.
[48] Preudhomme J, Tarte P. Infrared studies of spinels—III: the normal II–III spinels. Spectrochim Acta Part A Mol Spectrosc 1971;27:1817–35. https://doi.org/https://doi.org/10.1016/0584-8539(71)80235-0.
[49] Basak D, Ghose J. Infrared studies on some substituted copper chromite spinels. Spectrochim Acta Part A Mol Spectrosc 1994;50:713–8. https://doi.org/https://doi.org/10.1016/0584-8539(94)80008-1.
[50] Rong X, Parolin J, Kolpak AM. A fundamental relationship between reaction mechanism and stability in metal oxide catalysts for oxygen evolution. ACS Catal 2016;6:1153–8. https://doi.org/10.1021/acscatal.5b02432.
[51] Julien CM, Massot M, Poinsignon C. Lattice vibrations of manganese oxides: Part I. Periodic structures. Spectrochim Acta Part A Mol Biomol Spectrosc 2004;60:689–700. https://doi.org/10.1016/S1386-1425(03)00279-8.
[52] Parikh SJ, Chorover J. FTIR spectroscopic study of biogenic Mn-oxide formation by Pseudomonas putida GB-1. Geomicrobiol J 2005;22:207–18. https://doi.org/10.1080/01490450590947724.
[53] McCrory CCL, Jung S, Ferrer IM, Chatman SM, Peters JC, Jaramillo TF. Benchmarking hydrogen evolving reaction and oxygen evolving reaction electrocatalysts for solar water splitting devices. J Am Chem Soc 2015;137:4347–57. https://doi.org/10.1021/ja510442p.
[54] Suen NT, Hung SF, Quan Q, Zhang N, Xu YJ, Chen HM. Electrocatalysis for the oxygen evolution reaction: recent development and future perspectives. Chem Soc Rev 2017;46:337–65. https://doi.org/10.1039/c6cs00328a.
[55] Huang Y, Yang R, Anandhababu G, Xie J, Lv J, Zhao X, et al. Cobalt/Iron(Oxides) heterostructures for efficient oxygen evolution and benzyl alcohol oxidation reactions. ACS Energy Lett 2018;3:1854–60. https://doi.org/10.1021/acsenergylett.8b01071.
[56] Talic B, Hendriksen PV, Wiik K, Lein HL. Thermal expansion and electrical conductivity of Fe and Cu doped MnCo2O4 spinel. Solid State Ionics 2018;326:90–9. https://doi.org/10.1016/j.ssi.2018.09.018.
[57] Suntivich J, May KJ, Gasteiger HA, Goodenough JB, Shao-Horn Y. A perovskite oxide optimized for oxygen evolution catalysis from molecular orbital principles. Science 2011;334(80):1383–5. https://doi.org/10.1126/science.1212858.
[58] Han B, Risch M, Lee YL, Ling C, Jia H, Shao-Horn Y. Activity and stability trends of perovskite oxides for oxygen evolution catalysis at neutral pH. Phys Chem Chem Phys 2015;17:22576–80. https://doi.org/10.1039/c5cp04248h.
[59] Zhou S, Miao X, Zhao X, Ma C, Qiu Y, Hu Z, et al. Engineering electrocatalytic activity in nanosized perovskite cobaltite through surface spin-state transition. Nat Commun 2016;7:1–7. https://doi.org/10.1038/ncomms11510.
[60] Liu Y, Ying Y, Fei L, Liu Y, Hu Q, Zhang G, et al. Valence engineering via selective atomic substitution on tetrahedral sites in spinel oxide for highly enhanced oxygen evolution catalysis. J Am Chem Soc 2020;141:8136–45. https://doi.org/10.1021/jacs.8b13701.
[61] Menezes PW, Indra A, Sahraie NR, Bergmann A, Strasser P, Driess M. Cobalt-manganese-based spinels as multifunctional materials that unify catalytic water oxidation and oxygen reduction reactions. ChemSusChem 2015;8:164–7. https://doi.org/10.1002/cssc.201402699.
[62] Harada M, Kotegawa F, Kuwa M. Structural changes of spinel MCo2O4(M = Mn, Fe, Co, Ni, and Zn) electrocatalysts during the oxygen evolution reaction investigated by in situ X-ray absorption spectroscopy. ACS Appl Energy Mater 2022;5:278–94. https://doi.org/10.1021/acsaem.1c02824.

Supporting Information

Tuning of e_g electron occupancy of $MnCo_2O_4$ spinel for oxygen evolution reaction by partial substitution of Co by Fe at octahedral sites

Krystian Lankauf[*†], Karolina Górnicka[‡], Patryk Błaszczak[‡], Jakub Karczewski[‡], Jacek Ryl[‡], Grzegorz Cempura[§], Marcin Zając[#], Maciej Bik[₸], Maciej Sitarz[₸], Piotr Jasiński[†], Sebastian Molin[†]*

[†]Advanced Materials Center, Faculty of Electronics, Telecommunications and Informatics, Gdańsk University of Technology, ul. G. Narutowicza 11/12, 80-233 Gdańsk, Poland

[‡]Advanced Materials Center, Faculty of Applied Physics and Mathematics, Gdańsk University of Technology, ul. G. Narutowicza 11/12, 80-233 Gdańsk, Poland

[§]Faculty of Metals Engineering and Industrial Computer Science, Centre of Electron Microscopy for Materials Science, AGH University of Science and Technology, al. A. Mickiewicza 30, 30-059 Kraków, Poland

[#]National Synchrotron Radiation Centre Solaris, Jagiellonian University, 30-392 Kraków, ul. Czerwone Maki 98 Poland

[₸]AGH University of Science and Technology, Faculty of Materials Science and Ceramics, al. Mickiewicza 30, 30-059 Kraków, Poland

**e-mail: krystian.lankauf@pg.edu.pl*

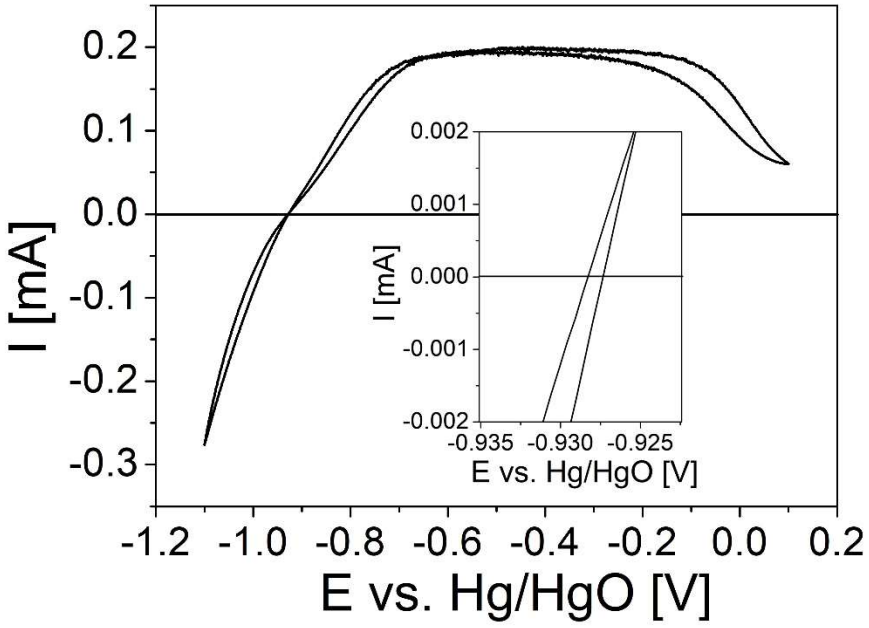

Figure S1. Calibration of Hg/HgO electrode against RHE in H2 saturated 0.1 M KOH electrolyte.

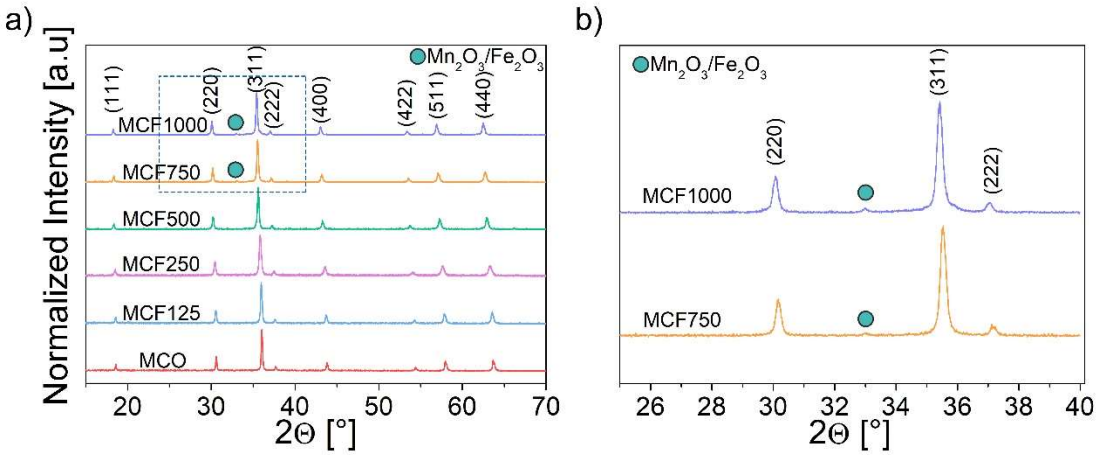

Figure S2. pXRD patterns of a) $MnCo_{2-x}Fe_xO_4$ spinel powders calcined at 800 °C and b) zoom-in of the MCF750 and MCF1000 patterns showing the existence of additional phase contributed to Mn and Fe oxides.

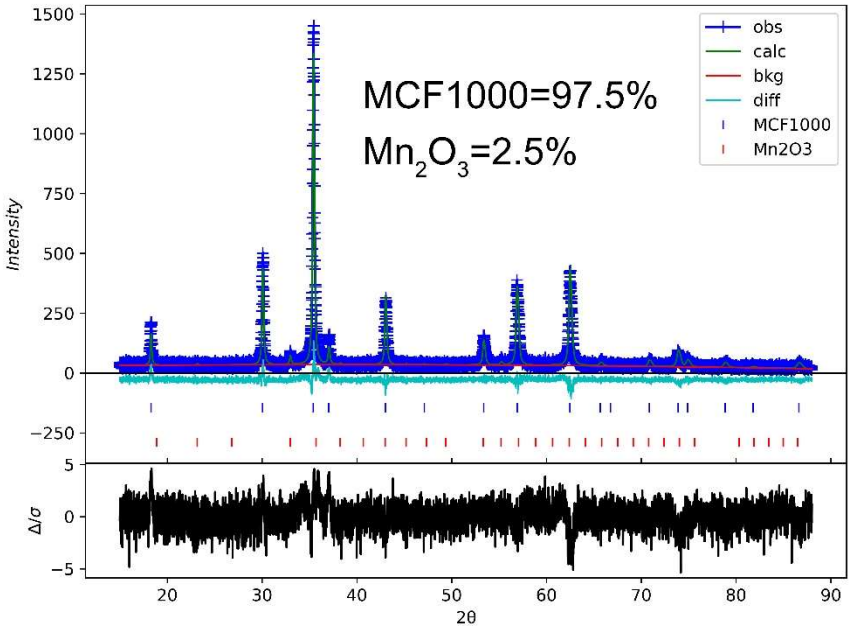

Figure S3. Rietveld refinement plots for pXRD histogram of non-milled MCF1000.

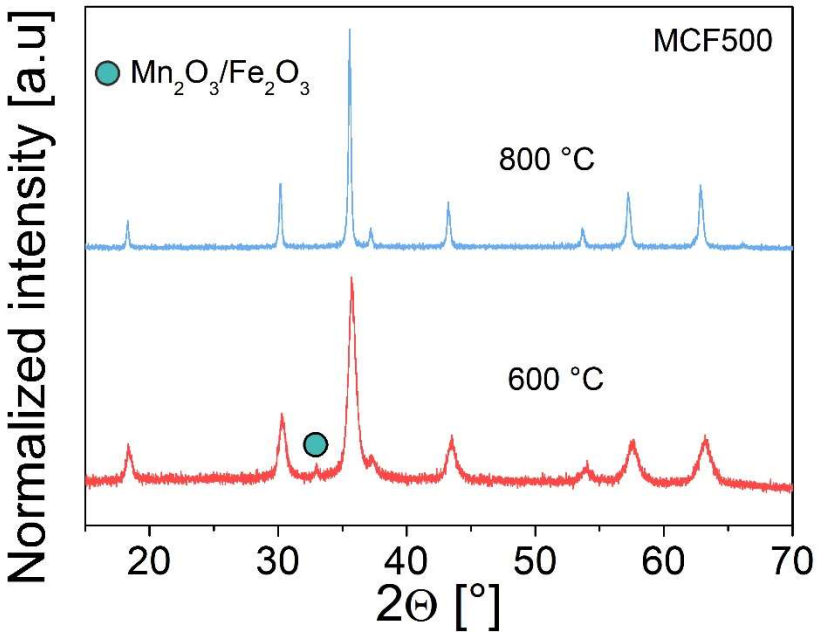

Figure S4. pXRD patterns of $MnCo_{1.5}Fe_{0.5}O_4$ spinel powders calcined at 600 and 800 °C.

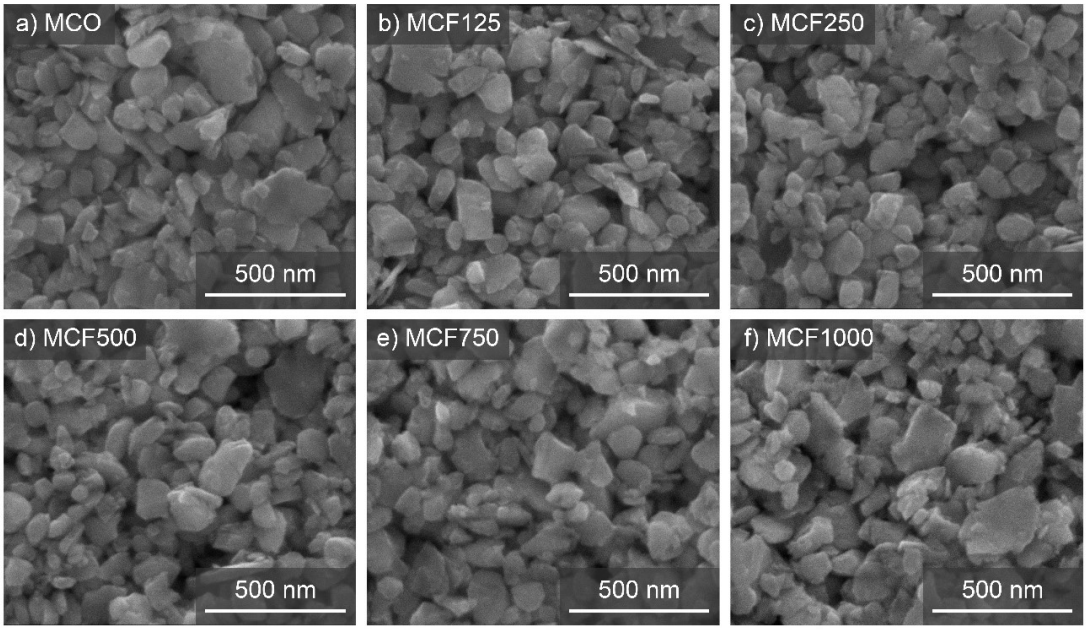

Figure S5. SEM images (x100 000 magnification) of synthesized and ball milled powders (a) MCO, (b) MCF125, (c) MCF250, (d) MCF500, (e) MCF750, and (f) MCF1000.

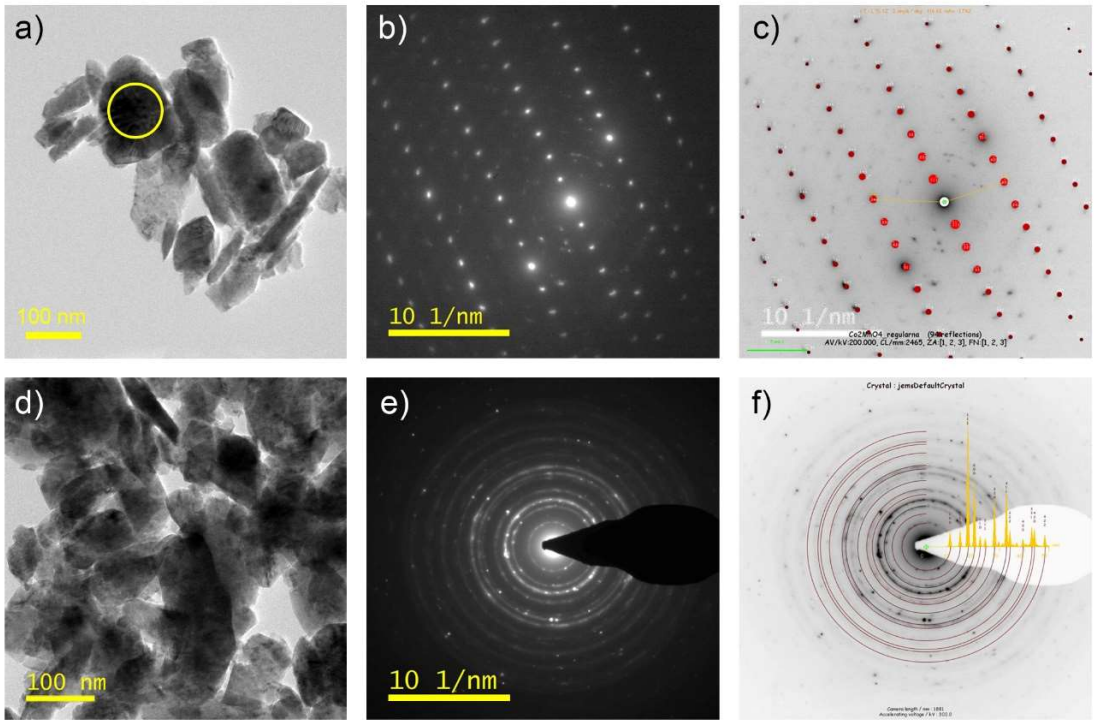

Figure S6. (a) BF-TEM image, (b) SAED pattern over one grain (c) with simulated theoretical pattern. (d) BF-(S)TEM image with (e) corresponding SAED pattern with (f) superimposed simulated theoretical pattern of the MCF500.

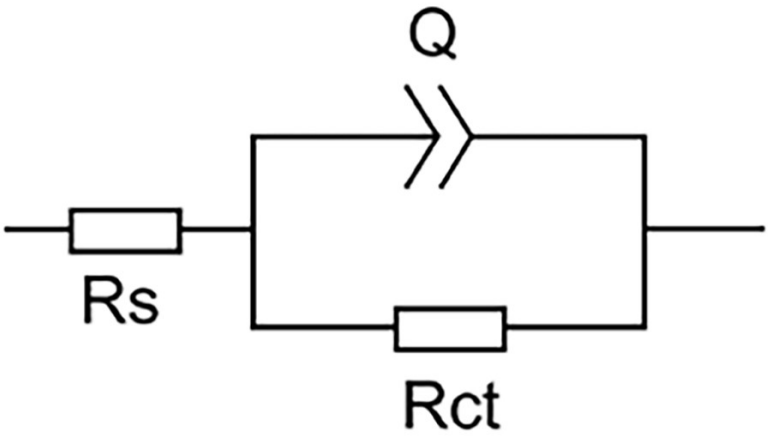

Figure S7. Randles equivalent circuit.

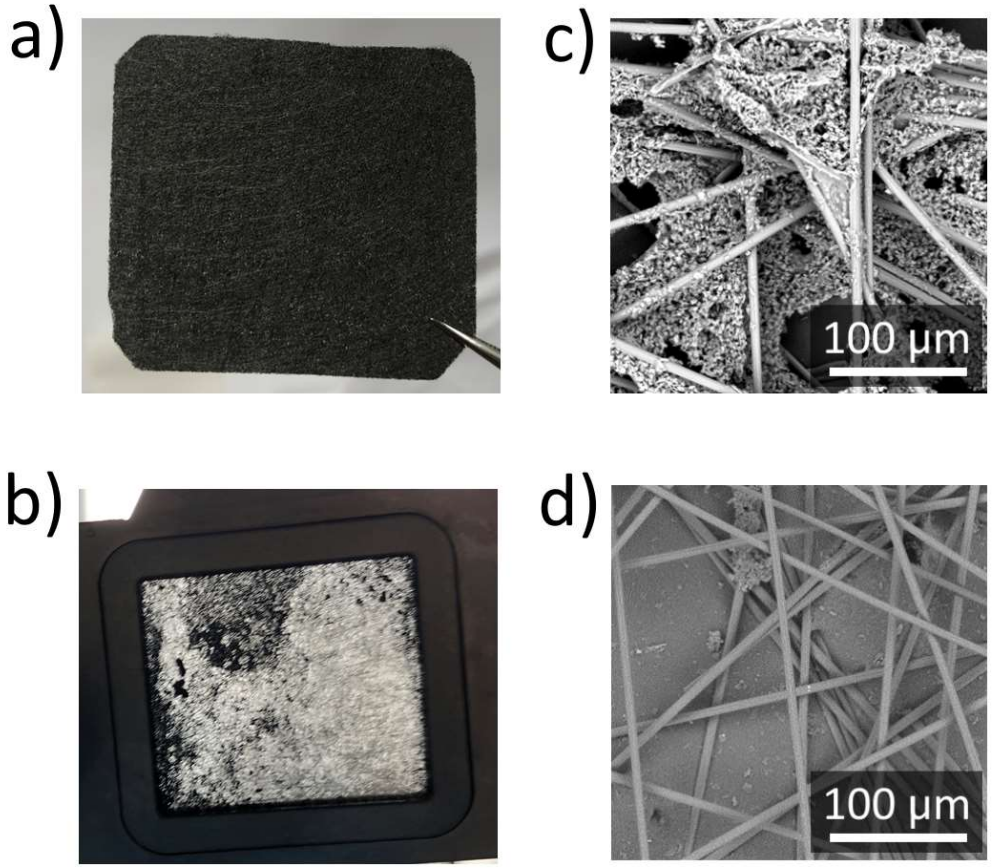

Figure S8. Pure Sigracet 39 AA carbon paper electrode (a, c) before and (b, d) after the chronopotentiometry durability test.

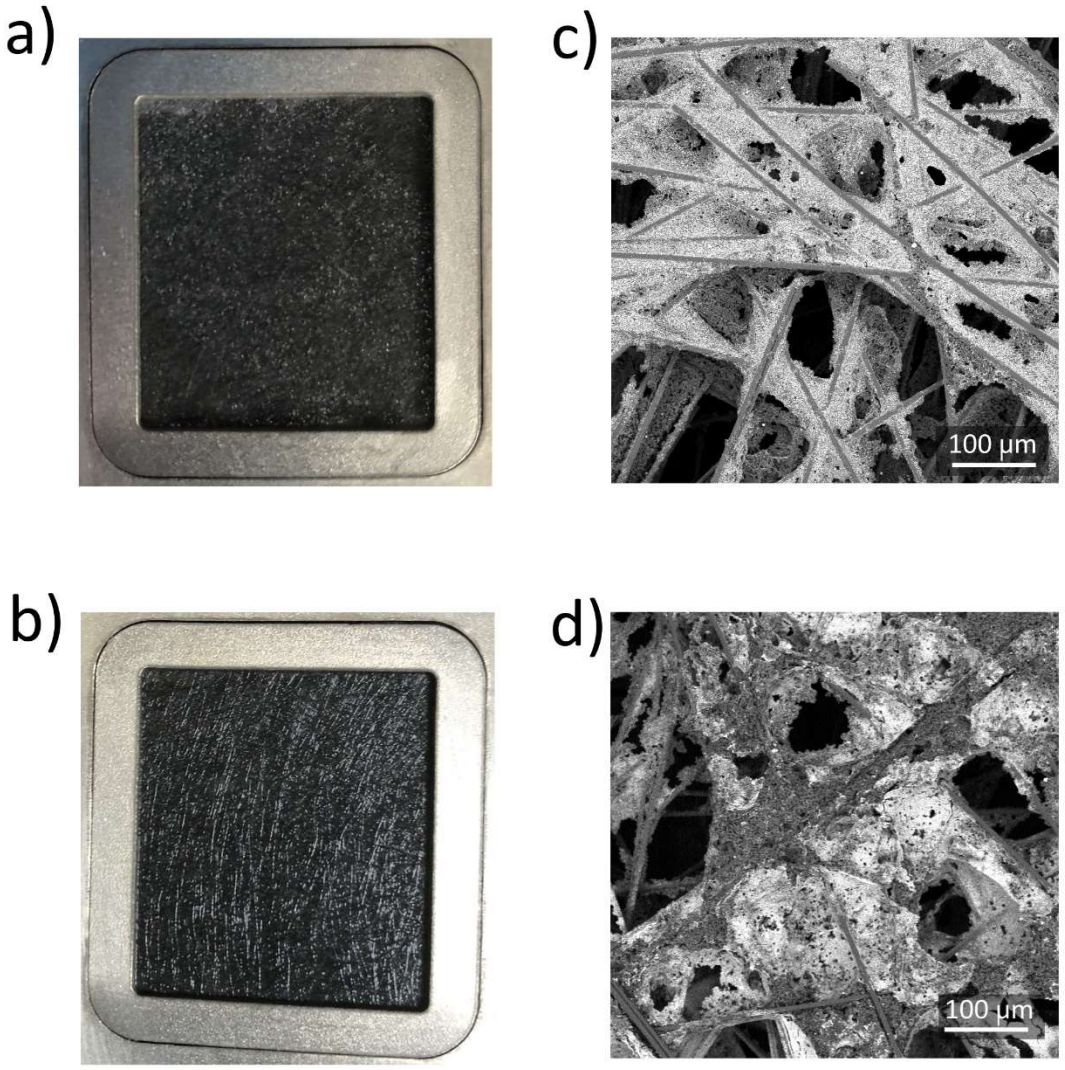

Figure S9. Sigracet 39 AA carbon paper electrode coated with MCF500 catalyst (a, c) before and (b, d) after the chronopotentiometry durability test.

Table S1. Chemical composition of the prepared $MnCo_{2-x}Fe_xO_4$ powders (ICP and EDS analyses results).

Material	ICP-OES analysis results			EDS analysis results			Corresponding composition
	Mn [at.%]	Co [at.%]	Fe [at.%]	Mn [at.%]	Co [at.%]	Fe [at.%]	
MCO	34.3	65.6	0.1	36.1	65.9	-	$Mn_{1.08}Co_{1.92}$
MCF125	32.7	63.1	4.2	35.0	60.1	4.9	$Mn_{1.02}Co_{1.85}Fe_{0.13}$
MCF250	32.7	59.3	8.0	33.7	57.2	9.2	$Mn_{1.02}Co_{1.73}Fe_{0.25}$
MCF500	33.3	50.7	16.3	34.4	48.3	17.3	$Mn_{1.03}Co_{1.47}Fe_{0.50}$
MCF750	33.3	41.6	25.1	34.2	40.1	25.8	$Mn_{1.03}Co_{1.20}Fe_{0.77}$
MCF1000	33.6	33.0	33.4	33.3	32.8	33.9	$Mn_{1.03}Co_{0.95}Fe_{1.02}$

Table S2. Properties of the prepared $MnCo_{2-x}Fe_xO_4$ powders (pXRD and BET analyses results)

Material	Cell parameters a=b=c [Å]	Surface area [$m^2\ g^{-1}$]
MCO	8.2609	27.9(1.4)
MCF125	8.2782	22.7(1.2)
MCF250	8.2994	22.6(1.2)
MCF500	8.3451	23.3(1.2)
MCF750	8.3810	23.3(1.2)
MCF1000	8.4013	23.9(1.2)

Table S3. XPS fitting parameters

Material	Peak 1 (eV)	%	Peak 2 (eV)	%	Peak 3 (eV)	%	Peak 4 (eV)	%	Peak 5 (eV)	%
Mn_2O_3[a]	640.8	18.9	641.9	44.5	643.1	25.3	644.6	8.5	646.2	3.1
MCO	640.9	18.2	642.0	32.6	643.2	31.2	644.6	13.3	646.2	4.7
MCF125	640.7	25.7	641.8	33.3	643.1	25.2	644.5	12.6	646.0	3.2
MCF250	640.7	31.0	641.9	34.8	643.1	22.0	644.5	9.7	646.1	2.4
MCF500	640.8	20.0	641.9	33.4	643.1	27.3	644.5	14.7	632.3	4.6

[a] Fitting parameters from the Biesinger et al. [1]

Table S4. OER activity data for $MnCo_{2-x}Fe_xO_4$ catalysts

Catalyst	ECSA [cm^2]	R_{ct} [Ω]	η at 10 mA cm^{-2}_{GEO} [mv]	Tafel slope [mV dec^{-1}]	η_{OX} at 50 μA cm^{-2}
MCO	11.2(0.3)	17(1)	406(4)	58(2)	378(3)
MCF125	11.2(0.3)	15.4(0.5)	391(4)	52(1)	363(3)
MCF250	9.6(0.7)	18.5(1.3)	395(3)	56(1)	362(1)
MCF500	9.9(0.6)	12.1(0.6)	376(3)	44(2)	351(3)
MCF750	6.9(0.6)	20.5(0.8)	395(3)	50(1)	356(2)
MCF1000	3.7(0.7)	39(3)	447(7)	56(1)	382(9)

Table S5. Reported OER electrocatalysts performance comparison

Material	Electrolyte	Supporting electrode	η at 10 mA cm^2 [mV]	E at 50 μA cm^{-2}_{OX} vs. RHE [V]	E at 25 μA cm^{-2}_{OX} vs. RHE [V]	Tafel slope [mV dec^{-1}]	Catalyst's loading [μg cm^{-2}]	Ref.
$MnCo_{1.5}Fe_{0.5}O_4$	0.1 M KOH	RDE-GC	376	1.58	-	44	45.5	This work
$MnCo_2O_4$	0.1 M KOH	RDE-GC	406	1.61	-	58	45.5	This work
MnCo2O4 (Co_3O_4+ $Mn_{1.4}Co_{1.6}O_4$)	1.0 M KOH	Ni foam	327	-	-	78.9	1300	[2]
$MnFe_2O_4$ – 400 °C	0.1 M KOH	RDE-GC	-	1.69	-	-	30.6	[3]
$MnFe_2O_4$ – 200 °C	0.1 M KOH	RDE-GC	-	1.76	-	-	30.6	[3]
$ZnFe_{0.4}Co_{1.6}O_4$	0.1 M KOH	RDE-GC	-	-	~1.58	-	255	[4]
$ZnFe_{0.4}Co_{1.6}O_4$	1.0 M KOH	RDE-GC	~340	~1.55	-	~37	255	[4]
$MnCo_2O_4$ microspheres	0.1 M KOH	RDE-GC	510	-	-	55	51	[5]
$ZnCo_2O_4$	0.1 M KOH	GC	~570	-	-	72.4	51	[6]
Te-Co_3O_4	1.0 M KOH	RDE-GC	313	-	-	75	240	[7]

REFERENCES

[1] Biesinger MC, Payne BP, Grosvenor AP, Lau LWM, Gerson AR, Smart RSC. Resolving surface chemical states in XPS analysis of first row transition metals, oxides and hydroxides: Cr, Mn, Fe, Co and Ni. Appl Surf Sci 2011;257:2717–30. https://doi.org/10.1016/j.apsusc.2010.10.051.

[2] Lankauf K, Cysewska K, Karczewski J, Mielewczyk-Gryń A, Górnicka K, Cempura G, et al. MnxCo3-xO4 spinel oxides as efficient oxygen evolution reaction catalysts in alkaline media. Int J Hydrogen Energy 2020;5. https://doi.org/10.1016/j.ijhydene.2020.03.188.

[3] Zhou Y, Du Y, Xi S, Xu ZJ. Spinel Manganese Ferrites for Oxygen Electrocatalysis: Effect of Mn Valency and Occupation Site. Electrocatalysis 2018;9:287–92. https://doi.org/10.1007/s12678-017-0429-z.

[4] Zhou Y, Sun S, Song J, Xi S, Chen B, Du Y, et al. Enlarged Co□O Covalency in Octahedral Sites Leading to Highly Efficient Spinel Oxides for Oxygen Evolution Reaction. Adv Mater 2018;30:1–7. https://doi.org/10.1002/adma.201802912.

[5] Menezes PW, Indra A, Sahraie NR, Bergmann A, Strasser P, Driess M. Cobalt-manganese-based spinels as multifunctional materials that unify catalytic water oxidation and oxygen reduction reactions. ChemSusChem 2015;8:164–7. https://doi.org/10.1002/cssc.201402699.

[6] Harada M, Kotegawa F, Kuwa M. Structural Changes of Spinel MCo2O4(M = Mn, Fe, Co, Ni, and Zn) Electrocatalysts during the Oxygen Evolution Reaction Investigated by in Situ X-ray Absorption Spectroscopy. ACS Appl Energy Mater 2022;5:278–94. https://doi.org/10.1021/acsaem.1c02824.

[7] Li G, Yu X, Yin F, Lei Z, Zhao X, He X, et al. High-performance Te-doped Co3O4 nanocatalysts for oxygen evolution reaction. Int J Energy Res 2022;46:5963–72. https://doi.org/10.1002/er.7536.

4.3. The effect of Fe on chemical stability and oxygen evolution performance of high surface area $SrTi_{x-1}Fe_xO_{3-d}$ mixed ionic-electronic conductors in alkaline media

W niniejszej pracy zbadany został wpływ dodatku żelaza do struktury perowskitu jakim jest tytanian strontu. Seria materiałów $SrTi_{1-x}Fe_xO_{3-d}$ (x = 0,35; 0,50; 0,70; 0,90 oraz 1,00) została przygotowana za pomocą wysokotemperaturowej syntezy w fazie stałej. Otrzymane proszki odznaczały się dużą powierzchnią właściwą, która została dodatkowo rozwinięta poprzez niskoenergetyczne mielenie, uzyskując maksymalnie 35 $m^2 g^{-1}$ dla $SrTi_{0,65}Fe_{0,35}O_{3-d}$. Najbardziej aktywnym elektrokatalizatorem OER okazał się perowskit $SrTi_{0,10}Fe_{0,90}O_{3-d}$ odznaczając się nadpotencjałem 410 mV przy 10 mA cm^{-2} w 0,1 M KOH. Rosnąca aktywność elektrochemiczna wraz ze zwiększeniem udziału żelaza w strukturze perowskitu wynika z większej ilości wakansów tlenowych w zewnętrznej warstwie atomowej przygotowanych proszków, co zostało potwierdzone za pomocą spektroskopii XPS.

Badania stabilności chemicznej pastylek zanurzonych w 0,1 M roztworze KOH wykazały, że stabilność chemiczna nie pokrywa się z aktywnością elektrochemiczną. Dla związków o zawartości żelaza powyżej 70% w podsieci B zauważono wydzielanie się strontu do elektrolitu i wizualną degradację powierzchni pastylek. W związku z tym to perowskit w którym połowa atomów tytanu jest podstawiona atomami żelaza wykazuje optymalne właściwości elektrokatalityczne z zachowanie stabilności chemicznej w środowisku zasadowym.

Do oryginalnych wyników zaliczam obserwację wpływu podstawiania tytanu żelazem w strukturze perowskitu $SrTi_{1-x}Fe_xO_{3-d}$ na właściwości fizykochemiczne i elektrochemiczne oraz zaproponowanie stechiometrii materiału, który posiada optymalną kombinację tych właściwości do zastosowania jako elektrokatalizator OER.

W przedstawionej publikacji samodzielne przygotowałem elektrody RDE z naniesionym katalizatorem. W dalszej kolejności przeprowadziłem pomiary elektrochemiczne. Ponadto odpowiadałem za analizę otrzymanych wyników, przygotowanie rysunków oraz napisanie manuskryptu. Jako autor korespondencyjny zgłosiłem artykuł do publikacji w czasopiśmie oraz przygotowałem poprawki w odpowiedzi na recenzje.

Oświadczenie współautorów o wkładzie w powstanie publikacji: „The effect of Fe on chemical stability and oxygen evolution performance of high surface area $SrTi_{x-1}Fe_xO_{3-d}$ mixed ionic-electronic conductors in alkaline media”

Imię i nazwisko autora	Wkład w powstanie pracy	Podpis
Krystian Lankauf	Konceptualizacja, metodologia, badania, pisanie – oryginalna wersja robocza, wizualizacja	
Aleksander Mroziński	Badania (synteza materiałów, pomiary elektryczne), pisanie – recenzja i redakcja	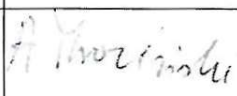
Patryk Błaszczak	Badania (BET), pisanie – recenzja i redakcja	
Karolina Górnicka	Badania (XRD), pisanie – recenzja i redakcja	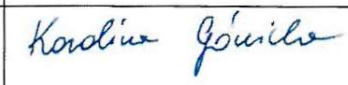
Justyna Ignaczak	Badania (SEM), pisanie – recenzja i redakcja	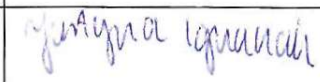
Marcin Łapiński	Badania (XPS), pisanie – recenzja i redakcja	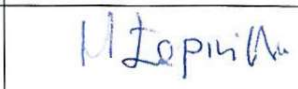
Jakub Karczewski	Badania (SEM), pisanie – recenzja i redakcja	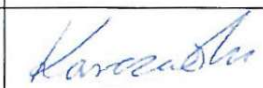
Grzegorz Cempura	Badania (TEM), pisanie – recenzja i redakcja	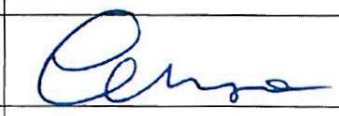
Piotr Jasiński	Pisanie – recenzja i redakcja, nadzór, zasoby	
Sebastian Molin	Konceptualizacja, pisanie – recenzja i redakcja, nadzór, zasoby, pozyskiwanie funduszy	

INTERNATIONAL JOURNAL OF HYDROGEN ENERGY 46 (2021) 28575–28590

Available online at www.sciencedirect.com

ScienceDirect

journal homepage: www.elsevier.com/locate/he

The effect of Fe on chemical stability and oxygen evolution performance of high surface area $SrTi_{x-1}Fe_xO_{3-\delta}$ mixed ionic-electronic conductors in alkaline media

Krystian Lankauf [a,*], *Aleksander Mroziński* [a], *Patryk Błaszczak* [b], *Karolina Górnicka* [b], *Justyna Ignaczak* [a], *Marcin Łapiński* [b], *Jakub Karczewski* [b], *Grzegorz Cempura* [c], *Piotr Jasiński* [a], *Sebastian Molin* [a]

[a] *Advanced Materials Center, Faculty of Electronics, Telecommunications and Informatics, Gdańsk University of Technology, Ul. G. Narutowicza 11/12, 80-233, Gdańsk, Poland*

[b] *Advanced Materials Center, Faculty of Applied Physics and Mathematics, Gdańsk University of Technology, Ul. G. Narutowicza 11/12, 80-233, Gdańsk, Poland*

[c] *International Centre of Electron Microscopy for Materials Science, AGH University of Science and Technology, Al. A. Mickiewicza 30, 30-059, Kraków, Poland*

HIGHLIGHTS

- High surface area $SrTi_{x-1}Fe_xO_{3-\delta}$ perovskites were prepared via a solid state reaction.
- The effect of Fe on electrical and physicochemical properties was investigated.
- Fe substitution increases activity toward OER.
- Chemical stability tests showed Sr dissolution for Fe content above 50%.

GRAPHICAL ABSTRACT

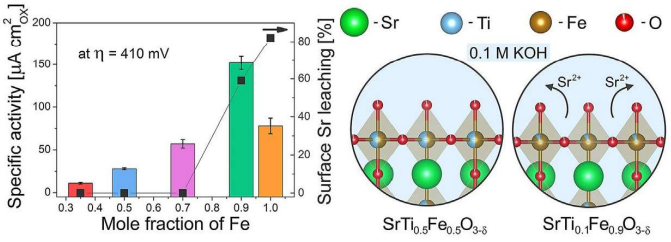

ARTICLE INFO

Article history:
Received 17 March 2021
Received in revised form
26 May 2021
Accepted 13 June 2021
Available online 10 July 2021

Keywords:
Perovskites

ABSTRACT

Development of environmentally friendly, high performing oxygen evolution reaction (OER) catalysts is an important research challenge. In this work, iron doped strontium titanates with a general formula $SrTi_{1-x}Fe_xO_{3-\delta}$ (x = 0.35, 0.50, 0.70, 0.90, and 1.00) denoted as STFx, were synthesized via a solid state reaction technique and characterized in terms of oxygen evolution reaction electrocatalysis in an alkaline electrolyte (0.1 M KOH). The produced powders were characterized by a high specific surface area (>20 $m^2\ g^{-1}$), beneficial for OER. The evaluation of specific activity indicated the following trend of increasing performance: STF35 < STF50 < STF70 < SFO < STF90. The lowest overpotential at 10 $mAcm^{-2}_{GEO}$ of 410 mV (350 mV at 25 $\mu A\ cm^{-2}_{OX}$) was achieved by STF90 with the

* *Corresponding author.*
E-mail address: krystian.lankauf@pg.edu.pl (K. Lankauf).

https://doi.org/10.1016/j.ijhydene.2021.06.088

Oxygen evolution reaction
Water splitting
Electrocatalysts
Chemical stability

corresponding Tafel slope of 60 mV dec^{-1}. The two materials with the highest Fe content (i.e. STF90 and SFO) showed, however, poor chemical stability in alkaline solution demonstrated by the dissolution of Sr. Based on the good electrochemical performance (~460 mV at 10 mA cm^{-2}_{GEO}, ~405 mV at 25 μA cm^{-2}_{OX}) and chemical stability for at least 30 days (no Sr dissolution) of STF50, it can be considered an interesting, working at room temperature OER catalyst based on non-toxic and abundant elements.

Introduction

Alkaline electrochemical water splitting is an important method for hydrogen production which can be used to accommodate an increasing share of renewable energy production [1,2]. The overall efficiency of water splitting is mainly determined by the sluggish oxygen evolution reaction (OER) kinetics. Precious metal oxides: RuO_2 and IrO_2, are known for superior OER activity, however, their low abundance and high price are a barrier against widespread use.

As potential alternative electrocatalysts, many different groups of materials have been researched, including especially oxides (perovskites [3–6] and spinels [7–10]), carbides [11–13], phosphides [14–16], and layered double hydroxides (LDHs) [17–19]. In recent years, highly active oxide electrocatalysts with the perovskite structure have been developed. Perovskites have a general formula of ABO_3 (where A is large rare earth or alkaline metal cation and B is a smaller, redox active transition metal cation) [20]. A wide range of element selection provides prospects of tailoring the physical and chemical properties, enhancing the catalytical activity [21,22]. Notable examples of the perovskites include especially cobalt and/or iron containing compounds. The high performance catalysts include: LSC, LSF, BSCF, SCF and their variations. For instance, Zhang et al. prepared series of perovskite-type oxide $La_{1-x}Sr_xCoO_3$ by sol-gel process [23]. $La_{0.2}Sr_{0.8}CoO_3$ exhibited the highest OER activity, which can be additionally tuned by changing the synthesis parameters, i.e. molar ratios of substrates, pH of the sol, calcination time and temperature. The OER performance of $SrTi_{0.1}Co_xFe_{0.9-x}O_{3-\delta}$ in alkaline media studied by Deng et al. revealed the highest OER activity of $SrTi_{0.1}Co_{0.5}Fe_{0.4}O_{3-\delta}$ [24]. The improved electrochemical performance is considered to originate from the highly oxidative oxygen species O_2^{2-}/ O^- formed upon moderate Fe doping. As demonstrated, the perovskites based on cobalt offer high electrochemical performance, although cobalt is proven to be a carcinogenic element with high price variations and ethical issues with mining. Due to the mentioned issues, substitution with the other elements is an active research topic in solid state chemistry.

Fe-based perovskites have been studied as potential alternatives for Co-based materials. Among the ferrites, the perovskites with B-site based on Ti and Fe have found considerable attention as model OER/ORR and hydrogen catalysts at high temperatures [25,26]. For example, $SrFe_{0.2}$, $_{0.3}TiO_{3-\delta}$ (SFT) and $SrFe_{0.2}Ti_{0.8}O_{3-\delta}$ (SFT)-ZnO composite heterostructure demonstrated high ionic conductivity at 520 °C and has been successfully applied as an electrolyte for low-temperature solid oxide fuel cell (LT-SOFC) [27,28]. Pure $SrTiO_3$ is a poor electronic conductor due to a stable Ti^{4+} cation, but upon partial substitution of Ti by Fe, the electronic conductivity increases and ionic conductivity is introduced via the formation of oxygen vacancies [29,30]. The opposite end member, $Sr_2Fe_2O_5$ ($SrFeO_{2.5}$), with the iron oxidation state of +3, can be treated as a highly oxygen deficient perovskite that crystallizes in an orthorhombic structure [31].

The compounds with both Fe and Ti at the catalytically active B-site show mixed ionic-electronic conductivity and high electrochemical performance, even though they have a relatively low electronic conductivity, especially compared to LSC or LSF perovskites [32,33]. The relations between the electronic conductivity, ionic conductivity, oxygen exchange and diffusion and stability are not yet well established at high temperatures, which also seems the case at low temperatures.

$Sr(Ti,Fe)O_{3-\delta}$ materials have been already considered as potential OER electrocatalysts. For example, Hayden et al. have used high throughput physical vapor deposition (HT-PVD) to deposit an array of 100 compositions with different Ti:Fe ratios for evaluation of OER/ORR [34]. The materials were prepared in the form of 300 nm thin films. The higher the Fe content was, the lower the OER onset potential was measured, whereby the stability showed an opposing trend. This developed screening study pointed out potentially interesting features of the $Sr(Ti,Fe)O_{3-\delta}$ materials for OER, which were, however, not carefully studied on well-defined powder catalysts in an RDE-setup and thus a direct comparison of their performance with other perovskites in the powder form is difficult.

In the present work, a series of $SrTi_{1-x}Fe_xO_{3-\delta}$ (x = 0.35, 0.50, 0.70, 0.90, and 1.00) (STFx) perovskites were prepared by the high temperature solid state reaction technique. The materials were examined for their crystallographic structure, chemical stability, electrical conductivity properties, and finally, the evaluation of the electrocatalytic OER activity in alkaline electrolyte (0.1 M KOH) at 25 °C was performed on a rotating disk electrode.

The main focus of our research was to investigate the influence of the Fe substitution on the chemical stability and electrocatalytic activity of $SrTi_{1-x}Fe_xO_{3-\delta}$ perovskites.

Experimental details

Material synthesis

Catalyst materials $SrTi_{1-x}Fe_xO_{3-\delta}$ (STFx) with x = 0.35, 0.50, 0.70, 0.90, and 1.00 were synthesized by a standard high

temperature solid state reaction method (HT-SSR). Starting materials were: strontium carbonate ($SrCO_3$), iron (III) oxide (Fe_2O_3) and titanium dioxide (TiO_2) with purity >99% (all from Sigma-Aldrich, USA). Reagents were mixed together in a planetary ball mill according to the details presented in the previous work [35,36]. The mixed reagents were calcined twice for 15 h in the form of large pellets ($\Phi = 1\ 1/8$", h ≈ 1.5 mm) with a re-grounding step between each calcinations. Due to the high sinter-ability of the $SrTi_{1-x}Fe_xO_{3-\delta}$ with x = 1.00, calcination temperature was set to 1100 °C, whereas for the remaining materials, the temperature peaked at 1200 °C. After the second calcination step, the pellets were ground into powders, milled in a ball mill (using 3 mm ZrO_2 balls in ethanol, Fritsch Pulverisette 7) and annealed in air at 600 °C to obtain oxygen stoichiometric powders [37].

For the specific surface area measurements, 1000 mg of powder was ball-milled for 96 h with the rotation speed of 100 rpm (Zoz Gmbh, Rollermill RM1) in 20 mm diameter glass vial of total 25 mL capacity filled with 35 g of 1 mm diameter yttria-stabilized zirconia (YSZ) grinding balls and 13 mL of ethanol. The reason of the ball-milling procedure was to mimic the catalysts' specific surface changes after ink ball-milling described further in the electrode preparation paragraph.

Dense STFx pellets for electrical measurements and chemical stability tests were prepared by uniaxial pressing at 50 MPa and sintering for 2 h at either 1100 °C (pure SFO) or 1200 °C (the remaining composition) under air atmosphere.

The chemical stability tests were performed by immersing the sintered pellets (~0.5 mm thick) in 0.1 M KOH solution (pH ~13) for 30 days. The samples' microstructures (SEM) and chemical compositions (EDS) were compared before and after the tests. For the tests, the pellets after the electrical conductivity tests were used. To reveal the grain boundaries, the surfaces of the sintered pellets were polished down to a ~1 μm finish and then thermally etched at 1200 °C for 5 min (except SFO: 900 °C, STF90, and STF35 at 1100 °C). An example of the thermal etching temperature selection procedure is described in Supporting Information (Figs. S1 and S2).

Material characterization

Synthesized powder morphologies were investigated using FEI Quanta 250 FEG Scanning Electron Microscope and a C_s-corrected Titan Cubed G2 60–300 (FEI) Scanning Transmission Electron Microscope (S/TEM). Chemical composition was examined using the ChemiSTEM EDX system based on four windowless Silicon Drift Detectors (Super X). The powders for TEM investigations were prepared traditionally: a drop of a water suspension containing the powder was placed onto a copper grid followed by vacuum drying. The maximum particle diameter was estimated, based on SEM images, using the ImageJ software [38].

Surface morphology and elemental composition of the pellets before and after exposures in 0.1 M KOH solution were investigated on a Phenom XL (Thermo Fisher Scientific) desktop SEM equipped with an integrated energy dispersive X-ray spectroscopy (EDS) microanalyzer.

The powders' specific surface area was measured using N_2 adsorption technique (Quantachrome, NovaTouch LX1) according to the BET isotherm model. The samples were degassed prior sorption measurement at 300 °C for 3 h under vacuum.

Powder X-ray diffraction (pXRD) was conducted at room temperature on a Bruker D2 Phaser diffractometer with CuK_α radiation ($\lambda = 1.5404$ Å) and a Lynxeye XE-T detector was used for crystalline phase identification. Unit cell parameter calculation was performed by Le-Bail refinement using the Fullprof software package [39]. The. cif files were downloaded from the Crystallography Open Database [40,41].

The chemical composition of samples was investigated by the X-ray photoelectron spectroscopy (XPS) method. Measurement was performed using Omicron Nanotechnology ultra-high vacuum equipment at a pressure below 1.1×10^{-6} Pa. Mg Kα X-ray source was operated at 15 kV and 300 W. Measurements were conducted at room temperature. Analyzes of the obtained results were performed using CASA XPS software package with Shirley background subtraction and least-square Gaussian-Lorentzian − GL (30) curve fitting algorithm. Calibration of the measured spectra to the binding energy of 285 eV for C1s line was conducted.

The electrical conductivity of the STFx dense pellets was measured using the Van der Pauw method [42]. Four silver contacts (electrodes A, B, C, D) were placed on the STFx pellets' surface, forming the square shape. The electrical conductivity (σ) can be obtained with the following equation:

$$\sigma = \frac{ln2}{\pi h} \frac{2}{R_{AB,CD} + R_{CA,DB}} \quad (1)$$

where σ is conductivity of the sample, h is thickness of the sample, $R_{AB,CD(CA,DB)}$ is the resistance, which is determined while applying current to electrodes A(C) and B(A) while the potential is measured between electrodes C(D) and D(B).

The study was performed in the synthetic air (20% O_2) and the temperatures ranging between 200 °C and room temperature with a preheating step at 400 °C for sintering of the contact silver paste. An automatic logging system was used for data collection. The acquired data were used to calculate the activation energy from the formula based on the Arrhenius equation:

$$ln\sigma = \frac{E_a}{k} \times \frac{1}{T} + ln\sigma_o \quad (2)$$

where E_a is an activation energy, σ is an electrical conductivity, T is a temperature, σ_o is a pre-exponential factor, and k is the Boltzmann's constant.

Electrode preparation

Glassy carbon rotating disk electrodes (RDE-GCE, 0.196 cm^2, ALS Co., Ltd) were used as support electrodes for powder catalysts. Before the deposition of the catalyst inks, the RDE-

GCE were polished for 5 min using 0.05 μm polishing alumina solution, sonicated for 10 min in deionized water and isopropanol, respectively, then dried overnight at ambient conditions. The electrocatalyst inks were prepared by mixing 120 mg of the prepared perovskite powders, 120 mg Super P Li Conductive Carbon (Imerys Graphite & Carbon), 11.4 mL Ethyl Alcohol Absolut 99.8% Pure (POCH, Poland), and 1.8 mL of K^+ exchanged Nafion solution.

The Nafion is added as a dispersing and binding agent, however, its strong acidity may cause corrosion of oxide catalysts [43,44]. In order to change the pH of the initial solution (pH of ~1–2) the K^+ exchanged Nafion solution was prepared by mixing 5 wt% Nafion 117 solution (Sigma-Aldrich) with 0.1 M potassium hydroxide solution (1 M KOH Titripur (Merck) diluted with DI water ~12 MΩ) at 2:1 vol ratio, resulting in pH change to ~9.

Subsequently, the prepared inks were ball-milled for 96 h (Zoz Gmbh, Rollermill RM1) in 20 mm diameter glass vial using 1 mm diameter yttria-stabilized zirconia (YSZ) grinding balls with the rotation speed of 100 rpm, followed by sonication in an ice-water bath for 30 min. The milling step was added to crush agglomerates and to better mix the catalyst powder with conductive carbon. SEM observations of inks drop-casted onto Ni foil are presented in Fig. S3. The ink made from the as-prepared powder (by ultrasonic dispersion with Nafion and conductive carbon) has visible agglomerates with diameters of >10 μm. The ink roller milled using 3 mm zirconia balls also ended up with some agglomerates, which were not visible after roll milling using 1 mm balls. Based on these results, all inks were made utilizing roller milling with 1 mm zirconia balls. The level of impurities introduced by milling media is very small, below the detection limit of EDS (<0.5 at.%). The Ni foil was chosen as a support for SEM observations due to the high electrical conductivity and because it does not contain any elements which are constituents of prepared STFx powders. For OER experiments, 5 μL of ink was drop-casted onto the RDE-GCE rotating at 700 rpm, achieving the catalyst mass loading of 45.5 μg. The rotation induced air flow over the casted ink droplet helps to obtain the uniform and homogenous film [45,46].

Electrochemical measurements

All electrochemical measurements were performed in a three-electrode Teflon cell system in 0.1 M KOH aqueous solution (prepared from 1 M KOH Titripur from Merck, diluted with DI water ~12 MΩ). A Hg/HgO in 0.1 M KOH solution (ALS Co., Ltd, Japan), a Pt coil, and a coated RDE-GCE were used as the reference (RE), counter (CE), and working (WE) electrodes, respectively. The electrochemical tests were performed on BP-300 (BioLogic) bipotentiostat connected with a rotating disk electrode (RDE) configuration (RRDE-3A Rotating Ring Disk Electrode Apparatus Ver.2.0, ALS Co., Ltd). An electrolyte temperature of 25 °C was maintained by a Julabo F12 thermostat. Before each experiment, the electrolyte was purged with 99.995% O_2 for 30 min, then the gas flow (50 mL min^{-1}) was kept over the electrolyte in order to maintain the O_2/H_2O equilibrium. The working electrode was activated by potential cycling 10 times in the range of 1.0–1.7 V vs. RHE at a scan rate of 100 mV s^{-1}. Cycling voltammetry (CV) scans were performed in the non-faradaic potential region of 1.0–1.1 V vs. RHE at scan rates of 10, 20, 40, 60, 80, 100 mV s^{-1} with 0 RPM rotation speed for the double-layer capacitance (C_{dl}) estimation. The electrochemical active surface area (ECSA) was calculated assuming the reference capacitance value of 40 μF cm^{-2} for oxides [47]. CV scans for OER were performed in the range from 1.1 to 1.9 V vs. RHE at a scan rate of 10 mV s^{-1} with 1600 rpm rotation speed. The charge transfer resistance (R_{ct}) was calculated from the electrochemical impedance spectroscopy (EIS) measurements in the frequency range from 10 kHz to 0.1 Hz at 1.7 V vs. RHE with an amplitude of 10 mV and the 1600 rpm rotation speed. Fitting to the modified Randles equivalent circuit was performed with EC-Lab® Software.

All measured potentials were converted to RHE by the experimental calibration of the reference electrode against RHE (Fig. S4) [48]. The value of E_{offset} equals the measured equilibrium potential of hydrogen electrocatalysis (HER/HOR) and was determined to be −928 mV. The potential conversion performed according to the equation:

$$E_{RHE} = E_{measured} + 928\ \text{mV} \tag{3}$$

For OER polarization curves, the background correction was performed by averaging the positive and negative-going scans [48]. All potential values were iR-corrected to eliminate the solution resistance factor according to the equation:

$$E_{iR-corrected} = E_{applied}\ iR_{un} \tag{4}$$

where i is current and R_{un} is an uncompensated ohmic electrolyte resistance determined by EIS measurement at OCV. The current density was normalized by the geometrical surface area of RDE-GCE (0.196 cm^2) (expressed in the unit mA cm^{-2}_{GEO}). The overpotential of OER was calculated using the equation:

$$\eta = E\left(10\ \text{mA cm}^{-2}\right)\ 1.23\ V\ vs\ RHE \tag{5}$$

The specific activity was determined by current normalization using the BET specific surface area of each oxide catalyst (expressed in the unit μA cm^2_{OX}). The catalyst mass activity at specific overpotential was calculated by current normalization by the catalyst mass loading of 45.5 μg (expressed in the unit A g^{-1}). For each material, at least 3 separate samples were prepared and tested, but the typical differences were negligible. The representative OER polarization curves obtained for STF50 are presented in Fig. S5.

Results and discussion

Catalyst structural characterization

$SrTi_{x-1}Fe_xO_{3-\delta}$ (x = 0.35, 0.5, 0.7, 0.9, and 1.0) (STFx) powders were synthesized by the high temperature solid state reaction method. The powders were denoted as STF35, STF50, STF70, STF90, and SFO.

Fig. 1a and b shows the SEM images of the STF70 powder (after the ink milling step). The images of the other powders are presented in Fig. S6. The powders are composed of small particles with diameters <250 nm. For increasing Fe content,

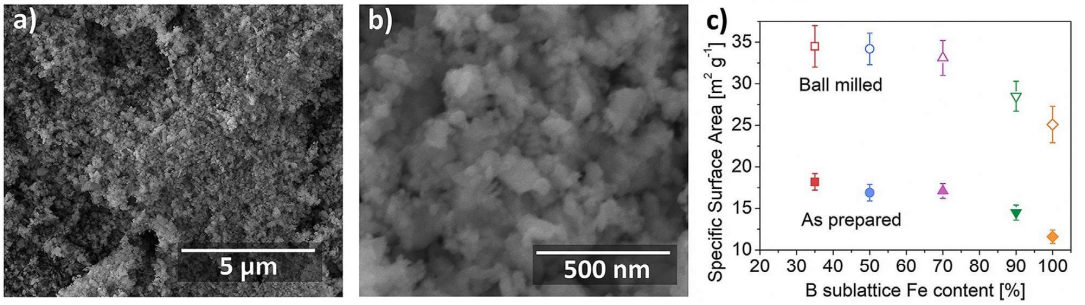

Fig. 1 – SEM images of synthesized STF70 powders (a) low (x10 000) magnification, (b) high (×100 000) magnification, and (c) BET surface areas of the as-produced and ball-milled $SrTi_{x-1}Fe_xO_{3-\delta}$ (STFx) powders.

the particle size increases. These microscopic observations were confirmed by sorption measurements (see Fig. 1c). As noted, the roller mill procedure reduces the agglomeration, which results in a nearly twofold increase of the specific surface area for ink-milled powders in comparison to the as-prepared. The BET area was the largest for the STF35 powder (~35 $m^2\ g^{-1}$), and reduced to ~25 $m^2\ g^{-1}$ for the SFO. Even though the SFO powder was prepared at the lowered temperature (1100 °C instead of 1200 °C) it still had a decreased surface area, indicating a stronger sintering/grain growth tendency for the Fe rich sample. Indeed, as investigated by Schulze-Küppers et al. [49], the sintering onset of SFO is ~750 °C and maximum shrinkage occurs at ~1100 °C, whereas for Ti containing compositions, these characteristic temperatures are at least 100 °C higher.

In general, the obtained particle sizes can be considered small, especially with regard to the synthesis route, including high temperature calcination. Such fine morphology should be advantageous for electrocatalysis, where high surface areas lead to high total current densities.

As indicated by Fabbri et al. [50], the surface areas typically obtained for perovskites are <4 $m^2\ g^{-1}$, which hinders their practical applications. For example, Su et al. have fabricated powders of $SrCo_{0.9}Ti_{0.1}O_{3-d}$ (SCT), $SrFe_{0.9}TiO_{3-d}$ (SFT) and $Ba_{0.5}Sr_{0.5}Co_{0.8}Fe_{0.2}O_{3-d}$ (BSCF) by a complexing sol-gel method [51]. After the final calcination step at 1000 °C, the obtained BET values were 0.91 $m^2\ g^{-1}$, 0.86 $m^2\ g^{-1}$, and 0.43 $m^2\ g^{-1}$ for SCT, SFT, and BSCF, respectively. Zhu et al. have studied $SrNb_{0.1}Co_{0.7}Fe_{0.2}O_{3-d}$ (SNCF) powders as effective OER catalysts, including the effects of powder ball milling [52]. The as-synthesized powder had a surface area of 0.25 $m^2\ g^{-1}$, whereas after milling the area increased to 6.45 $m^2\ g^{-1}$. The raw powder seems to have been highly agglomerated. Cheng et al. have studied BSCF catalysts in the form of the as-produced and ball-milled powders. The surface area increased upon milling from 3 $m^2\ g^{-1}$ to 5 $m^2\ g^{-1}$ [53]. In the case of $SmBa_{0.5}Sr_{0.5}Co_2O_{6-d}$ (SBSC) fibers prepared by electrospinning [54], the BET surface area varied from ~13 $m^2\ g^{-1}$ for fibers calcined at 800 °C down to 3 $m^2\ g^{-1}$ after calcination at 1100 °C. For the synthesis of dedicated high surface area perovskites, Fabbri et al. used a flame spray synthesis, which produced BSCF and LSC powders with high specific surface areas of ~25 $m^2\ g^{-1}$ and ~46 $m^2\ g^{-1}$. In contrast, traditionally prepared BSCF and LSC powders were characterized by specific surface areas of 4 and 1.5 $m^2\ g^{-1}$.

Interestingly, our results show that it is possible to obtain high surface area (>30 $m^2\ g^{-1}$) perovskite powders even using traditional high temperature synthesis methods. This opens the possibilities to produce technically relevant powders via traditional powder processing routes.

Fig. 2a shows the powder XRD patterns of the prepared STFx perovskites. All of the prepared samples crystalized in a cubic crystal structure (space group *Pm-3m*, No. 221). The position of the characteristic reflection (110) shifted towards higher 2θ angles with increasing Fe content in the perovskite structure, indicating the reduction of a lattice size (exact values are presented in Table S1). Fig. 2c shows the lattice parameters obtained from the Le-Bail refinement as the function of Fe content (refinement plots are demonstrated in Fig. S7).

The plot also includes the available unit cell data that is found in the literature for the end-members: $SrTiO_3$ (COD ID 7212245) and $SrFeO_{2.96}$ (COD ID 1528364), the line (Vegard's slope), which follows the composition $Sr(Ti^{4+})_{1-x}(Fe^{4+})_xO_3$ [41,55]. The +4 valence state of iron (ionic radii 0.585 Å) would mean full iron oxidation, which is rarely the case at the standard conditions [44]. The oxidation state of iron equal to 3+ was reported for STFx compounds sintered in nitrogen, while it reduced the iron ions. As proposed by Rothschild et al. [33] the proper framework to analyze the STFx materials family is the $Sr^{2+}(Ti^{4+}_{1-x}Fe^{3+}_x)O_{3-x/2-d}$, though the STFx typically also contains a considerable amount of Fe^{4+}, which is a charge carrier (hole) and is believed to be an important factor in creating an optimal O–Fe covalency for OER [21]. The Fe^{3+} in

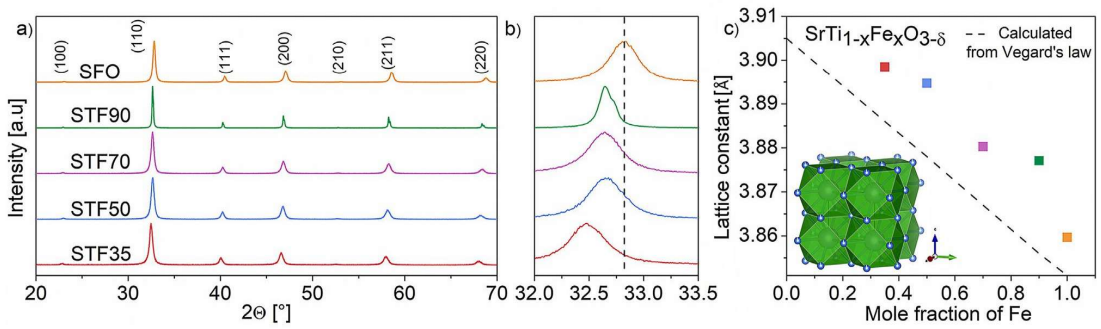

Fig. 2 – (a) Powder XRD patterns of synthesized $SrTi_{x-1}Fe_xO_{3-\delta}$ (STFx), (b) zoom-in of the patterns showing the main reflection (110) shift, (c) and calculated unit cell parameters.

the high spin state has a relatively large diameter (0.645 Å), which should result in an expansion of the unit cell upon substitution of Ti^{4+}, which is not experimentally observed. One of the possibilities is a formation of a low spin (LS) Fe^{3+} (0.55 Å), which would result in unit cell size reduction. The issue has been discussed for a similar material system of $SrSn_{1-x}Fe_xO_{3-d}$ [56].

Filatova et al. have used soft X-ray XAS to determine the atomic and electronic structure of STFx powders [57]. The analysis of Fe2p ($L_{2,3}$) absorption spectra revealed the main state of Fe to be +3 with part of iron ions at +4 state. The authors confirmed the octahedral position of the Fe cations in perovskites. Interestingly, for higher Fe content samples, there is also a possibility of Fe^{3+} at tetrahedral positions and even for some Fe^{2+} at octahedral position.

Formation of the oxygen vacancies (and more generally, changes in oxygen stoichiometry), resulting from the charge compensation of Fe^{3+} substitution, might also result in unit cell size changes. STFx compounds are also sometimes considered as "oxygen deficient" perovskites [58], where oxygen content is decreased, but no vacancies are formed. The oxygen vacancies are reported to have a similar (+- 10%) size as oxygen ions in the lattice [59], so they typically have a smaller influence on the unit cell size than the cation changes. The change in oxygen content might result in the formation of O–Fe–O or O–V_o–O complexes, which have been reported to change the coordination number of Fe from 6 to 5 and thus change the ionic radii of iron.

It has also been reported, that in the case of STFx materials, the XRD does not fully resolve the crystallographic structure [60,61]. Steinsvik et at. employed advanced electron microscopy (selected area diffraction – SAD and electron energy loss spectroscopy - EELS) for characterization of STFx materials [61]. The authors reported formation of the superstructures due to oxygen vacancies ordering in iron rich STFx.

All of these effects can have a complex influence on the unit cell size where basic predictions based on Shannon's ionic radii principles are not precise.

Though the STFx seem to present a complex cationic structure, some of the reported crystallographic data is fairly consistent. The unit cell dimensions obtained in the present work agree very well with several of the reported literature values. Schulze-Küppers et al. reported the lattice parameter of ~3.905 Å and ~3.895 Å for the 0% and 50% Fe containing compositions, respectively [49]. The lattice constant was also consistently higher than theoretically expected based on Fe^{4+}. Miruszewski et al. studied the full range of STFx compositions and obtained ~3.895 Å for the 50% iron composition and ~3.860 Å for the 100% iron composition, the same as in the current work [62].

Based on the obtained data and the available literature, it might be concluded that the composition of the perovskites synthesized in this work contains a mixture of octahedrally coordinated Fe^{4+} and Fe^{3+}.

Further microstructural characterization of STF70 powder was performed by transmission electron microscopy (TEM). In Fig. 3a–c the high-angle annular dark-field (HAADF) and bright field (BF) images are presented. The observed area consists of an agglomerate of nanocrystals up to 200 nm in size, which is consistent with SEM imaging of the powders. The selected area electron diffraction (SAD) patterns (Fig. 3d and e) indicate the well-defined polycrystalline cubic structure of the Pm-3m space group, which agrees with the macroscopic XRD results. Uniform dispersion of the constituent elements (Sr, Fe, Ti) was confirmed by TEM-EDS elemental analysis (Fig. 3f–j). As observed in TEM images, the STF70 particles can be considered relatively small even though the powder was obtained via sintering at 1200 °C, which usually leads to a formation of the micrometric particles.

The full XPS element survey scans of $SrTi_{x-1}Fe_xO_{3-\delta}$ powders are presented in Fig. S8. Peaks corresponding to Sr, Ti, Fe, O and C are clearly observed (the detected carbon is associated with the species adsorbed from the ambient air). The performed XPS spectra fitting is demonstrated in Fig. 4. The Sr3d spin-orbit doublet has been deconvoluted into pairs originating from different Sr chemical coordination, i.e. perovskite lattice Sr at lower binding energies along with secondary phases at higher binding energies, all with an energy separation of 1.8 eV. The distinguished secondary phases (most likely $SrCO_3$) result from

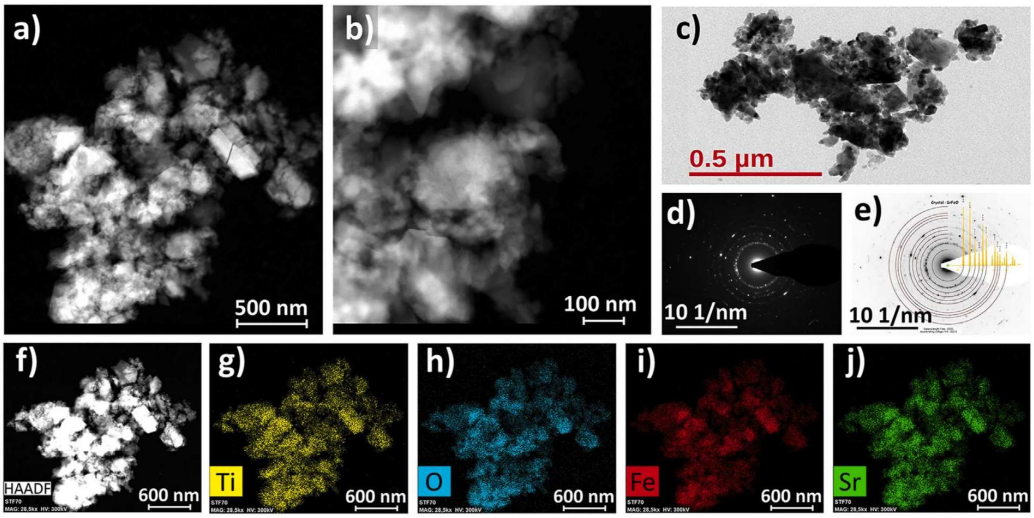

Fig. 3 – (a–c) HAADF-(S)TEM images and (d) corresponding SAD pattern with (e) superimposed theoretical pattern of the STF70. (f–j) TEM-EDS elemental maps of (g) titanium, (h) oxygen, (i) iron, (j) and strontium.

the Sr surface segregation and are the products of Sr reaction with chemisorbed gases [63–65]. Two kinds of Fe species were detected in the Fe2p spectra, Fe^{3+} and Fe^{4+} with an energy separation of 13.6 eV. It points out that the perovskite structures examined in this work should be described as $SrTi_{1-x}[Fe^{3+}, Fe^{4+}]_xO_{3-\delta}$, consistent with the discussion in the XRD results section. For comparison, Ghaffari et al. synthesized $SrTi_{x-1}Fe_xO_{3-\delta}$ (x = 0, 0.2, 0.4, 0.6, 0.8 and 1) powders via HT-SSR technique and observed a systematic decrease of Fe^{3+}/Fe^{4+} ratio from 2.83 for x = 0.2 to 1.28 for x = 1 [66]. Interestingly, in our study, the Fe^{3+}/Fe^{4+} ratio was relatively constant with a value ~1.5. The relative amount of Sr and Fe species calculated from the areas of deconvoluted peaks is collected in Table S3 and Table S4.

Measured O1s spectra in Fig. 4c presents the changes of the surface oxygen species of STFx powders with higher Fe content in B sublattice. The lowest observed binding energy of O1s for STF50 and STF90 was ~526 eV, when in fact the lowest

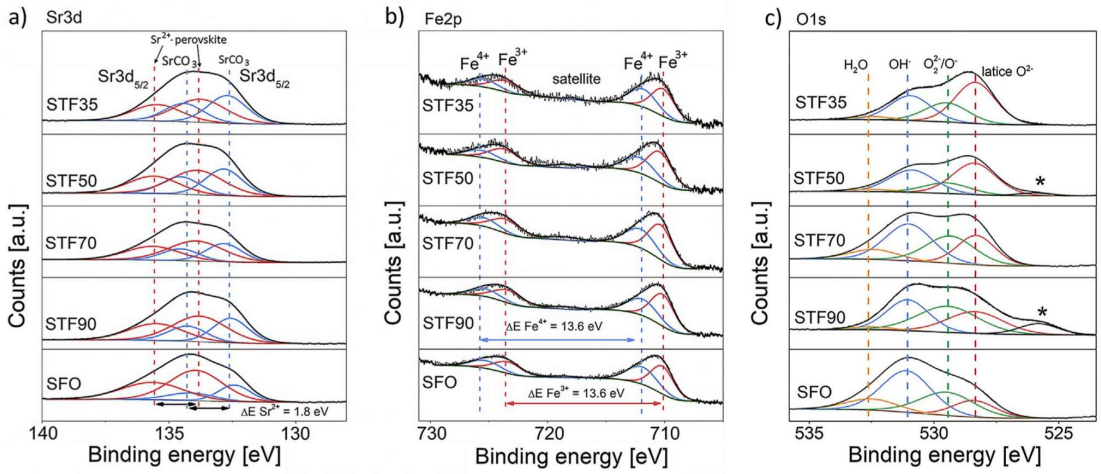

Fig. 4 – (a) Sr3d, (b) Fe2p and (c) O1s X-ray photoelectron spectra of $SrTi_{x-1}Fe_xO_{3-\delta}$ powders.

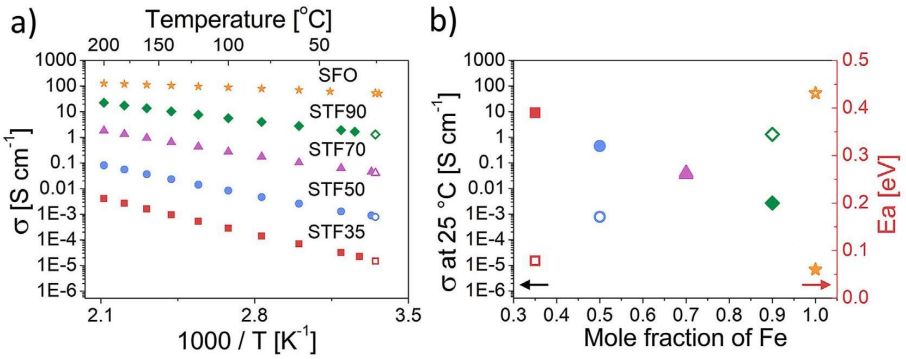

Fig. 5 – (a) Temperature dependence of $SrTi_{x-1}Fe_xO_{3-\delta}$ (STFx) measured DC electrical conductivity (filled symbols) and extrapolated value of conductivity at 25 °C (blank symbols). (b) Activation energies of electrical conductivity (filled symbols) and the extrapolated electrical conductivity at 25 °C (blank symbols) as the function of Fe mole fraction in $SrTi_{x-1}Fe_xO_{3-\delta}$ perovskite structure.

expected one is 528 eV for metal oxides. Those additional artifact signals (marked by *), may be due to the "double charge" effect and/or hardware issues [67]. It is likely that the signal from the carbon tape (to which the powders were glued) was also collected during the analysis. However, the shape changes of the spectra with Ti substitution by Fe may be assigned to the increase of highly oxidative oxygen species (O_2^{2-}/O^- at ~528.3 eV) concentration associated with the surface oxygen vacancies (the calculated values are gathered in Table S5) [68]. The XPS spectra of Ti2p indicates that Ti was in +4 oxidation state (Fig. S9).

Electrical conductivity study

The DC electrical conductivity of $SrTi_{x-1}Fe_xO_{3-\delta}$ (STFx) materials was measured on sintered pellets by Van der Pauw method in the temperature range from 200 °C to ambient in air.

The results are presented in Fig. 5a and summarized in Table S2. The conductivity values increase considerably with the increasing Fe content [36] and represent a thermally activated process. The six orders of magnitude increase from ~10^{-5} S cm^{-1} to ~50 S cm^{-1} between the STF35 and SFO samples at 25 °C is consistent with literature reports [29,69]. As evidenced in Fig. 5b, the increase of conductivity seems to follow a logarithmic dependence on the Fe content. The calculated activation energies of the electrical conductivity, presented in Fig. 5b, decrease linearly with the higher mole fraction of Fe and are in the range from 0.39 eV to 0.06 eV.

The defect chemistry of STFx has been considered in detail by Rothschild et al. [32] and Kuhn et al. [70]. The energy band diagram for STFx has been proposed by Rothschild. With increasing Fe concentration, the valence band was proposed to shift closer to the conduction band. The band-gap energy varies from 3.2 eV for STO to ~2 eV for SFO. The top of the valence band formed by Fe^{3+}/Fe^{4+} redox pairs is overlapping with the top of the O2p band, similarly as is the case of strontium ferrite [32]. In the oxidizing conditions used in this work, as discussed by Perry et al. the predominant electronic species (in the case of STF35) are holes [71]. Assuming localization of holes on iron (redox active ion), the concentration of the holes is proportional to $[Fe^{4+}]$ with the Fe^{3+} being the neutral species. As discussed in the XPS section, the relative ratio of Fe^{3+}/Fe^{4+} seems to be constant for different STFx compounds, but the overall charge carrier concentration increases with the increasing Fe content in STFx. The increasing Fe^{3+}/Fe^{4+} charge carrier (localized holes) concentration explains the increasing conductivity values and translates into lowered activation energy.

Such a high difference of the electronic conductivity obtained for the different STFx materials is an interesting case for the comparison with the electrocatalytic measurements. The increased electronic conductivity is usually correlated with an improvement of the overall charge transport and hence boosts the electrochemical performance of the catalyst [72,73]. STFx in general, represent lower values of room temperature conductivity than some of the most active perovskites, e.g. the conductivity of $La_{0.6}Sr_{0.4}CoO_{3-\delta}$ (LSC64) exceeds 600 S cm^{-1} [74] and the conductivity of $(La,Sr)FeO_{3-\delta}$ is within 1–10 S cm^{-1} range [75].

Cheng et al. have studied ex-situ (based on compressed powders) electronic conductivity of the $La_{1-x}Sr_xCoO_3$ (x from 0 to 1) [76]. The A-site cation was varied between a larger Sr^{2+} (1.44 Å) and smaller La^{3+} (1.36 Å), whereas the B-site, redox active cation remained unchanged. The authors also reported a wide range of electrical conductivity values, ranging between ~$3 \cdot 10^{-5}$ S cm^{-1} for $LaCoO_3$ to 0.3 S cm^{-1} for $La_{0.2}Sr_{0.8}CoO_3$. In their case, the crystallographic structure of the materials varied across different x (Sr) levels, so there was a difference in both crystal structure and its electrical conductivity. In the case of STFx, the cubic structure was retained, which makes the influence of the electronic conductivity of the STFx materials more directly comparable. The work by Cheng et al. also shows the possibility to tailor the

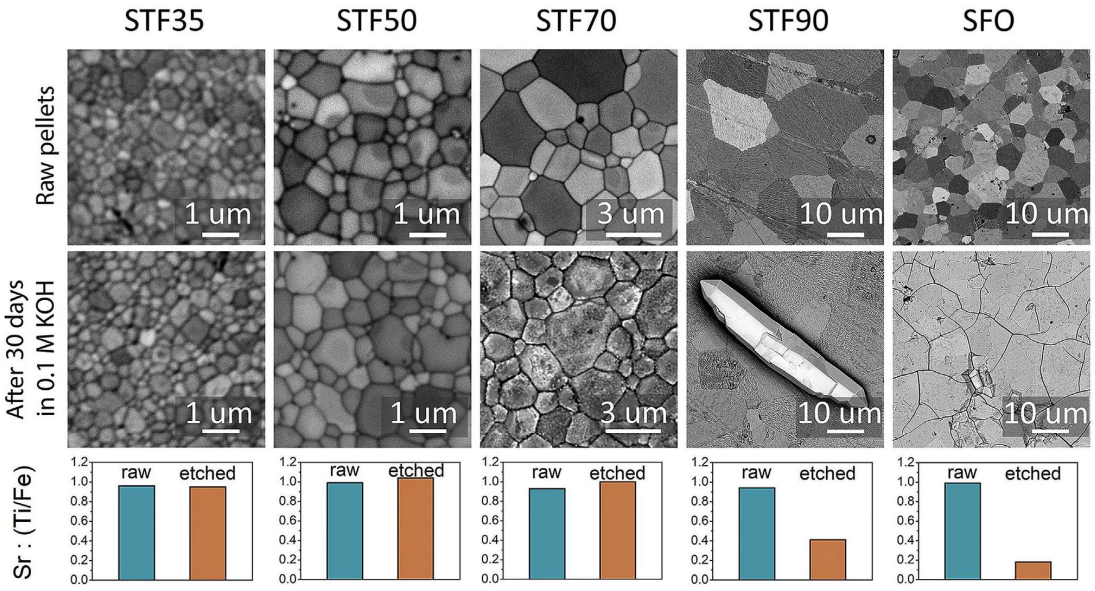

Fig. 6 – $SrTi_{x-1}Fe_xO_{3-\delta}$ pellets chemical stability test performed in 0.1 M KOH.

conductivity value of STF by modification of the A-site cations by partial substitution by La, which might be an interesting topic for future studies.

Conductivity within the STFx system was studied by Hayden et al. based on the 300 nm thin-film samples prepared by physical vapor deposition [34]. The electrical conductivity values were ranging from 10^{-5} S cm^{-1} for STF50 to 0.043 S cm^{-1} for pure SFO. Above a Fe content of 0.75, the conductivity plot remained constant. The values reported in our work differ by even two orders of magnitude in comparison to results obtained by Hayden. The lower than expected conductivity values were attributed by the authors to the potential oxygen deficiency of the films.

Chemical stability of the catalysts

The stability of the strontium-based perovskite compounds at high pH solutions has not been studied in sufficient detail. Several works have emphasized the dissolution of strontium in alkaline solutions [65,77]. However, the influence of the B-site cations on the solubility of the A-site strontium has not been discussed thoroughly.

For the purpose of the present work, the chemical stability of $SrTi_{x-1}Fe_xO_{3-\delta}$ (STFx) was studied using a 30-day immersion test of sintered pellets in an alkaline solution (0.1 M KOH, pH~13). The materials were thus studied without external electrochemical polarization, i.e. purely chemical degradation has been examined. The pellets were prepared in the same manner as the pellets for the electrical conductivity test. To evaluate the extent of Sr dissolution, the surfaces were analyzed for the chemical composition changes via electron microscopy and EDS spectrometry. The results are presented in Fig. 6. The images in the first row of Fig. 6 present surfaces of the sintered pellets after mechanical polishing and thermal etching, which can be considered the initial state, prior to exposure in alkaline solution. The images in the second row of Fig. 6 show the surfaces of the pellets after a 30-day-long exposure to 0.1 M KOH solution. The samples with low Fe content (STF35 and STF50) did not show visible morphological changes. The samples with increased iron content showed increased altering of the surface morphology. The surface of STF70 exhibited an observable increase of roughness, but the individual grains and grain boundaries were still observable. On the STF90 pellet surface, the growth of Sr-rich crystals was noticed (further analyzed by EDS in Fig. S10, the new phase is most likely $SrCO_3$). The grain morphology was still visible, but the grain boundaries, promoted initially by thermal etching, were chemically etched and thus less visible. The surface of SFO shows prominent changes, where no grain/grain boundaries could be observed. The surface also shows large cracks/trenches caused by the etching of Sr.

The morphological changes are connected to the dissolution of Sr from the surface. The EDS results of the studied surfaces are shown in the third row of Fig. 6. The graphs show a ratio of A-site and B-site cations in the perovskite structure (all EDS data is gathered in Table S6). It evidences the

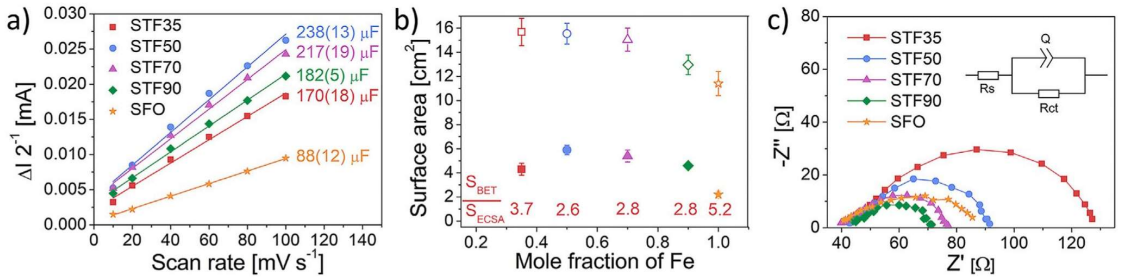

Fig. 7 – (a) Double layer capacitance, (b) comparison of catalyst BET SSA (open symbols) and ECSA (filled symbols) (c) EIS spectra at potential of 1.7 V vs. RHE. Electrochemical tests were performed in 0.1 M KOH electrolyte.

substantial Sr loss in the surface layer of STF90 and SFO pellets due to the chemical degradation. STF70 shows no Sr dissolution, but the pellet surface is rougher after the immersion test, which might indicate the onset of the reaction. The STF50 seems to be unchanged by alkaline environment; no elemental and morphological changes were observed. This observation was further confirmed by cross section studies of STF50 pellets before and after a 30-day-long exposure to 0.1 M KOH solution presented in Fig. S11.

The additional test in Ar-bubbled KOH solution proved that the large crystals visible on STF90 surface are due to a reaction with CO_2 dissolved in electrolyte. Although its amount is very small, it readily reacted with Sr forming $SrCO_3$. The removal of CO_2 from the electrolyte had no visible influence on Sr leaching, which was still pronounced (Fig. S12).

Dissolution of Sr in STFx has also been highlighted by Hayden et al. [34] in their thin film study. They analyzed the chemical content of the films (by EDS) before and after the electrochemical cycling (oxygen evolution reaction). The authors explained the dissolution of Sr in iron-rich compounds by an electrochemical process involving redox active $Fe^{3+/4+}$. Based on our results, the degradation can be narrowed down to a chemical dissolution, not necessarily occurring under oxygen evolution potentials (>1.23 V vs. RHE) but also, to a large extent, at open circuit potential (1.1 V vs. RHE).

The pellet-exposure test showed an important influence of Ti^{4+} content on chemical stability. The compositions with relative Fe content not exceeding 50% seem to be stable chemically, which is an important determinant for materials application.

Electrocatalytic activity

The electrocatalytic activity toward the OER of the $SrTi_{x-1}Fe_xO_{3-\delta}$ (STFx) perovskites was evaluated in 0.1 M KOH solution (pH ~13). Firstly, the electrochemically active surface area (ECSA) was determined. Fig. 7a illustrates the relationship between the current density and the scan rate obtained from cyclic voltammetry in the non-faradaic potential region (at 0 rpm). The values of ECSA estimated from the measured C_{dl} are presented in Fig. 7b. ECSA is a commonly implemented descriptor of metal oxide active sites, accessible for electrocatalysis reactions [48,78–82].

To facilitate the comparison, BET SSA values of the ball-milled catalyst presented in Fig. 1 were multiplied by the mass of the drop-casted catalyst.

For STF35, a low value of ECSA was found. The reason might be the low amount of redox active Fe in the B-site, dominated by the Ti^{4+}. For low Fe content, the percolation between the Fe-containing octahedra cannot form, possibly

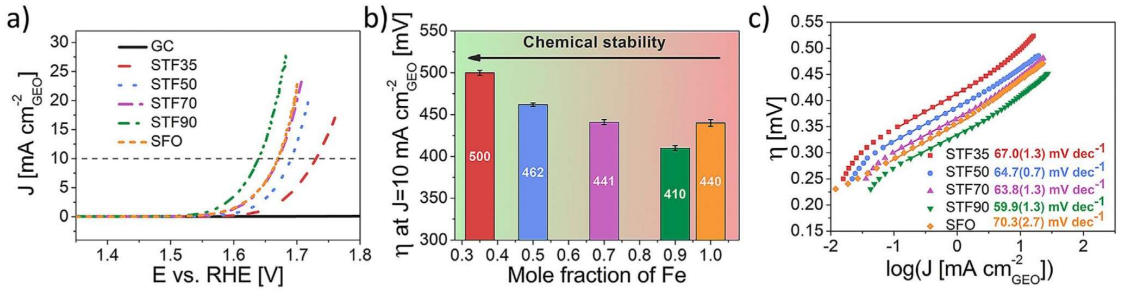

Fig. 8 – (a) OER polarization curves, (b) the overpotentials (η) at 10 mA cm^{-2} current density, and (c) and corresponding Tafel plots measured in O_2 saturated 0.1 M KOH at 10 mV s^{-1} with the rotation speed of 1600 rpm.

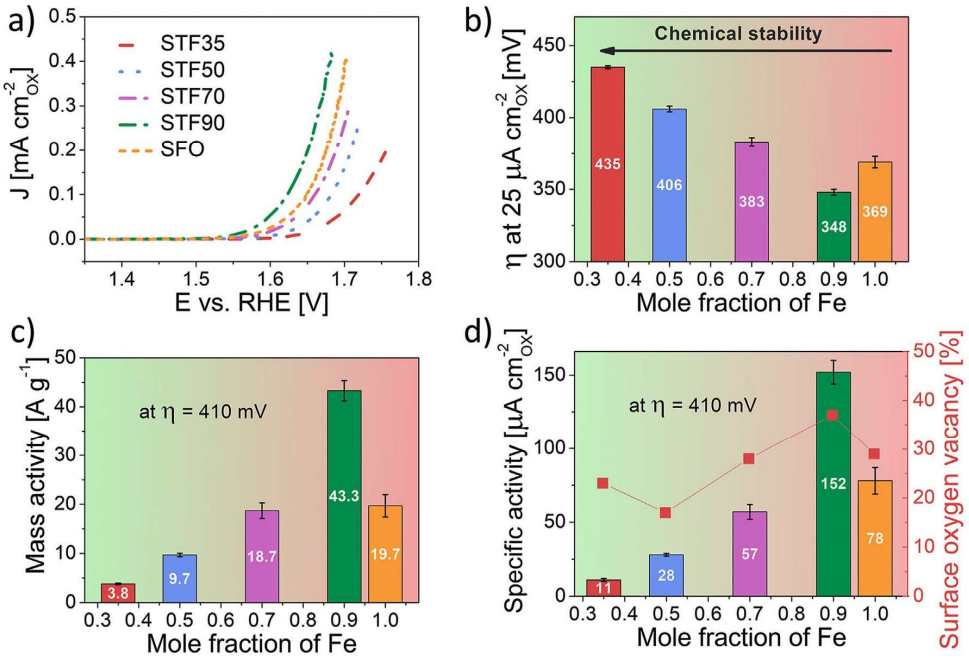

Fig. 9 – (a) OER polarization curves with current density normalized by BET SA, (b) specific surface activity, (c) mass activity and (d) relationship between specific activities and surface oxygen vacancies of $SrTi_{x-1}Fe_xO_{3-\delta}$ (STFx) catalyst powders.

influencing the electrocatalytic activity. The highest ECSA was obtained for the STF50, which also showed the highest BET specific surface area. For the STF70 and STF90, the ECSA showed a decrease. The most likely reason for this was the lower BET specific surface area of these powders. Interestingly, the ratio of BET SSA to ECSA was the same for STF50, STF70, and STF90. Increasing the relative iron content in STFx had no visible influence on the active sites, at least when taking into account ECSA. Pure SFO showed relatively low ECSA with a significant divergence between the ECSA and BET surface areas, possibly caused by the chemical instability of the material.

The electrochemical impedance spectroscopy (EIS) was used to determine the charge transfer resistance (R_{ct}) of the catalysts, one of the factors determining the enhanced activity toward OER [83–85]. The Nyquist plots of all prepared materials are illustrated in Fig. 7c. The incorporation of iron into the perovskite structure induced a systematic drop of the R_{ct} from 90 Ω for STF35 to 28 Ω for STF90 (Table S7). The SFO sample, without structure stabilizing titanium ions, again does not fit the measured trend.

The general OER performance of the $SrTi_{x-1}Fe_xO_{3-\delta}$ (STFx) perovskite catalysts, determined based on the geometrical surface area of the glassy carbon (GC) electrode, is presented in Fig. 8a. The performance of a blank glassy carbon electrode is shown for comparison. The pure SFO shows high performance, inferior only to STF90, but again, SFO does not follow the trend for Ti and Fe-containing samples. The influence of Sr dissolution cannot be accounted for, so it is hard to accurately compare the SFO with Ti/Fe-containing compounds. For the latter, the overall activity toward OER increases monotonically with increasing Fe content in the perovskite structure. As the first benchmark, the overpotentials (η) at 10 mA cm^{-2} current density (based on the geometric area of GC) are presented in Fig. 8b. For the stable STF35 and STF50 perovskites, the overpotentials of 500 mV and 462 mV were obtained. For the less stable STF70 and STF90, lower overpotentials of 441 mV and 410 mV were achieved, with the latter being the lowest. SFO showed an overpotential of 440 mV at 10 mA cm^{-2}. The relative errors, as obtained for three different electrodes, were small, indicating good reproducibility of the measurements, also taking into account the relative instability of the Fe-rich materials. For comparison, the pure RDE-GC electrode demonstrated unnoticeable activity what evidences the negligible contribution into current density growth during OER experiments.

Analysis of the Tafel plots, illustrated in Fig. 8c, revealed that all examined materials are driven by the similar OER mechanism (comparable values of Tafel slopes, 60–70 mV dec^{-1}). The slope of ~60 mV dec^{-1} for STF90 indicates the

chemical step to be the rate-determining step of OER [86]. The higher values of Tafel slopes obtained for the rest of the examined perovskite materials suggest a possibility of a mixed mechanism (e.g. a parallel process) to have an impact on overall OER performance. The Tafel slope of the SFO material was ~70 mV dec^{-1}, which again indicates different behavior of this compound.

Based on the measured BET specific surface areas of the catalysts, the surface specific performance metrics can be compared. The OER polarization plots with the current density normalized by BET specific surface area are presented in Fig. 9a. As the surface of the catalysts was comparable, the trend of surface-specific catalyst activity remained unchanged. Fig. 9b depicts the overpotential determined at 25 μA cm^{-2} (in respect to oxide surface area). The lowest overpotential value of 348 mV was obtained by STF90, followed by 369 mV for SFO. For the stable STF50, an overpotential of 406 mV was determined. Another useful performance metric is the mass specific benchmark, though there is no standard overpotential value for which it is reported. Fig. 9c presents the mass activities of the catalysts determined at the arbitrary overpotential of 410 mV (value of STF90 to achieve a geometrical current density of 10 mA cm^{-2}). The mass activity of the stable STF50 is ~10 A g^{-1}, whereas for the unstable STF90 it is 4x higher. Fig. 9d correlates the specific activity with relative surface oxygen vacancy concentration estimated by XPS studies. The increasing OER performance of STFx with oxygen vacancies is observed. However, due to the pronounced instability, the SFO does not follow the trend.

It has been considered that oxygen vacancies in perovskites can improve the electrocatalytic performance toward OER. For instance, Lu et al. have created oxygen vacancies in $LaCoO_3$ perovskite by Sr doping and Ar plasma treatment [87]. It was shown that abundant oxygen vacancies acted as active sites and showed high intrinsic activity. Oxygen vacancies concentration increase, promoted by partial Sr^{2+} substitution for La^{3+}, resulted in Tafel slope decrease from 92.1 to 74.2 mV dec^{-1} for $LaCoO_{3-\delta}$ and $La_{0.7}Sr_{0.3}Co_{3-\delta}$, respectively. Additionally, the Ar plasma treatment was applied to further manufacture oxygen vacancies and the Tafel slope reduction of $La_{0.7}Sr_{0.3}Co_{3-\delta}$ to 70.8 mV dec^{-1} was reported. Hona and Ramezanipour reported the facile synthesis method of the oxygen-deficient $SrMnO_{3-\delta}$ [88]. It was shown that the electrocatalytic properties are correlated with the structure and oxygen vacancy. $SrMnO_{2.5}$, the most oxygen-deficient among prepared materials, exhibited the best electrocatalytic activity for the OER. She et al. have established a direct correlation between the surface oxygen vacancies along with the surface Fe oxidation state and the specific activity enhancement of the $La_{1-x}Sr_xFeO_{3-\delta}$ (x = 0, 0.2, 0.5, 0.8 and 1) [89]. In their work, they found the optimum amount of surface oxygen vacancies in $La_{0.2}Sr_{0.8}FeO_{3-\delta}$, resulting in the lowest OER overpotential and Tafel slope among examined catalysts.

The activity of the STFx (given by specific overpotential values) seems to correlate linearly with the amount of iron in the perovskite, especially for the compounds with Ti. The cubic perovskite structure is retained for all the studied compounds. Moreover, the (logarithm) of the total electrical conductivity increases linearly vs. the iron content. For the compound without Ti, the electrochemical activity, which is inferior to STF90, might be decreased due to the rapid dissolution of Sr, also influencing the Tafel slope of the catalyst. The two other high-Fe content compounds (STF90 and STF70), although show high electrochemical performance, also tend to dissolve Sr, rendering them not stable. Hayden et al. have proposed that the reason for the increased Sr-dissolution at high Fe-compounds, might be the activation of the lattice oxygen mechanism (LOM) [34]. Our study has shown that the dissolution occurs also at OCV, where no oxygen evolution takes place, so the origin is purely chemical. The Tafel slope obtained for all the STFx materials was quite similar. In the case of triggering LOM mechanism, a change in Tafel slope could probably be expected [90]. Though the mechanism and the relative scale of A-site Sr-dissolution of OER catalysts are not clear, our work shows that the presence of Ti ions (up to 50/50 Fe/Ti composition) stabilize the perovskite structure and limits the A-site cation dissolution. The Tafel slope of ~60 mV dec^{-1}, obtained for all STFx compounds can arise from the rate limiting reaction: $MOOH + OH^- <=> MOO^- + H_2O$ [91]. The Tafel slope of ~60 mV dec^{-1} is often reported for high performance perovskites [92]. In this case, increasing the number of active sites (able to create MOO^-/MOOH - Fe in B-site octahedra) would lead to increasing electrochemical performance, which is consistent with our work. On the other hand, the proposed rate limiting mechanism does not involve the electronic charge carriers. Therefore, the observed dependency of the performance vs. electrical conductivity is a secondary, non-critical aspect. It is affirmed by the fact that for the less conducting, lower Fe-content compounds, a slight increase in the Tafel slope has been observed. The electronic conductivity is nonetheless the requirement for efficient charge collection, thus its value should be maximized for efficient electrode materials. Based on these assumptions, we propose that in the case of STFx materials, the active sites include metal ion site (adsorbate evolution mechanism).

The recently reported OER results for perovskites are collected in Table S8. The presented data defines STFx as decent OER catalysts. Due to presented stability issues, only the STF50 shows a reasonable mixture of stability and performance. It shows an overpotential of 460 mV at 10 mA cm^{-2}, which might seem quite high, but taking into account its high surface area (~35 m^2 g^{-1}), the oxide surface (406 mV at 25 μA cm^{-2}) and mass specific (~10 A g^{-1} at 410 mV) performance, it is comparable to other perovskite catalysts.

In the study by Hayden et al. [34] on thin films, the analysis of the onset (ignition) potential and current density achieved at 370 mV (1.6 V vs. RHE) showed improved performance of Fe-rich compositions. The authors concluded that high OER activity was correlated with the low stability of the oxides. For high Fe catalysts, participation of lattice oxygen in OER was discussed. The composition based on 50Fe/50Ti has been proposed as a viable, stable catalyst, which showed the current density at 370 mV of ~2 mA cm^{-2}, comparable to the performance of STF reported here (taking into account the geometric area).

The best perovskite OER catalyst is the monoclinic $SrIrO_3$ developed by Yu et al. [93]. The noble metal containing catalyst was prepared by solid-state reaction, which resulted in powder with BET of 14.6 m^2 g^{-1}. In 0.1 M KOH, the overpotential required for 10 mA cm^{-2} (geometric area) was

~300 mV with a low Tafel slope of 42 mV dec^{-1} and the mass activity of ~50 A g^{-1} (at 320 mV).

$SrCo_{0.9}Ti_{0.1}O_{3-d}$, $SrF_{0.9}Ti_{0.1}O_{3-d}$ and $Ba_{0.5}Sr_{0.5}Co_{0.8}Fe_{0.2}O_{3-d}$ perovskites (with surface areas of <1 m^2 g^{-1}) were studied by Su et al. [51] In 0.1 M KOH, the materials showed overpotentials of 510 mV, 520 mV and 490 mV, much higher than in the present study. The respective Tafel slopes were 88 mV dec^{-1}, 102 mV dec^{-1} and 84 mV dec^{-1}, indicating inferior kinetics than in our case.

Zhu et al. proposed $SrNb_{0.1}Co_{0.7}Fe_{0.2}O_{3-d}$ (SNCF) as a highly active catalyst for OER [52]. Similarly to STFx, SNCF contains a single A-site cation (Sr) and the B-sublattice contains Fe. The material was prepared by solid state reaction and benchmarked against BSCF. The low surface area (<1 m^2 g^{-1}) SNCF showed an overpotential (in 0.1 M KOH, at 10 mA cm^{-2}) of 500 mV, which decreased to 420 mV for ball milled (BM-SNCF) powder (surface area ~6 m^2 g^{-1}). The BSCF showed an overpotential of 510 mV. The Tafel slopes for the SNCF and BM-SNCF were 76 mV dec^{-1} and 90 mV dec^{-1}, respectively. Even though the overpotential obtained for BM-SNCF was lower than for un-milled SNCF, the specific activity was not improved by the milling. The mass activity of the BM-SNCF was ~93 A g^{-1} (at 500 mV).

In comparison to many good oxide catalysts developed in the last years, STF50 is based on abundant, environmentally friendly elements and shows a comparable performance, which can make it an attractive alternative as the OER catalyst.

Conclusions

The series of $SrTi_{1-x}Fe_xO_{3-\delta}$ with x = 0.35, 0.50, 0.70, 0.90 and 1.00 (STFx) perovskites have been fabricated via the solid state reaction synthesis technique and tested as potential oxygen evolution catalysts in alkaline electrolyte. The powders showed a remarkably high specific surface area of >30 m^2 g^{-1}. The chemical stability test, based on immersion of pellets in the electrolyte, indicated that up to Fe content of 50%, the materials were stable in 0.1 M KOH, whereas the samples with higher Fe content showed dissolution of strontium. The surface morphology change induced by Sr dissolution was especially pronounced for the $SrFeO_{3-\delta}$ (SFO) composition. Electrocatalytic oxygen evolution tests showed an inverse linear correlation (excluding the unstable $SrFeO_{3-\delta}$) between the iron content and OER overpotential. Overall, the samples presented satisfactory performance, especially when surface specific values were compared. The redox active B-site containing $Fe^{3+/4+}$ together with inherent surface oxygen vacancies and the high surface area of the catalyst powders provide performance which is comparable to other recently reported highly active perovskite catalysts. Based on earth abundant and non-toxic elements, the $Sr(Ti,Fe)O_{3-\delta}$ (STFx) materials are an interesting, environmentally friendly catalyst alternative.

Declaration of competing interest

The authors declare that they have no known competing financial interests or personal relationships that could have appeared to influence the work reported in this paper.

Acknowledgment

The presented research is part of the "Nanocrystalline ceramic materials for efficient electrochemical energy conversion" project, carried out within the First TEAM programme of the Foundation for Polish Science (grant agreement nr. POIR.04.04.00-00-42E9/17-00), co-financed by the European Union under the European Regional Development Fund. Funding from Statutory Funds of WETI PG is also acknowledged.

Appendix A. Supplementary data

Supplementary data to this article can be found online at https://doi.org/10.1016/j.ijhydene.2021.06.088.

REFERENCES

[1] Godula-Jopek A, Millet P, Guillet N, Laurencin J, Mougin J, Bourasseau C, et al. Hydrogen production by electrolysis. Weinheim: Wiley-VCH Verlag GmbH & Co. KGaA; 2015.
[2] Fabbri E, Schmidt TJ. Oxygen evolution reaction—the enigma in water electrolysis. ACS Catal 2018;8:9765–74. https://doi.org/10.1021/acscatal.8b02712.
[3] Li Z, Lv L, Ao X, Li JG, Sun H, An P, et al. An effective method for enhancing oxygen evolution kinetics of LaMO3 (M = Ni, Co, Mn) perovskite catalysts and its application to a rechargeable zinc–air battery. Appl Catal B Environ 2020;262. https://doi.org/10.1016/j.apcatb.2019.118291.
[4] Yu L, Xu N, Zhu T, Xu Z, Sun M, Geng D. La0.4Sr0.6Co0.7Fe0.2Nb0.1O3-δ perovskite prepared by the sol-gel method with superior performance as a bifunctional oxygen electrocatalyst. Int J Hydrogen Energy 2020;45:30583–91. https://doi.org/10.1016/j.ijhydene.2020.08.105.
[5] Hegde GS, Ghosh A, Badam R, Matsumi N, Sundara R. Role of defects in low-cost perovskite catalysts toward ORR and OER in lithium-oxygen batteries. ACS Appl Energy Mater 2020;3(2):1338–48. https://doi.org/10.1021/acsaem.9b01727.
[6] Omari E, Omari M. Cu-doped GdFeO3 perovskites as electrocatalysts for the oxygen evolution reaction in alkaline media. Int J Hydrogen Energy 2019;44:28769–79. https://doi.org/10.1016/j.ijhydene.2019.09.088.
[7] Hao Z, Wei P, Yang Y, Sun J, Song Y, Guo D, et al. Self-assembled CuCo2S4 nanosheets with rich surface Co3+ as efficient electrocatalysts for oxygen evolution reaction. Appl Surf Sci 2021;536:147826. https://doi.org/10.1016/j.apsusc.2020.147826.
[8] Xiong P, Yang F, Ding Z, Jia Y, Liu J, Yan X, et al. Preparation and electrocatalytic properties of spinel CoxFe3-xO4 nanoparticles. Int J Hydrogen Energy 2020;45:13841–7. https://doi.org/10.1016/j.ijhydene.2020.03.098.
[9] Peng X, wang zhao. Facile route of P-doped defect-rich manganese-cobalt oxide spinel with enhanced oxygen evolution reaction performance. ChemNanoMat 2020;6(12):1812–8. https://doi.org/10.1002/cnma.202000475.
[10] Lankauf K, Cysewska K, Karczewski J, Mielewczyk-Gryń A, Górnicka K, Cempura G, et al. MnxCo3-xO4 spinel oxides as efficient oxygen evolution reaction catalysts in alkaline media. Int J Hydrogen Energy 2020;5. https://doi.org/10.1016/j.ijhydene.2020.03.188.
[11] Wang P, Qin R, Ji P, Pu Z, Zhu J, Lin C, et al. Synergistic coupling of Ni nanoparticles with Ni3C nanosheets for highly

efficient overall water splitting. Small 2020;16:1–10. https://doi.org/10.1002/smll.202001642.
[12] Zakaria MB, Zheng D, Apfel UP, Nagata T, Kenawy ERS, Lin J. Dual-heteroatom-doped reduced graphene oxide sheets conjoined CoNi-based carbide and sulfide nanoparticles for efficient oxygen evolution reaction. ACS Appl Mater Interfaces 2020;12:40186–93. https://doi.org/10.1021/acsami.0c06141.
[13] Zhu S, Lei J, Zhang L, Lu L. Efficient electrocatalytic oxygen evolution by Fe3C nanosheets perpendicularly grown on 3D Ni foams. Int J Hydrogen Energy 2019;44:16507–15. https://doi.org/10.1016/j.ijhydene.2019.04.214.
[14] Li Y, Ge L, Zhou Y, Li L, Li W, Xu J, et al. KB-templated, in situ synthesis of highly dispersed bimetallic NiFe phosphides as efficient oxygen evolution catalysts. Inorg Chem Front 2020;7:4930–8. https://doi.org/10.1039/D0QI00627K.
[15] Zhang Y, Xu J, Ding Y, Wang C. Tuning the d-band center enables nickel-iron phosphide nanoprisms as efficient electrocatalyst towards oxygen evolution. Int J Hydrogen Energy 2020;45:17388–97. https://doi.org/10.1016/j.ijhydene.2020.04.213.
[16] Xie Y, Chen M, Cai M, Teng J, Huang H, Fan Y, et al. Hollow cobalt phosphide with N-doped carbon skeleton as bifunctional electrocatalyst for overall water splitting. Inorg Chem 2019;58:14652–9. https://doi.org/10.1021/acs.inorgchem.9b02333.
[17] Karmakar A, Karthick K, Kumaravel S, Sankar SS, Kundu S. Enabling and inducing oxygen vacancies in cobalt iron layer double hydroxide via selenization as precatalysts for electrocatalytic hydrogen and oxygen evolution reactions. Inorg Chem 2021;60(3):2023–36. https://doi.org/10.1021/acs.inorgchem.0c03514.
[18] Ma G, Du X, Zhang X. Facile synthesis of molybdenum-based layered double hydroxide nanorods for boosting water oxidation reaction. Int J Hydrogen Energy 2020;45(58):33641–7. https://doi.org/10.1016/j.ijhydene.2020.09.097.
[19] Cysewska K, Rybarczyk MK, Cempura G, Jasinski P, Molin S. The influence of the electrodeposition parameters on the properties of Mn-Co-based nanofilms as anode materials for alkaline electrolysers. Materials 2020;13. https://doi.org/10.3390/ma13112662.
[20] Antipin D, Risch M. Trends of epitaxial perovskite oxide films catalyzing the oxygen evolution reaction in alkaline media. J Phys Energy 2020;2:032003. https://doi.org/10.1088/2515-7655/ab812f.
[21] Suntivich J, May KJ, Gasteiger HA, Goodenough JB, Shao-Horn Y. A perovskite oxide optimized for oxygen evolution catalysis from molecular orbital principles. Science 2011;334:1383–5. https://doi.org/10.1126/science.1212858. 80-.
[22] Tasleem S, Tahir M. Recent progress in structural development and band engineering of perovskites materials for photocatalytic solar hydrogen production: a review. Int J Hydrogen Energy 2020;45:19078–111. https://doi.org/10.1016/j.ijhydene.2020.05.090.
[23] Zhang Z, Zhou D, Wu X, Bao X, Liao J, Wen M. Synthesis of La 0.2 Sr 0.8 CoO 3 and its electrocatalytic activity for oxygen evolution reaction in alkaline solution. Int J Hydrogen Energy 2019;44:7222–7. https://doi.org/10.1016/j.ijhydene.2019.01.268.
[24] Deng H, Shu L, Wang Z, Mao J, Liang F. SrTi0.1CoxFe0.9-xO3-δ Perovskites for enhanced oxygen evolution reaction activity. Int J Hydrogen Energy 2020;45:13129–38. https://doi.org/10.1016/j.ijhydene.2020.03.057.
[25] Zhang SL, Cox D, Yang H, Park BK, Li CX, Li CJ, et al. High stability SrTi1-: XFexO3- δ electrodes for oxygen reduction and oxygen evolution reactions. J Mater Chem 2019;7:21447–58. https://doi.org/10.1039/c9ta07548h.
[26] Zhang S, Wang H, Yang T, Lu MY, Li C, Li C, et al. Advanced oxygen-electrode-supported solid oxide electrochemical cells with Sr(Ti,Fe)O3-δ-based fuel electrodes for electricity generation and hydrogen production. J Mater Chem 2020;8:25867–79. https://doi.org/10.1039/d0ta06678h.
[27] Shah MAKY, Rauf S, Mushtaq N, Tayyab Z, Ali N, Yousaf M, et al. Semiconductor Fe-doped SrTiO3-δ perovskite electrolyte for low-temperature solid oxide fuel cell (LT-SOFC) operating below 520 °C. Int J Hydrogen Energy 2020;45:14470–9. https://doi.org/10.1016/j.ijhydene.2020.03.147.
[28] Kamran Yousaf Shah MA, Mushtaq N, Rauf S, Xia C, Zhu B. The semiconductor SrFe0.2Ti0.8O3-δ-ZnO heterostructure electrolyte fuel cells. Int J Hydrogen Energy 2019;44:30319–27. https://doi.org/10.1016/j.ijhydene.2019.09.145.
[29] Zhuang Y, Lin Y, Zhu D, Zheng Y, Yu Z. A study of conductivity in the Sr(Fe1–xTix)O3–δ system. J Am Ceram Soc 1989;72:1444–6. https://doi.org/10.1111/j.1151-2916.1989.tb07671.x.
[30] Kharton VV, Kovalevsky AV, Tsipis EV, Viskup AP, Naumovich EN, Jurado JR, et al. Mixed conductivity and stability of A-site-deficient Sr(Fe,Ti)O 3-δ perovskites. J Solid State Electrochem 2002;7:30–6. https://doi.org/10.1007/s10008-002-0286-3.
[31] Galakhov VR, Kurmaev EZ, Kuepper K, Neumann M, McLeod JA, Moewes A, et al. Valence band structure and X-ray spectra of oxygen-deficient ferrites SrFeOx. J Phys Chem C 2010;114:5154–9. https://doi.org/10.1021/jp909091s.
[32] Rothschild A, Menesklou W, Tuller HL, Ivers-Tiffée E. Electronic structure, defect chemistry, and transport properties of SrTi 1-xFe xO 3-y solid solutions. Chem Mater 2006;18:3651–9. https://doi.org/10.1021/cm052803x.
[33] Litzelman SJ, Rothschild A, Tuller HL. The electrical properties and stability of SrTi0.65Fe0.35O3–δ thin films for automotive oxygen sensor applications. Sensor Actuator B Chem 2005;108:231–7. https://doi.org/10.1016/j.snb.2004.10.040.
[34] Hayden BE, Rogers FK. Oxygen reduction and oxygen evolution on SrTi1 – xFexO3 – y (STFO) perovskite electrocatalysts. J Electroanal Chem 2018;819:275–82. https://doi.org/10.1016/j.jelechem.2017.10.056.
[35] Mroziński A, Molin S, Karczewski J, Miruszewski T, Jasiński P. Electrochemical properties of porous Sr 0.86 Ti 0.65 Fe 0.35 O 3 oxygen electrodes in solid oxide cells: impedance study of symmetrical electrodes. Int J Hydrogen Energy 2019;44:1827–38. https://doi.org/10.1016/j.ijhydene.2018.11.203.
[36] Mroziński A, Molin S, Karczewski J, Kamecki B, Jasiński P. The influence of iron doping on performance of SrTi. ECS Trans 2019;91:1299–307. https://doi.org/10.1149/09101.1299ecst.
[37] Mroziński A, Molin S, Jasiński P. Study of oxygen electrode reactions on symmetrical porous SrTi0.30Fe0.70O3-δ electrodes on Ce0.8Gd0.2O1.9 electrolyte at 800 °C–500 °C. Electrochim Acta 2020:346. https://doi.org/10.1016/j.electacta.2020.136285.
[38] Schneider CA, Rasband WS, Eliceiri KW. NIH Image to ImageJ: 25 years of image analysis. Nat Methods 2012;9:671–5. https://doi.org/10.1038/nmeth.2089.
[39] Rodriguez-Carvajal J. Recent advances in magnetic structure determination by neutron powder diffraction. Phys B 1993;55–69. https://doi.org/10.1016/0921-4526(93)90108-I.
[40] Adler P, Eriksson S. Structural properties, Mössbauer spectra, and magnetism of perovskite-type oxides SrFe1-xTixO3-y. Zeitschrift Fur Anorg Und Allg Chemie 2000;626:118–24. https://doi.org/10.1002/(sici)1521-3749(200001)626:1<118::aid-zaac118>3.0.co;2-k.

[41] Blasco J, Stankiewicz J, García J. Phase segregation in the Gd1-xSrxFeO 3-δ series. J Solid State Chem 2006;179:898–908. https://doi.org/10.1016/j.jssc.2005.12.023.
[42] VAN DER Pauw LJ. A method of measuring the resistivity and Hall coefficient on lamellae of arbitrary shape. Philips Tech Rev 1958;20:220–4.
[43] Suntivich J, Gasteiger HA, Yabuuchi N, Shao-Horn Y. Electrocatalytic measurement methodology of oxide catalysts using a thin-film rotating disk electrode. J Electrochem Soc 2010;157:B1263. https://doi.org/10.1149/1.3456630.
[44] Yagi S, Yamada I, Tsukasaki H, Seno A, Murakami M, Fujii H, et al. Covalency-reinforced oxygen evolution reaction catalyst. Nat Commun 2015;6:1–6. https://doi.org/10.1038/ncomms9249.
[45] Garsany Y, Ge J, St-Pierre J, Rocheleau R, Swider-Lyons KE. Analytical procedure for accurate comparison of rotating disk electrode results for the oxygen reduction activity of Pt/C. J Electrochem Soc 2014;161:628–40. https://doi.org/10.1149/2.036405jes.
[46] Alia SM, Pivovar BS. Evaluating hydrogen evolution and oxidation in alkaline media to establish baselines. J Electrochem Soc 2018;165:F441–55. https://doi.org/10.1149/2.0361807jes.
[47] McCrory CCL, Jung S, Peters JC, Jaramillo TF. Benchmarking heterogeneous electrocatalysts for the oxygen evolution reaction. J Am Chem Soc 2013;135:16977–87. https://doi.org/10.1021/ja407115p.
[48] Wei C, Rao RR, Peng J, Huang B, Stephens IEL, Risch M, et al. Recommended practices and benchmark activity for hydrogen and oxygen electrocatalysis in water splitting and fuel cells. Adv Mater 2019;1806296:1–24. https://doi.org/10.1002/adma.201806296.
[49] Schulze-Küppers F, Ten Donkelaar SFP, Baumann S, Prigorodov P, Sohn YJ, Bouwmeester HJM, et al. Structural and functional properties of SrTi1-xFexO3-δ ($0 \leq x \leq 1$) for the use as oxygen transport membrane. Separ Purif Technol 2015;147:414–21. https://doi.org/10.1016/j.seppur.2014.12.020.
[50] Fabbri E, Nachtegaal M, Binninger T, Cheng X, Kim B-J, Durst J, et al. Dynamic surface self-reconstruction is the key of highly active perovskite nano-electrocatalysts for water splitting. Nat Mater 2017;1–8. https://doi.org/10.1038/nmat4938.
[51] Su C, Wang W, Chen Y, Yang G, Xu X, Tadé MO, et al. SrCo0.9Ti0.1O3-δ as a new electrocatalyst for the oxygen evolution reaction in alkaline electrolyte with stable performance. ACS Appl Mater Interfaces 2015;7:17663–70. https://doi.org/10.1021/acsami.5b02810.
[52] Zhu Y, Zhou W, Chen ZG, Chen Y, Su C, Tadé MO, et al. SrNb0.1Co0.7Fe0.2O3-δ perovskite as a next-generation electrocatalyst for oxygen evolution in alkaline solution. Angew Chem Int Ed 2015;54:3897–901. https://doi.org/10.1002/anie.201408998.
[53] Cheng X, Fabbri E, Kim B, Nachtegaal M, Schmidt TJ. Effect of ball milling on the electrocatalytic activity of Ba0.5Sr0.5Co0.8Fe0.2O3 towards the oxygen evolution reaction. J Mater Chem 2017;5:13130–7. https://doi.org/10.1039/c7ta00794a.
[54] Zhang H, Guan D, Gao X, Yu J, Chen G, Zhou W, et al. Morphology, crystal structure and electronic state one-step co-tuning strategy towards developing superior perovskite electrocatalysts for water oxidation. J Mater Chem 2019;7:19228–33. https://doi.org/10.1039/c9ta06020k.
[55] Longo VM, Das Graça Sampaio Costa M, Zirpole Simões A, Rosa ILV, Santos COP, Andrés J, et al. On the photoluminescence behavior of samarium-doped strontium titanate nanostructures under UV light. A structural and electronic understanding. Phys Chem Chem Phys 2010;12:7566–79. https://doi.org/10.1039/b923281h.
[56] Kim CS, Bishop SR, Perry NH, Tuller HL. Electro-chemo-mechanical studies of perovskite-structured mixed ionic-electronic conducting SrSn1-xFexO3-x/2+δpart I: defect chemistry. J Electroceram 2017;38:74–80. https://doi.org/10.1007/s10832-017-0064-3.
[57] Filatova EO, Egorova YV, Galdina KA, Scherb T, Schumacher G, Bouwmeester HJM, et al. Effect of Fe content on atomic and electronic structure of complex oxides Sr(Ti,Fe)O3 − δ. Solid State Ionics 2017;308:27–33. https://doi.org/10.1016/j.ssi.2017.05.016.
[58] Badreldin A, Abusrafa AE, Abdel-Wahab A. Oxygen-deficient perovskites for oxygen evolution reaction in alkaline media: a review. Emergent Mater 2020;3:567–90. https://doi.org/10.1007/s42247-020-00123-z.
[59] Chatzichristodoulou C, Norby P, Hendriksen PV, Mogensen MB. Size of oxide vacancies in fluorite and perovskite structured oxides. J Electroceram 2015;34:100–7. https://doi.org/10.1007/s10832-014-9916-2.
[60] Falcón H, Barbero JA, Alonso JA, Martínez-Lope MJ, Fierro JLG. SrFeO3-δ perovskite oxides: chemical features and performance for methane combustion. Chem Mater 2002;14:2325–33. https://doi.org/10.1021/cm011292l.
[61] Steinsvik S, Bugge R, Gjønnes J, Taftø J, Norby T. The defect structure of SrTi 1−x Fe x O 3−y (x = 0–0.8) investigated by electrical cdoncutivity measurements and electron energy loss spectroscopy (EELS). J Phys Chem Solid 1997;58:969–76. https://doi.org/10.1016/S0022-3697(96)00200-4.
[62] Miruszewski T, Dzierzgowski K, Winiarz P, Wachowski S, Mielewczyk-Gryń A, Gazda M. Structural properties and water uptake of STi1-xFexO3-x/2-δ. Materials 2020;13. https://doi.org/10.3390/ma13040965.
[63] Koo B, Kim K, Kim JK, Kwon H, Han JW, Jung WC. Sr segregation in perovskite oxides: why it happens and how it exists. Joule 2018;2:1476–99. https://doi.org/10.1016/j.joule.2018.07.016.
[64] Nenning A, Opitz AK, Rameshan C, Rameshan R, Blume R, Hävecker M, et al. Ambient pressure XPS study of mixed conducting perovskite-type SOFC cathode and anode materials under well-defined electrochemical polarization. J Phys Chem C 2016;120:1461–71. https://doi.org/10.1021/acs.jpcc.5b08596.
[65] Boucly A, Fabbri E, Artiglia L, Cheng X, Pergolesi D, Ammann M, et al. Surface segregation acts as surface engineering for the oxygen evolution reaction on perovskite oxides in alkaline media. Chem Mater 2020;32:5256–63. https://doi.org/10.1021/acs.chemmater.0c01396.
[66] Ghaffari M, Shannon M, Hui H, Tan OK, Irannejad A. Preparation, surface state and band structure studies of SrTi (1-X)Fe (x)O (3-δ) (x = 0-1) perovskite-type nano structure by X-ray and ultraviolet photoelectron spectroscopy. Surf Sci 2012;606:670–7. https://doi.org/10.1016/j.susc.2011.12.013.
[67] Fetisov AV, Kozhina GA, Estemirova SK, Fetisov VB, Gulyaeva RI. XPS study of the chemical stability of DyBa2Cu3O6+δ superconductor. Phys C Supercond Its Appl 2015;508:62–8. https://doi.org/10.1016/j.physc.2014.11.003.
[68] Zhu J, Li H, Zhong L, Xiao P, Xu X, Yang X, et al. Perovskite oxides: preparation, characterizations, and applications in heterogeneous catalysis. ACS Catal 2014;4:2917–40. https://doi.org/10.1021/cs500606g.
[69] Torrance JB, Lacorro P, Asavaroengchai C, Metzger RM. Simple and perovskite oxides of transition-metals: why some are metallic, while most are insulating. J Solid State Chem 1991;90:168–72. https://doi.org/10.1016/0022-4596(91)90182-H.
[70] Kuhn M, Kim JJ, Bishop SR, Tuller HL. Oxygen nonstoichiometry and defect chemistry of perovskite-

structured BaxSr1-xTi1-yFeyO 3-y/2+δ solid solutions. Chem Mater 2013;25:2970–5. https://doi.org/10.1021/cm400546z.
[71] Perry NH, Kim JJ, Bishop SR, Tuller HL. Strongly coupled thermal and chemical expansion in the perovskite oxide system Sr(Ti,Fe)O3-α. J Mater Chem 2015;3:3602–11. https://doi.org/10.1039/c4ta05247a.
[72] Fabbri E, Nachtegaal M, Cheng X, Schmidt TJ. Superior bifunctional electrocatalytic activity of Ba0.5Sr0.5Co0.8Fe0.2O3-δ/Carbon composite electrodes: insight into the local electronic structure. Adv Energy Mater 2015;5:1–5. https://doi.org/10.1002/aenm.201402033.
[73] Wang H, Zhou M, Choudhury P, Luo H. Perovskite oxides as bifunctional oxygen electrocatalysts for oxygen evolution/reduction reactions – a mini review. Appl Mater Today 2019;16:56–71. https://doi.org/10.1016/j.apmt.2019.05.004.
[74] Kamecki B, Karczewski J, Abdoli H, Chen M, Jasiński G, Jasiński P, et al. Deposition and electrical and structural properties of La0.6Sr0.4CoO3 thin films for application in high-temperature electrochemical cells. J Electron Mater 2019;48:5428–41. https://doi.org/10.1007/s11664-019-07372-7.
[75] Vogt UF, Sfeir J, Richter J, Soltmann C, Holtappels P. B-site substituted lanthanum strontium ferrites as electrode materials for electrochemical applications. Pure Appl Chem 2008;80:2543–52. https://doi.org/10.1351/pac200880112543.
[76] Schmidt TJ, Marzari N, El Kazzi M, Haumont R, Castelli IE, Fabbri E, et al. Oxygen evolution reaction on La 1– x Sr x CoO 3 perovskites: a combined experimental and theoretical study of their structural, electronic, and electrochemical properties. Chem Mater 2015;27:7662–72. https://doi.org/10.1021/acs.chemmater.5b03138.
[77] Hirai S, Ohno T, Uemura R, Maruyama T, Furunaka M, Fukunaga R, et al. Ca1-xSrxRuO3 perovskite at the metal-insulator boundary as a highly active oxygen evolution catalyst. J Mater Chem 2019;7:15387–94. https://doi.org/10.1039/c9ta03789f.
[78] Practices B, Performance RE. Best practices for reporting electrocatalytic performance of nanomaterials. 2018. p. 10–3. https://doi.org/10.1021/acsnano.8b07700.
[79] Liu Y, Yin S, Shen PK. Asymmetric 3d electronic structure for enhanced oxygen evolution catalysis. ACS Appl Mater Interfaces 2018;10:23131–9. https://doi.org/10.1021/acsami.8b06106.
[80] Bhowmick S, Dhankhar A, Sahu TK, Jena R, Gogoi D, Peela NR, et al. Low overpotential and stable electrocatalytic oxygen evolution reaction utilizing doped perovskite oxide, La 0.7 Sr 0.3 MnO 3 , modified by cobalt phosphate. ACS Appl Energy Mater 2020;3(2):1279–85. https://doi.org/10.1021/acsaem.9b02167.
[81] Lin Q, Zhu Y, Hu Z, Yin Y, Lin HJ, Chen C Te, et al. Boosting the oxygen evolution catalytic performance of perovskites: via optimizing calcination temperature. J Mater Chem 2020;8:6480–6. https://doi.org/10.1039/c9ta13972a.
[82] Baumung M, Schönewald F, Erichsen T, Volkert CA, Risch M. Influence of particle size on the apparent electrocatalytic activity of LiMn2O4 for oxygen evolution. Sustain Energy Fuels 2019;3:2218–26. https://doi.org/10.1039/c8se00551f.
[83] Xu S, Wang M, Saranya G, Chen N, Zhang L, He Y, et al. Pressure-driven catalyst synthesis of Co-doped Fe3C@Carbon nano-onions for efficient oxygen evolution reaction. Appl Catal B Environ 2020;268:118385. https://doi.org/10.1016/j.apcatb.2019.118385.
[84] Shen Z, Zhuang Y, Li W, Huang X, Oropeza FE, Hensen EJM, et al. Increased activity in the oxygen evolution reaction by Fe 4+ -induced hole states in perovskite La 1–x Sr x FeO 3. J Mater Chem 2020:4407–15. https://doi.org/10.1039/c9ta13313e.
[85] Song S, Zhou J, Sun J, Zhang S, Lin X, Hu Z, et al. Understanding the origin of high oxygen evolution reaction activity in the high Sr-doped perovskite. Chin J Catal 2020;41:592–7. https://doi.org/10.1016/S1872-2067(19)63441-8.
[86] Doyle RL, Godwin IJ, Brandon MP, Lyons MEG. Redox and electrochemical water splitting catalytic properties of hydrated metal oxide modified electrodes. Phys Chem Chem Phys 2013;15:13737–83. https://doi.org/10.1039/c3cp51213d.
[87] Lu Y, Ma A, Yu Y, Tan R, Liu C, Zhang P, et al. Engineering oxygen vacancies into LaCoO 3 perovskite for efficient electrocatalytic oxygen evolution. ACS Sustainable Chem Eng 2019;7:2906–10. https://doi.org/10.1021/acssuschemeng.8b05717.
[88] Hona RK, Ramezanipour F. Effect of the oxygen vacancies and structural order on the oxygen evolution activity: a case study of SrMnO3-δ featuring four different structure types. Inorg Chem 2020;59:4685–92. https://doi.org/10.1021/acs.inorgchem.9b03774.
[89] She S, Yu J, Tang W, Zhu Y, Chen Y, Sunarso J, et al. Systematic study of oxygen evolution activity and stability on La 1– x Sr x FeO 3–δ perovskite electrocatalysts in alkaline media. ACS Appl Mater Interfaces 2018;10:11715–21. https://doi.org/10.1021/acsami.8b00682.
[90] Pan Y, Xu X, Guan D, Hayre RO, Shao Z, Zhong Y, et al. Direct evidence of boosted oxygen evolution over perovskite by enhanced lattice oxygen participation. Nat Commun 2020:1–10. https://doi.org/10.1038/s41467-020-15873-x.
[91] Shinagawa T, Garcia-Esparza AT, Takanabe K. Insight on Tafel slopes from a microkinetic analysis of aqueous electrocatalysis for energy conversion. Sci Rep 2015;5:1–21. https://doi.org/10.1038/srep13801.
[92] Zhu Y, Tahini HA, Hu Z, Chen Z, Zhou W, Komarek AC, et al. Boosting oxygen evolution reaction by creating both metal ion and lattice-oxygen active sites in a complex oxide. 2019. p. 1–8. https://doi.org/10.1002/adma.201905025. 1905025.
[93] Yu J, Yu J, Wu X, Guan D, Hu Z, Weng SC, et al. Monoclinic SrIrO3: an easily synthesized conductive perovskite oxide with outstanding performance for overall water splitting in alkaline solution. Chem Mater 2020;32:4509–17. https://doi.org/10.1021/acs.chemmater.0c00149.

Supplementary materials

The effect of Fe on chemical stability and oxygen evolution performance of high surface area $SrTi_{x-1}Fe_xO_{3-\delta}$ mixed ionic-electronic conductors in alkaline media

Krystian Lankauf[1*], Aleksander Mroziński[1], Patryk Błaszczak[2], Karolina Górnicka[2], Justyna Ignaczak[1], Marcin Łapiński[2], Jakub Karczewski[2], Grzegorz Cempura[3], Piotr Jasiński[1], Sebastian Molin[1]

[1]Advanced Materials Center, Faculty of Electronics, Telecommunications and Informatics, Gdańsk University of Technology, ul. G. Narutowicza 11/12, 80-233 Gdańsk, Poland

[2] Advanced Materials Center, Faculty of Applied Physics and Mathematics, Gdańsk University of Technology, ul. G. Narutowicza 11/12, 80-233 Gdańsk, Poland

[3]International Centre of Electron Microscopy for Materials Science, AGH University of Science and Technology, al. A. Mickiewicza 30, 30-059 Kraków, Poland

*e-mail: krystian.lankauf@pg.edu.pl

Island-like Fe-rich phase was observed on STF35 pellets surface for chemical stability tests sintered at 1200 °C (Fig. S6 and S7). In order to hinder such growth, the lower etching temperatures were tested. If the temperature of thermal etching was too low the grains' boundary etching did not occur. Under these conditions, the etching temperature for STF35 of 1100 °C was chosen.

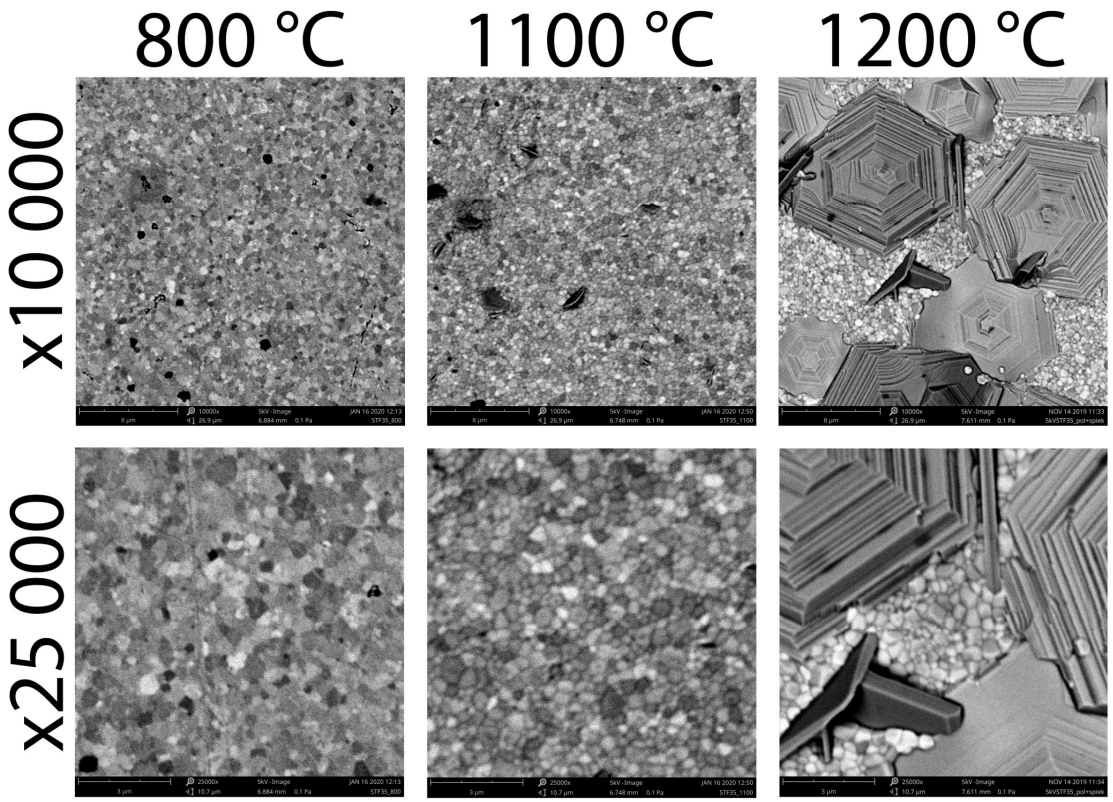

Fig. S1 – Thermal surface etching of STF35 pellets performed at different temperatures.

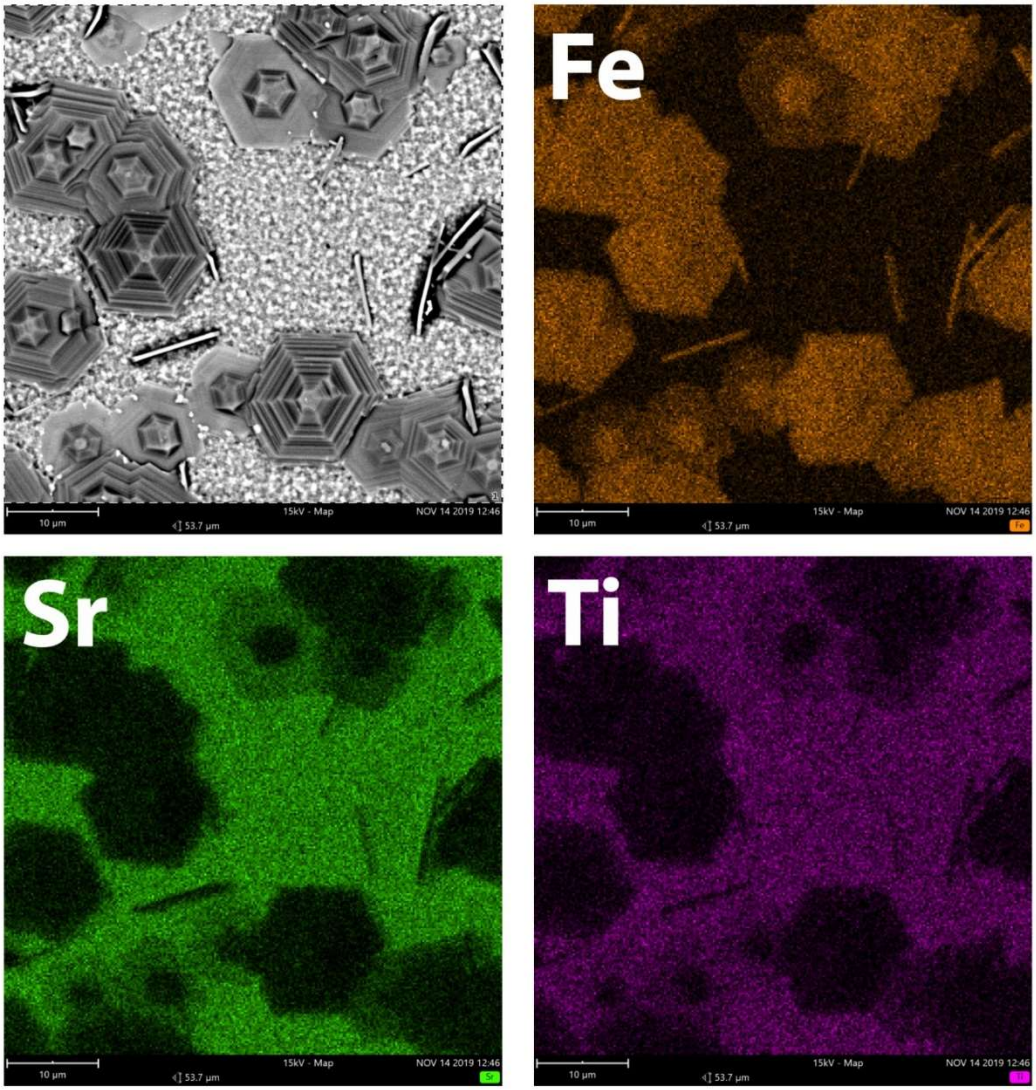

Fig. S2 – EDS maps of STF35 pellet thermally etched at 1200 °C.

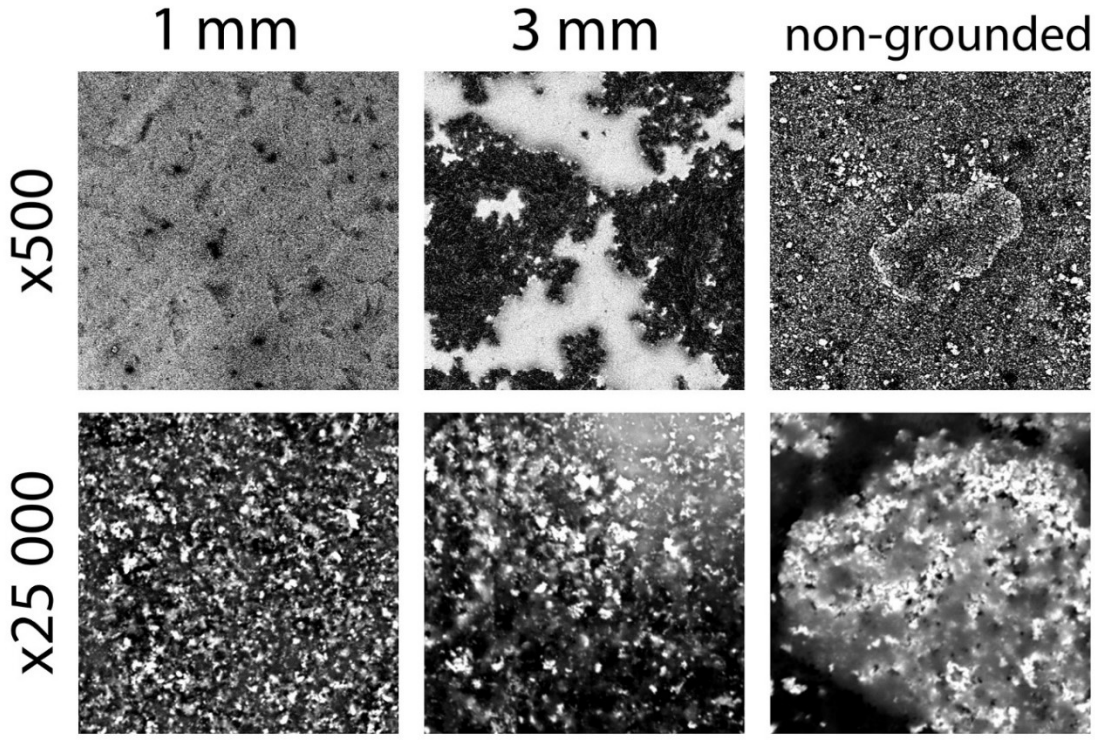

Fig. S3 – SEM images of Ni foil coated with catalyst inks ball-milled using 1 and 3 mm diameter YSZ balls and non-grounded one.

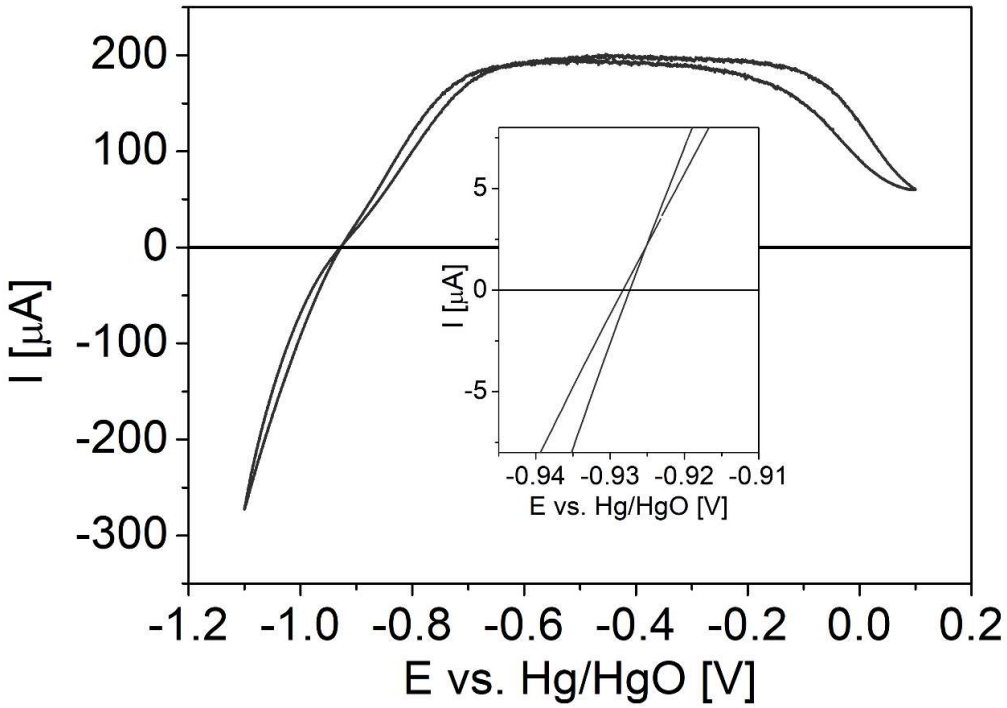

Fig. S4 – Calibration of Hg/HgO electrode against RHE in H_2 saturated 0.1 M KOH electrolyte.

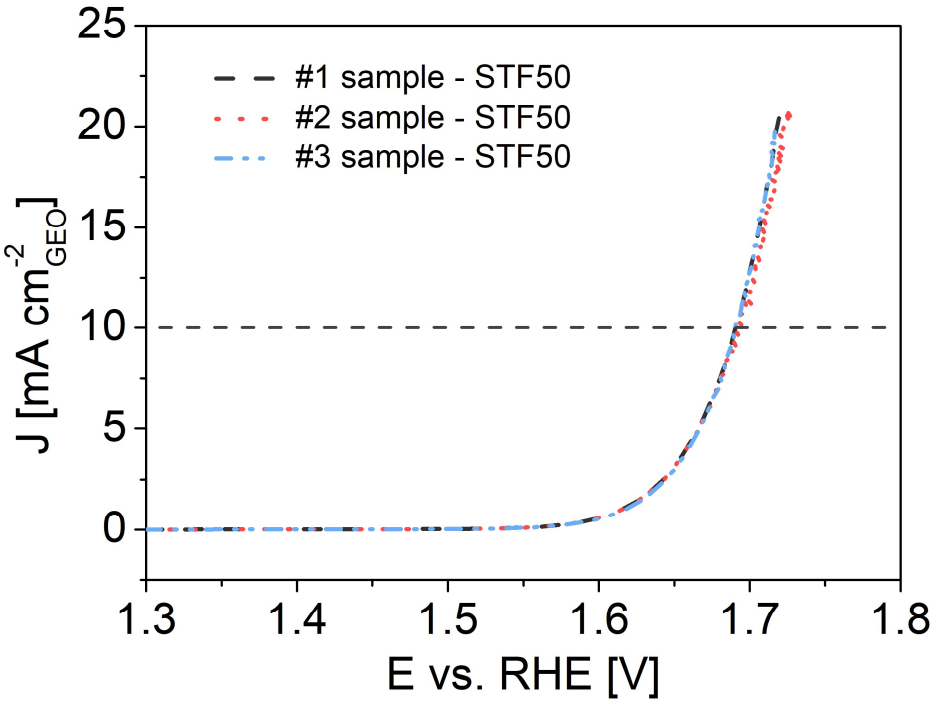

Fig. S5 - OER polarization curves obtained for STF50.

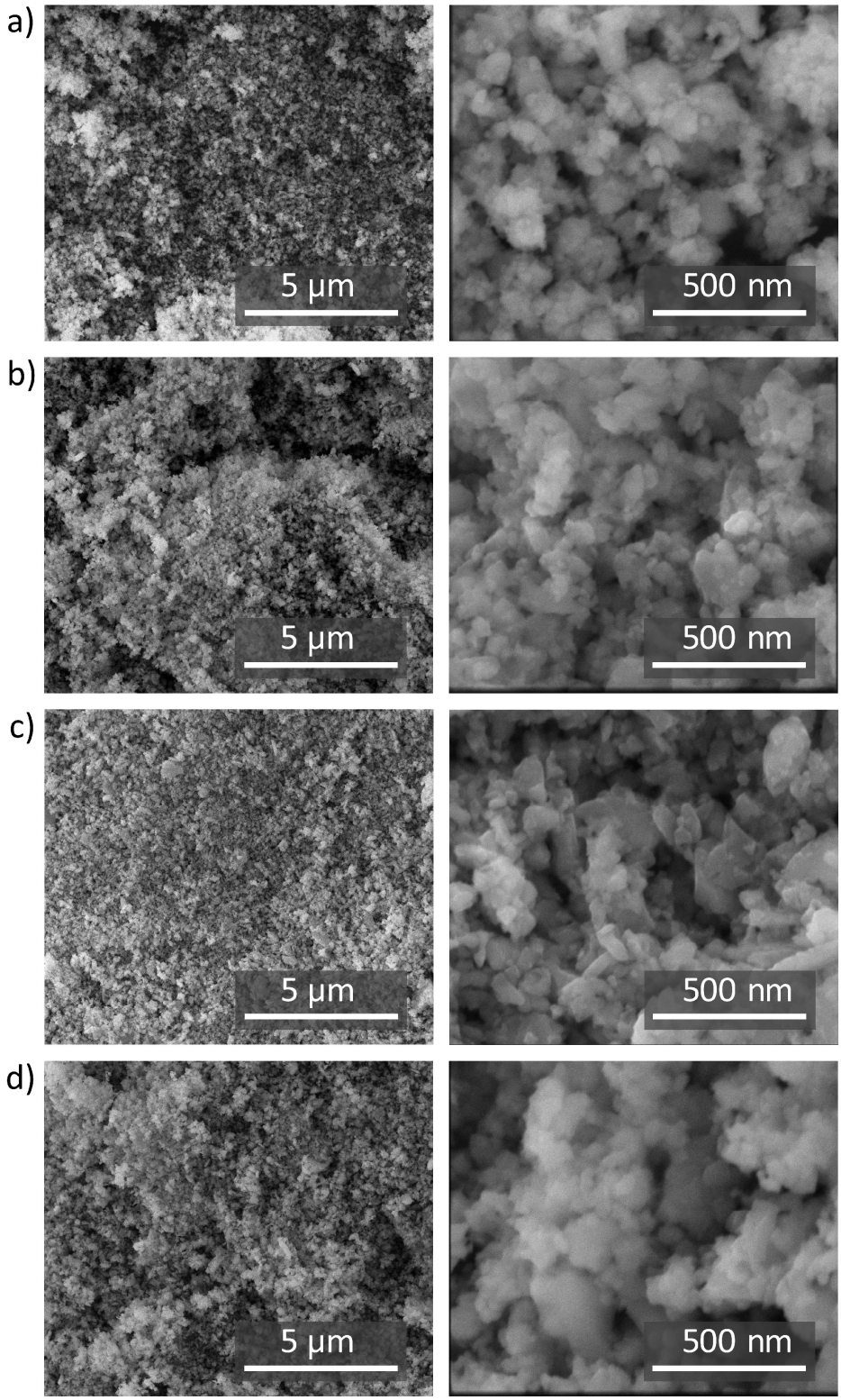

Fig. S6 – SEM images of synthesized and ball milled powders (a) STF35, (b) STF50, (c) STF90, and (d) SFO. Magnification of left column is x10 000 and the right one is x100 000.

Table S1 – Unit cell parameters calculated by Le Bail refinement and BET specific surface area of the $SrTi_{x-1}Fe_xO_{3-\delta}$ (x= 0.35, 0.5, 0.7, 0.9, and 1)

Material	Cell parameters a=b=c [Å]	Surface Area [$m^2\,g^{-1}$]	Surface Area after ball milling [$m^2\,g^{-1}$]
STF35	3.8985	18.2(1.0)	34.5(2.5)
STF50	3.8947	16.9(1.0)	34.2(1.9)
STF70	3.8803	17.1(0.9)	33.1(2.1)
STF90	3.8771	14.5(0.9)	28.5(1.8)
SFO	3.8597	11.6(0.8)	25.1(2.2)

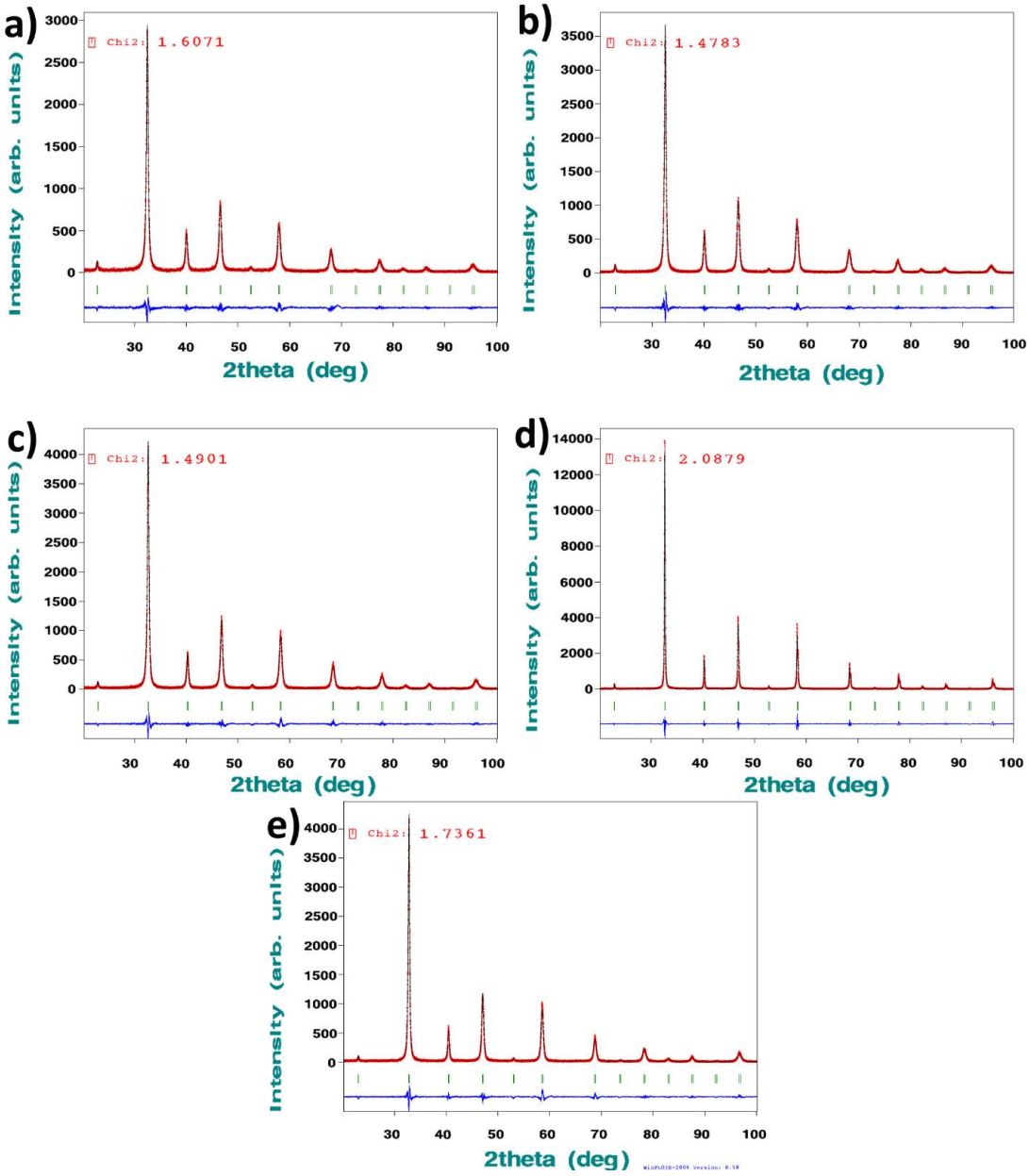

Fig. S7 – Le Bail refinement plots of the pXRD diffractions patterns of a) STF35, (b) STF50, (c) STF70, (d) STF90, and (e) SFO.

Table S2 – Conductivity at 25 °C and activation energies of $SrTi_{x-1}Fe_xO_{3-\delta}$ pellets.

Sample	Conductivity at 25 °C [S cm^{-1}]	Activation energy [eV]
STF35	$1.48 \cdot 10^{-5}$	0.39
STF50	$7.87 \cdot 10^{-4}$	0.32
STF70	$4.09 \cdot 10^{-2}$	0.26
STF90	1.3	0.20
SFO	53	0.06

Table S3 – The relative amounts of the different Sr species of SrTix-1FexO3-δ powders calculated by fitting Sr3d spectra.

Sample	Sr2+ - perovskite [%]	SrCO3 [%]
STF35	50	50
STF50	55	45
STF70	60	40
STF90	60	40
SFO	75	25

Table S4 – The relative amounts of the different Fe species of $SrTi_{x-1}Fe_xO_{3-\delta}$ powders calculated by fitting Fe2p spectra.

Sample	Fe^{3+} [%]	Fe^{4+} [%]	Average valence
STF35	55	45	3.45
STF50	60	40	3.4
STF70	60	40	3.4
STF90	60	40	3.4
SFO	55	45	3.45

Table S5 – The relative amounts of the different surface oxygen species of $SrTi_{x-1}Fe_xO_{3-\delta}$ powders calculated by fitting O1s spectra.

Sample	H_2O [%]	OH^- [%]	O_2^{2-}/O^-	lattice O^{2-}
STF35	4	28	23	45
STF50	4	37	17	42
STF70	10	37	28	25
STF90	3	31	37	29
SFO	12	44	29	15

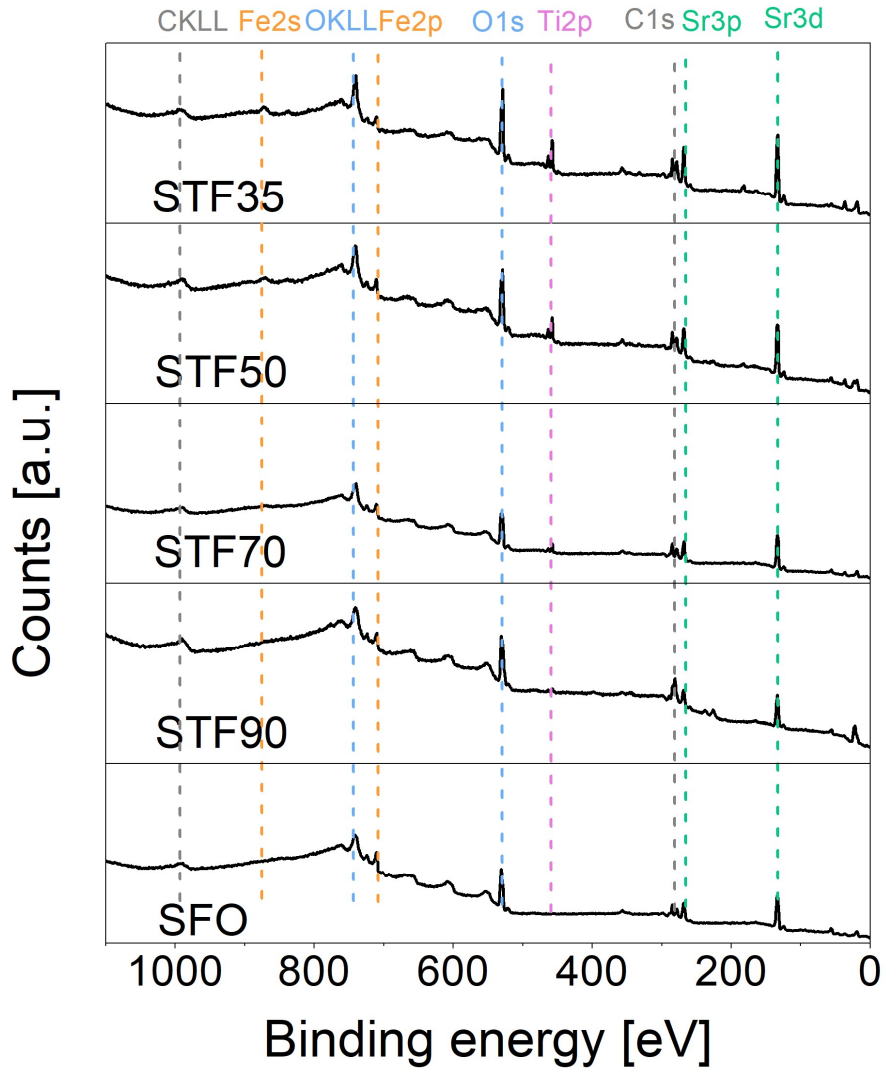

Fig. S8 – Full XPS element survey scans of $SrTi_{x-1}Fe_xO_{3-\delta}$ powders.

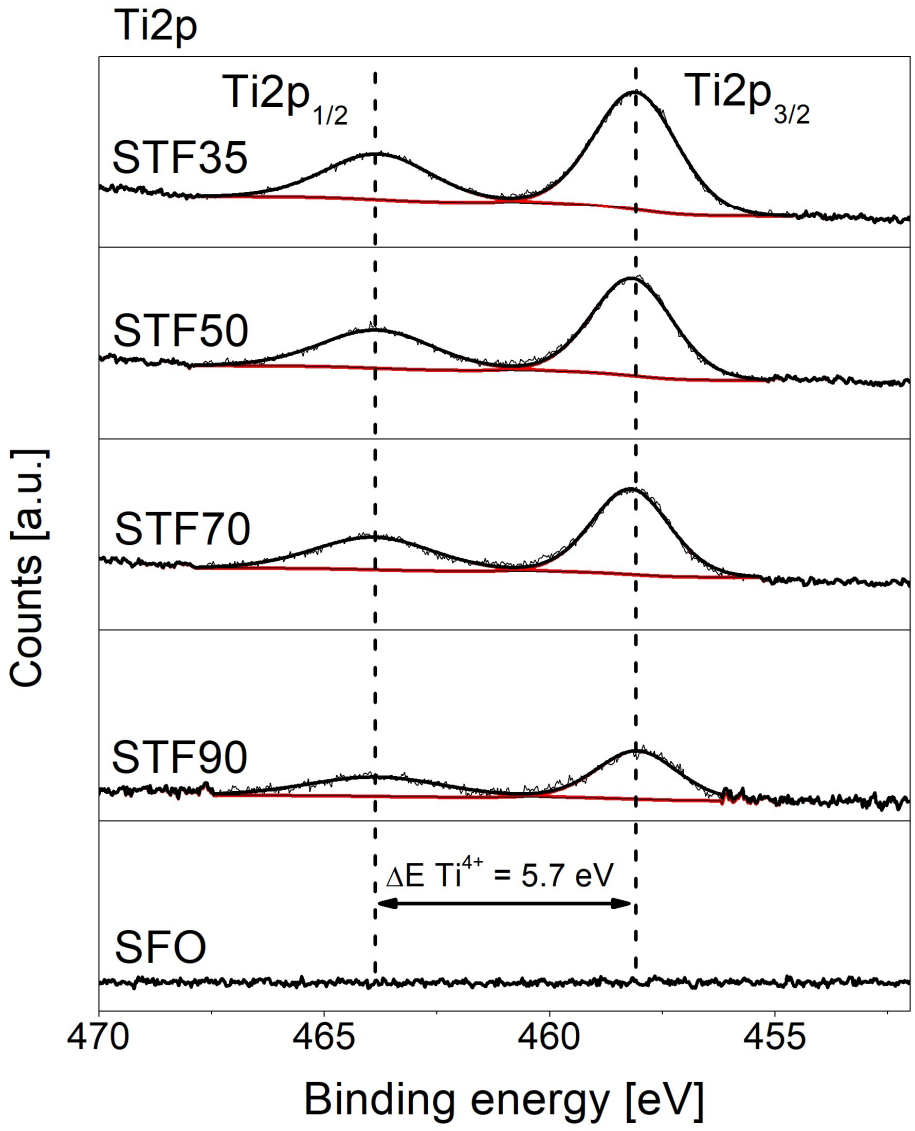

Fig. S9 – Ti2p X-ray photoelectron spectra of $SrTi_{x-1}Fe_xO_{3-\delta}$ powders.

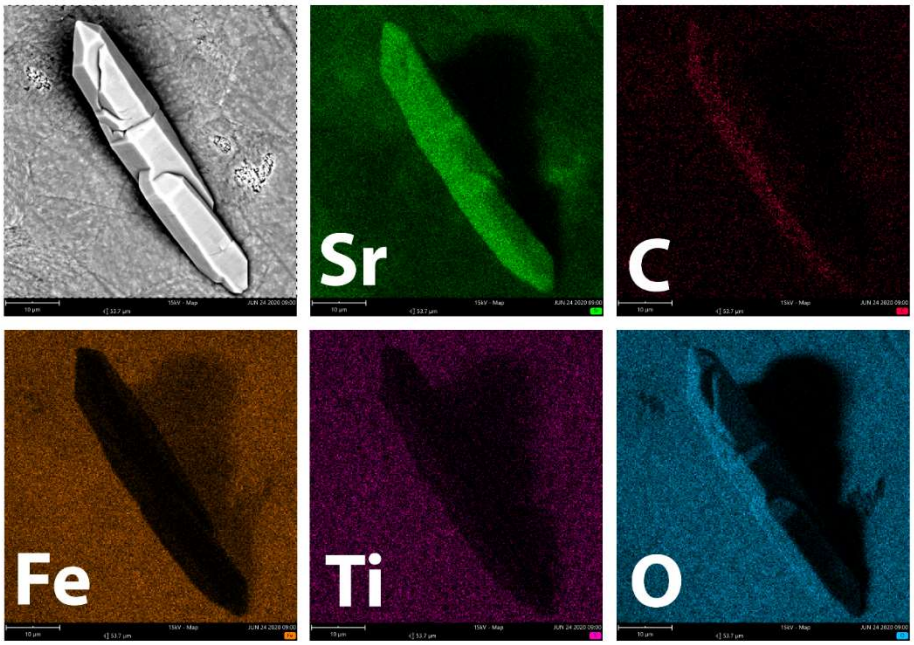

Fig. S10 – EDS map of STF90 pellet etched in 0.1 M KOH for 30 days.

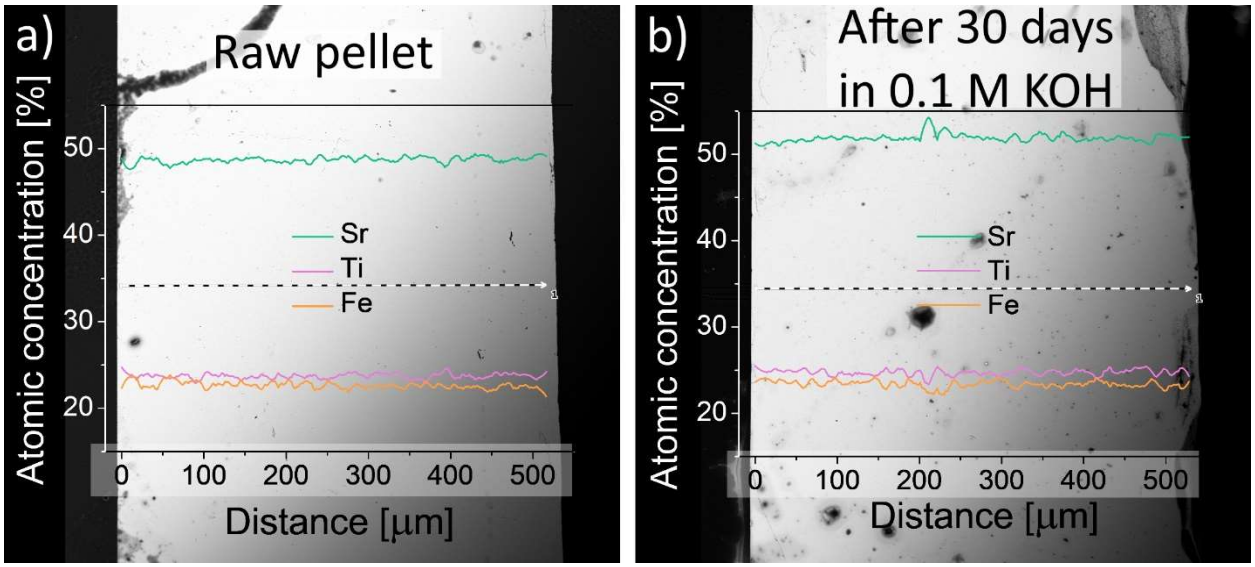

Fig. S11 – STF50 pellets cross section of a) raw and b) after 30 days immersion in 0.1 M KOH pellet.

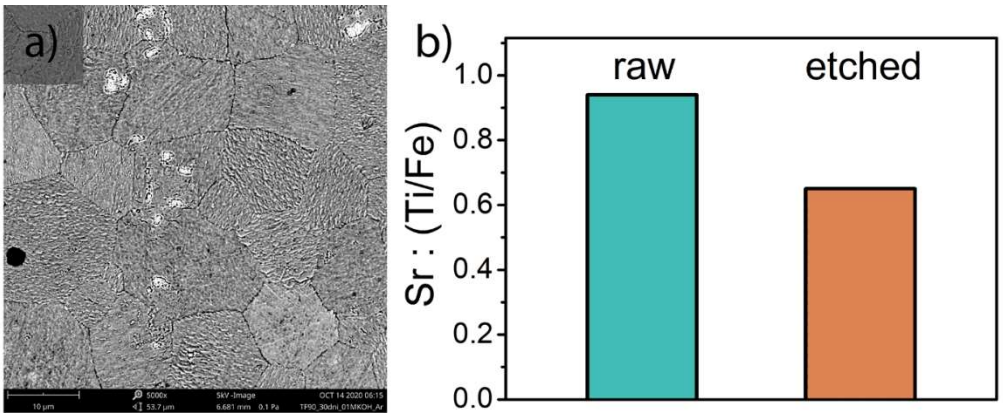

Fig. S12 – (a) Surface of STF90 pellet etched for 30 days in Ar saturated 0.1 M KOH and (b) A:B cations ratio before and after etching.

Table S6 – EDS chemical composition analysis results performed on raw and chemically etched $SrTi_{x-1}Fe_xO_{3-\delta}$ pellets.

	At. conc. in raw pellets [%]				At. conc. After 30 days in 0.1 M KOH [%]			
	Sr	Ti	Fe	O	Sr	Ti	Fe	O
STF35	14.5	9.8	5.3	70.4	14.7	9.9	5.6	69.8
STF50	14.7	7.5	7.3	70.0	13.9	6.8	6.6	72.3
STF70	15.1	4.6	10.5	69.7	13.5	4.5	10.0	71.6
STF90	15.2	1.7	14.5	68.6	6.7	1.6	14.6	76.6
SF0	15.5	-	15.6	68.9	3.9	-	21.6	74.5

Table S7 – OER performance data of examined $SrTi_{x-1}Fe_xO_{3-\delta}$ catalysts. Colors of the rows highlights the chemical stability of the catalysts (green – high stability, red – poor stability).

Electrode material	η_{GEO} at 10 mA cm^{-2} [mV]	η_{OX} at 25 µA cm^{-2} [mV]	Tafel slope [mV dec^{-1}]	R_{ct} [Ω]	ECSA [cm^2]
STF35	500(3)	435(1)	67.0(1.3)	90(9)	4.3(0.5)
STF50	462(2)	405(2)	64.7(0.7)	51(2)	5.9(0.4)
STF70	441(3)	382(3)	63.8(1.5)	38(2)	5.4(0.5)
STF90	410(3)	347(2)	59.9(0.4)	28(2)	4.6(0.2)
SFO	440(4)	369(4)	70.3(2.7)	44(5)	2.2(0.3)

Table S8 – Comparison of reported OER electrocatalysts including Fe containing perovskites.

Material	Electrolyte	Supporting electrode	η at 10 mA cm^{-2} [mV]	Tafel slope [mV dec^{-1}]	Catalyst's loading [mg cm^{-2}]	Ref.
STF90	0.1 M KOH	RDE-GC	410	59.9	0.232	This work
STF70			441	65.8		
STF50			460	64.7		
$SrIrO_3$	0.1 M KOH	RDE-GC	300			[1]
$La_{0.7}Sr_{0.3}MnO_3$ /Co-Pi	1.0 M NaOH	FTO	220	62	-	[2]
GFC20600	1.0 M KOH	Ni-plate	367	139	15	[3]
$La_{0.2}Sr_{0.8}FeO_3$		RDE-GC	318 at 50 mA μm^2 oxide	58	0.25 mg	[4]
$LaFeO_{2.85}Cl_{0.15}$	0.1 M KOH		500	67	0.283	[5]
$SrTi_{0.1}Co_{0.5}Fe_{0.4}O_{3-\delta}$			370	94.82	0.232	[6]
$SrCo_{0.5}Fe_{0.5}O_{3-\delta}$ (800 °C)			327	62	0.278	[7]
$SrCo_{0.5}Fe_{0.5}O_{3-\delta}$ (1000 °C)			377	74	0.278	[7]
$SrCo_{0.5}Fe_{0.5}O_{3-\delta}$ (1200 °C)			407	76	0.278	[7]
$SrNb_{0.1}Co_{0.7}Fe_{0.2}O_{3-\delta}$			420	90	0.232	[8]
$SrFe_{0.9}Ti_{0.1}O_{3-\delta}$			520	102	0.32	[9]
$SrCo_{0.9}Ti_{0.1}O_{3-\delta}$			510	88	0.32	[9]
$SrFeO_{3-\delta}$			480	74.92	0.232	[10]
$La_{0.2}Sr_{0.8}FeO_{3-\delta}$			370	60.10	0.232	[10]

REFERENCES

[1] Yu J, Yu J, Wu X, Guan D, Hu Z, Weng SC, et al. Monoclinic SrIrO3: An Easily Synthesized Conductive Perovskite Oxide with Outstanding Performance for Overall Water Splitting in Alkaline Solution. Chem Mater 2020;32:4509–17. https://doi.org/10.1021/acs.chemmater.0c00149.

[2] Bhowmick S, Dhankhar A, Sahu TK, Jena R, Gogoi D, Peela NR, et al. Low Overpotential and Stable Electrocatalytic Oxygen Evolution Reaction Utilizing Doped Perovskite Oxide, La 0.7 Sr 0.3 MnO 3 , Modified by Cobalt Phosphate. ACS Appl Energy Mater 2020. https://doi.org/10.1021/acsaem.9b02167.

[3] Omari E, Omari M. Cu-doped GdFeO3 perovskites as electrocatalysts for the oxygen evolution reaction in alkaline media. Int J Hydrogen Energy 2019;44:28769–79. https://doi.org/10.1016/j.ijhydene.2019.09.088.

[4] Shen Z, Zhuang Y, Li W, Huang X, Oropeza FE, Hensen EJM, et al. Increased activity in the oxygen evolution reaction by Fe 4+ -induced hole states in perovskite La 1−x Sr x FeO 3 . J Mater Chem A 2020:4407–15. https://doi.org/10.1039/c9ta13313e.

[5] Zhang J, Cui Y, Jia L, He B, Zhang K, Zhao L. Engineering anion defect in LaFeO2.85Cl0.15 perovskite for boosting oxygen evolution reaction. Int J Hydrogen Energy 2019;44:24077–85. https://doi.org/10.1016/j.ijhydene.2019.07.162.

[6] Deng H, Shu L, Wang Z, Mao J, Liang F. SrTi0.1CoxFe0.9-xO3-d Perovskites for enhanced oxygen evolution reaction activity 2020:1–10. https://doi.org/10.1016/j.ijhydene.2020.03.057.

[7] Lin Q, Zhu Y, Hu Z, Yin Y, Lin HJ, Chen C Te, et al. Boosting the oxygen evolution catalytic performance of perovskites: Via optimizing calcination temperature. J Mater Chem A 2020;8:6480–6. https://doi.org/10.1039/c9ta13972a.

[8] Zhu Y, Zhou W, Chen ZG, Chen Y, Su C, Tadé MO, et al. SrNb0.1Co0.7Fe0.2O3-δ perovskite as a next-generation electrocatalyst for oxygen evolution in alkaline solution. Angew Chemie - Int Ed 2015;54:3897–901. https://doi.org/10.1002/anie.201408998.

[9] Su C, Wang W, Chen Y, Yang G, Xu X, Tadé MO, et al. SrCo0.9Ti0.1O3-δ As a New Electrocatalyst for the Oxygen Evolution Reaction in Alkaline Electrolyte with Stable Performance. ACS Appl Mater Interfaces 2015;7:17663–70. https://doi.org/10.1021/acsami.5b02810.

[10] She S, Yu J, Tang W, Zhu Y, Chen Y, Sunarso J, et al. Systematic Study of Oxygen Evolution Activity and Stability on La 1– x Sr x FeO 3−δ Perovskite Electrocatalysts in Alkaline Media. ACS Appl Mater Interfaces 2018;10:11715–21. https://doi.org/10.1021/acsami.8b00682.

4.4. Tailoring a Low-Energy Ball Milled $MnCo_2O_4$ Spinel Catalyst to Boost Oxygen Evolution Reaction Performance

W następującej pracy przedstawiono wpływ niskoenergetycznego mielenia, dodatku przewodzącego węgla ora jonomeru na właściwości fizykochemiczne oraz aktywność elektrochemiczną komercyjnego proszku spinelu $MnCo_2O_4$. Zastosowanie mielenia bezpośrednio wpływa na rozdrobnienie ziaren proszku, a stopień rozdrobnienia zależy od czasu procesu. Na podstawie obserwacji SEM zauważono, że proces rozdrabniania zachodzi w czasie nawet do 30 dni. Co więcej, obserwacje te są potwierdzone przez pomiary powierzchni właściwej za pomocą izotermy adsorpcji BET. Metodą dyfraktometrii proszków XRD zbadano brak wpływu mielenia na strukturę krystaliczną spinelu, tzn. zachowana jest faza regularna spinelu. Natomiast wyraźnie widoczne jest poszerzenie refleksów wraz z wydłużonym czasem mielenia, co jest pośrednią obserwacją rozdrobnienia krystalitów. Badania spektroskopowe wykazały różnice w stopniach utlenienia atomów na powierzchni proszków w zależności czy proszki te były mielone w obecności dodatku węgla przewodzącego czy nie. Ważnym zjawiskiem jest powstawanie warstwy wodorotlenku kobaltu na powierzchni proszku spinelu po mieleniu z dodatkiem węgla przewodzącego. Warstwa ta znacząco poprawia aktywność katalityczną materiału. Ponadto wykazano, że niskoenergetyczne mielenie proszku katalizatora w czasie 6 dni obniża nadpotencjał OER o 60 mV w porównaniu do nierozdrobnionej próbki referencyjnej. Kolejnym zbadanym aspektem jest wpływ grubości warstwy jonomeru na obniżenie mierzonej aktywność elektrokatalitycznej. Im grubsza warstwa jonomeru, tym bardziej blokowana jest powierzchni katalizatora, a zatem ograniczony jest transport masowy reagentów.

Do oryginalnych wyników zaliczam kompleksową analizę wielu czynników wpływających na obserwowaną aktywność elektrokatalityczną spinelu $MnCo_2O_4$. Zbadany został wzajemny wpływ czasu mielenia (rozdrobnienia ziaren) katalizatora, dodatku węgla przewodzącego oraz jonomeru na obserwowaną aktywność elektrokatalityczną materiału. Podkreśla to jak wiele uwagi należy poświęcić przygotowaniu badanych elektrod z użyciem katalizatora o danej stechiometrii, żeby móc rzetelnie przedstawić otrzymane wyniki i porównać je z literaturą.

W przedstawionej publikacji odpowiadałem za częściowe przeprowadzenie analizy stanu wiedzy oraz dopracowanie stanowiska do badania aktywności elektrokatalitycznej przygotowanych próbek. Ponadto brałem czynny udział w pomiarach za pomocą rentgenowskiej spektroskopii absorpcyjnej oraz byłem odpowiedzialny za przeprowadzenie analizy LeBaila dyfraktogramów rentgenowskich. Służyłem również wsparciem merytorycznym i brałem udział w dyskusji wyników, mając wpływ końcową wersję artykułu.

Oświadczenie współautorów o wkładzie w powstanie publikacji: „Tailoring a low-energy ball milled $MnCo_2O_4$ spinel catalyst to boost oxygen evolution reaction performance"

Imię i nazwisko autora	Wkład w powstanie pracy	Podpis
Sylwia Pawłowska	Konceptualizacja, metodologia, badania, pisanie – oryginalna wersja robocza, wizualizacja	
Krystian Lankauf	Badania (XRD, XAS), pisanie – recenzja i redakcja	
Patryk Błaszczak	Badania (BET), pisanie – recenzja i redakcja	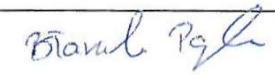
Jakub Karczewski	Badania (SEM), pisanie – recenzja i redakcja	
Karolina Górnicka	Badania (XRD), pisanie – recenzja i redakcja	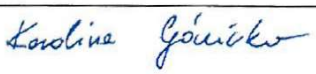
Grzegorz Cempura	Badania (TEM), pisanie – recenzja i redakcja	
Piotr Jasiński	Pisanie – recenzja i redakcja, nadzór, zasoby	
Sebastian Molin	Konceptualizacja, pisanie – recenzja i redakcja, nadzór, zasoby, pozyskiwanie funduszy	

Applied Surface Science 619 (2023) 156720

Contents lists available at ScienceDirect

Applied Surface Science

journal homepage: www.elsevier.com/locate/apsusc

Full Length Article

Tailoring a low-energy ball milled $MnCo_2O_4$ spinel catalyst to boost oxygen evolution reaction performance

Sylwia Pawłowska [a,*], Krystian Lankauf [a], Patryk Błaszczak [b], Jakub Karczewski [b], Karolina Górnicka [b], Grzegorz Cempura [c], Piotr Jasiński [a], Sebastian Molin [a]

[a] Advanced Materials Center, Faculty of Electronics, Telecommunications and Informatics, Gdańsk University of Technology, ul. G. Narutowicza 11/12, 80-233 Gdańsk, Poland
[b] Advanced Materials Center, Faculty of Applied Physics and Mathematics, Gdańsk University of Technology, ul. G. Narutowicza 11/12, 80-233 Gdańsk, Poland
[c] International Centre of Electron Microscopy for Materials Science, AGH University of Science and Technology, al. A. Mickiewicza 30, 30-059 Kraków, Poland

ARTICLE INFO

Keywords:
Oxygen evolution reaction
$MnCo_2O_4$ spinel
Electrocatalyst
Ball-milling process
Ink composition
Nafion ionomer

ABSTRACT

The development of cost-efficient oxygen evolution reaction (OER) catalysts is one of the most important tasks facing modern techniques for hydrogen production. In this work, for the first time, a low-energy ball milling process of $MnCo_2O_4$ (MCO) spinel powders, with a mechanical modification time exceeding 1 day was used. After 6 days of ball-milling, the obtained overpotential of the electrocatalyst reached the value of 375 mV at 10 mA cm^{-2}, which is a relatively low value obtained for this type of compound. The studies showed how the mechanical (low-energy long-term milling process) and chemical modification of the fragmented spinel powder nanoparticle surfaces affects the increase of the electrocatalytic properties. The addition of the appropriate amount of conductive carbon black (cCB) and Nafion ionomer to the ink of the MCO spinel also has a significant effect on the improvement of the catalytic performance of the manganese-cobalt oxide during the milling process. By reducing the amount of Nafion to 10 % of its initial value, the overpotential dropped to 352 mV at 10 mA cm^{-2} after 30 days of ball-milling. This shows that catalyst ink and layer composition are important factors influencing the catalyst's efficiency in the OER.

1. Introduction

The constantly growing demand for electricity means that there is a need for new solutions to meet these requirements. Hydrogen obtained through electrolytic processes seems to be one of the most promising directions for development. The key point that hinders the electrolysis process is the sluggish oxygen evolution reaction (OER) kinetics in the electron charge transfer reaction, which results in high overpotentials of the reaction. The OER is an energy conversion reaction necessary both for charging metal-air batteries and for the direct splitting of water [1–5]. To accelerate the electrochemical reactions of water splitting, the development of efficient electrocatalysts is necessary. Highly efficient OER catalysts are required to lower the energy barrier [6–8]. Currently, most of the work has been devoted to the development of OER electrocatalysts based on 3d transition metals and their oxides, such as perovskite and spinel structures. They exhibit good OER performance with significantly reduced production costs [7,9–11]. Spinel-type metal oxide electrocatalysts are promising candidates for the development of low cost, readily available, highly active, stable bifunctional catalysts for energy conversion and storage applications [6,12,13]. The development of low-cost transition non-noble metal-based (such as Mn and Co) water-oxidation catalysts is very appealing due to their high availability [14–17]. $MnCo_2O_4$ (MCO) is one of the spinel oxides that possess structural flexibility and mixed-valence states. Most of the MCO-based catalysts presented in the literature have good activity toward OER [18–23].

Catalytic properties are related to the active surface of the catalyst [24,25]. Ball milling is an efficient method to mechanically activate materials, to affect chemical reactions and employ alloying. The ball milling process is called a mechanochemical method used for the synthesis of metal oxides [26–28]. During the milling process, the ground powder particles are subject to a combination of impact, shear, and friction forces, resulting in the continuous exposure of fresh particle surfaces, creating defects, and breaking bonds [29–31]. As a result, the ball-milling process reduces the particle agglomeration and the size of the catalyst crystallites, modifies its particle size distribution, and

* Corresponding author.
E-mail address: sylwia.pawlowska@pg.edu.pl (S. Pawłowska).

https://doi.org/10.1016/j.apsusc.2023.156720
Received 5 December 2022; Received in revised form 27 January 2023; Accepted 9 February 2023
Available online 11 February 2023

increases the number of structural defects [32]. Additionally, with the decrease of the particle size the concentration of atoms and ions located at the particle surfaces increases [33]. Mechanical milling can affect the physico-chemical properties of the catalyst, as well as its OER performance. Mechanical modification is a very promising way to modify the structure of materials because, during the milling process, the moving balls apply their kinetic energy to the ground material. As a consequence, chemical bonds are broken and new surfaces are obtained by cracking the material's particles. Additionally, the newly formed surfaces are chemically reactive due to the presence of the dangling bonds formed as a result of the milling process [34–37]. The great advantage of the ball milling technique is the possibility of large-scale production, which significantly reduces the costs of production or modification of materials subjected to the milling process. During a single cycle, depending on the size of the mill or roller, it is possible to process large volumes of modified material [26]. After the ball milling process, the resulting particles can be applied to any surface. In comparison, the electrochemical deposition method requires a conductive substrate such as glassy carbon, metals, or alloys [38]. The ball milling process itself also does not require the use of specific chemical reagents. Typically, the use of typical organic solvents, such as alcohols, or use of aqueous solutions is sufficient. In comparison, the chemical vapor deposition method requires the use of often toxic, explosive, or corrosive precursors in chemical vapor deposition is essential. In addition, this method involves the production of by-products, which can also be dangerous [39]. As can be seen, out of many methods commonly used for the fabrication of catalytic materials, ball milling seems to be one of the simplest methods to implement, which does not require very expensive equipment, and instead allows the milling process to be carried out even in a very large scale.

The electrocatalytic efficiency of the OER process is also greatly influenced by the composition of the ink used for the application to the electrode. In addition to the catalyst particles, the amounts of ionomer and conductive carbon black (cCB) are also crucial [40–45]. The main purpose of the application of Nafion ionomer in water electrolysers is to improve the distribution and separation of the catalyst particles in the ink (maximised catalyst utilisation). Nafion is also a binder to prevent the catalyst layer from detaching from the electrode, ensuring its proper stability [45,46]. Additionally, as numerous studies have shown, the appropriate ionomer to catalyst ratio (I/C) is very important as it affects the form of the reaction interface and accordingly affects the efficiency of the OER reaction. The uniform distribution of the catalyst particles in the ink increases the active area of the surface by preventing their aggregation. Too much Nafion ionomer leads to it blocking the electrolyte's access to the catalyst surface, hindering the transport of mass, ions, and electrons. The role of the ionomer in the OER is therefore very important as it regulates the properties of the ink and the physical and electrochemical behaviour of the catalyst layer at the interface, i.e. in the electrical double layer (EDL) [44]. The cCB is an equally important component of the catalyst layer of electrodes used in electrochemical energy conversion. Its main task is to improve the electronic conductivity of weakly conducting electrocatalysts, such as metal oxides. Indeed, the addition of carbon materials to low-conductive oxides contributes to a strong increase in the conductive properties and thus the efficiency of these catalysts. As a result, they are widely used in modelling OERs in alkaline media as an indispensable additive to the ink [47–50]. A new strategy observed in the latest research is the synthesizing of carbon-supported electrocatalysts. Such electrocatalytic materials are characterized by a three-dimensional structure and high porosity, which improves the efficiency of water splitting processes [51–53].

In this work, the effect of physical/chemical treatments of MCO spinel on the OER performance is investigated. We present the effect of ball milling and the addition of carbon on the physico-chemical properties of the MCO. Here, the OER performance of MCO prepared in the form of ink after various ball-milling process times are reported. The results show that the ball milling process of the MCO spinel catalyst could significantly enhance its OER activity. This finding is associated with a decrease in the particle size, and not simply with the modification of a surface layer produced during the ball milling process with cCB. By comparing the OER activity of a different catalyst ink preparation, we confirm that carbon has a definite influence on the surface modification of the catalyst particles. However, this influence is much smaller than that by mechanical treatment. The composition of the ink applied to the electrode has a similar importance for the electrocatalytic efficiency in OER. Our work confirmed that the activity of the catalyst increases with a decrease in the amount of Nafion ionomer and an increase in the amount of cCB. The research presented in this paper shows a promising direction for further research to create low-cost and highly efficient electrocatalysts based on spinel oxides.

2. Materials and methods

2.1. Sample preparation

Commercially available manganese cobalt spinel $MnCo_2O_4$ powder (MCO, Marion Technologie, France) was used for each analysis. It is a solid solution of manganese and cobalt oxide in a composition equal to: Mn: 0.98 ± 0.03 and Co: 2.02 ± 0.03 (analysis provided by the producer). The average particle size was determined by granulometry and was equal to 300 ± 30 nm, and specific surface area 7.6 ± 0.8 $m^2\ g^{-1}$, declared by the manufacturer. The spinel powder was subjected to a grinding process in a roller mill (Zoz GmbH, Germany) rotating at a speed of 100 rpm using yttria-stabilised zirconia (YSZ, Inframat®Advanced Materials™, USA) spherical grinding media (1 mm diameter). Ball-milled samples were analysed at different time points: 1, 2, 3, 4, 5, 6, 7, 10, and 30 days. Two variants of powders after milling were used for physicochemical analysis: pure spinel (MCO) and spinel with Super P Li Conductive Carbon Black (cCB, Imerys, Belgium) (MCO-cCB) suspended in ethyl alcohol. After a time-defined grinding procedure, the powders were dried in a laboratory drier at 100 °C in the air. To test the catalytic properties, inks based on the MCO and cCB were used (a detailed description of the ink preparation is presented in the next section), then subjected to the process of milling and analysis after specific time points (milling times).

2.2. Morphological and physicochemical characterisation of spinel powder samples

To investigate the morphologies and chemical properties of ball-milled $MnCo_2O_4$ powder, an FEI Quanta FEG 250 scanning electron microscope (FE-SEM) under an acceleration voltage of 10 kV, and a Cs-corrected Titan Cubed G2 60–300 (FEI) scanning transmission electron microscope (S/TEM) were used. The specific surface area of the powders was determined using the N2 adsorption technique (Quantachrome, NovaTouch LX1) Brunauer-Emmett-Teller (BET) isotherm model. Before sorption measurement, the samples were degassed at 300 ℃ for 3 h in a high vacuum. The specific surface area (SSA) from BET analysis was useful for calculating the mean sizes of the powders' particles, on the assumption of particles having spherical geometry. The following equation was used:

$$d = \frac{6000}{A_{BET}\rho}$$

where d is the particle diameter, A_{BET} is the BET specific surface area, and ρ is the theoretical density calculated based on data obtained from LeBail analysis of XRD patterns. The obtained values after individual milling times were compared with the particle sizes determined based on SEM images, and the hydrodynamic size distribution of the particles evaluated by dynamic light scattering (DLS, Malvern Zetasizer) (DLS measurement details in the Supplementary Material).

Crystalline phase identification for powders after each milling time

was carried out at room temperature by powder X-ray diffraction (pXRD, Bruker D2 Phaser diffractometer) with CuK_α radiation ($\lambda = 0.15404$ nm) and a Lynxeye XE-T detector. The Fullprof software package, based on the LeBail method, was used to develop the measurement results. To perform the analyses, the cif files were downloaded from the Crystallography Open Database [54]. X-ray photoelectron spectroscopy (XPS, Axis Supra spectrometer, Kratos Analytical) measurements were performed to investigate the valence state of the Mn and Co in the MCO spinel. The spectroscope was equipped with an Al Kα source. The pass energy and the spot size diameter were 20 eV and 2 × 0.7 mm, respectively. Metallic gold and copper were used for the instrument calibration. The CasaXPS 2.3.18 software on a Shirley background was used to analyse the obtained spectra. The XPS binding energies were corrected using the C 1s peak at 284.6 eV. For a deeper understanding of the oxidation and electronic states of each element in the catalysts, soft X-ray absorption spectroscopy (XAS, Solaris National Synchrotron Radiation Centre) measurements across the Mn, Co, and C $L_{2,3}$-edges, as well as the O K-edge, were performed. Measurements were carried out at the available energy range of 150–2000 eV with the beamline at the bending magnet source (1.21 T), a flux at a sample of $\sim 10^{10}$ photon/s/0.1A, and energy resolution $\Delta E/E \sim 2.5 \times 10^{-4}$.

2.3. Electrode preparation

The ink subjected to the milling process and then analysed for its electrocatalytic properties was a mixture consisting of 100 mg of MCO spinel, 100 mg of cCB, 1.5 mL of K^+ exchanged 5 % Nafion 117 as a binder, 9.5 mL of ethyl alcohol (absolute 99.8 % pure, POCH, Poland), and 35 g of YSZ spherical balls. Potassium substituted Nafion was used to avoid the highly acidic environment of Nafion solution (pH about 2) which may corrode the oxide catalysts. For this purpose, 5 wt% Nafion 117 solution (Sigma-Aldrich) was mixed at a proportion of 2:1 of volume ratio with 0.1 M potassium hydroxide (KOH, Titripur®, Merck, Germany, 1 M solution diluted with deionised water). This alkaline Nafion was prepared according to the procedure reported in the literature [55]. The final pH of the NafionK + was equal to about 9.

For examining the effect of the amount of NafionK+ and cCB on the electrochemical properties of the catalyst, the amounts were reduced from 18 μg of Nafion to 9 μg, 4.5 μg, and 1.8 μg (corresponding to a Nafion/catalyst (I/C) ratio of 0.4, 0.2, 0.1, and 0.04, respectively), and from 100 mg of cCB to 200 mg, 150 mg, 50 mg, 25 mg, and 10 mg (corresponding to a conductive carbon/catalyst (cCB/C) ratio of 2, 1.5, 1, 0.5, 0.25, and 0.1, respectively). Before the deposition, the electrode surface was polished to a mirror finish using Struers Tegramin-20 equipment and 1 μm of diamond suspensions, and with the following parameters: pressure on the electrode 15 N, time of polishing 5 min, rotation speed 300 rpm. The ink that was not milled with balls was only sonicated (ultrasonic bath, Bandelin Sonorex RK 102H, 480 W) for 30 min in an ice-water bath. 5 μL of the ink was dropped onto a rotating glassy carbon (GC) electrode (0.196 cm^2) at 700 rpm, and adhesive tape was used as a limiter enabling the application of the ink only to the GC surface. The loading of the catalyst was 0.23 mg cm^{-2}. The prepared electrode was dried overnight. For each ball-milling time point, three samples of electrodes with the catalyst were analysed.

2.4. Electrochemical analysis

Rotating Ring Disk Electrode (RDE-3A) equipment was used to reveal the OER kinetics of the catalyst after milling. The electrochemical measurements were performed in a standard three-electrode system with a custom-made Teflon cell at room temperature. The electrolyte was a 0.1 M KOH (Titripur®, Merc, Germany) solution prepared with deionised water. The OER was investigated using a BioLogic BP-300 potentiostat/impedance meter in O_2-saturated electrolyte at 1600 rpm. In all measurements, a Hg/HgO as the reference electrode (928 mV vs the reversible hydrogen electrode RHE) and a Pt wire as the counter electrode were used. The potential of the reference electrode Hg/HgO was calibrated on a daily basis using a hydrogen generator. Calibration of the Hg/HgO electrode is described in the Supplementary Material and an exemplary calibration graph is shown in Fig. S1.

As a first step, the electrolyte was purged with high purity oxygen for 30 min before each measurement. For conditioning, the working electrode was cycled between 1.0 V and 1.7 V vs RHE at a scan rate of 10 mV s^{-1} (10 cycles). The goals of this treatment procedure were to achieve stable performance and reproducible results. To estimate the double-layer capacitance (C_{dl}), cycling voltammetry (CV) scans were performed at scan rates of 10, 20, 40, 60, 80, and 100 mV s^{-1}. The non-faradaic potential region was applied (from 1 V to 1.7 V vs RHE). The double-layer capacitance is useful for calculating the analysed material's electrochemical active surface area (ECSA). Linear sweep voltammetry (LSV) data was collected from 1.1 to 2.0 V (vs RHE) at a scan rate of 10 mV s^{-1}. To investigate the electrical properties of the materials, such as the charge transfer resistance (R_{ct}), electrochemical impedance spectroscopy (EIS) measurements were performed in the frequency range from 10 kHz to 0.1 Hz at 1.7 V vs RHE with an amplitude of 10 mV.

All potential values were first converted to the values versus the reversible hydrogen electrode (RHE, $E_{RHE} = E_{Hg/HgO} + 0.928$ V) and then iR-corrected to remove the effect of solution resistance ($E_{iR\text{-}corrected} = E_{applied} - iR_{ucom}$), taking into account uncompensated ohmic resistance (iR_{ucom}). To estimate the overpotential for the OER at 10 mA cm^{-2}, the following equation was used: $\eta = E - 1.23$ V (vs RHE) [20]. The catalyst oxide loading and the geometric surface area of the working electrode were equal to 0.045 mg and 0.196 cm^2, respectively. These parameters were used to calculate the catalyst mass activity at specific overpotential values and current density.

The stability tests was examined by chronopotentiometry at 10 mA cm^2 in 0.1 M KOH and using commercial electrolyzer cell (ElectroCell, Micro Flow Cell). The electrolyzer cell consisted of Sigracet 39 AA (SGL Carbon) carbon paper support as anode, Ti cathode, and Zirfon® Perl 500 UTP diaphragm (AGFA). Both electrodes had the active geometrical area equal 10 cm^2. Sealed reference electrode LF-1 Ag/AgCl (ElectroCell) was used for measuring of the anode potential. A water pump (12 V, 1.2 L/min, 1200 mA) was used to generate the electrolyte flow through the electrolyzer cell. The flow rate was 200 mL/min.

3. Results and discussion

3.1. Morphological and structural characterization

A commercially available manganese-cobalt spinel MCO was used for the analysis, which was subjected to an ultrasonic bath (0.5 h of us) or mechanical treatment via ball milling for 1, 2, 3, 4, 5, 6, 7, 10, and 30 days. The analysis also included MCO samples treated with conductive carbon black (MCO-cCB) and without (MCO). The SEM images presented in Fig. 1 (and Fig. S2) revealed the mechanical milling effect of spinel particle defragmentation. As the milling time increases, the fragmentation of the spinel particles increases.

The shape of the particles in each examined sample is random, and the size ranges are from a few to several hundred nanometers in diameter. Milling for 30 days resulted in drastic fragmentation of the MCO powder particles. The contours of individual grains are difficult to clearly define, which translates into problems with estimating their approximate size. Values of the particle size of the spinel powders were determined based on SEM analysis, assuming that they are spherical particles and not, as they are in reality, objects of various shapes. The obtained values of the average particle diameters after specific ball-milling times (d_{SEM}) are presented in Table 1, and for spinel particles after 6 days of grinding and for spinel without any treatment (pure MCO) are 125.8 nm and 231.4 nm, respectively. Extending the grinding time to 10 days resulted in an almost 3-fold reduction in particle size compared to the pure MCO sample. As mentioned above, continuous grinding for 30 days resulted in significant fragmentation of the

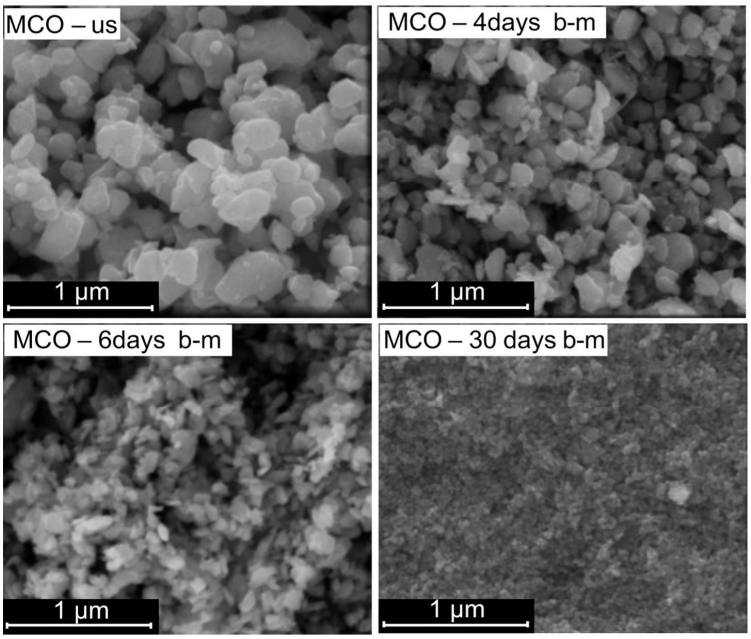

Fig. 1. Morphology analysis of MCO powder – SEM images of spinel powder after different milling times with 1 mm yttria-stabilised zirconia spherical balls using a roller rotating at a speed of 100 rpm.

Table 1
Comparison of the SSA and particle size of MCO powders: without treatment, after ultrasonic treatment, and after different times of ball-milling.

	d_{SEM} [nm]	d_{BET} [nm]	SSA [m^2/g]
pure MCO	231.4	135.0	7.8 ± 0.4
0.5 h of us (0 days of b-m)	204.5 ± 92.9	148.3	7.1 ± 0.4
1 day of b-m	198.9 ± 65.4	84.8	12.4 ± 0.6
2 days of b-m	187.5 ± 47.5	63.4	16.6 ± 0.8
3 days of b-m	180.8 ± 48.2	49.7	21.2 ± 1.1
4 days of b-m	143.3 ± 33.2	45.8	23 ± 1.2
5 days of b-m	133.3 ± 36.7	41.4	25.4 ± 1.3
6 days of b-m	125.8 ± 36.2	39.3	28.6 ± 1.4
7 days of b-m	98.4 ± 35.0	26.2	40.2 ± 2.0
10 days of b-m	80.5 ± 22.7	17.0	62 ± 3.1
30 days of b-m	20 ± 4.1	9.5	110.8 ± 5.5

particles, making it nearly impossible to determine their size. Exemplary spinel particle size distribution histograms from the SEM microscope data for three selected samples (pure MCO – without treatment and after 3 and 6 days of milling) (Fig. S3a), as well as size results from DLS analysis (Fig. S3b) and value of the SSA determined by BET (Fig. S3c), are presented in the Supplementary Material.

Spinel grain fragmentation is also revealed in the growth of the specific surface area (SSA) of the spinel powders determined by BET analysis (Fig. S3c, Table 1). These values were measured for samples milled for nine different time points as well as for spinel powders treated by ultrasonication and powder without any treatment (pure MCO). After 6 days of grinding, the specific surface area increased more than 3 times compared to the control sample (pure MCO). From the 7th day of the grinding process, a stronger increase in SSA was observed, which increased by 40 % compared to the sample milled for 6 days. However, after 10 days, this increase was already more than 2-fold (in relation to the "6 days" sample). Extending the grinding time to 30 days resulted in an almost 4-fold increase in the SSA compared to the sample that underwent 6 days of ball-milling and more than 14-fold compared to the sample that did not undergo any treatment (pure MCO). Such a high value of the SSA was expected, taking into account the degree of fragmentation visible in the SEM images (Fig. 1). A larger total surface area should provide more active sites for the electrochemical reaction [12,56,57].

Based on the SSA value, the mean sizes of the powders' particles for a spherical geometry, were calculated. The results are presented in Table 1. The differences in the mean particle size of the powder determined from BET are on average 3 times smaller for the powders subjected to the milling process (regardless of time), and less than twice for a powder without milling, compared to the values obtained from the analysis of the SEM images. As mentioned above, both methods are subject to some errors, as they assume a perfectly spherical shape of the powder particles, which in fact have a more complex shape. Heidinger et al. presented the difference between the use of high- and low-energy ball milling of oxide particles. They showed that high-energy ball milling (1060 rpm) drastically reduces the average crystal size even to ~ 20 nm, along with the formation of dense aggregates. Due to this strong aggregation, the active surface remains small. The use of the low-energy ball milling process (450 rpm) as the next stage causes deagglomeration of the particles and increases the surface area of the powder particles several times [57].

To characterise the MCO catalyst samples after ball-milling with and without cCB, TEM analyses were performed (Fig. 2). High-angle annular dark-field (HAADF) images and TEM-EDS elemental analyses were used to detect differences between the MCO spinel powders milled for 6 days with and without cCB. The TEM images (Fig. 2a,b) present no differences in the degree of fragmentation of the particles of the MCO and MCO-cCB samples. Fig. 2c,d,e show pictures at the particle boundary in selected regions. The HRTEM patterns present that the MCO sample (Fig. 2c) has lattice fringes with inter-planar spacings of 0.29 nm and 0.48 nm, corresponding to the <220> and <111> planes, respectively. In the case of the MCO-cCB sample (Fig. 2d), only 0.29 nm inter-planar

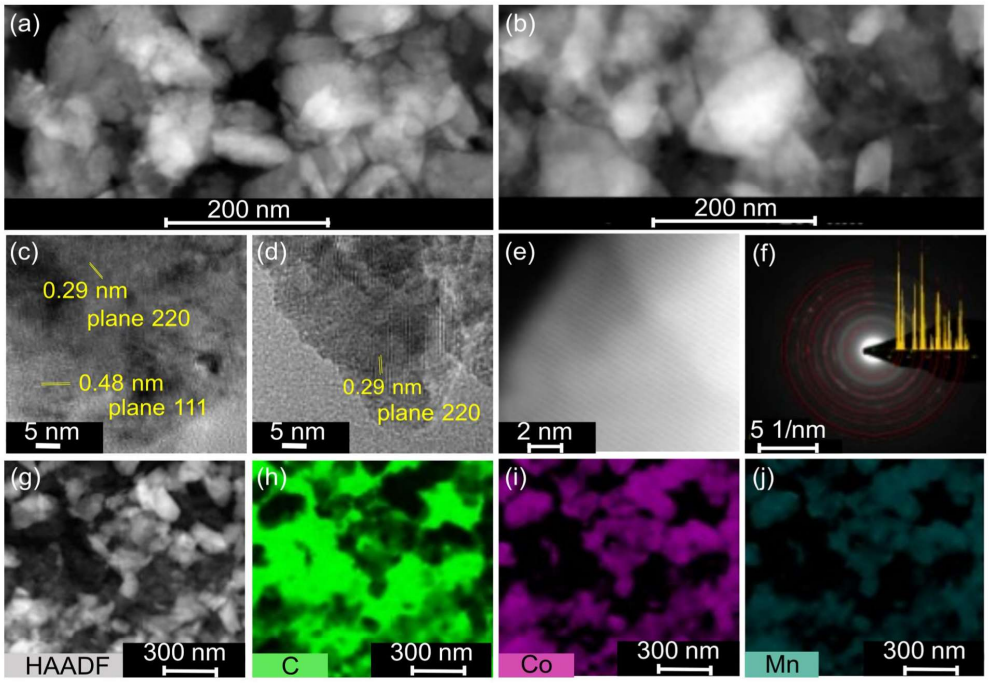

Fig. 2. HAADF-STEM images of the catalyst powder milled for 6 days without conductive carbon black (MCO) (a) and with conductive carbon black (MCO-cCB) (b, e, g). HRTEM patterns of MCO (c) and MCO-cCB (d) powders. SAED pattern of MCO-cCB sample (f). STEM-EDS elemental maps: carbon (h), cobalt (i), manganese (j).

spacings (<220> plane) are observed. Fig. 2e presents a HAADF image of the MCO-cCB sample with very clearly visible lattice fringes. However, due to the lack of perfect sample orientation, since the image resolution is a bit lower, the estimated values for the inter-planar spacings may be unreliable. Regardless of the technique chosen, it is clear that the MCO and MCO-cCB samples after 6 days of grinding show complete crystallinity with no signs of amorphisation. The selected area electron diffraction (SAED) patterns (Fig. 2f) confirm the well-defined crystalline MCO structure.

TEM/EDS analysis of the MCO-cCB (Fig. 2g–j and Fig. S4a) and MCO (Fig. S4b–e) confirm the presence of cobalt, manganese, and oxygen in the structure of the particles and carbon derived from the carbon mesh used as a substrate for the tested samples. In the case of the sample ground with conductive carbon black (MCO-cCB), it is difficult to determine whether there are any carbon residues on the surface of the MCO particles. The analysis also revealed trace amounts of other elements (Al, Na, Si) that may be impurities from the ball-milling treatment step (Fig. S4f–j).

Fig. 3a and 3b present the XRD patterns of the MCO spinel powder milled with and without cCB at different times of the milling process (3 days and 6 days) as well as for spinel powder treated by 0.5 h of ultrasonication. For the MCO compound, all diffraction peaks correspond to the cubic crystal structure (Fig. 4c) and belong to the space symmetry group *Fd–3 m* (No. 227) [22,58,59]. Additionally, after ball-milling of the powders, the number and positions of the observed peaks are intact, which indicates that the applied ball–milling procedure does not impair the structure of the MCO [32].Comparison of the results for the samples with and without cCB shows that its addition to the spinel powder does not affect any differences related to the crystallinity of the analysed compound, whether it is the ball milling process or dispersion using ultrasonication. However, significant differences can be seen when considering the method of mechanical treatment and its duration. The spinel samples treated by ultrasonication have narrower peaks. Fig. 3b shows that the diffraction peaks for the tested samples occur almost exactly in the same angular positions, which proves very similar lattice constants. Based on the obtained diffraction pattern, a LeBail refinement was performed, and the obtained changes of the unit cell parameters were insignificant in terms of statistical error (Fig. 3d, Table S1). As the grinding time increases, broadened diffraction peaks are noticeable due to the decreased crystallite sizes of the MCO powder [12]. Thus, the increase in the blur of the reflex shape and the width values of the half-width of the diffraction reflex of the samples with the increasing grinding time proves the progressive grinding of the spinel grains to form nanocrystals and introduce the internal stresses and deformations of the lattice structure. The catalyst being nanoscale usually translates into better catalytic activity due to the increased availability of its surface area. Broadening of the diffraction peaks with increasing grinding time is a typical behaviour manifested by small size crystallite and also internal strain induced by mechanical deformation [60].

The oxidation state of the Co and Mn as well as for the O and C in MCO powders without and with milling treatment as well as with and without the addition of cCB was determined by XPS analysis (Fig. 4). The samples labelled MCO did not contain any cCB during grinding. It is a commercial spinel and described by the manufacturer as pure oxide. Any trace amounts of additional compounds may result from the presence of impurities after the synthesis of the oxide or after the grinding/sonication treatment in ethanol as a medium. In the case of the treated samples (milling, sonication) without the addition of carbon (MCO), no qualitative changes were observed for the manganese and cobalt. Fig. 4a (black line) shows two peaks at 641.3 eV for $Mn2p_{3/2}$ and 652.9 eV for Mn $2p_{1/2}$ with an average spin–orbit level energy spacing for different milling times equal 11.5 eV, which is typical for Mn^{3+}-based materials [19,61]. The Co2p spectrum (Fig. 4b, black line) shows peaks at 780.1 eV for $Co2p_{3/2}$ and 795.6 eV for $Co2p_{1/2}$. Additionally, the Co^{2+} and

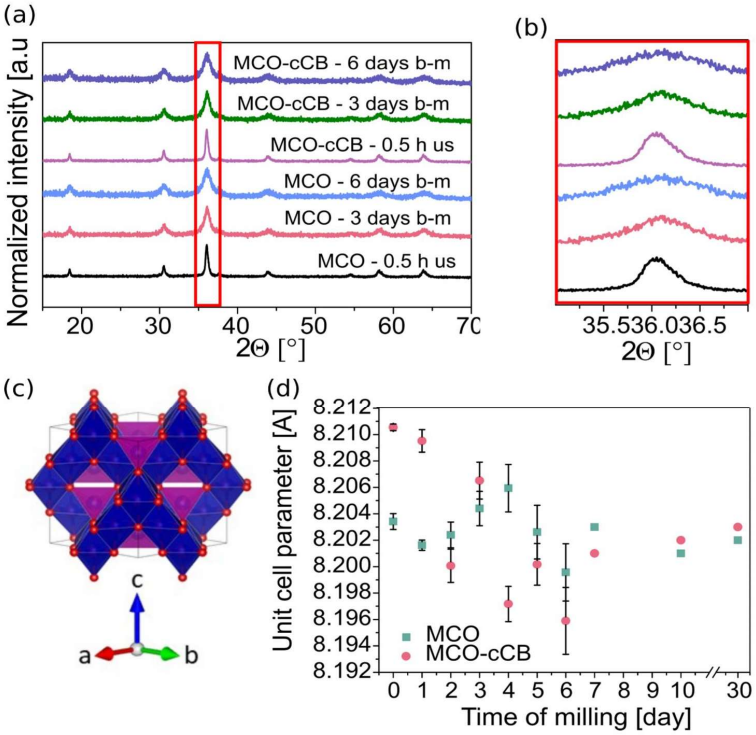

Fig. 3. XRD patterns (a) and partially enlarged patterns (b), and unit cell parameters (d) of MCO powder after treatment (ultrasonic or ball-milling process) with (MCO-cCB) and without (MCO) conductive carbon black. Cubic spinel unit cell (c).

Co^{3+} have similar 2p binding energies but can be described by the Co $2p_{1/2}$-$2p_{3/2}$ spin–orbit level energy spacing, which for high-spin Co^{2+} and low-spin Co^{3+} are equal 16.0 eV and 15.0 eV, respectively. In our case, the Co $2p_{3/2}$-$2p_{1/2}$ spin–orbit level energy separation for different milling times is approximately 15.44 eV, which indicates Co in the mixed + 2/+3 oxidation state reported in the literature [15,22,62,63]. The main changes can be seen in the analysis of elements such as carbon and oxygen. As the milling time increases, the share of C—O (532.4 eV) and Me-OH (530.9 eV) bonds increases significantly (Fig. 4c and 4d, black lines).

A very interesting result was obtained for the MCO powders milled or sonicated with conductive carbon black (MCO-cCB, red lines on Fig. 4). First of all, a difference is visible when comparing different milling times. In the case of manganese (Fig. 4a), it is seen that the Mn species ratio changes with different degrees of oxidation as the grinding time increases. For powders treated with ultrasound for 0.5 h, there is a clear advantage of Mn^{4+} ($2p_{3/2}$ 643.3 eV and $2p_{1/2}$ 654.7 eV) over Mn^{3+} ($2p_{3/2}$ 641.7 eV and $2p_{1/2}$ 652.9 eV) and Mn^{2+}. The use of milling changes this relation more and more. After 6 days of grinding MCO-cCB, it can be seen that Mn^{4+} and Mn^{3+} are in equilibrium, but at the same time, the Mn^{3+}/Mn^{4+} ratio is higher for MCO-cCB after 6 days of milling than after 0.5 h of ultrasonication.

Huang et al. in their work showed that the optimal electrical conductivity was reached only when the concentrations of Mn^{3+} and Mn^{4+} were equal [64]. For comparison, Wang et al. presented that in the case of their α-MnO_2 NRs/*N*-KB prepared in different temperatures, those characterised by a higher Mn^{3+}/Mn^{4+} ratio had much better ORR/OER activity [65]. Zheng et al. declared a similar observation about the ratio of Mn^{3+} and Mn^{4+} ions [56]. Additionally, a higher content of Mn^{3+} can be characterised by better electrocatalytic parameters due to there being a single electron in the σ*-orbital (e_g) of Mn^{3+}. This is related to the principle that high covalency in bonding to oxygen and near-unity occupancy of the e_g orbital of surface transition metal ions can strengthen the OER activity of catalyst transition metal oxides in alkaline solution [10,56,65,66].

Some differences can be seen when comparing the MCO-cCB samples after 0.5 h of ultrasonication and after 3 days or 6 days of milling in terms of the presence of Mn^{2+} peaks. It indicates a small share of Mn^{2+} after 0.5 h of ultrasonication, which is further reduced by milling of MCO in the presence of cCB. According to the literature, this peak should appear at around 641 eV (for $2p_{3/2}$), and it coincides with Mn^{3+} (~642 eV) [64]. However, the visible change of the peak range for samples after milling compared to the sample without milling (not resulting from the shift of the entire spectrum) indicates a more significant share of Mn^{2+} cations for MCO-cCB after 0.5 h of treatment by ultrasonication and their significant lowering as a result of mechanical treatment.

In the case of the Co spectra (Fig. 4b), there is a clear shift of 0.7–1.0 eV of the peaks for the samples treated with cCB (red lines) compared to the peaks without carbon (black lines). This is related to the formation of cobalt hydroxide on the spinel powder surface [19]. The increase in the cobalt hydroxide fraction due to the addition of cCB during treatment by ultrasounds or ball-milling is also evident in the O1s spectrum (Fig. 4c red lines). Regardless of the milling time, intense peaks are seen at 532.4 eV and 530.9 eV, corresponding to C—O and Me-OH, respectively. They are more intense than the powders treated (milling or ultrasonication) without the addition of cCB. On the other hand, the addition of carbon resulted in the disappearance of the peak at 530 eV corresponding to metal–oxygen bonds of metal oxide. Additionally, it

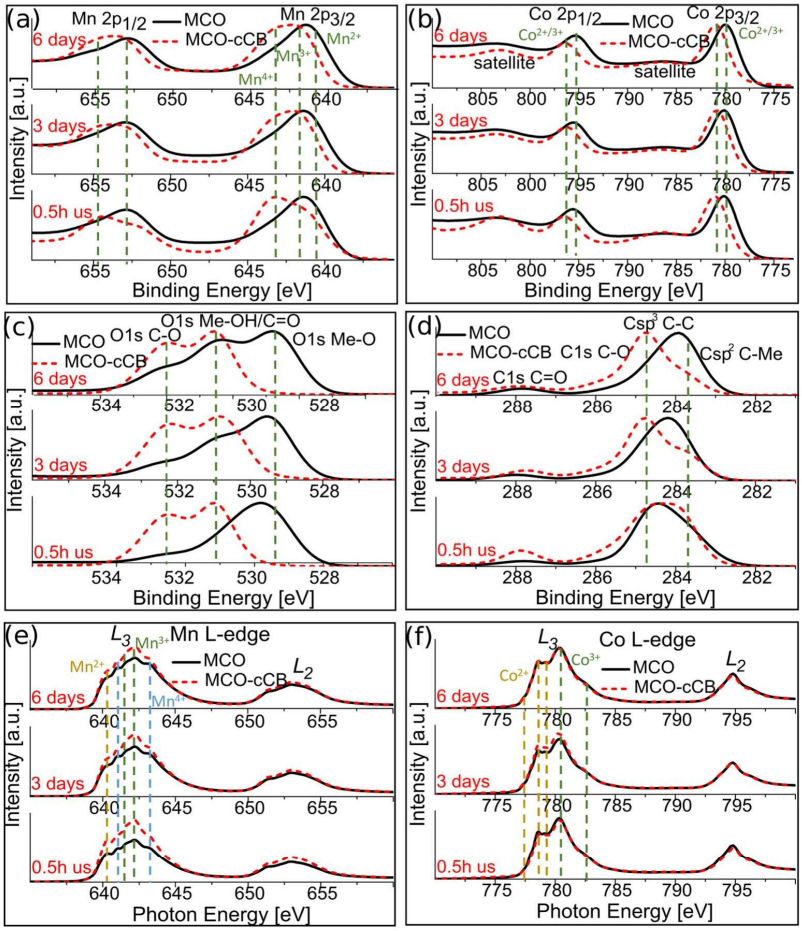

Fig. 4. XPS spectra of MCO powder after ultrasonic treatment (0.5 h us) and 3 days and 6 days of ball-milling with conductive carbon black (MCO-cCB, red dash lines) and without (MCO, black lines): Mn_{2p} (a), Co_{2p} (b), O_{1s} (c), C (d). Mn L-edge (e) and Co L-edge (f) XAS spectra of MCO after 0.5 h of ultrasonication, as well as 3 days and 6 days of ball-milling with conductive carbon black (MCO-cCB, red lines) and without (MCO, black lines).

indicates hydroxylation of the material surface due to the presence of surface hydroxides or the substitution of oxygen atoms at the surface by hydroxyl groups [11,15,67]. The increase in the amount of Me-OH translates into an increase in the efficiency of the OER process of electrochemical reaction, described in the next section. Additionally, Fig. 4d (red lines) shows that extending the grinding time increases the proportion of carbon in sp^3 C—C hybridisation (284.7 eV) at the expense of sp^2 hybridisation C=C (283.7 eV).

XAS studies of the Mn L_2 and L_3 edges of the MCO spinel samples ball-milled with and without cCB showed two main peaks in energy regions from 638.5 eV to 647.0 eV for L_3-edge, and from 649.9 eV to 656.6 eV for L_2-edge. Fig. 4e shows the spectra with visible manganese characteristic peaks at 2+, 3+, and 4 + oxidation states. The peak at 640.3 eV corresponds to Mn^{2+}, while the peaks at 641.7 eV and 642.2 eV indicate the presence of manganese in the 3 + oxidation state. Mn^{4+} has two characteristic peaks at 641.1 eV and 643.2 eV. Long and co-workers showed a similar mixed degree of manganese oxidation in the compounds they studied [68]. The Co L-edge XAS spectra of the MCO spinel samples also showed two main peaks in energy regions: from 773 to787 eV and from 791 to 800 eV for the L_3 and L_2 edges, respectively. As can be seen in Fig. 4f for all six analysed samples, the obtained XAS spectra appear comparable. Of particular importance are the peaks seen at 780.3 eV and 782 eV. Their presence and intensity testify to a higher content of Co^{3+}. The peaks at 777.4 eV, 778.6 eV, and 779.2 eV are characteristic of Co^{2+}. Therefore, we are dealing here with a mixed degree of cobalt oxidation 2+/3+, regardless of the type of $MnCo_2O_4$ sample tested (ball milling treatment, the presence of conductive carbon, or its absence). Similar conclusions were reached by Indra et al. in their research on $CoFe_2O_4$ [69]. Additionally, all $MnCo_2O_4$ spectra are very similar to the Co_3O_4 spinel spectrum, which proves that Co^{2+} and Co^{3+} occupy tetrahedral and octahedral sites, respectively [68]. Rebekah et al. observed that Co^{2+} ions occupy both tetrahedral and octahedral sites for their Zn-substituted $MnCo_2O_4$ nanostructure anchored over rGO [13]. Consequently, the XPS and XAS spectra demonstrate that the Mn^{3+}/Mn^{4+} and Co^{2+}/Co^{3+} mixed-species coexist in the MCO spinel, which could provide good catalytic activity for OER [70].

3.2. Electrochemical properties

To further demonstrate the synergetic effects of the MCO (treated as ink with cCB) ball-milling time, the electrochemical activity of the electrocatalysts towards OER was performed in 0.1 M KOH. The linear sweep voltammetry polarisation curves (LSV) at a scan rate of 10 mVs^{-1} (Fig. 5a), and the electrode overpotential (η) determined at a current density of 10 mA cm^{-2} (Fig. 5b), show that the electrocatalytic activity of MCO-cCB strongly depends on the ball-milling time. For spinel samples not subjected to the milling process (only ultrasonication for 0.5 h), the obtained overpotential value was 448 mV, while the use of ball milling successively decreased this value. After 6 days of milling, the overpotential value was 375 mV, so it was 63 mV lower compared to the MCO-cCB powder without the milling process. To the authors' knowledge, this is one of the best results obtained for this type of material. Table 2 compares the results obtained for the manganese-cobalt spinel investigated by us, with the data obtained by other groups for this type of compound. It is seen that the $MnCo_2O_4$ spinel subjected to the low-energy ball-milling process obtains one of the best activities as a catalyst for OER. Additionally, compared to other similar materials (e.g. spinels, perovskites), $MnCo_2O_4$ presents very good and promising results (Table S2). For example, Wang et al. reported the overpotential for $MnCo_2O_4$, Co_3O_4, Mn_2O_4, and the mixture of the last two as equal to 400 mV, 390 mV, 500 mV, and 410 mV, respectively [18]. After further days of ball-milling (longer than 6 days), there are no further changes in the catalytic activity of the electrode, and all differences are within the ranges of the statistical error. Therefore, it was assumed that from the 6 days of grinding, a flattening of the voltage dependence as a function of milling time is observed.

Cheng et al. also studied the effect of milling catalyst powders on their OER activity [32]. They milled Ba0.5Sr0.5Co0.8Fe0.2O3 (BSCF) powders in a planetary mill (high-energy milling process) for one day and also reported an increase in catalytic activity compared to the untreated material. Zhu et al. came to similar conclusions. Milling of SrCo0.8Fe0.2O3-δ (at 400 rpm for 1 h in a planetary mill (high-energy milling process)) reduced the overpotential in relation to the powder without ball-milling by 40 mV [71]. Lankauf et al. after 6 days of the ball milling process of $MnCo_{1.5}Fe_{0.5}O_4$ catalyst powder obtained overpotential at 10 mV/s (in 0.1 M KOH) equal to 376 mV [72].

The catalytic activity data aligns with the double-layer capacitance results (C_{dl}), which describe the relationship between the current density and scan rate obtained from cycling voltammetry in the non-faradaic potential range (Fig. 5c). As is visible, the double-layer capacitance also increases as the milling time increases, up to 6 days. After this time, a visible decrease in C_{dl} is observed, which remained at a comparable level for 7 days (values within the statistical error). The C_{dl} of MCO after 6 days of ball-milling (987 μF) is over 6 times higher compared to the sample without milling treatment (only ultrasonication) (161 μF). For comparison, C_{dl} for the electrodeposited NiOx catalyst (in 1 M NaOH electrolyte) was 91 μF [58]. Double-layer capacitance results were used for calculation of the electrochemically active surface area (ECSA), according to the equation: $ECSA = C_{dl}/C_s$ assuming, following the literature data, that the specific capacitance C_s of the oxide sample in the alkaline electrolyte is equal to 0.040 mF/cm^2 [58–60]. The ECSA and the roughness factor calculated for our electrode sample with the ink ball-milled for 6 days were 25 cm^2 and 126, respectively, while McCrory et al. [58] informed about 21 cm^2 for IrO_x in 1 M NaOH (for a 5 mm diameter GC electrode). In the same electrolyte conditions, Zhang and co-workers obtained ECSA for Fe:Ni$(OH)_2$ on a nickel foam equal to 18.04 cm^2 [61]. After converting to the weight of the catalyst used, the ECSA after 6 days of ball-milling was 56 m^2/g. For $SrNb_{0.1}Co_{0.7}Fe_{0.2}O_{3-\delta}$ and $SrNb_{0.1}Co_{0.7}Fe_{0.2}O_{3-\delta}$ nanorods, Zhu et al. got values of 74 m^2/g and 175 m^2/g, respectively [62]. $MnCo_2O_4$ microsphere with oxygen vacancies had ECSA equal 32.1 cm^2 [73]. The drop in capacity after a certain milling time is a very interesting phenomenon, the explanation of which, apart from a few cases, was not given by the scientists. There are unclear assumptions in the literature that the capacity decrease was related to the re-aggregation of the catalyst particles. After some critical machining time, the particles re-agglomerate, and the average particle size increases. As already described in the previous section and presented in Table 1, the SSA after 6 days of ball-milling (26.8 m^2 g^{-1}) increased almost fourfold compared to spinel

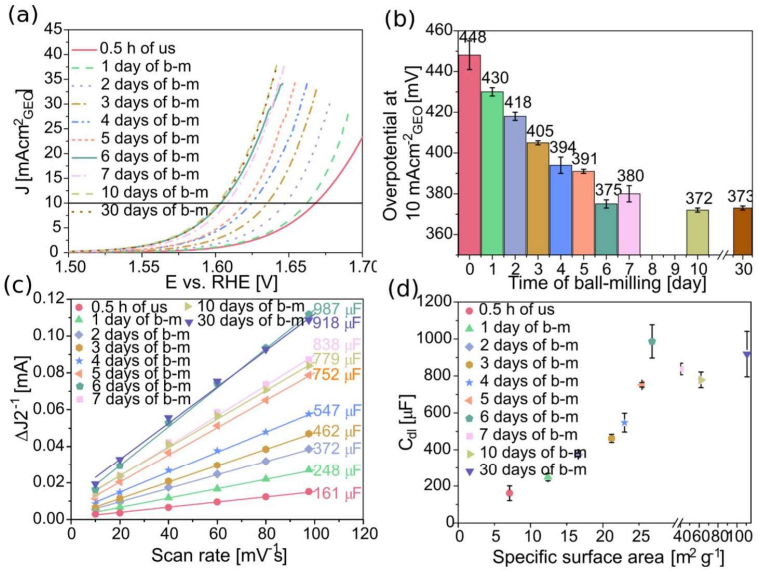

Fig. 5. Polarisation curves (a), overpotential (b), and double-layer capacitance (C_{dl}) for the OER on MCO electrodes after ultrasound treatment (us) and different ball-milling times (b-m) of catalyst ink (c). Dependence of double-layer capacitance of the electrode on the specific surface area of catalyst nanoparticles (d). All tests were performed in 0.1 M KOH electrolyte at 1600 rpm.

Table 2
Comparison of OER electrocatalysts reported in the literature. All analyses were performed in 0.1 M KOH. I – Nafion ionomer; C – catalyst; cC – conductive carbon.

Catalyst	Substr.	I/C	cC/C	η at 10 mA cm^{-2} [mV]	η at 25 μA cm_{OX}^{-2} [mV]	Tafel slope [mV dec^{-1}]	Loading of catalyst [mg cm^{-2}]	Ref.
$MnCo_2O_4$ after 6 days of ball-milling	GC	0.4	1	375	328	63	0.23	This work
$MnCo_2O_4$ after 30 days of ball-milling	GC	0.04	1	352	340	62	0.23	This work
$MnCo_2O_4$	GC	0.2	0.5	400	–	90	0.20	[18]
Co_3O_4	GC	0.2	0.5	390	–	71	0.20	[18]
Mn_2O_3	GC	0.2	0.5	500	–	146	0.20	[18]
$Mn_2O_3 + Co_3O_4$	GC	0.2	0.5	410	–	103	0.20	[18]
$MnCo_2O_4$	GC	0.16	–	510	–	55	0.05	[15]
$CoMn_2O_4$	GC	0.16	–	600	–	64	0.05	[15]
$Mn_{0.3}Co_{2.7}O_4$	fluorine doped tin oxide	–	–	390	–	–	1.0	[19]
$MnCo_2O_4$	GC	36	1	490	–	112	0.4	[73]
V_O-$MnCo_2O_4$	GC	36	1	410	–	87	0.4	[73]

powders treated by ultrasonication (7.1 m^2 g^{-1}). Fig. 5d shows the exponential dependence of C_{dl} on the SSA from BET analysis during the first 6 days of milling. After this time (from the 7th day) the SSA increased very quickly (more than a 2-fold increase in 4 days of additional milling), while the C_{dl} did not increase, but only oscillated in the ranges of statistical errors. Additionally, as confirmed by electrochemical analysis (Fig. 5b), from the 6th day of ball-milling, no increase in catalytic activity is observed. Thus, the increase in the specific surface area did not translate into either C_{dl} or OER activity of the electrocatalyst. We considered several possible theories to explain this phenomenon:

a) Day 6 of milling may be a critical time, after which the defragmentation of the MCO spinel particles is already so great that the entire volume of the particles formed, not just their surface, is involved in the electrochemical process. As a result, the further comminution of the powder particles does not affect the further increase in catalytic activity.
b) To bind the catalyst particles to the electrode surface, it is necessary to use a binder, which is usually Nafion. In the case of smaller particles, there may be a situation where the ratio of the Nafion layer to the particle diameter is too big so that the electrocatalyst particles are immersed in it and therefore less accessible to the electrolyte than particles with a larger size.
c) As a result of the strong defragmentation of the spinel powder, the packing structure of its nanoparticles forming the catalyst layer on the electrode surface may change. Smaller particles are more tightly packed, so there is less space between them than in the case of larger-sized particles. As a result, the surface of such nanoparticles is less accessible to the electrolyte. Additionally, the total number of available surface defects and active sites may be smaller. This may translate into lower overall catalytic activity of the tested sample.

The solution to this problem was possible thanks to the study presented in the next section of this paper, which concerned the impact of the ink composition on the electrochemical properties.

The Tafel plots presented in Fig. 6a provided information about the

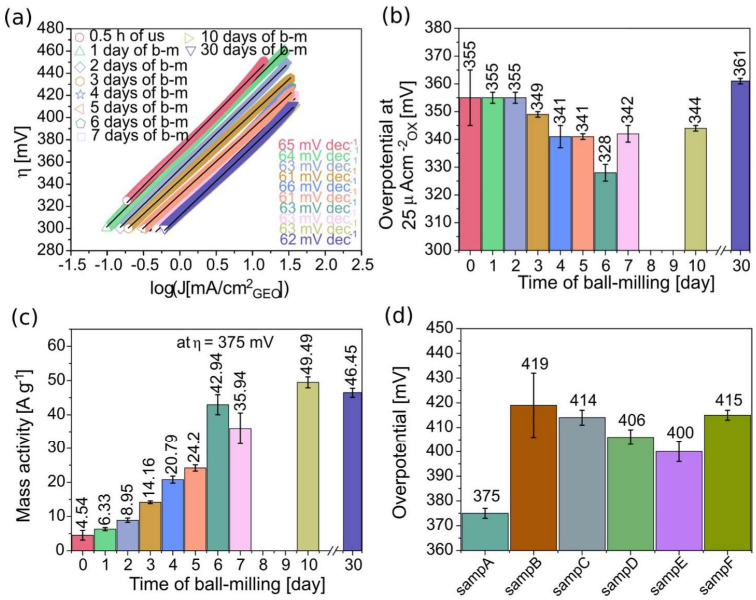

Fig. 6. Tafel plots (a), specific surface activity at 25 μA cm_{ox}^{-2} (b), and mass catalytic activity at η = 375 mV (c) of MCO catalyst powder after ultrasonic treatment (us) or various ball-milling times (b-m). Comparison of various methods of catalyst ink preparation by mixing MCO with cCB (D): sampA – MCO + cCB milling for 6 days as ink; sampB – MCO milling for 6 days and drying, then mixing with cCB by 0.5 h of ultrasonication; sampC – MCO + cCB milling 6 days and drying, then 0.5 h of ultrasonication (as ink); sampD – MCO milling for 6 days as ink, then mixing with cCB by 0.5 h of ultrasonication; sampE – MCO and cCB milling for 6 days as ink (separately from each other), then mixing in proportion 1:1 by 0.5 h of ultrasonication; sampF – MCO milling by planetary mill (12 cycles, 5 min of milling per cycle, 45 min break for cooling between each cycle), then mixing with cCB by 0.5 h of ultrasonication. All tests were performed in 0.1 M KOH electrolyte at 1600 rpm.

kinetic nature of the rate–determining steps for a multistep electron transfer reaction. The electrocatalyst is more efficient when the value of the Tafel slope is lower [3,12,15,63,74]. Evaluated by linear regression of the experimental data, the Tafel slope results are very similar for all measured samples (60–66 mV dec^{-1}). It means that the tested samples have a similar OER mechanism. Water oxidation could be a 1 to 4 electron transfer process depending on the condition and potential applied [75,76]. Tafel slope values in the range of 60–66 mV dec^{-1}, refer to 2 or 3 electron transfer processes, with the dominance of 3 electron transfer. The increase in surface coverage with hydroxyl groups is responsible for the decrease in the Tafel slope, at best to 30 mV dec^{-1} [77]. This property may account for the increase in the catalytic activity of the studied MCO after the ball-milling process, due to the formation of hydroxides as a result of the mechanical treatment.

The overpotential divided by the catalyst surface was compared, taking into account the BET SSA of each spinel powder after different times of ball milling (Fig. 6b). The overpotential values were determined at 25 μA cm_{ox}^{-2}. The lowest overpotential value deviating from the others was obtained after 6 days of milling. For the rest of the samples, independently of milling time, the results are quite similar, and no large differences are noticed. The specific mass activities of the catalysts determined at $\eta = 375$ mV and the surface-specific activity (based on SSA) were also compared for all tested samples and the results are shown in Fig. 6c. The presented results show that with the increasing milling time, the mass activity of the MCO catalyst also increases. For a sample of MCO catalyst after 6 days of ball milling, the mass activities were equal to 42.94 A g^{-1}. Compared to the sample milled for 1 day, this value was almost 7 times higher. Moreover, the samples after 5 days of milling had almost 2 times lower activity values compared to the catalyst powders subjected to the grinding process for one day longer (6 days).

All values were calculated using the mass of catalyst supplied on a GC electrode (45 μg), so inside 5 μL of ink. For comparison, Cheng et al. obtained mass activity of $Ba_{0.5}Sr_{0.5}Co_{0.8}Fe_{0.2}O_3$ equal to 5.01 A g^{-1} (at 1.55 V) after 24 h using a planetary mill (high-energy milling process), with 2 times higher loading of the catalyst compared to our electrode samples [32]. Zhu and co-workers obtained mass activity for ball-milled $SrCo_{0.8}Fe_{0.2}O_{3-\delta}$ at about 90 A g^{-1} and this result was more than 2 times higher compared to the same material not subjected to the milling process [71]. The above results suggest that reducing the particle size by ball-milling treatment is an efficient way to improve the mass activity of spinel electrocatalysts.

To compare the impact of the carbon addition during the ball-milling process, different types of catalyst ink preparation procedures were investigated. Fig. 6d presents the results, where the overpotential evaluated for the MCO catalyst treated with cCB for 6 days of the ball-milling process (sampA) is compared with the following catalyst inks: sampB – MCO dried after 6 days of ball-milling, then mixed with cCB by 0.5 h of ultrasonication as ink; sampC – MCO + cCB dried after 6 days of ball-milling, then 0.5 h of ultrasonication as ink; sampD – MCO milling for 6 days as ink, then mixing with cCB powder by 0.5 h of ultrasonication; sampE – MCO and cCB inks ball-milled separately for 6 days, later mixed in proportion 1:1 (by weight) by 0.5 h of ultrasonication; sampF – MCO milling by planetary mill (12 cycles, 5 min of milling per cycle, 45 min break for cooling between each cycle), then mixed with cCB by 0.5 h of ultrasonication as ink. A more detailed description of the differences between samples can be found in Table S3 in the Supplementary Material. The results of the overpotential obtained for the sample, where the spinel was milled for 6 days with cCB, and then dried and used in powder form for the preparation of the ink (sampC), was almost 40 mV higher than for the samples prepared without the drying step (sampA). Better results were obtained when separately milled MCO and cCB were combined in the form of an ink (sampE), although the results of the electrocatalytic activity of the catalyst prepared in this way are still not better (overpotential 400 mV) than for sampA. Nevertheless, regardless of the method of sample preparation, the effect of the ball milling is much more pronounced and significant.

Comparing the results obtained for the MCO-cCB catalyst treated with sample after ultrasound only (compare Fig. 5b, sample after 0.5 h us (equal to 0 h of milling)), it can be seen that the obtained overpotential results are at least 20 mV lower. Besides, it can be seen that re-drying the powders after their previous grinding causes re-aggregation. The latter observation was confirmed by DLS analysis (Fig. S3b), where additional wide peaks above 1 μm of diameter are visible, indicating the presence of particle powder agglomerates. Cheng et al. in their work showed that carbon, present during the ball-milling process, acts only as a reducing agent to functionalise $Ba_{0.5}Sr_{0.5}Co_{0.8}Fe_{0.2}O_3$ perovskite but it does not participate in the OER [32]. The ball milling process can also be an easy and effective method to prepare different composites of metal oxides with carbon. Also, Fabbri et al. showed that the presence of carbon as an additive to the catalyst is not important for OER as it acts as a reducing agent [9]. They showed that the removal of carbon from the electrode after BSCF perovskite functionalisation did not deteriorate OER activity, and more importantly, removed the problem of carbon corrosion during operation. However, our research has shown that the presence of cCB in the milling process of MCO powder is an important, but not predominant, factor influencing the future OER performance of the catalyst.

3.3. Impact of ink composition on electrochemical properties

The influence of other components forming the ink on the electrochemical properties of the resulting electrode was also investigated. For this purpose, the ball-milling process was applied to the preparation of the inks in which the amount of NafionK+ or cCB was reduced by 2-, 4- and 10-times, compared to the amounts commonly used in numerous articles, as well as in the first part of this paper. Nafion, belonging to the group of ionomers, is added to change the form of the reaction interface and influence the reaction yield accordingly. It is important that its amount is on the one hand sufficient to ensure good contact with the catalyst nanoparticles, and on the other hand not so high as not to inhibit mass diffusion. The influence of Nafion ionomer on the OER process in 0.1 M KOH solution as an electrolyte was investigated using electrochemical measurements allowing the determination of the CV and LSV curves in the ranges described in the previous section of the article. Fig. 7a shows how the values of the obtained overpotentials changed with the amount of Nafion ionomer used after 1, 3, 6, 10, and 30 days of the grinding process of the catalyst particles. Reducing the amount of Nafion per electrode to the ionomer to catalyst ratio (I/C) of 0.04, i.e. by 90 % in relation to the original I/C ratio of 0.4, resulted in a decrease in the overpotential by an average of 10–25 mV depending on the ball-milling time. After 30 days of this mechanical treatment, the sample in which the I/C was 0.04 obtained an overpotential of 352 mV with a current density of 10 mA cm^{-2}, which is a very good result for the group of manganese-cobalt catalysts (Table 2). It is visible that the reduction of the amount of ionomer used contributes to the improvement of the efficiency of the OER process taking place on the surface of the catalyst. According to Li et al., increasing the amount of ionomer, resulting in the ratio of ionomer-to-catalyst exceeding 0.5, contributes to the formation of large aggregates of both components [45]. As a result, mass transport can be blocked while reducing the active surface area of the catalyst. In our case, the ionomer/catalyst ratio ranged from 0.04 to 0.4 (Table S4), therefore it does not exceed the limit above which aggregation of the catalyst particles could occur. In contrast, completely removing Nafion ionomer from the catalyst layer results in poor stability of the OER process due to poor connectivity of the catalyst particles to the GC electrode layer. Li and co-workers also showed that this phenomenon is observed regardless of the type of catalyst [45].

It is assumed that as the I/C ratio increases, the electrode capacitance decreases. On the other hand, the reduction of the contribution of Nafion ionomer to the MCO catalyst resulted in an increase in capacity, which can be observed in Fig. 7b. The electrode capacity is presented in the SSA

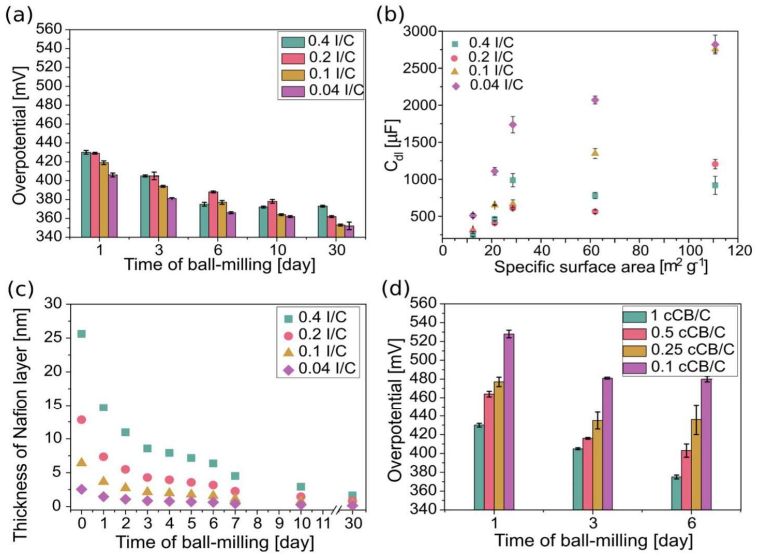

Fig. 7. Effect of the amount of NafionK+ (a) and cCB (d) on the electrochemical properties of the catalyst depending on the ball-milling time. Comparison of the SSA of the impact of the catalyst nanoparticles on the C_{dl} of the electrode depending on the amount of NafionK + used in the ink (b). The thickness of the Nafion layer surrounding a single MCO particle depending on the milling time and the amount of NafionK + used (c).

function, so the parameter is closely related to the reduction of the particle diameter as a result of the ball-milling process. In the case of samples with 0.4 and 0.2 of I/C, it is clearly seen that after 6 days of milling (corresponding to an SSA of 28.6 m^2/g), there is no linear relationship. In the case of the other two samples with a smaller amount of Nafion, an increase in the C_{dl} value can be seen with the increase in the SSA of the catalyst particles. Thus, the capacity increases with the extension of the grinding time, which is not observed after the 6th day of ball-milling, when the I/C ratio exceeds at least 0.2. It happens because when the amount of Nafion is large, the effect of reducing active sites on the surface of the catalyst by covering it with this ionomer is present. The reduction of electrochemical active sites translates into the electrical double layer (EDL) charging [45,58]. The availability of the catalyst surface for the electrolyte is blocked by the forming layer of Nafion which is a kind of separator. Such a layer blocks the transport of electrons in the EDL, as well as the adsorption of electroactive intermediates such as *OH, *O, and *OOH. The thickness of this layer varies depending on the amount of ionomer used. The amount of ionomer, therefore, has a significant influence on the number of active sites available on the surface of the catalyst particles. Li and co-workers also came to similar conclusions [45]. Likewise, the thickness effect of Nafion on catalytic performance is different depending on the size of the particles surrounding the ionomer layer. Fig. 7c shows how the thickness of the Nafion layer changed depending on the amount of its addition and the MCO particle size dependent on the ball-milling time. The calculations assumed the sphericity of the MCO particles and their average diameter value determined from the SEM images. However, the presence of cCB particles, the size of which also decreased proportionally as a result of the milling, was ignored, so the thickness of the Nafion on the cCB surface can be considered as changes to the same extent as in the case of MCO. It should also be remembered that in a given volume of ink applied to the surface of the electrode, the amount of catalyst particles increases with the increase in the degree of their fragmentation, which is the result of the mechanical treatment. The total surface area of the MCO particles thus changes from 0.32 10^{-3} m^2 to 5 10^{-3} m^2 for particles in ink after ultrasonic treatment and 30 days of ball milling, respectively. In the calculations, it was assumed that the spinel particles have a perfect spherical shape and do not form aggregates so that the Nafion layer surrounds each particle in the same way. It is visible that with a decrease in the amount of Nafion ionomer used and an increase in the ball-milling time, the thickness of the Nafion layer on the surface of the catalyst particles decreases. This is a desirable phenomenon that explains the strong decrease in the overpotential value (up to 352 mV with a current density of 10 mA cm^{-2}) for samples with the lowest I/C (0.04 in 5 μL of ink loaded on the electrode) and the longest time of mechanical treatment (30 days). These results also confirm that the hypothesis put forward in the previous section concerning the inhibition of the improvement of the catalytic properties of the electrode after 6 days of ball-milling as a result of blocking the surface of the MCO catalyst particles by a too-thick layer of Nafion was correct.

In the case of reducing the amount of cCB in the ink, the effects (in the range of the amount of cCB that was checked) were opposite to the Nafion (Fig. 7d). Reducing the ratio of conductive carbon black to catalyst (cCB/C) in the ink portion applied to the GC electrode from 1 to 0.1 resulted in an overpotential increase of 100 mV after 6 days of ball-milling. Nevertheless, reducing the cCB contribution to the catalyst layer reduced the number of conduction paths as manifested by a lower yield of manganese cobalt spinel. When the amount of cCB was increased from 1 cCB/C to 1.5 and 2, no further improvements in activity were observed (Fig. S5a). It is related to the supersaturation of the catalytic layer with conductive particles cCB. The density of catalytic active sites decreases as a result of a decrease in the amount of MCO catalyst particles in a given volume in favor of conductive carbon particles cCB. A similar observation of the deterioration of the catalytic properties of the NiSe-Ni_3Se_2/MWCNT catalyst after increasing the amount of MWCNT carbon nanotubes was made by Oyetade and Kriek [50]. Also, the electrode capacity tended to decrease with the decrease in the amount of cCB in the catalyst layer (Fig. S5b). It is visible that the amount of conducting particles is very important and affects the use of the electrocatalyst in the OER reaction. Mattick et al. obtained very similar results showing that the lower the catalyst/carbon ratio (increasing carbon content), the lower the values of the overpotential of the OER reaction [49]. Equally

important, the addition of cCB also contributes to an increase in the stability of the samples in subsequent cycles of the OER process [48,78].

3.4. Long-term stability tests

The long-term stability tests at 10 mA cm^{-2} were evaluated by the chronopotentiometry method. The analysis was performed in 0.1 M KOH with a commercial electrolyzer cell (ElectroCell, Micro Flow Cell). Fig. 8a presented results for conductive carbon (cCB) and $MnCo_2O_4$ (C) ratio equal to 1 cCB/C and 2 cCB/C. The analysis was carried out for 50 h at room temperature. In the case of sample 1 cCB/C, we observed a stable voltage for the first 3 h, then it increased by about 120 mV during the next 4 h. For the next 43 h, the voltage at a relatively constant level was observed again, although periodic increases and decreases of about 50 mV were visible (Fig. 8b). These fluctuations were most likely related to the formation (voltage increase) and subsequent detachment (voltage decrease) of oxygen bubbles accumulating on the surface of the porous carbon paper support. For 50 h of the electrolysis process with a catalytic layer of 1 cCB/C, the potential increased by a maximum of 9 %. In the case of a sample with 2 times more cCB than the MCO catalyst in the catalytic layer (2 cCB/C), the graph of voltage stability over time looked very similar (Fig. 8c). Nevertheless, in this case, the initial voltage increase at the very start of the electrolysis process lasted for the first 10 h. Then, for the next 30 h (i.e. up to 40 h of the process), slight but recurring voltage increases and decreases were observed. They were caused, as in the case of sample 1 cCB/C, by the formation and detachment of oxygen bubbles. For about 40 h, a slight but continuous increase in voltage was observed, which indicates a slow degradation of the carbon paper support with the catalytic layer. It is difficult to clearly determine whether this degradation was the result of the disintegration of carbon paper or the fall off of particles forming the catalyst layer. As Lankauf et al. showed, pure carbon paper support in the conditions of 0.1 M KOH began to degrade after 30 min [72]. The presence of a higher concentration of conductive carbon particles (cCB) in the catalytic layer has some effect on the stability of the system in long-term tests. However, further research is needed to determine this impact precisely.

4. Conclusion

A commercially available $MnCo_2O_4$ spinel powder was treated using a ball-milling process to refine the powder particles and thus increase their electrocatalytic efficiency. The results of the morphological analysis and the BET measurement showed a clear increase in the fragmentation of the spinel particles with the extension of the milling time. This is visible in the growth of the SSA, the size of which increased almost 3-fold after 6 days of machining. Physicochemical analysis revealed some differences between the MCO samples milled in the presence of cCB and its absence. First of all, the addition of cCB caused the formation of cobalt hydroxide on the surface of the spinel, which significantly improved the catalytic properties of the compounds modified in this way. The performed electrochemical studies indicated that 6 days of ball milling of MCO spinel particles resulted in a decrease in the obtained overpotential by more than 60 mV compared to the original sample (without mechanical treatment). In the case of the morphology after 30 days of the ball-milling process, the size of the spinel particles is drastically decreased. The obtained results of material electrochemical activity towards OER are among the best for this type of spinel-based materials presented in the literature.

The presented results also show that the catalytic properties in the OER process are decisively influenced by the use of mechanical treatment of MCO spinel particles. The use of the low-energy ball-milling process contributed both to the fragmentation of the spinel particles, as well as to the breakdown of the resulting agglomerates of nanoparticles of powder formed in the milling process. It was also found that the addition of cCB has a more negligible effect on the increasing electrochemical activity of the MCO catalyst than mechanical modification. Studies of the effect of the ball-milling process on the electrochemical activation of oxide catalysts are very interesting and show a promising way to fabricate low-cost and high active electrocatalysts. The presence of Nafion prevents the catalyst from detaching from the electrode surface, but also facilitates the creation of an efficient interface for charge transport and the OER process. The blocking effect of Nafion on the mass transport and electrochemical reactions can be considered a common phenomenon with alkaline OER regardless of the catalyst loading and the type of materials used. Additionally, it needs to be highlighted that the presence of an optimisation process of Nafion and cCB content is necessary to form a stable and efficient catalyst layer for OER. Based on the obtained data, we conclude that the improvement of the electrocatalytic properties of the manganese-cobalt spinel subjected to the milling process is the result of the synergistic effect of (Fig. 9): (1) chemical changes that occur on the surface of the MCO catalyst particles as a result of mechanical treatment with cCB; (2) physical changes resulting from the mechanical fragmentation of spinel particles, which however, has a much stronger impact; (3) the appropriate composition of the components forming the catalyst layer. Determining the weight of the importance of the individual factors is complicated and requires further and more complex research.

Based on the results obtained in this article, we can recommend a certain methodology for the preparation of OER electrocatalysts. First of all, the appropriate fragmentation of the starting material produces a very strong improvement in the activity of the catalyst layer. The reason for this is both an increase in the active surface area of the catalyst and possible changes in the valence of the ions that make up the catalyst. Of course, depending on the material, the time needed for fragmentation of the catalyst material to obtain the best possible results in a relatively short time may vary. Nevertheless, as our research has shown that fragmentation of the oxide material by low-energy ball-milling is an efficient and necessary process that should be added to any procedure

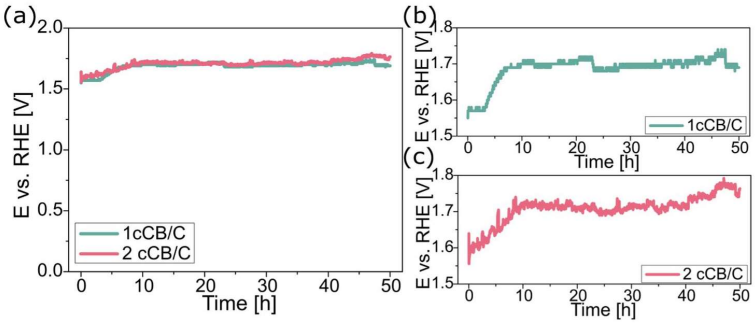

Fig. 8. Long-term stability tests of $MnCo_2O_4$ catalyst with ratio conductive carbon black (cCB) and MCO catalyst (C) equal 1 cCB/C and 2 cCB/C at 10 mA/cm^2.

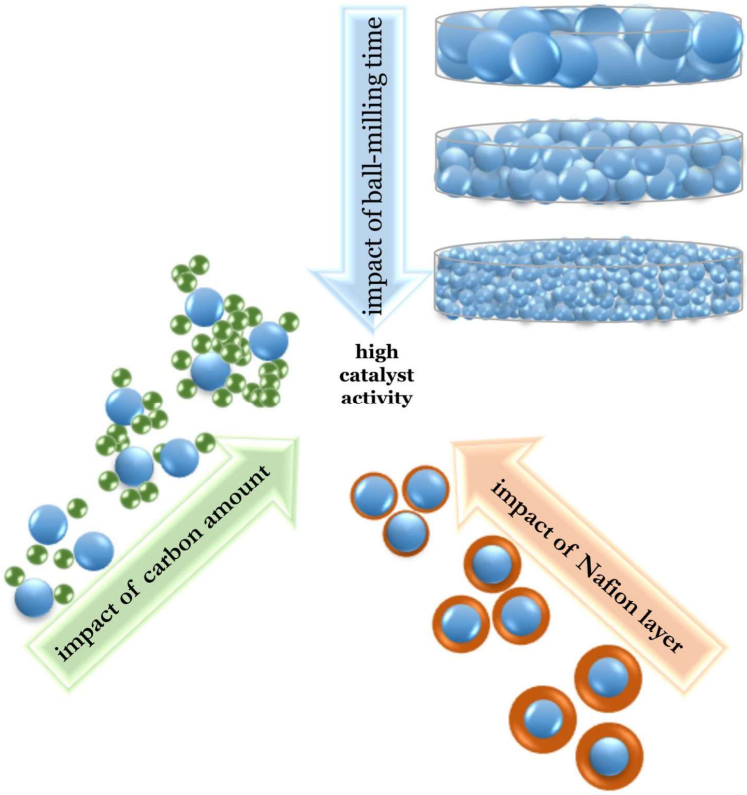

Fig. 9. Impact of ball-milling process and ink composition on electrochemical activity of catalyst layer for OER.

for the preparation of metal oxide-based electrocatalysts. Secondly, the ratio of Nafion to catalyst should not exceed 0.1 to provide the smallest possible barrier separating the catalyst surface from the electrolyte, thus increasing the availability of active sites of the catalyst. This is of particular importance when the catalyst particles are subjected to the milling process, so the ratio of their size to the Nafion layer is smaller and smaller, and the ionomer used can block more. Third, the right amount of electron conductive particles (e.g. conducting carbon) is crucial. According to our findings, the weight ratio of carbon-catalyst should not be less than 1. The recommendations presented should be verified and adjusted to the various materials for the desired effects to be achieved. Nevertheless, focussing on these three aspects is important and should be optimised at the very beginning of work aimed at developing efficient OER electrocatalysts.

CRediT authorship contribution statement

Sylwia Pawłowska: Writing – original draft, Investigation, Data curation. **Krystian Lankauf:** Investigation, Writing – review & editing. **Patryk Błaszczak:** Investigation, Writing – review & editing. **Jakub Karczewski:** Investigation, Writing – review & editing. **Karolina Górnicka:** Investigation, Writing – review & editing. **Grzegorz Cempura:** Investigation, Writing – review & editing. **Piotr Jasiński:** Writing – review & editing. **Sebastian Molin:** Writing – review & editing, Funding acquisition, Project administration.

Declaration of Competing Interest

The authors declare that they have no known competing financial interests or personal relationships that could have appeared to influence the work reported in this paper.

Data availability

Data will be made available on request.

Acknowledgement

The presented research is part of the "Nanocrystalline ceramic materials for efficient electrochemical energy conversion" project, carried out within the First TEAM programme of the Foundation for Polish Science (grant agreement nr. POIR.04.04.00-00-42E9/17-00).

Appendix A. Supplementary material

Supplementary data to this article can be found online at https://doi.org/10.1016/j.apsusc.2023.156720.

References

[1] S. Yagi, I. Yamada, H. Tsukasaki, A. Seno, M. Murakami, H. Fujii, H. Chen, N. Umezawa, H. Abe, N. Nishiyama, S. Mori, Covalency-reinforced oxygen evolution reaction catalyst, Nat. Commun. 6 (2015) 8249, https://doi.org/10.1038/ncomms9249.

[2] X. Ge, A. Sumboja, D. Wuu, T. An, B. Li, F.W.T. Goh, T.S.A. Hor, Y. Zong, Z. Liu, Oxygen reduction in alkaline media: from mechanisms to recent advances of catalysts, ACS Catal. 5 (2015) 4643–4667, https://doi.org/10.1021/acscatal.5b00524.

[3] W. Chu, Z. Shi, Y. Hou, D. Ma, X. Bai, Y. Gao, N. Yang, Trifunctional of phosphorus-doped NiCo2O4 nanowire materials for asymmetric supercapacitor, oxygen evolution reaction, and hydrogen evolution reaction, ACS Appl. Mater. Interfaces 12 (2020) 2763–2772, https://doi.org/10.1021/acsami.9b13182.

[4] Z. Wang, J. Huang, L. Wang, Y. Liu, W. Liu, S. Zhao, Z.-Q. Liu, Cation-tuning inducedd-band center modulationon co-based spinel oxide for oxygen reduction/evolution reaction, Angew. Chem. Int. Ed. 61 (2022) e202114696.

[5] G. Nazir, A. Rehman, S. Hussain, S. Aftab, K. Heo, M. Ikram, S.A. Patil, M.A.U. Din, Recent advances and reliable assessment of solid-state materials for hydrogen storage: a step forward toward a sustainable H_2 economy, Adv. Sustain. Syst. (2022) 2200276, https://doi.org/10.1002/adsu.202200276.

[6] X. Cao, C. Jin, F. Lu, Z. Yang, M. Shen, R. Yang, Electrochemical properties of MnCo2O4 spinel bifunctional catalyst for oxygen reduction and evolution reaction, J. Electrochem. Soc. 161 (2014) H296–H300, https://doi.org/10.1149/2.029405jes.

[7] X. Lu, C. Zhao, Electrodeposition of hierarchically structured three-dimensional nickel-iron electrodes for efficient oxygen evolution at high current densities, Nat. Commun. 6 (2015) 6616, https://doi.org/10.1038/ncomms7616.

[8] J.S. Chen, J. Ren, M. Shalom, T. Fellinger, M. Antonietti, Stainless steel mesh-supported NiS nanosheet array as highly efficient catalyst for oxygen evolution reaction, ACS Appl. Mater. Interfaces 8 (2016) 5509–5516, https://doi.org/10.1021/acsami.5b10099.

[9] E. Fabbri, X. Cheng, T.J. Schmidt, Highly active Ba0.5Sr0.5Co0.8Fe0.2O3-single material electrode towards the oxygen evolution reaction for alkaline water splitting applications, ECS Trans. 69 (2015) 869–875, https://doi.org/10.1149/06917.0869ecst.

[10] J. Suntivich, K.J. May, H.A. Gasteiger, J.B. Goodenough, Y. Shao-Horn, A perovskite oxide optimized for oxygen evolution catalysis from molecular orbital principles, Science 334 (2011) 1383–1385, https://doi.org/10.1126/science.1212858.

[11] X. Ma, J. Wen, S. Zhang, H. Yuan, K. Li, F. Yan, X. Zhang, Y. Chen, Crystal CoxB (x = 1–3) synthesized by a ball-milling method as high-performance electrocatalysts for the oxygen evolution reaction, ACS Sustain. Chem. Eng. (2017) 10266–10274, https://doi.org/10.1021/acssuschemeng.7b02281.

[12] H. Liu, D. Guo, W. Zhang, R. Cao, Co(OH)2 hollow nanoflowers as highly efficient electrocatalysts for oxygen evolution reaction, J. Mater. Res. 33 (2018) 568–580, https://doi.org/10.1557/jmr.2017.390.

[13] A. Rebekah, S. Anantharaj, C. Viswanthan, N. Ponpandian, Zn-substituted MnCo2O4 nanostructure anchored over rGO for boosting the electrocatalytic performance towards methanol oxidation and oxygen evolution reaction (OER), Int. J. Hydrogen Energy (2020), https://doi.org/10.1016/j.ijhydene.2020.03.231.

[14] X. Zou, A. Goswami, T. Asefa, Efficient noble metal-free (electro)catalysis of water and alcohol oxidations by zinc-cobalt layered double hydroxide, J. Am. Chem. Soc. 135 (2013) 17242–17245, https://doi.org/10.1021/ja407174u.

[15] P.W. Menezes, A. Indra, N.R. Sahraie, A. Bergmann, P. Strasser, M. Driess, Cobalt-manganese-based spinels as multifunctional materials that unify catalytic water oxidation and oxygen reduction reactions, ChemSusChem 8 (2015) 164–171, https://doi.org/10.1002/cssc.201402699.

[16] M. García-Mota, M. Bajdich, V. Viswanathan, A. Vojvodic, A.T. Bell, J.K. Nørskov, Importance of correlation in determining electrocatalytic oxygen evolution activity on cobalt oxides, J. Phys. Chem. C 116 (2012) 21077–21082, https://doi.org/10.1021/jp306303y.

[17] K.A. Stoerzinger, M. Risch, B. Han, Y. Shao-Horn, Recent insights into manganese oxides in catalyzing oxygen reduction kinetics, ACS Catal. 5 (2015) 6021–6031, https://doi.org/10.1021/acscatal.5b01444.

[18] W. Wang, L. Kuai, W. Cao, M. Huttula, S. Ollikkala, T. Ahopelto, A.-P. Honkanen, S. Huotari, M. Yu, B. Geng, Mass-production of mesoporous $MnCo_2O_4$ spinels with manganese (IV)- and cobalt (II)-rich surfaces for superior bifunctional oxygen electrocatalysis, Angew. Chemie 129 (2017) 15173–15177, https://doi.org/10.1002/ange.201708765.

[19] P.W. Menezes, A. Indra, V. Gutkin, M. Driess, Boosting electrochemical water oxidation through replacement of Oh Co sites in cobalt oxide spinel with manganese, Chem. Commun. 53 (2017) 8018–8021, https://doi.org/10.1039/c7cc03749j.

[20] K. Lankauf, K. Cysewska, J. Karczewski, A. Mielewczyk-Gryń, K. Górnicka, G. Cempura, M. Chen, P. Jasiński, S. Molin, MnxCo3-XO4 spinel oxides as efficient oxygen evolution reaction catalysts in alkaline media, Int. J. Hydrogen Energy 45 (2020) 14867–14879, https://doi.org/10.1016/j.ijhydene.2020.03.188.

[21] X. Ge, Y. Liu, F.W.T. Goh, T.S.A. Hor, Y. Zong, P. Xiao, Z. Zhang, S.H. Lim, B. Li, X. Wang, Z. Liu, Dual-phase spinel MnCo2O4 and spinel MnCo 2O4/nanocarbon hybrids for electrocatalytic oxygen reduction and evolution, ACS Appl. Mater. Interfaces 6 (2014) 12684–12691, https://doi.org/10.1021/am502675c.

[22] S. Wang, Y. Hou, X. Wang, Development of a stable MnCo2O4 cocatalyst for photocatalytic CO2 reduction with visible light, ACS Appl. Mater. Interfaces 7 (2015) 4327–4335, https://doi.org/10.1021/am508766s.

[23] J. Béjar, F. Espinosa-Magaña, M. Guerra-Balcázar, J. Ledesma-García, L. Álvarez-Contreras, N. Arjona, L.G. Arriaga, Three-dimensional-order macroporous AB2O4 spinels (A, B =Co and Mn) as electrodes in Zn-Air batteries, ACS Appl. Mater. Interfaces 12 (2020) 53760–53773, https://doi.org/10.1021/acsami.0c14920.

[24] M. Zhao, J. Deng, J. Liu, Y. Li, J. Liu, Z. Duan, J. Xiong, Z. Zhao, Y. Wei, W. Song, Y. Sun, Roles of surface-active oxygen species on 3DOM cobalt-based spinel catalysts MxCo3-XO4 (M = Zn and Ni) for NOx-assisted soot oxidation, ACS Catal. 9 (2019) 7548–7567, https://doi.org/10.1021/acscatal.9b01995.

[25] S. Chen, D. Huang, D. Liu, H. Sun, W. Yan, J. Wang, M. Dong, X. Tong, W. Fan, Hollow and porous $NiCo_2O_4$ nanospheres for enhanced methanol oxidation reaction and oxygen reduction reaction by oxygen vacancies engineering, Appl. Catal. B 291 (2021), 120065, https://doi.org/10.1016/j.apcatb.2021.120065.

[26] T. Tsuzuki, Mechanochemical synthesis of metal oxide nanoparticles, Commun. Chem. 4 (2021) 143, https://doi.org/10.1038/s42004-021-00582-3.

[27] P.P. Chin, J. Ding, J.B. Yi, B.H. Liu, Synthesis of FeS2 and FeS nanoparticles by high-energy mechanical milling and mechanochemical processing, J. Alloy. Compd. 390 (2005) 255–260, https://doi.org/10.1016/j.jallcom.2004.07.053.

[28] Y. Lin, K.A. Watson, S. Ghose, J.G. Smith, T.V. Williams, R.E. Crooks, W. Cao, J. W. Connell, Direct mechanochemical formation of metal nanoparticles on carbon nanotubes, J. Phys. Chem. C 113 (2009) 14858–14862, https://doi.org/10.1021/jp905076u.

[29] A.F. Fuentes, L. Takacs, Preparation of multicomponent oxides by mechanochemical methods, J. Mater. Sci. 48 (2013) 598–611, https://doi.org/10.1007/s10853-012-6909-x.

[30] N.L. Michels, S. Mitchell, J. Pérez-Ramírez, Effects of binders on the performance of shaped hierarchical MFI zeolites in methanol-to-hydrocarbons, ACS Catal. 4 (2014) 2409–2417, https://doi.org/10.1021/cs500353b.

[31] G.N. Hermann, C. Bolm, Mechanochemical rhodium (III)-catalyzed C-H bond amidation of arenes with dioxazolones under solventless conditions in a ball mill, ACS Catal. 7 (2017) 4592–4596, https://doi.org/10.1021/acscatal.7b00582.

[32] X. Cheng, E. Fabbri, B. Kim, M. Nachtegaal, T.J. Schmidt, Effect of ball milling on the electrocatalytic activity of Ba0.5Sr0.5Co0.8Fe0.2O3 towards the oxygen evolution reaction, J. Mater. Chem. A 5 (2017) 13130–13137, https://doi.org/10.1039/c7ta00794a.

[33] A. Talimian, V. Pouchly, H.F. El-Maghraby, K. Maca, D. Galusek, Impact of high energy ball milling on densification behaviour of magnesium aluminate spinel evaluated by master sintering curve and constant rate of heating approach, Ceram. Int. 45 (2019) 23467–23474, https://doi.org/10.1016/j.ceramint.2019.08.051.

[34] W. Wang, D.D. Babu, Y. Huang, J. Lv, Y. Wang, M. Wu, Atomic dispersion of Fe/Co/N on graphene by ball-milling for efficient oxygen evolution reaction, Int. J. Hydrogen Energy 43 (2018) 10351–10358, https://doi.org/10.1016/j.ijhydene.2018.04.108.

[35] X. Fan, D.W. Chang, X. Chen, J.B. Baek, L. Dai, Functionalized graphene nanoplatelets from ball milling for energy applications, Curr. Opin. Chem. Eng. 11 (2016) 52–58, https://doi.org/10.1016/j.coche.2016.01.003.

[36] M.A.R. Anjum, M.H. Lee, J.S. Lee, Boron- and nitrogen-codoped molybdenum carbide nanoparticles imbedded in a BCN network as a bifunctional electrocatalyst for hydrogen and oxygen evolution reactions, ACS Catal. 8 (2018) 8296–8305, https://doi.org/10.1021/acscatal.8b01794.

[37] W. Ding, M. Sun, B. Gao, W. Liu, Z. Ding, S. Anandan, A ball-milling synthesis of N-graphyne with controllable nitrogen doping sites for efficient electrocatalytic oxygen evolution and supercapacitors, Dalton Trans. 49 (2020) 10958–10969, https://doi.org/10.1039/D0DT01855D.

[38] S.G. Sayyed, M.A. Mahadik, A.V. Shaikh, J.S. Jang, H.M. Patha, Nano-metal oxide based supercapacitor via electrochemical deposition, ES Energy Environ. 3 (2019) 25–44. 10.30919/esee8c211.

[39] J.R. Creighton, P. Ho, Introduction to Chemical Vapor Deposition (CVD), ASM International, ISBN-10:087170692X, ISBN-13:978-0871706928.

[40] T. Suzuki, S. Tsushima, S. Hirai, Effects of Nafion® ionomer and carbon particles on structure formation in a proton-exchange membrane fuel cell catalyst layer fabricated by the decal-transfer method, Int. J. Hydrogen Energy 36 (2011) 12361–12369, https://doi.org/10.1016/j.ijhydene.2011.06.090.

[41] M. Bühler, F. Hegge, P. Holzapfel, M. Bierling, M. Suermann, S. Vierrath, S. Thiele, Optimization of anodic porous transport electrodes for proton exchange membrane water electrolyzers, J. Mater. Chem. A 7 (2019) 26984–26995, https://doi.org/10.1039/c9ta08396k.

[42] F.M. Sapountzi, S.C. Divane, E.I. Papaioannou, S. Souentie, C.G. Vayenas, The role of nafion content in sputtered IrO2 based anodes for low temperature PEM water electrolysis, J. Electroanal. Chem. 662 (2011) 116–122, doi: 10.1016/j.jelechem.2011.04.005.

[43] T. Schuler, T. Kimura, T.J. Schmidt, F.N. Büchi, Towards a generic understanding of oxygen evolution reaction kinetics in polymer electrolyte water electrolysis, Energ. Environ. Sci. 13 (2020) 2153–2166, https://doi.org/10.1039/d0ee00673d.

[44] G. Li, L. Anderson, Y. Chen, M. Pan, P.Y. Abel Chuang, New insights into evaluating catalyst activity and stability for oxygen evolution reactions in alkaline media, Sustain. Energy Fuels 2 (2018) 237–251, https://doi.org/10.1039/c7se00337d.

[45] G.F. Li, D. Yang, P.Y. Abel Chuang, Defining nafion ionomer roles for enhancing alkaline oxygen evolution electrocatalysis, ACS Catal. 8 (2018) 11688–11698, https://doi.org/10.1021/acscatal.8b02217.

[46] A. Kusoglu, A.Z. Weber, New insights into perfluorinated sulfonic-acid ionomers, Chem. Rev. 117 (2017) 987–1104, https://doi.org/10.1021/acs.chemrev.6b00159.

[47] I.S. Filimonenkov, C. Bouillet, G. Kéranguéven, P.A. Simonov, G.A. Tsirlina, E. R. Savinova, Carbon materials as additives to the OER catalysts: RRDE study of carbon corrosion at high anodic potentials, Electrochim. Acta 321 (2019) 134657, https://doi.org/10.1016/j.electacta.2019.134657.

[48] R. Mohamed, X. Cheng, E. Fabbri, P. Levecque, R. Kötz, O. Conrad, T.J. Schmidt, Electrocatalysis of perovskites: the influence of carbon on the oxygen evolution activity, J. Electrochem. Soc. 162 (2015) F579–F586, https://doi.org/10.1149/2.0861506jes.

[49] V.F. Mattick, X. Jin, R.E. White, K. Huang, Understanding the role of carbon in alkaline oxygen electrocatalysis: a case study on La0.6Sr0.4CoO3-Δ/Vulcan carbon

composite electrocatalyst, Int. J. Hydrogen Energy 44 (2019) 2760–2769, https://doi.org/10.1016/j.ijhydene.2018.12.048.
[50] O.A. Oyetade, R.J. Kriek, NiSe-Ni3Se2/multiwalled carbon nanotube composites as efficient electrocatalysts for the oxygen evolution reaction in alkaline media, Electrocatalysis 11 (2020) 35–45, https://doi.org/10.1007/s12678-019-00558-x.
[51] Z.H. Ibupoto, A. Tahira, A.A. Shah, U. Aftab, M.Y. Solangi, J.A. Leghari, A. H. Samoon, A.L. Bhatti, M.A. Bhatti, R. Mazzaro, V. Morandi, M.I. Abro, A. Nafady, A.M. Al-Enizi, M. Emo, B. Vigolo, $NiCo_2O_4$ nanostructures loaded onto pencil graphite rod: an advanced composite material for oxygen evolution reaction, Int. J. Hydrogen Energy 47 (2022) 6650–6665, https://doi.org/10.1016/j.ijhydene.2021.12.024.
[52] M.A. Kazakova, D.M. Morales, C. Andronescu, K. Elumeeva, A.G. Selyutin, A. V. Ishchenko, G.V. Golubtsov, S. Dieckhöfer, W. Schuhmann, J. Masa, Fe/Co/Ni mixed oxide nanoparticles supported on oxidized multi-walled carbon nanotubes as electrocatalysts for the oxygen reduction and the oxygen evolution reactions in alkaline media, Catal. Today 357 (2020) 259–268, https://doi.org/10.1016/j.cattod.2019.02.047.
[53] J. Xu, J. Li, Q. Yang, Y. Xiong, C. Chen, In-situ synthesis of MnO_2@graphdiyne oxides nanocomposite with enhanced performance of supercapacitors, Electrochim. Acta 251 (2017) 672–680, https://doi.org/10.1016/j.electacta.2017.07.102.
[54] A. Purwanto, A. Fajar, H. Mugirahardjo, J.W. Fergus, K. Wang, Cation distribution in spinel (Mn Co, Cr)3O4 at room temperature, J. Appl. Cryst. 43 (2010) 394–400, https://doi.org/10.1107/S0021889810008150.
[55] O. Diaz-Morales, I. Ledezma-Yanez, M.T.M. Koper, F. Calle-Vallejo, Guidelines for the rational design of Ni-based double hydroxide electrocatalysts for the oxygen evolution reaction, ACS Catal. 5 (2015) 5380–5387, https://doi.org/10.1021/acscatal.5b01638.
[56] X. Zheng, L. Yu, B. Lan, G. Cheng, T. Lin, B. He, W. Ye, M. Sun, F. Ye, Three-dimensional radial A-MnO2 synthesized from different redox potential for bifunctional oxygen electrocatalytic activities, J. Power Sources (2017) 332–341, https://doi.org/10.1016/j.jpowsour.2017.07.027.
[57] B. Heidinger, S. Royer, H. Alamdari, J.M. Giraudon, J.F. Lamonier, Reactive grinding synthesis of LaBo3 (B: Mn, Fe) perovskite; properties for toluene total oxidation, Catalysts 9 (2019) 1–18, https://doi.org/10.3390/catal9080633.
[58] N. Padmanathan, S. Selladurai, Mesoporous MnCo2O4 spinel oxide nanostructure synthesized by solvothermal technique for supercapacitor, Ionics (Kiel) 20 (2014) 479–487, https://doi.org/10.1007/s11581-013-1009-8.
[59] S. Sahoo, K.K. Naik, C.S. Rout, Electrodeposition of spinel MnCo2O4 nanosheets for supercapacitor applications, Nanotechnology 26 (2015) 455401, doi:10.1088/0957-4484/26/45/455401.
[60] O.M. Lemine, Effect of milling conditions on the formation of ZnFe2O4 nanocrystalline, Int. J. Phys. Sci. 8 (2013) 380–387, https://doi.org/10.5897/IJPS10.575.
[61] M. Jahan, S. Tominaka, J. Henzie, Phase pure α-Mn2O3 prisms and their bifunctional electrocatalytic activity in oxygen evolution and reduction reactions, Dalt. Trans. 45 (2016) 18494–18501, https://doi.org/10.1039/c6dt03158g.
[62] P.W. Menezes, A. Indra, D. González-Flores, N.R. Sahraie, I. Zaharieva, M. Schwarze, P. Strasser, H. Dau, M. Driess, High-performance oxygen redox catalysis with multifunctional cobalt oxide nanochains: morphology-dependent activity, ACS Catal. 5 (2015) 2017–2027, https://doi.org/10.1021/cs501724v.
[63] Y. Ha, L. Shi, X. Yan, Z. Chen, Y. Li, W. Wei Xu, R. Wu, Multifunctional electrocatalysis on a porous N-doped NiCo2O4@C nanonetwork, ACS Appl. Mater. Interfaces 11 (2019) 45546–45553, https://doi.org/10.1021/acsami.9b13580.
[64] Z. Huang, W. Zhou, C. Ouyang, J. Wu, F. Zhang, J. Huang, Y. Gao, J. Chu, High performance of Mn-Co-Ni-O spinel nanofilms sputtered from acetate precursors, Sci. Rep. 5 (2015) 10899, https://doi.org/10.1038/srep10899.
[65] M. Wang, K. Chen, J. Liu, Q. He, G. Li, F. Li, Efficiently enhancing electrocatalytic activity of α-MnO2 nanorods/N-doped Ketjenblack carbon for oxygen reduction reaction and oxygen evolution reaction using facile regulated hydrothermal treatment, Catalysts 8 (2018) 138, https://doi.org/10.3390/catal8040138.
[66] C. Wei, Z. Feng, G.G. Scherer, J. Barber, Y. Shao-Horn, Z.J. Xu, Cations in octahedral sites: a descriptor for oxygen electrocatalysis on transition-metal spinels, Adv. Mater. 29 (2017) 1606800, https://doi.org/10.1002/adma.201606800.
[67] S.V. Devaguptapu, S. Hwang, S. Karakalos, S. Zhao, S. Gupta, D. Su, H. Xu, G. Wu, Morphology control of carbon-free spinel NiCo2O4 catalysts for enhanced bifunctional oxygen reduction and evolution in alkaline media, ACS Appl. Mater. Interfaces 9 (2017) 44567–44578, https://doi.org/10.1021/acsami.7b16389.
[68] X. Long, P. Yu, N. Zhang, C. Li, X. Feng, G. Ren, S. Zheng, J. Fu, F. Cheng, X. Liu, Direct spectroscopy for probing the critical role of partial covalency in oxygen reduction reaction for cobalt-manganese spinel oxides, Nanomaterials 9 (2019) 577, https://doi.org/10.3390/nano9040577.
[69] A. Indra, P.W. Menezes, N.R. Sahraie, A. Bergmann, C. Das, M. Tallarida, D. Schmeißer, P. Strasser, M. Driess, Unification of catalytic water oxidation and oxygen reduction reactions: amorphous beat crystalline cobalt iron oxides, J. Am. Chem. Soc. 136 (2014) 17530–17536, https://doi.org/10.1021/ja509348t.
[70] J.G. Kim, Y. Kim, Y. Noh, W.B. Kim, MnCo2O4 nanowires anchored on reduced graphene oxide sheets as effective bifunctional catalysts for Li-O2 battery cathodes, ChemSusChem 8 (2015) 1752–1760, https://doi.org/10.1002/cssc.201500123.
[71] Y. Zhu, W. Zhou, Z.G. Chen, Y. Chen, C. Su, M.O. Tadé, Z. Shao, SrNb0.1Co0.7Fe0.2O3-δ perovskite as a next-generation electrocatalyst for oxygen evolution in alkaline solution, Angew. Chemie - Int. Ed. 54 (2015) 3897–3901, https://doi.org/10.1002/anie.201408998.
[72] K. Lankauf, K. Górnicka, P. Błaszczak, J. Karczewski, J. Ryl, G. Cempura, M. Zając, M. Bik, M. Sitarz, P. Jasinski, S. Molin, Tuning of Eg electron occupancy of $MnCo_2O_4$ spinel for oxygen evolution reaction by partial substitution of Co by Fe at octahedral sites, Int. J. Hydrogen Energy (in press), doi: 10.1016/j.ijhydene.2022.12.013.
[73] K. Zeng, W. Li, Y. Zhou, Z. Sun, C. Lu, J. Yan, J.-H. Choi, R. Yang, Multilayer hollow $MnCo_2O_4$ microsphere with oxygen vacancies as efficient electrocatalyst for oxygen evolution reaction, Chem. Eng. J. (2020), 127831, https://doi.org/10.1016/j.cej.2020.127831.
[74] M.P. Browne, H. Nolan, G.S. Duesberg, P.E. Colavita, M.E.G. Lyons, Low-Overpotential high-activity mixed manganese and ruthenium oxide electrocatalysts for oxygen evolution reaction in alkaline media, ACS Catal. 6 (2016) 2408–2415, https://doi.org/10.1021/acscatal.5b02069.
[75] S. Anantharaj, P.E. Karthik, S. Kundu, Self-assembled IrO2 nanoparticles on a DNA scaffold with enhanced catalytic and oxygen evolution reaction (OER) activities, J. Mater. Chem. A 3 (2015) 24463–24478, https://doi.org/10.1039/c5ta07075a.
[76] S. Anantharaj, K. Karthick, S. Kundu, Evolution of layered double hydroxides (LDH) as high performance water oxidation electrocatalysts: a review with insights on structure, activity and mechanism, Mater. Today Energy 6 (2017) 1–26, https://doi.org/10.1016/j.mtener.2017.07.016.
[77] T. Shinagawa, A.T. Garcia-Esparza, K. Takanabe, Insight on Tafel slopes from a microkinetic analysis of aqueous electrocatalysis for energy conversion, Sci. Rep. 5 (2015) 13801, https://doi.org/10.1038/srep13801.
[78] M. Risch, K.A. Stoerzinger, S. Maruyama, W.T. Hong, I. Takeuchi, La0.8Sr0.2MnO3−δ decorated with Ba0.5Sr0.5Co0.8Fe0.2O3−δ: a bifunctional surface for oxygen electrocatalysis with enhanced stability and activity, J. Am. Chem. Soc. 136 (2014) 5229–5232, https://doi.org/10.1021/ja5009954.

SUPPLEMENTARY MATERIAL

Tailoring a low-energy ball milled $MnCo_2O_4$ spinel catalyst to boost oxygen evolution reaction performance

Sylwia Pawłowska [a], Krystian Lankauf [a], Patryk Błaszczak [b], Jakub Karczewski [b], Karolina Górnicka [b], Grzegorz Cempura [c], Piotr Jasiński [a], Sebastian Molin [a]*

Calibration of Hg/HgO reference electrode: Standard three-electrode system and Rotating Ring Disk Electrode (RDE-3A) equipment were used, with a rotating platinum disc (diameter 3 mm) as the working electrode and a Pt wire as the counter electrode. 0.1 M KOH electrolyte was saturated with high-purity H_2 for 30 minutes. After that time, the hydrogen flow was maintained above the electrolyte solution throughout the calibration. Cycling voltammetry (CV) was used with a scan rate of 10 mV s^{-1}. Calibration was carried out until the potential was stabilised, which required 30–40 cycles. The thermodynamic potential for the hydrogen electrode reactions is where the current crossed zero. The working electrode rotated at a speed of 1600 rpm. Hydrogen for the calibration process was produced using a hydrogen generator.

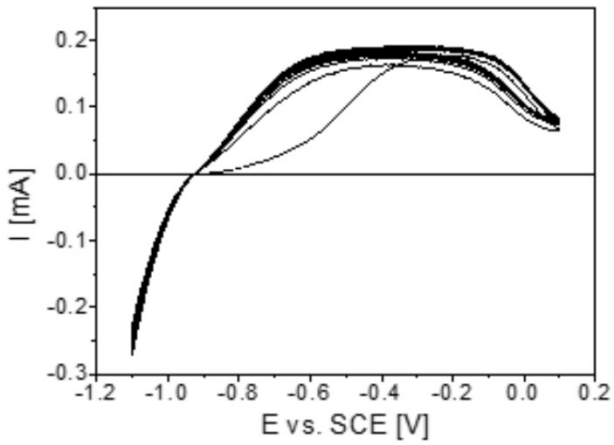

Fig. S1. Example graph showing the calibration process of the Hg/HgO reference electrode using a hydrogen generator to determine its equilibrium potential.

Morphology of milled $MnCo_2O_4$ spinel particles:

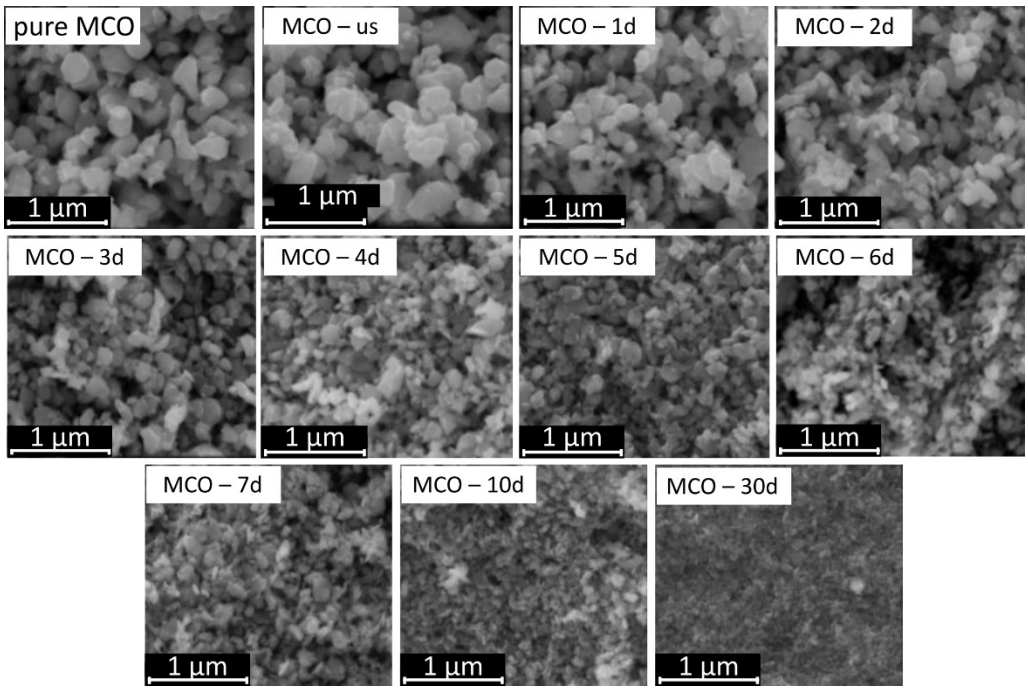

Fig. S2. MCO spinel particle morphology analysis without any modification (pure MCO), after 30 minutes of ultrasonication (MCO – us), and after 1, 2, 3, 4, 5, 6, 7, 10, and 30 days of ball-milling treatment.

$MnCo_2O_4$ spinel particle size analysis: In comparison, powders without any treatment and after 0.5 hours of sonication have a higher variety in size than powders after grinding (Fig. S3a). This is confirmed by the data of the particle size distribution of the powders obtained by dynamic light scattering analysis (DLS). Suspensions for DLS were

prepared by suspended powders in ethanol (viscosity 2.781 cP). DLS measurements were performed at 25 °C, assuming that the refractive index for the wavelength of 633 nm was 2.0 and 1.36 for the dispersed particles and the solvent, respectively. The measurement was carried out with a disposable micro cuvette with a measurement position of 3 mm from the bottom. Figure 2b shows the particle size distribution of spinel without any treatment (pure MCO) and powders after grinding for 3 and 6 days. In general, it was observed that all spinel powders subjected to the milling process, regardless of the time used (Figure S3b), show the presence of an additional fraction in the range close to 5 μm. At a particle size smaller than 20 μm, the surface forces prevail. The grinding stock begins to stick. For all tested powder samples, peaks ranging from 300 to 900 nm were observed, which may correspond to the size values of the $MnCo_2O_4$ spinel powders declared by the manufacturer (300–500 nm). It should be emphasised, however, that the values determined by DLS, just like any similar technique based on the analysis of nanoparticles suspended in a liquid, are hydrodynamic. Thus, their physical size is increased by the thickness of the electrical double layer surrounding the particle. Determining the size of non-spherical particles with DLS is very difficult and ambiguous, and the result is also influenced by the sedimentation of the powder particles. The height at which the light beam was transmitted in the DLS analysis was 3 mm from the base of the measuring cell, i.e. in the place where mainly large particles and aggregates could accumulate. However, this analysis gives a general view of the size range of the analysed objects and the differences in the size between the powder particles after different durations of the grinding process.

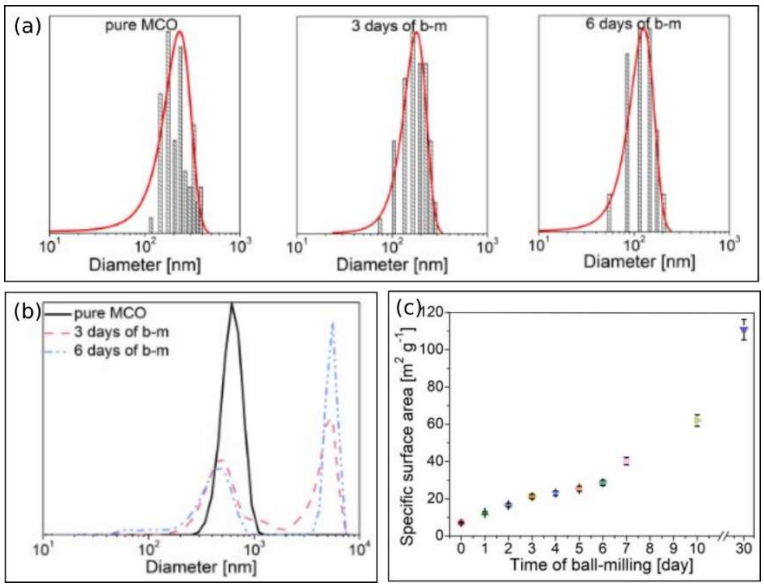

Fig. S3. Morphology analysis of $MnCo_2O_4$ (MCO) spinel powder: (a) histograms of size distributions of a chosen sample (pure MCO without any treatments, MCO after 3 days of milling, MCO after 6 days of milling); (b) results of dynamic light scattering (DLS); the specific surface area (SSA) value of spinel powder dependent on the grinding time.

TEM and EDS analysis of MCO and MCO-cCB powders after 6 days of ball-milling:

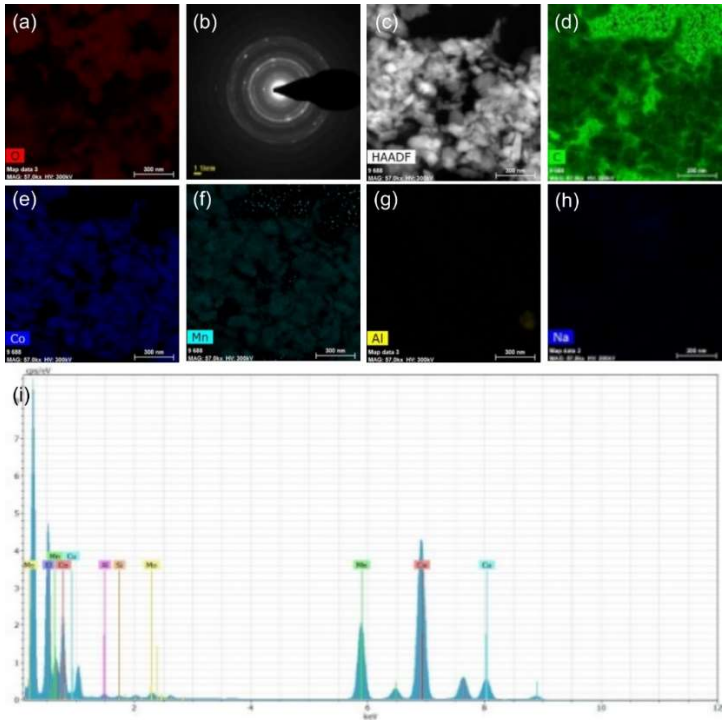

Fig. S4. Visualisation of oxygen on of MCO-cCB powders detected by EDS analysis (a); SAED pattern of MCO sample (b); HAADF-(S)TEM images of MCO (d); the presence of carbon, cobalt, and manganese in the structure of MCO spinel particles (d–f); analysis of other elements (Al, Na, Si) that can be present as a result of the ball-milling of spinel powder treatments (g–j).

Analysis of unit cell parameters of $MnCo_2O_4$ spinel powders:

Table S1. LeBail analysis results – unit cell parameters.

Sample MCO	ac [Å]	ρ [g cm^{-3}]	Sample MCO-cCB	ac [Å]	ρ [g cm^{-3}]
pure MCO	8.2003±5.65 10^{-4}	5.7049			
0.5h us	8.2034±5.99 10^{-4}	5.6983	0.5h us	8.2106±2.56 10^{-4}	5.6835
1d b-m	8.2016±3.89 10^{-4}	5.7021	24h b-m	8.2095±8.53 10^{-4}	5.6856
2d b-m	8.2024±9.71 10^{-4}	5.7004	48h b-m	8.2001±12.6 10^{-4}	5.7053
3d b-m	8.2059±18.0 10^{-4}	5.7016	72h b-m	8.2065±14.0 10^{-4}	5.6919
4d b-m	8.2045±18.7 10^{-4}	5.6931	96h b-m	8.1972±13.4 10^{-4}	5.7114
5d b-m	8.2026±20.3 10^{-4}	5.7	120h b-m	8.2002±15.7 10^{-4}	5.7051
6d b-m	8.1996±21.7 10^{-4}	5.7063	144h b-m	8.1959±25.3 10^{-4}	5.7140
7d b-m	8.1927±22.8 10^{-4}	5.7207	168h b-m	8.2002±17.8 10^{-4}	5.7050
10d b-m	8.1663±30.4 10^{-4}	5.7763	240h b-m	8.2124±25.9 10^{-4}	5.6797
30d	8.1581±20.3 10^{-4}	5.7939		8.2202±20.6 10^{-4}	5.6635

OER activity of different electrocatalysts:

Table S2. Comparison of OER electrocatalysts reported in the literature. All analyses were performed in 0.1M KOH. I – Nafion ionomer; C – catalyst; cC – conductive carbon.

Catalyst	**Substr.**	**I/C**	**cC/C**	**η at 10 mA cm^{-2} [mV]**	**η at 25 μA cm^{-2}$_{ox}$ [mV]**	**Tafel slope [mV dec^{-1}]**	**Loading of catalyst [mg cm^{-2}]**	**Ref.**
$MnCo_2O_4$ after 6 days of ball-milling	GC	0.4	1	375	328	63	0.23	This work
$MnCo_2O_4$ after 30 days of ball-milling	GC	0.04	1	352	340	62	0.23	This work
$MnCo_2O_4$	GC	0.2	0.5	400	-	90	0.20	[1]
Co_3O_4	GC	0.2	0.5	390	-	71	0.20	[1]
Mn_2O_3	GC	0.2	0.5	500	-	146	0.20	[1]
Mn_2O_3 + Co_3O_4	GC	0.2	0.5	410	-	103	0.20	[1]
Pt/C	GC	0.2	0.5	620	-	265	0.20	[1]
$MnCo_2O_4$	GC	0.16	-	510	-	55	0.05	[2]
$CoMn_2O_4$	GC	0.16	-	600	-	64	0.05	[2]

$Mn_{0.3}Co_{2.7}O_4$	fluorine doped tin oxide	-	-	390	-	-	1.0	[3]
Co_3O_4	fluorine doped tin oxide	-	-	430	-	-	1.0	[3]
Crystalline $CoFe_2O_4$	GC	0.16	-	560	-	61	0.51	[4]
Amorphous $CoFe_2O_{3.66}$	GC	0.16	-	490	-	48	0.51	[4]
$SrCo_{0.8}Fe_{0.2}O_{3-\delta}$	GC	0.4	1	300	-	90	0.23	[5]
$SrNb_{0.1}Co_{0.7}Fe_{0.2}O_{3-\delta}$	GC	0.4	1	500	-	76	0.23	[6]
$SrNb_{0.1}Co_{0.7}Fe_{0.2}O_{3-\delta}$ nanorods	GC	0.4	1	390	-	61	0.23	[7]
IrO2	GC	0.4	1	450	-	83	0.23	[7]
$LaFeO_3$	GC	0.2	0.4	-	340	-	0.26	[7]
$PrFeO_3$	GC	0.2	0.4	-	365	-	0.26	[7]
$GdFeO_3$	GC	0.2	0.4	-	390	-	0.26	[7]
$YFeO_3$	GC	0.2	0.4	-	430	-	0.26	[7]
$ZnFe_2O_4$	GC	0.2	0.4	-	475	-	0.26	[7]
$ZnCo_2O_4$	GC	0.2	0.2	-	390	-	0.26	[8]
$ZnFe_{0.4}Co_{1.6}O_4$	GC	0.2	0.2	-	330	-	0.26	[8]
$ZnFeCoO_4$	GC	0.2	0.2	-	400	-	0.26	[8]
$ZnFe_{1.8}Co_{0.2}O_4$	GC	0.2	0.2	-	490	-	0.26	[8]
$ZnFeO_4$	GC	0.2	0.2	-	570	-	0.26	[8]
NiSe-Ni_3Se_2/MWCNT	GC	0.02	0.25	325	-	70	0.37	[9]
NiSe-Ni_3Se_2/MWCNT	GC	0.02	1	434	-	211	0.37	[9]
$MnCo_{1.5}Fe_{0.5}O_4$	GC	0.4	1	376	-	44	0.23	[10]

Ink preparation:

Table S3. The various methods of catalyst ink preparation for OER.

	sampA	**sampB**	**sampC**	**sampD**	**sampE**	**sampF**
MCO and cCB ball-milled together as ink	+		+			

MCO and cCB ball-milled separately			+	
MCO milled only	+		+	+
Powder dried after milling	+	+		+
Powder milling by planetary mill				+
cCB added without milling	+		+	+

Impact of ink composition:

Table S4. Ratio of Nafion ionomer and conductive carbon (cCB) to catalyst particles in the catalyst layer.

	100%	50%	25%	10%
Mass of NafionK+ in 5 µL of ink	18 µg	9 µg	4.5 µg	1.8 µg
Thickness of NafionK+	417 nm	208 nm	104 nm	41.6 nm
I/C (Nafion ionomer/catalyst)	0.4	0.2	0.1	0.04
Mass of cCB in 5 µL of ink	45 µg	22.5 µg	11.3 µg	4.5 µg
cCB/C (conductive carbon/catalyst)	1	0.5	0.25	0.1

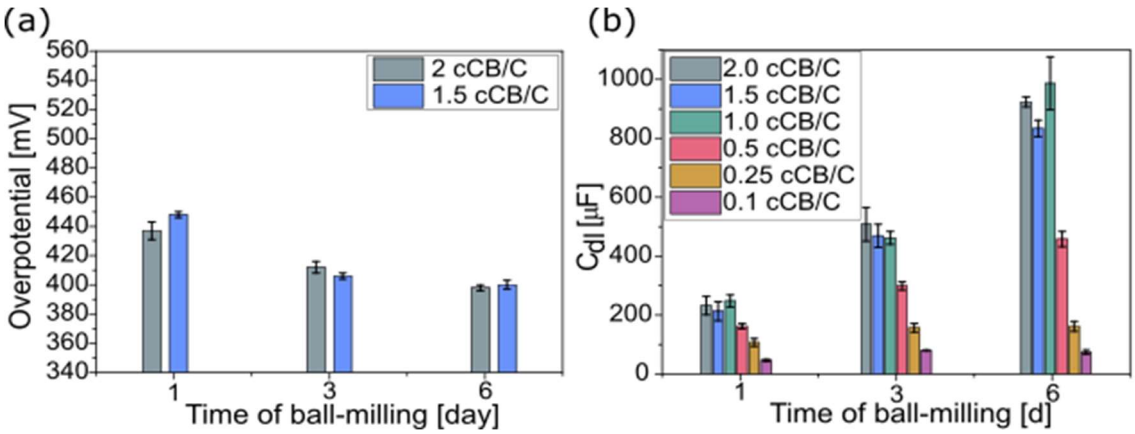

Fig. S5. Influence of cCB amount and ball-milling time on overpotential (a) and double-layer capacitance of electrode (b).

Stability test:

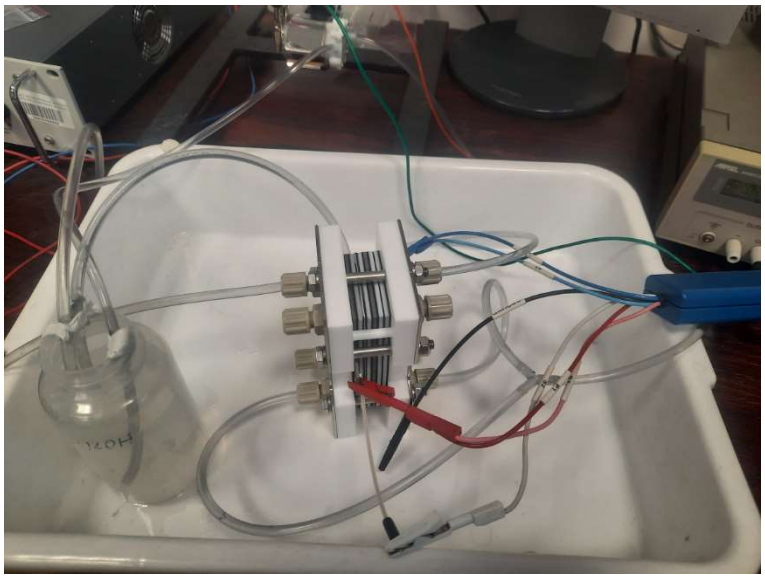

Fig. S6. System for stability tests using a commercial electrolyzer cell.

References:

[1] W. Wang, L. Kuai, W. Cao, M. Huttula, S. Ollikkala, T. Ahopelto, A.-P. Honkanen, S. Huotari, M. Yu, B. Geng, Mass-Production of Mesoporous MnCo2O4 Spinels with Manganese(IV)- and Cobalt(II)-Rich Surfaces for Superior Bifunctional Oxygen Electrocatalysis. Angew. Chemie 129 (2017) 15173–15177. https://doi.org/10.1002/ange.201708765.

[2] P.W. Menezes, A. Indra, N.R. Sahraie, A. Bergmann, P. Strasser, M. Driess, Cobalt-Manganese-Based Spinels as Multifunctional Materials That Unify Catalytic Water Oxidation and Oxygen Reduction Reactions. ChemSusChem 8 (2015) 164–167. https://doi.org/10.1002/cssc.201402699.

[3] P.W. Menezes, A. Indra, V. Gutkin, M. Driess, Boosting Electrochemical Water Oxidation through Replacement of Oh Co Sites in Cobalt Oxide Spinel with Manganese. Chem. Commun. 53 (2017) 8018–8021. https://doi.org/10.1039/c7cc03749j.

[4] A. Indra, P.W. Menezes, N.R. Sahraie, A. Bergmann, C. Das, M. Tallarida, D. Schmeißer, P. Strasser, M. Driess, Unification of Catalytic Water Oxidation and Oxygen Reduction Reactions: Amorphous Beat Crystalline Cobalt Iron Oxides. J. Am. Chem. Soc. 136 (2014) 17530–17536. https://doi.org/10.1021/ja509348t.

[5] Y. Zhu, W. Zhou, Z.G. Chen, Y. Chen, C. Su, M.O. Tadé, Z. Shao, SrNb0.1Co0.7Fe0.2O3-δ Perovskite as a next-Generation Electrocatalyst for Oxygen Evolution in Alkaline Solution. Angew. Chemie - Int. Ed. 54 (2015) 3897–3901. https://doi.org/10.1002/anie.201408998.

[6] Y. Zhu, W. Zhou, Y. Zhong, Y. Bu, X. Chen, Q. Zhong, M. Liu, Z. Shao, A Perovskite Nanorod as Bifunctional Electrocatalyst for Overall Water Splitting. Adv. Energy Mater. 7 (2017) 10–17. https://doi.org/10.1002/aenm.201602122.

[7] H. Li, Y. Chen, S. Xi, J. Wang, S. Sun, Y. Sun, Y. Du, Z.J. Xu, Degree of Geometric Tilting Determines the Activity of FeO6 Octahedra for Water Oxidation. Chem. Mater. 30 (2018) 4313–4320. https://doi.org/10.1021/acs.chemmater.8b01321.

[8] Y. Zhou, S. Sun, J. Song, S. Xi, B. Chen, Y. Du, A.C. Fisher, F. Cheng, X. Wang, H. Zhang, Z.J. Xu, Enlarged Co-O Covalency in Octahedral Sites Leading to Highly Efficient Spinel Oxides for Oxygen Evolution Reaction. Adv. Mater. 30 (2018) 1–7. https://doi.org/10.1002/adma.201802912.

[9] O. A. Oyetade, R. J. Kriek, NiSe-Ni3Se2/Multiwalled Carbon Nanotube Composites as Efficient Electrocatalysts for the Oxygen Evolution Reaction in Alkaline Media. Electrocatalysis 11 (2020) 35–45. https://doi.org/10.1007/s12678-019-00558-x

[10] K. Lankauf , K. Górnicka, P. Błaszczak, J. Karczewski, J. Ryl, G. Cempura, M. Zając, M. Bik, M. Sitarz, P. Jasinski, S. Molin, Tuning of eg electron occupancy of MnCo2O4 spinel for oxygen evolution reaction by partial substitution of Co by Fe at octahedral sites. International Journal of Hydrogen Energy, in press. https://doi.org/10.1016/j.ijhydene.2022.12.013

4.5. Enhanced Electrochemical Performance of $MnCo_{1.5}Fe_{0.5}O_4$ Spinel for Oxygen Evolution Reaction through Heat Treatment

W tej publikacji przedstawiono kontynuację prac nad spinelem $MnCo_{1,5}Fe_{0,5}O_4$. Materiał został przygotowany za pomocą standardowej techniki zol-żel, natomiast zmodyfikowane zostały ostateczne temperatury kalcynacji. Otrzymane proszki zostały poddane obróbce cieplnej w 400, 600, 800 oraz 1000°C w celu zmiany stopni utlenienia atomów tworzących strukturę spinelu. Celem pracy było zbadanie wpływu tej obróbki na właściwości fizykochemiczne oraz aktywność elektrokatalityczną spinelu $MnCo_{1,5}Fe_{0,5}O_4$.

Zaproponowana obróbka cieplna miała bezpośredni wpływ na rozrost otrzymanych krystalitów z 12 nm dla 400°C do 49 nm dla 1000°C, który został wyznaczony z dyfraktogramów rentgenowskich. Za pomocą rentgenowskiej spektroskopii absorpcyjnej zbadano, że wyższe temperatury kalcynacji indukują zmniejszenie liczby kationów Mn^{4+} oraz Co^{3+}, natomiast kationy Fe zachowują +3 stopień utlenienia. Co ciekawe zastosowanie niskoenergetycznego mielenia ma równie znaczący wpływ na zmianę wartościowości pierwiastków. Po rozmieleniu wzrasta udział kationów Mn^{2+}, natomiast liczba kationów Co^{3+} powraca do tej z przed obróbki cieplnej.

Aktywność elektrokatalityczna spinelu $MnCo_{1,5}Fe_{0,5}O_4$, wyznaczona z geometrycznej gęstości prądu, zmniejsza się wraz z rosnącą temperaturą kalcynacji, co wynika bezpośrednio z mniejszej powierzchni aktywnej materiału dostępnej dla reagentów w trakcie elektrolizy wody. Natomiast w momencie gdy prąd zostanie znormalizowany względem powierzchni właściwiej, okazuje się, że właściwa aktywność elektrokatalityczna związana z rozkładem kationowym materiału, a nie tylko fizyczną powierzchnią, jest najwyższa dla próbki otrzymanej w temperaturze 800°C. Analiza wartościowości manganu i kobaltu w próbkach przed i po zastosowaniu jako elektrokatalizatorów OER wykazała wyraźne zmiany stopni utlenienia z $Mn^{2+/3+}$ do $Mn^{3+/4+}$ oraz z $Co^{2+} > Co^{3+}$ do $Co^{2+} < Co^{3+}$. Dowodzi to powstawaniu fazy CoOOH w warunkach utleniających, która jest właściwą formą, na której zachodzi reakcja OER. Przeprowadzając elektrolizę w rosnących temperaturach wyznaczono pozorną energię aktywacji procesu o wartości 20 kJ mol^{-1}.

Do oryginalnych wyników zaliczam wyznaczenie wpływu temperatury kalcynacji na właściwości fizykochemiczne i elektrokatalityczne spinelu $MnCo_{1,5}Fe_{0,5}O_4$. Łącząc techniki spektroskopowe i elektrochemiczne zaobserwowałem zmiany wartościowości pierwiastków tworzących wybrany materiał i powiązałem je z aktywnością elektrokatalizy reakcji OER.

W przedstawionej publikacji samodzielne przeprowadziłem syntezę materiałów w różnych temperaturach oraz przygotowałem elektrody RDE z naniesionym katalizatorem. W dalszej kolejności przeprowadziłem pomiary elektrochemiczne w różnych warunkach (stężenie i temperatura elektrolitu). Przeprowadzałem również pomiary spektroskopowe w zakresie miękkiego promieniowania rentgenowskiego na linii badawczej PIRX w Narodowym Centrum Promieniowania Synchrotronowego SOLARIS. Ponadto odpowiadałem za analizę otrzymanych wyników, przygotowanie rysunków oraz napisanie manuskryptu. Jako autor korespondencyjny

zgłosiłem artykuł do publikacji w czasopiśmie oraz przygotowałem poprawki w odpowiedzi na recenzje.

Oświadczenie współautorów o wkładzie w powstanie publikacji: „Enhanced Electrochemical Performance of $MnCo_{1.5}Fe_{0.5}O_4$ Spinel for Oxygen Evolution Reaction through Heat Treatment"

Imię i nazwisko autora	Wkład w powstanie pracy	Podpis
Krystian Lankauf	Konceptualizacja, metodologia, badania, pisanie – oryginalna wersja robocza, wizualizacja	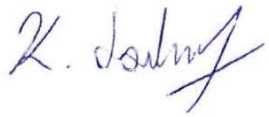
Bartłomiej Lemieszek	Badania (XAS), pisanie – recenzja i redakcja	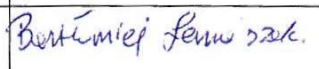
Karolina Górnicka	Badania (XRD), pisanie – recenzja i redakcja	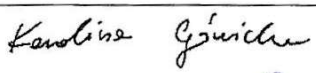
Patryk Błaszczak	Badania (BET), pisanie – recenzja i redakcja	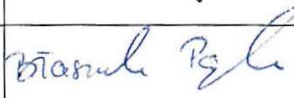
Marcin Zając	Badania (XAS), pisanie – recenzja i redakcja	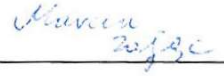
Piotr Jasiński	Pisanie – recenzja i redakcja, nadzór, zasoby	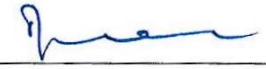
Sebastian Molin	Konceptualizacja, pisanie – recenzja i redakcja, nadzór, zasoby, pozyskiwanie funduszy	

energy&fuels

pubs.acs.org/EF
Article

Enhanced Electrochemical Performance of $MnCo_{1.5}Fe_{0.5}O_4$ Spinel for Oxygen Evolution Reaction through Heat Treatment

Krystian Lankauf,* Bartłomiej Lemieszek, Karolina Górnicka, Patryk Błaszczak, Marcin Zając, Piotr Jasiński, and Sebastian Molin

Cite This: https://doi.org/10.1021/acs.energyfuels.3c02875
Read Online

ABSTRACT: $MnCo_{1.5}Fe_{0.5}O_4$ spinel oxide was synthesized using the sol−gel technique, followed by heat treatment at various temperatures (400, 600, 800, and 1000 °C). The prepared materials were examined as anode electrocatalysts for water-splitting systems in alkaline environments. Solid-state characterization methods, such as powder X-ray diffraction and X-ray absorption spectroscopy (XAS), were used to analyze the materials' crystallographic structure and surface characteristics. The intrinsic activity of the $MnCo_{1.5}Fe_{0.5}O_4$ was fine-tuned by altering the electronic structure by controlling the calcination temperature, and the highest activity was observed for the sample treated at 800 °C. A shift in the valence state of surface cations under oxidative conditions in an alkaline solution during the oxygen evolution reaction was detected through ex situ XAS measurements. Moreover, the influence of the experimental conditions on the electrocatalytic performance of the material, including the pH of the electrolyte and the temperature, was demonstrated.

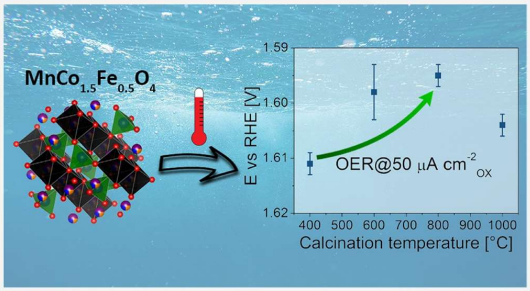

1. INTRODUCTION

$MnCo_2O_4$ spinel oxide is a material of interest in several applications, for example, as an anode material for water-splitting systems,[1] a protective coating for solid oxide fuel cells' interconnects,[2−4] supercapacitors,[5,6] solid oxide electrolysis cells' electrodes,[7] and lithium-ion and lithium−oxygen batteries.[8,9] Generally, $MnCo_2O_4$ is considered an inverse spinel with the Mn cations occupying the octahedral sites; however, depending on the preparation method and calcination temperature, a complex spinel structure may occur as $Co^{2+}[Co^{2+}Mn^{4+}]O_4$, $Co^{3+}[Mn^{2+}Co^{3+}]O_4$, $Co^{2+}[Mn^{3+}_{x}Co^{3+}_{2-x}]O_4$, or $Co^{2+}_{0.965}Mn^{2+}_{0.035}[Mn^{3+}_{0.78}Mn^{4+}_{0.21}Co^{2+}_{0.21}Co^{III}_{0.8}]$.[10,11] The spinel crystallizes in a cubic structure with the space group $Fd\bar{3}m$ (no. 227). The spinel unit cell comprises 8 face-centered cubic (FCC) cells, where oxide anions occupy 32 FCC lattice points and metal cations occupy 8 tetrahedral and 16 octahedral voids.

Among the numerous materials proposed for electrocatalytic reactions, the spinel family has garnered significant interest due to the vast array of constituent elements, offering extensive tunability of the properties. For instance, Wang et al. investigated the composition effect of $ZnMn_xCo_{2-x}O_4$ (x = 0−2.0) spinel oxides on CO oxidation,[12] utilizing the local chemistry and valency characterizations of the cations. The authors suggested that Mn cations are the primary species affecting the spinel's ability to oxidize CO. The key to achieving high activity lies in the coexistence of Mn^{4+} and Mn^{3+} cations, with a ratio slightly above 1 (Mn^{4+}:Mn^{3+} ratio of 1.58). The moderate oxygen adsorption strength facilitates O vacancy refilling, which is a rate-determining step during CO oxidation.

In our recent work, $Mn_xCo_{3-x}O_4$ (x = 0, 0.5, 1, 1.5, and 2) spinel powders, fabricated via a facile EDTA-CA-EG method, were evaluated as oxygen evolution reaction (OER) electrocatalysts.[1] The findings revealed that the addition of Mn ($x \leq 1$) to the cubic Co_3O_4 phase results in an enhanced electrocatalytic performance. The lowest overpotential was achieved for the sample designated as $MnCo_2O_4$, exhibiting a dual-phase structure (~30% Co_3O_4 and ~70% $Mn_{1.4}Co_{1.6}O_4$). A comparatively low overpotential of 327 mV was used to achieve the benchmark current density of 10 mA cm^{-2}. In another study, Chowdhury et al. investigated Ni−Co spinel oxides with varying Ni:Co ratios to examine the influence of compositional variation on the electrocatalytic activity.[13] Among the synthesized catalysts, Ni−Co oxide with a Ni:Co ratio of 1:3 demonstrated the best electrochemical perform-

Received: August 1, 2023
Revised: November 27, 2023
Accepted: December 14, 2023

ance, with onset potentials of 1.51 V vs RHE for the OER. The authors concluded that the enhanced electrocatalytic activity was primarily attributed to improved electronic communication through Co^{3+}/Co^{2+} and Ni^{3+}/Ni^{2+} redox couples, and a high ECSA providing ample accessible active sites. Recently, we have further improved the OER activity of $MnCo_2O_4$ by partially substituting Co with Fe.[14] When compared to pristine $MnCo_2O_4$, an ideal amount of Fe incorporated into the octahedral sites ($MnCo_{1.5}Fe_{0.5}O_4$) improved the overpotential of the OER by 30 mV (at a benchmark 10 mA cm^{-2} GEO current density). A volcano-type shape function of the e_g occupancy at octahedra sites and the OER-specific activity was observed.

Spinel oxides provide tunability of their properties through alterations to the synthesis conditions.[15−17] Magalhães et al. studied the impact of heat treatment on the catalytic properties of iron cobaltite ($FeCo_2O_4$) nanoparticles prepared via coprecipitation.[18] The XPS results revealed a higher cobalt content on the surface of nonheated samples compared to those treated to 900 °C, which was attributed to the enhanced catalytic activity in the unannealed samples. Qi et al. prepared $FeMn_2O_4$ spinel nanoparticles using coprecipitation and postannealing at varying temperatures, allowing modulation of the cationic oxidation states and optimization of the OER performance.[19] Increasing the postannealing temperature led to the changes in the spinel internal structure, with higher Fe^{2+}/Fe^{3+} and slightly increased Mn^{3+}/Mn^{2+} ratios, which were favorable for the OER performance. Under alkaline conditions, the material produced at 500 °C exhibited the best OER activity. Wei et al. prepared a series of $MnCo_2O_4$ cubic spinels by a solid-sate chemistry method at various temperatures.[20] They have observed that the Mn valence state ranges from +3.2 to +3.7, while Co does not change and remains at ∼+2.5. The authors concluded that the OER activity of various $MnCo_2O_4$ exhibits a volcano shape as a function of the Mn valence state in octahedral sites, which depends on the materials preparation temperature.

In this study, $MnCo_{1.5}Fe_{0.5}O_4$ spinel oxide (MCF500) was synthesized using the sol−gel method and subjected to heat treatment at various temperatures (400, 600, 800, and 1000 °C) to alter the valence of the constituent cations. The research focused on examining the effects of these changes on the material's physicochemical and electrochemical properties, particularly its OER electrocatalytic activity in alkaline electrolytes.

2. EXPERIMENTAL SECTION

2.1. Materials Synthesis. $MnCo_{1.5}Fe_{0.5}O_4$ spinel oxide powders were prepared using the EDTA-citric acid method described in detail in previous work.[14] The obtained powders were heat-treated at various temperatures (400, 600, 800, and 1000 °C) for 2 h in air on alumina trays. Using yttria-stabilized zirconia (YSZ, Inframat) spherical grinding media (1 mm), the calcined powders were ball-milled in ethanol for 144 h in 20 mm diameter glass vials with a rotation speed of 100 rpm to improve the electrocatalytic performance.

2.2. Characterization. With CuK radiation (= 1.5404) and a Lynxeye XE-T detector in the range of 5 to 110° with a 0.01° step size, powder X-ray diffraction (pXRD) was carried out at room temperature on a Bruker D2 Phaser diffractometer. The mean crystallite size was calculated using the Scherrer equation:

$$\tau = \frac{K\lambda}{\beta\cos\theta} \quad (1)$$

where τ is the mean size of the crystallites, K is a dimensionless shape factor ($K = 0.9$), λ is the X-ray wavelength, β is the line broadening at half the maximum intensity (fwhm), and θ is the Bragg angle.

The $MnCo_{1.5}Fe_{0.5}O4$ samples were subjected to X-ray absorption spectroscopy (XAS) observations for the L2,3-edge spectra of Mn, Co, and Fe at the SOLARIS National Synchrotron Radiation Centre's 04BM PIRX (formerly PEEM/XAS) beamline.[21] A 1.31 T bending magnet is used by the PIRX beamline to deliver a photon energy range of 100 to 2000 eV with a maximum energy resolution of 2.510^{-4}. The size of the beam spot illuminating the sample was 50 μm × 40 μm (horizontal × vertical). Powder samples were placed on the carbon tape and mounted on the Omicron-type plate sample holder. The total electron yield detection mode (TEY), which reflects an information depth of several nm, was used to record the XANES spectra. Data was collected at room temperature and in UHV. The Bessy program was used to process the obtained data. The data were first adjusted to the actual incident photon flux I_0. To further analyze the data, a straight line fitted to the L_3 pre-edge region was subtracted, a polynomial function (degree 0) fitted to the L_2 postedge region was divided, and the intensity was normalized to a maximum of 1.

According to the BET isotherm model, the N2 adsorption technique (Quantachrome, NovaTouch LX1) was used to quantify the specific surface area of the powders. Prior to the sorption test, the samples were degassed for 3 h at 300 °C in a vacuum.

2.3. Electrode Preparation and Electrochemical Measurements. The powder catalysts were placed on glassy carbon rotating disc electrodes (RDE-GCE, 0.196 cm^2, ALS Co., Ltd.). The RDE GCE was polished for 5 min with 9, 3, and 1 μm polishing diamond solutions prior to the deposition of the catalyst inks. After being sonicated for 10 min in deionized water or isopropanol, it was dried overnight at room temperature. Using 1 mm YSZ grinding balls, the catalyst and Super P Li Conductive Carbon Black (CCB) (Imerys Graphite & Carbon) powder was ball-milled in ethanol for 144 h in the same manner as catalyst powders. In the proper proportion, dried spinel powder, CCB, and 5 wt % Nafion 117 solution (Sigma-Aldrich) were combined to create 1 mL of ink with a solids weight ratio of 5:5:2 (catalyst:CCB:Nafion). The inks were then sonicated for 30 min in an ice−water bath. The RDE-GCE was then drop-cast with 5 μL of the ink while it was rotating at 500 rpm, resulting in a catalyst total mass loading of 45.5 μg. In a specially constructed, three-electrode Teflon cell system with a water jacket, all electrochemical experiments were carried out in 0.1 M KOH aqueous solution (produced from 1 M KOH Titripur from Merck, diluted with DI water ∼12 MΩ). As the working (WE), counter (CE), and reference (RE) electrodes, a catalyst-coated RDE-GCE, a Pt coil, and Hg/HgO in 0.1 M KOH solution (ALS Co., Ltd., Japan) were used, respectively. The rotating disc electrode (RDE) system (RRDE-3A Rotating Ring Disc Electrode Apparatus ver. 2.0, ALS Co., Ltd.) was used in the electrochemical testing along with a BP-300 (BioLogic) bipotentiostat. To maintain the equilibrium of the O_2/H_2O over the electrolyte, a gas flow of 50 mL min^{-1} was maintained over the electrolyte for 30 min before each experiment using a 99.995% O_2 purge. A Julabo F12 thermostat was used to maintain a 25 °C electrolyte temperature. The same procedure was used for all electrocatalytic tests. Through experimental calibration of the Hg/HgO reference electrode against RHE, all recorded potentials were converted to RHE. The range of (−928: −920) mV was found to correspond to the value of E_{Offset} versus RHE, which is equivalent to the measured equilibrium potential of hydrogen electrocatalysis (HER/HOR). Ten voltage cycles in the range of 1.0−1.7 V versus RHE at a scan rate of 100 mV s were used to condition the disc electrode. The background correction for the OER polarization curves was carried out by averaging the positive- and negative-going scans. To remove the resistance of the solution, all potential values were *iR*-corrected. Electrochemical impedance spectroscopy in the frequency range of 10 kHz to 0.1 Hz at 0 V versus OCV with an amplitude of 10 mV and a rotation speed of 1600 rpm was used to compute the uncompensated resistance (R_u). Using the EC-Lab software, the Randles equivalent circuit was fitted. The geometric surface area of the RDE-GCE (0.196 cm^2) was used to normalize the current density

https://doi.org/10.1021/acs.energyfuels.3c02875
Energy Fuels XXXX, XXX, XXX−XXX

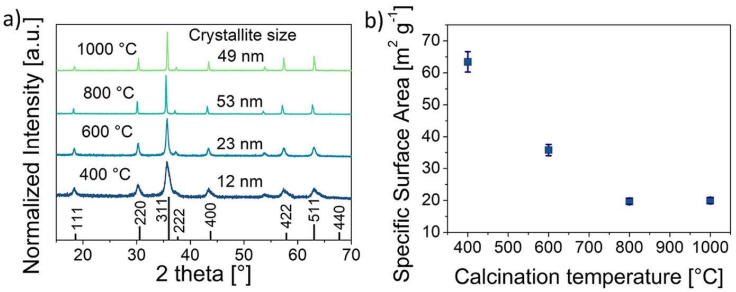

Figure 1. (a) pXRD patterns of $MnCo_{1.5}Fe_{0.5}O_4$ powders calcined at different temperatures; the XRD pattern at the bottom corresponds to reference $MnCo_2O_4$ (COD ID 2300280, $Fd\bar{3}m$, no. 227);[22] (b) specific surface area determined by BET measurements.

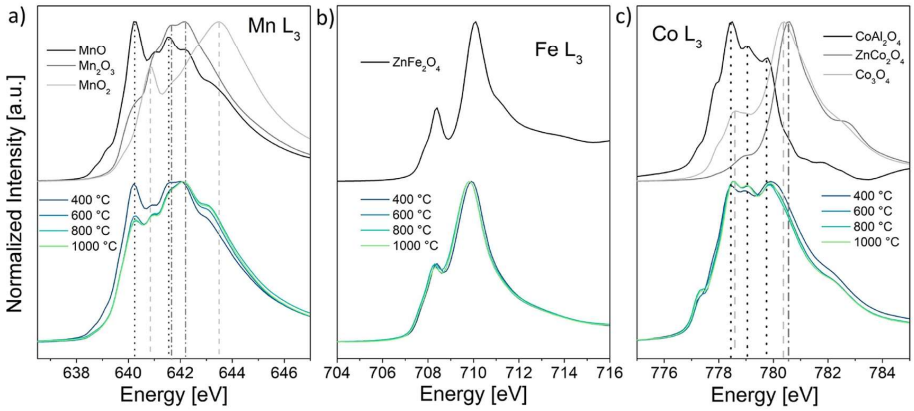

Figure 2. (a) Mn L_3, (b) Fe L_3, and (c) Co L_3 XANES spectra of $MnCo_{1.5}Fe_{0.5}O_4$ powders and several reference materials.

(expressed in the unit mA cm^{-2}_{GEO}). The difference between the potential at 10 mA cm^{-2}_{GEO} and the typical potential of oxygen electrocatalysis (1.23 V) was used to compute the OER overpotential. Current normalization using the BET specific surface area of each oxide catalyst was used to calculate the specific (expressed in the unit μA cm^{-2}_{OX}). At least three different samples of each substance were made and tested for repeatability.

For the ex situ XAS measurements, 25 μL of the catalyst containing ink was deposited onto the Sigracet 39 AA carbon paper covering a surface area of 5 × 10 mm (presented in Figure S1). The electrode was subjected to OER conditions by performing the following OER protocol: 1, conditioning (10 cycles, 10 mV s^{-1}, 1−1.7 V vs RHE); 2, OER polarization (3 cycles, 10 mV s^{-1}, 1−1.9 V vs RHE); 3, chronopotentiometry (10 mA cm^{-2}_{GEO}, 1 h). Data collected during this protocol are presented in Figure S2. Subsequently, the electrode was dried and the XAS spectra of the Mn, Fe, and Co were collected at the PIRX beamline.

The OER tests at various temperatures were performed using a Julabo F12 thermostat to control the temperature inside the electrochemical cell (25, 31, 33, 37.5, 43.5, and 50 °C). From the experimental OER current-polarization curves, the values of a current at 0 V overpotential i_0 were extracted and used to construct Arrhenius plots. The following equation was used to calculate the apparent activation energy E_a:

$$\frac{d\ln(i_0)}{d(1/T)} = -\frac{E_a}{R} \quad (2)$$

where T is the temperature and R is the gas constant.

The influence of the pH on the OER activity was tested in the electrolytes of the following concentrations: 0.01, 0.1, and 1.0 M KOH. The exact value of the pH was measured with the CP-401 pH-meter (Elmetron) coupled with ERH-11 combination pH electrode (Hydromet). Prior to the experiment, the pH-meter was calibrated in five buffer solutions (pH = 2, 4, 7, 9, and 12, Chempur).

3. RESULTS AND DISCUSSION

A series of $MnCo_{1.5}Fe_{0.5}O_4$ spinel oxides were synthesized using the sol−gel method, followed by calcination at various temperatures. As depicted in Figure 1, the samples used in this study were phase-pure and well-crystallized in a cubic structure (space group $Fd\bar{3}m$, no. 227). The peaks in the X-ray diffraction patterns became progressively narrower as the calcination temperature increased, indicating the growth of powder particles. According to the Scherrer equation, the crystallite diameter increased 4-fold when the calcination temperature was raised from 400 to 800 °C. Furthermore, the growth of the powder particles was corroborated by the decrease in the specific surface area, as determined by Brunauer−Emmett−Teller (BET) measurements, from 64, 36, 20, to 20 m^2 g^{-1}.

X-ray absorption near-edge spectroscopy (XANES) data for the L_3 edges were collected to investigate the valence of Mn, Co, and Fe in the prepared spinel oxides (Figure 2). Additionally, reference samples with stable and specified valence states of their constituent transition metal cations were compared (Co^{2+} in $CoAl_2O_4$, Co^{3+} in $ZnCo_2O_4$, Co^{2+} and Co^{3+} in Co_3O_4, Fe^{3+} in $ZnFe_2O_4$, Mn^{2+} in MnO, Mn^{3+} in Mn_2O_3, and Mn^{4+} in MnO_2). Since the measurements in the total electron yield mode (TEY) are surface-sensitive (nano-

https://doi.org/10.1021/acs.energyfuels.3c02875
Energy Fuels XXXX, XXX, XXX−XXX

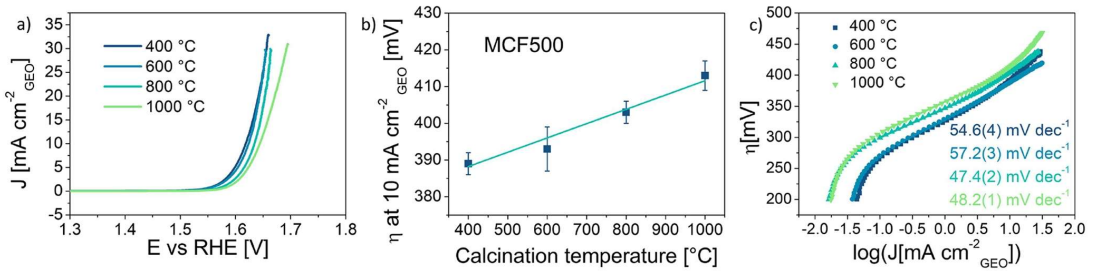

Figure 3. (a) Oxygen evolution polarization curves, corresponding (b) overpotentials η, and (c) Tafel slopes of $MnCo_{1.5}Fe_{0.5}O_4$ catalysts prepared at various temperatures.

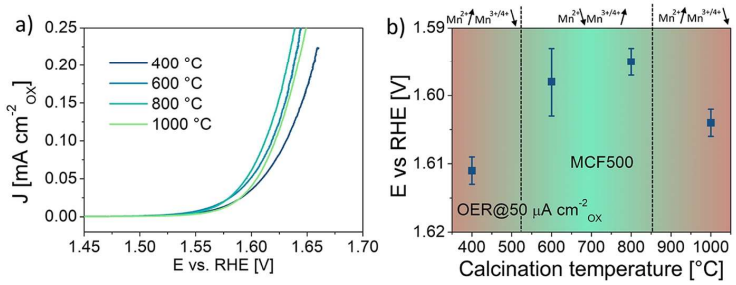

Figure 4. (a) Oxygen evolution polarization curves with current normalized by the BET specific surface area; (b) correlation between OER potentials at 50 μA cm$^{-2}_{OX}$ and calcination temperature of $MnCo_{1.5}Fe_{0.5}O_4$ powders.

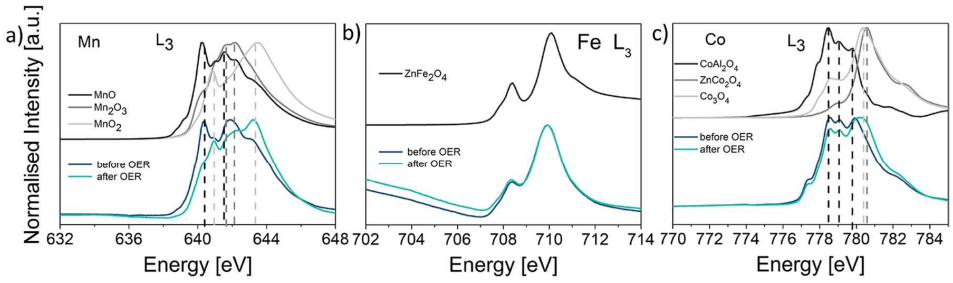

Figure 5. (a) Mn L_3, (b) Fe L_3, and (c) Co L_3 XANES spectra of $MnCo_{1.5}Fe_{0.5}O_4$ calcined at 800 °C before and after the OER testing protocol.

meter depth), the obtained results describe the valence state of surface cations.[23]

The Mn spectrum of the sample prepared at 400 °C overlaps with that of a mixture of MnO and Mn_2O_3 phases. For powder calcined at 400 °C, the relative Mn^{2+} concentration is higher than that for the powders processed at higher temperatures. The average Mn oxidation state increases with increasing processing temperature. For the powder annealed at 1000 °C, a slight shift, within the experimental error, indicating a possible lower average Mn oxidation state can be noticed at the right shoulder. As presented in Figure 2b, neither heat treatment had an impact on the Fe oxidation state. According to the Co L_3 edge spectra, all the samples exhibit a Co^{2+}/Co^{3+} ratio close to 1; however, the sample annealed at 400 °C shows a slightly lower amount of Co^{2+} (in a tetrahedral position) vs $Co^{3+/4+}$.

After low-temperature preparation at 400 °C, the sample contains more Mn in the tetrahedral position at the +2 oxidation state, whereas higher processing temperatures shift Mn to the octahedral position. The increase of $Mn^{3+/4+}$ at octahedral positions increases the concentration of active sites as well as polaron charge carriers, influencing the electrical conductivity and electrocatalytic performance.[24,25]

The OER electrocatalytic activity of the prepared materials was tested in an alkaline environment (0.1 M KOH). As shown in Figure 3a, all the samples exhibit an onset reaction potential above 1.5 V vs RHE. To better illustrate the differences between the specific samples, the overpotentials (η) required to achieve a geometric current density of 10 mA cm^{-2} are presented in Figure 3b. The overpotentials increase linearly with the calcination temperature, ranging from approximately 390 to 415 mV. The Tafel slopes of the reported samples fall within the range of 40−60 mV dec^{-1}, suggesting that the number of electrons transferred in the rate-determining step is between 3 and 4. These values align with the evolution of O_2 through the simultaneous oxidation and formation of hydroxide and oxyhydroxide during OER.[26] The sample prepared at 800 °C exhibits the lowest Tafel slope, indicating

https://doi.org/10.1021/acs.energyfuels.3c02875
Energy Fuels XXXX, XXX, XXX−XXX

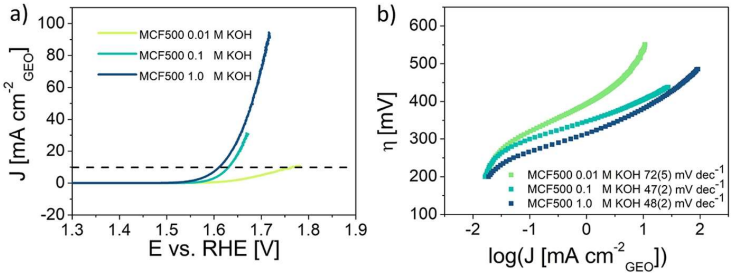

Figure 6. OER polarization curves of $MnCo_{1.5}Fe_{0.5}O_4$ 800 °C scanned in (a) different KOH solutions (12.15−14.15 pH) and (b) corresponding Tafel slopes.

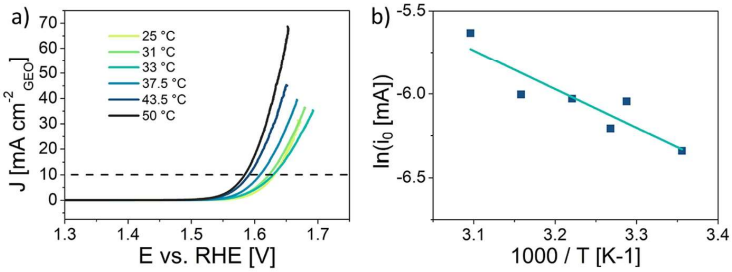

Figure 7. OER polarization curves of $MnCo_{1.5}Fe_{0.5}O_4$ 800 °C scanned in (a) 0.1 M KOH in different temperatures and (b) corresponding Arrhenius plot.

the fastest reaction kinetics among the tested materials due to a higher number of active sites.

To gain a better understanding of the intrinsic electrocatalytic properties of the materials, the measured polarization curves were normalized using the specific surface area values obtained from the BET, as shown in Figure 4a. Due to the broad particle size distribution, which is reflected by BET surface area values ranging from 20 to 64 $m^2\ g^{-1}$, the observed trend differs significantly from that of the polarization curves normalized with respect to the geometrical surface area. As depicted in Figure 4b, the sample calcined at 800 °C is characterized by the lowest overpotential required to sustain a current density of 50 $\mu A\ cm^{-2}_{OX}$. This aligns with previous observations including the shift to a lower Tafel value, substantiated by a higher availability of active sites, in accordance with the XANES results.

To examine the influence of oxidative conditions in the alkaline solution, ex situ XAS measurements were performed on a carbon paper electrode coated with a $MnCo_{1.5}Fe_{0.5}O_4$ 800 °C catalyst. As shown in Figure 5, the spectra of Mn and Co changed significantly, while the Fe spectrum after the OER protocol was barely affected in the background pre-edge region. After the OER protocol, the Mn spectrum shape is altered in a manner that closely aligns with the MnO_2 spectrum, with a small contribution from the Mn_2O_3 spectrum. This indicates a valence shift from $Mn^{2+/3+}$ to $Mn^{3+/4+}$ for surface cations. Similarly, Bergmann et al. observed a shift of the edge position in the XANES spectra corresponding to an increase of the mean Mn oxidation state to almost +4.0 of the MnO_x after applying oxidative potential in 0.1 M KPi.[27] The optimal Mn valence for the OER on various Mn oxides ranges from $Mn^{3.6+}$ to $Mn^{3.8+}$.[28] A similar shift toward a higher oxidation state is observed for the Co cations. As depicted in Figure 5c, after the OER, there is a change in the high-/low-energy peak ratio, illustrating the transition of Co cations with an oxidation state from $Co^{2+} > Co^{3+}$ to $Co^{2+} < Co^{3+}$. According to Calvillo et al., the increase of Co(III) species in octahedral sites is in agreement with the formation of CoOOH in Co−Fe spinels under oxidative conditions.[29] The CoOOH is identified as the catalytic OER phase. Overall, based on the XAS results, after the OER test, the surface Mn^{2+} oxidizes to the $^{+3/+4}$ state, and the Co^{2+} oxidizes toward Co^{3+}, indicating the formation of the active sites based on Mn and Co, while Fe remains inactive.

3.1. Influence of pH and Temperature on Activity. The OER activity of the $MnCo_{1.5}Fe_{0.5}O_4$ calcined at 800 °C was tested in electrolytes with varying concentrations (0.01 M, pH = 12.15, 0.1 M, pH = 13.15, 1 M, pH = 14.15). The strong influence of the pH on the electrochemical performance is evident in Figure 6a, with the highest performance obtained in the 1 M KOH electrolyte.

The pH-dependent electrocatalyst performance suggests the presence of decoupled proton−electron transfer during the catalytic reaction.[30] A decrease in the Tafel slopes is also observed (Figure 6b). This change in the Tafel slope indicates a variation in the number of electrons transferred in the rate-determining step.[26]

Following the study of the influence of the pH, the performance of the OER was tested at various electrolyte temperatures. As illustrated in Figure 7a, a noticeable increase in activity occurs with the rising temperature. Based on the slope of the Arrhenius plot shown in Figure 7b, the apparent activation energy was calculated according to eq 1, presented in the 2. A value of 20 kJ mol^{-1} is slightly lower than the 25 kJ mol^{-1} reported for $NiFeO_x$ by Nurlaela et al.,[31] yet significantly

https://doi.org/10.1021/acs.energyfuels.3c02875
Energy Fuels XXXX, XXX, XXX−XXX

lower than the 71 kJ mol^{-1} for $NiCoO_x$[32] and 75 kJ mol^{-1} for Ni.[33]

The enhanced OER electrocatalysis with increasing electrolyte temperature could be attributed to accelerated kinetics and temperature-induced variations in active species. As demonstrated by Zhou et al., the active species of $NiCo_2O_4$ nanorod arrays at room temperature is $NiCo_2O_4$; however, under elevated temperature conditions, the active species transitions from $NiCo_2O_4$ to oxyhydroxides.[34] Moreover, NiOOH exhibits a lower overpotential compared to $NiCo_2O_4$.

4. CONCLUSIONS

In conclusion, this study successfully synthesized $MnCo_{1.5}Fe_{0.5}O_4$ spinel oxide using the sol−gel technique, followed by heat treatment at various temperatures. The structural properties were investigated through the XRD and XAS techniques. It was found that the preparation conditions significantly impacted the material's specific surface area and valence states, which directly influenced the electrocatalytic performance. The powder annealing temperature could be correlated with the number of active sites (redox active species). For the powder processed at 400 °C, a higher amount of Mn^{2+} was observed. For powders processed at 600 °C and especially at 800 °C, the concentration of $Mn^{3+/4+}$ was the highest, whereas for the powder processed at 1000 °C, the average Mn oxidation state decreased again. Electrochemical studies revealed that the intrinsic activity of the $MnCo_{1.5}Fe_{0.5}O_4$ spinel could be fine-tuned by controlling the powder calcination temperature. Furthermore, the pH-dependent studies of electrocatalyst performance suggested the presence of decoupled proton−electron transfer during the catalytic reaction.

■ ASSOCIATED CONTENT

Supporting Information

The Supporting Information is available free of charge at https://pubs.acs.org/doi/10.1021/acs.energyfuels.3c02875.

Optical image of the catalyst containing ink deposited onto the Sigracet 39 AA carbon paper; polarization curves of the OER protocol performed on the Sigracet 39 AA carbon paper electrode coated with $MnCo_{1.5}Fe_{0.5}O_4$ 800 °C desired for the XAS ex situ measurements (PDF)

■ AUTHOR INFORMATION

Corresponding Author

Krystian Lankauf − *Advanced Materials Center, Faculty of Electronics, Telecommunications and Informatics, Gdańsk University of Technology, Gdańsk 80-233, Poland;* orcid.org/0000-0002-9941-7337; Email: krystian.lankauf@pg.edu.pl

Authors

Bartłomiej Lemieszek − *Advanced Materials Center, Faculty of Electronics, Telecommunications and Informatics, Gdańsk University of Technology, Gdańsk 80-233, Poland*

Karolina Górnicka − *Advanced Materials Center, Faculty of Applied Physics and Mathematics, Gdańsk University of Technology, Gdańsk 80-233, Poland*

Patryk Błaszczak − *Advanced Materials Center, Faculty of Applied Physics and Mathematics, Gdańsk University of Technology, Gdańsk 80-233, Poland*

Marcin Zając − *National Synchrotron Radiation Centre Solaris, Jagiellonian University, Kraków 30-392, Poland*

Piotr Jasiński − *Advanced Materials Center, Faculty of Electronics, Telecommunications and Informatics, Gdańsk University of Technology, Gdańsk 80-233, Poland*

Sebastian Molin − *Advanced Materials Center, Faculty of Electronics, Telecommunications and Informatics, Gdańsk University of Technology, Gdańsk 80-233, Poland;* orcid.org/0000-0002-8335-7632

Complete contact information is available at: https://pubs.acs.org/10.1021/acs.energyfuels.3c02875

Notes

The authors declare no competing financial interest.

■ ACKNOWLEDGMENTS

The presented research is part of the "Nanocrystalline ceramic materials for efficient electrochemical energy conversion" project, carried out within the First TEAM programme of the Foundation for Polish Science (grant agreement no. POIR.04.04.00-00-42E9/17-00), cofinanced by the European Union under the European Regional Development Fund. Funding from Statutory Funds of WETI PG is also acknowledged.

■ REFERENCES

(1) Lankauf, K.; Cysewska, K.; Karczewski, J.; Mielewczyk-Gryń, A.; Górnicka, K.; Cempura, G.; Chen, M.; Jasiński, P.; Molin, S. $Mn_xCo_{3-X}O_4$ Spinel Oxides as Efficient Oxygen Evolution Reaction Catalysts in Alkaline Media. *Int. J. Hydrogen Energy* **2020**, *45*, 14867−14879.

(2) Yoon, M. Y.; Lee, E. J.; Song, R. H.; Hwang, H. J. Preparation and Properties of a $MnCo_2O_4$ for Ceramic Interconnect of Solid Oxide Fuel Cell via Glycine Nitrate Process. *Met. Mater. Int.* **2011**, *17* (6), 1039−1043.

(3) Saoutieff, E.; Bertrand, G.; Zahid, M.; Gautier, L. APS Deposition of $MnCo_2O_4$ on Commercial Alloys K41X Used as Solid Oxide Fuel Cell Interconnect: The Importance of Post Heat-Treatment for Densification of the Protective Layer. *ECS Meet. Abstr.* **2009**, *MA2009−02* (12), 1258−1258.

(4) Molin, S.; Jasinski, P.; Mikkelsen, L.; Zhang, W.; Chen, M.; Hendriksen, P. V. Low Temperature Processed $MnCo_2O_4$ and $MnCo_{1.8}Fe_{0.2}O_4$ as Effective Protective Coatings for Solid Oxide Fuel Cell Interconnects at 750 °C. *J. Power Sources* **2016**, *336*, 408−418.

(5) Padmanathan, N.; Selladurai, S. Mesoporous $MnCo_2O_4$ Spinel Oxide Nanostructure Synthesized by Solvothermal Technique for Supercapacitor. *Ionics* **2014**, *20* (4), 479−487.

(6) Tholkappiyan, R.; Naveen, A. N.; Sumithra, S.; Vishista, K. Investigation on Spinel $MnCo_2O_4$ Electrode Material Prepared via Controlled and Uncontrolled Synthesis Route for Supercapacitor Application. *J. Mater. Sci.* **2015**, *50* (17), 5833−5843.

(7) Zhang, L.; Tian, Y.; Liu, Y.; Jia, L.; Yang, J.; Chi, B.; Pu, J.; Li, J. Direct Electrolysis of CO_2 in a Symmetrical Solid Oxide Electrolysis Cell with Spinel $MnCo_2O_4$ as Electrode. *ChemElectroChem.* **2019**, *6* (5), 1359−1364.

(8) Chen, C.; Liu, B.; Ru, Q.; Ma, S.; An, B.; Hou, X.; Hu, S. Fabrication of Cubic Spinel $MnCo_2O_4$ Nanoparticles Embedded in Graphene Sheets with Their Improved Lithium-Ion and Sodium-Ion Storage Properties. *J. Power Sources* **2016**, *326*, 252−263.

(9) Zou, L.; Cheng, J.; Jiang, Y.; Gong, Y.; Chi, B.; Pu, J.; Jian, L. Spinel $MnCo_2O_4$ Nanospheres as an Effective Cathode Electrocatalyst for Rechargeable Lithium-Oxygen Batteries. *RSC Adv.* **2016**, *6* (37), 31248−31255.

(10) Zhao, Q.; Yan, Z.; Chen, C.; Chen, J. Spinels: Controlled Preparation, Oxygen Reduction/Evolution Reaction Application, and Beyond. *Chem. Rev.* **2017**, *117* (15), 10121−10211.
(11) Bordeneuve, H.; Tenailleau, C.; Guillemet-Fritsch, S.; Smith, R.; Suard, E.; Rousset, A. Structural Variations and Cation Distributions in $Mn_{3-X}Co_xO_4$ ($0 \leq x \leq 3$) Dense Ceramics Using Neutron Diffraction Data. *Solid State Sci.* **2010**, *12* (3), 379−386.
(12) Wang, T.; Sun, Y.; Zhou, Y.; Sun, S.; Hu, X.; Dai, Y.; Xi, S.; Du, Y.; Yang, Y.; Xu, Z. J. Identifying Influential Parameters of Octahedrally Coordinated Cations in Spinel $ZnMn_xCo_{2-X}O_4$ Oxides for the Oxidation Reaction. *ACS Catal.* **2018**, *8* (9), 8568−8577.
(13) Roy Chowdhury, S.; Ray, A.; Chougule, S. S.; Min, J.; Jeffery, A. A.; Ko, K.; Kim, Y.; Das, S.; Jung, N. Mixed Spinel Ni-Co Oxides: An Efficient Bifunctional Oxygen Electrocatalyst for Sustainable Energy Application. *ACS Appl. Energy Mater.* **2022**, *5* (4), 4421−4430.
(14) Lankauf, K.; Górnicka, K.; Błaszczak, P.; Karczewski, J.; Ryl, J.; Cempura, G.; Zając, M.; Bik, M.; Sitarz, M.; Jasiński, P.; Molin, S. Tuning of E_g Electron Occupancy of $MnCo_2O_4$ Spinel for Oxygen Evolution Reaction by Partial Substitution of Co by Fe at Octahedral Sites. *Int. J. Hydrogen Energy* **2023**, *48* (24), 8854−8866.
(15) Baig, M. M.; Yousuf, M. A.; Agboola, P. O.; Khan, M. A.; Shakir, I.; Warsi, M. F. Optimization of Different Wet Chemical Routes and Phase Evolution Studies of $MnFe_2O_4$ Nanoparticles. *Ceram. Int.* **2019**, *45* (10), 12682−12690.
(16) Jbara, H. B.; Aubry, E.; Kanzari, M.; Billard, A.; Yazdi, M. A. P. Effect of Thermal Annealing on the Optoelectronic Properties of Cu-Fe-O Thin Films Deposited by Reactive Magnetron Co-Sputtering. *Thin Solid Films* **2021**, *721*, No. 138538.
(17) Chavarriaga, E. A.; Lopera, A. A.; Bender Wermuth, T.; Arcaro, S.; Bezzon, V. D. N.; García, C.; Alarcón, J.; Gabriel Ramirez, J.; Moreno, R.; Pérez Bergmann, C. Influence of Caffeine and Citrulline on Magnetic Properties When Used as New Fuels in the Synthesis of $CoFe_2O_4$ Nanoparticles by Gel Combustion. *J. Magn. Magn. Mater.* **2022**, *560*, No. 169632.
(18) Magalhães, R.; Bargiela, P.; da Rocha, M. D. G.; Gil, E.; de Souza, A. Iron Cobaltite ($FeCo_2O_4$) Nanocatalysts for Water-Oxidation: Effects of Annealing Temperature on Catalytic Properties. *J. Braz. Chem. Soc.* **2022**, *33* (10), 1163−1171.
(19) Qi, C.; Liu, Q.; Dong, Y.; Zhang, G.; Jiang, X.; Gao, D. Fe 3+ in a Tetrahedral Position Determined the Electrocatalytic Properties in $FeMn_2O_4$. *RSC Adv.* **2022**, *12* (42), 27206−27211.
(20) Wei, C.; Feng, Z.; Scherer, G. G.; Barber, J.; Shao-Horn, Y.; Xu, Z. J. Cations in Octahedral Sites: A Descriptor for Oxygen Electrocatalysis on Transition-Metal Spinels. *Adv. Mater.* **2017**, *29*, 1606800.
(21) Zając, M.; Giela, T.; Freindl, K.; Kollbek, K.; Korecki, J.; Madej, E.; Pitala, K.; Kozioł-Rachwał, A.; Sikora, M.; Spiridis, N.; Stępień, J.; Szkudlarek, A.; Ślęzak, M.; Ślęzak, T.; Wilgocka-Ślęzak, D. The First Experimental Results from the 04BM (PEEM/XAS) Beamline at Solaris. *Nucl. Inst. Methods Phys. Res., Sect. B* **2021**, *492*, 43−48, DOI: 10.1016/j.nimb.2020.12.024.
(22) Purwanto, A.; Fajar, A.; Mugirahardjo, H.; Fergus, J. W.; Wang, K. Cation Distribution in Spinel $(Mn,Co,Cr)_3O_4$ at Room Temperature. *J. Appl. Crystallogr.* **2010**, *43* (3), 394−400.
(23) Abbate, M.; Goedkoop, J. B.; de Groot, F. M. F.; Grioni, M.; Fuggle, J. C.; Hofmann, S.; Petersen, H.; Sacchi, M. Probing Depth of Soft X-ray Absorption Spectroscopy Measured in Total-electron-yield Mode. *Surf. Interface Anal.* **1992**, *18* (1), 65−69.
(24) Gillot, B.; Kharroubi, M.; Metz, R.; Legros, R.; Rousset, A. Electrical Properties of Copper Manganite Spinels $CuxMn_{3-x}O_4$ ($0 > x > 1$). *Phys. Status Solidi* **1991**, *124* (1), 317−325.
(25) DORRIS, S. E.; MASON, T. O. Electrical Properties and Cation Valencies in Mn_3O_4. *J. Am. Ceram. Soc.* **1988**, *71* (5), 379−385.
(26) Anantharaj, S.; Karthick, K.; Kundu, S. Evolution of Layered Double Hydroxides (LDH) as High Performance Water Oxidation Electrocatalysts: A Review with Insights on Structure, Activity and Mechanism. *Mater. Today Energy* **2017**, *6*, 1−26.
(27) Bergmann, A.; Zaharieva, I.; Dau, H.; Strasser, P. Electrochemical Water Splitting by Layered and 3D Cross-Linked Manganese Oxides: Correlating Structural Motifs and Catalytic Activity. *Energy Environ. Sci.* **2013**, *6* (9), 2745−2755.
(28) Risch, M.; Stoerzinger, K. A.; Han, B.; Regier, T. Z.; Peak, D.; Sayed, S. Y.; Wei, C.; Xu, Z.; Shao-Horn, Y. Redox Processes of Manganese Oxide in Catalyzing Oxygen Evolution and Reduction: An in Situ Soft X-Ray Absorption Spectroscopy Study. *J. Phys. Chem. C* **2017**, *121* (33), 17682−17692.
(29) Calvillo, L.; Carraro, F.; Vozniuk, O.; Celorrio, V.; Nodari, L.; Russell, A. E.; Debellis, D.; Fermin, D.; Cavani, F.; Agnoli, S.; Granozzi, G. Insights into the Durability of Co-Fe Spinel Oxygen Evolution Electrocatalysts: Via Operando Studies of the Catalyst Structure. *J. Mater. Chem. A* **2018**, *6* (16), 7034−7041.
(30) Zhou, Y.; Sun, S.; Song, J.; Xi, S.; Chen, B.; Du, Y.; Fisher, A. C.; Cheng, F.; Wang, X.; Zhang, H.; Xu, Z. J. Enlarged Co-O Covalency in Octahedral Sites Leading to Highly Efficient Spinel Oxides for Oxygen Evolution Reaction. *Adv. Mater.* **2018**, *30* (32), 1−7.
(31) Nurlaela, E.; Shinagawa, T.; Qureshi, M.; Dhawale, D. S.; Takanabe, K. Temperature Dependence of Electrocatalytic and Photocatalytic Oxygen Evolution Reaction Rates Using NiFe Oxide. *ACS Catal.* **2016**, *6* (3), 1713−1722.
(32) Davidson, C.; Kissel, G.; Srinivasan, S. Electrode Kinetics of the Oxygen Evolution Reaction at $NiCo_2O_4$ from 30% KOH. Dependence on Temperature. *J. Electroanal. Chem.* **1982**, *132* (C), 129−135.
(33) Miles, M. H.; Kissel, G.; Lu, P. W. T.; Srinivasan, S. Effect of Temperature on Electrode Kinetic Parameters for Hydrogen and Oxygen Evolution Reactions on Nickel Electrodes in Alkaline Solutions. *J. Electrochem. Soc.* **1976**, *123* (3), 332−336.
(34) Zhou, T.; Wang, C.; Shi, Y.; Liang, Y.; Yu, Y.; Zhang, B. Temperature-Regulated Reversible Transformation of Spinel-To-Oxyhydroxide Active Species for Electrocatalytic Water Oxidation. *J. Mater. Chem. A* **2020**, *8* (4), 1631−1635.

https://doi.org/10.1021/acs.energyfuels.3c02875
Energy Fuels XXXX, XXX, XXX−XXX

Supporting Information

Enhanced Electrochemical Performance of the $MnCo_{1.5}Fe_{0.5}O_4$ Spinel for Oxygen Evolution Reaction through Heat Treatment

Krystian Lankauf[a], Bartłomiej Lemieszek[a], Karolina Górnicka[b], Patryk Błaszczak[b], Marcin Zając[c], Piotr Jasiński[a], Sebastian Molin[a]*

[a]*Advanced Materials Center, Faculty of Electronics, Telecommunications and Informatics, Gdańsk University of Technology, ul. G. Narutowicza 11/12, 80-233 Gdańsk, Poland*

[b]*Advanced Materials Center, Faculty of Applied Physics and Mathematics, Gdańsk University of Technology, ul. G. Narutowicza 11/12, 80-233 Gdańsk, Poland*

[c]*National Synchrotron Radiation Centre Solaris, Jagiellonian University, 30-392 Kraków, ul. Czerwone Maki 98 Poland*

*e-mail: krystian.lankauf@pg.edu.pl

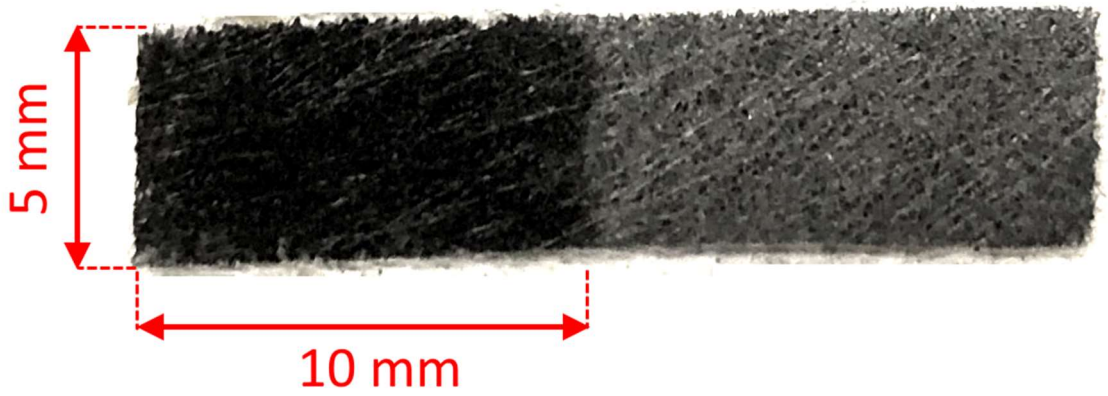

Figure S1. 25 uL of catalyst containing ink deposited onto the Sigracet 39 AA carbon paper covering the surface area of 5x10 mm

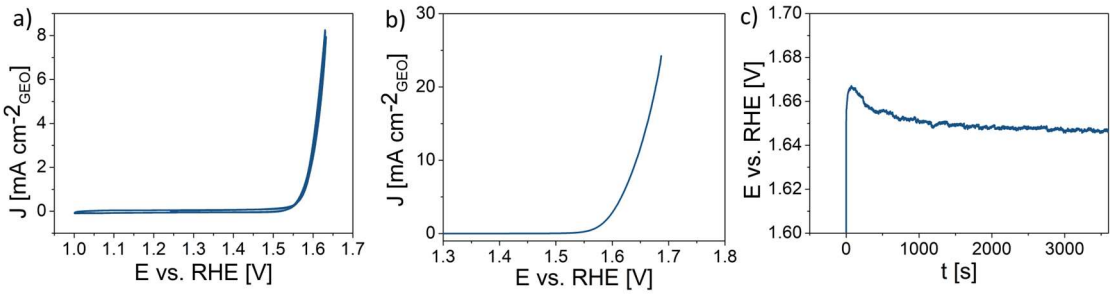

Figure S2. OER protocol performed on the Sigracet 39 AA carbon paper electrode coated with $MnCo_{1.5}Fe_{0.5}O_4$-800 °C desired for the XAS ex-situ measurements.

5. PODSUMOWANIE

W przedstawionej rozprawie omówiony został temat wytwarzania nanokrystalicznych materiałów elektrokatalitycznych do zastosowania jako materiały elektrodowe w alkalicznej elektrolizie wody. Elektroliza wody jest to proces służący do produkcji wodoru i tlenu poprzez reakcje elektrochemiczne. Z założeniem zasilania z odnawialnych źródeł energii otrzymywany wodór klasyfikowany jest jako wodór zielony, a więc o minimalnym wpływie na środowisko. W związku z planem odejścia od paliw kopalnych przez wiele z krajów oraz w ogóle z ograniczonymi rezerwami tych paliw, niezbędne jest przejście na alternatywne źródło energii. Przy aktualnym stanie wiedzy jedną z najbardziej obiecujących ścieżek jest wykorzystanie właśnie wodoru jako paliwa do wytwarzania energii elektrycznej w ogniwach paliwowych, ze względu na bez emisyjność tego procesu. Najbardziej znaczącą przeszkodą przed zastosowaniem elektrolizy wody do produkcji wodoru na masową skalę są zbyt wysokie koszty wynikające z braku optymalnych materiałów elektrodowych mogących zastąpić platynę i iryd.

W niniejszej rozprawie przeprowadzono badania nad tlenkami o strukturze spinelu lub perowskitu do zastosowania jako elektrokatalizatory reakcji utlenienia tlenu, tj. jednej z reakcji zachodzących w trakcie rozpadu wody, która obarczona jest dominującymi nadpotencjałami ograniczającymi całościowy proces. Materiały te zostały przygotowane nieskomplikowanymi metodami syntezy chemicznej, które mogą być skalowane do zapotrzebowania przemysłowego. Ponadto szczególny nacisk położony został na modyfikacji tych materiałów w celu zaindukowania zmian właściwości fizykochemicznych, a w rezultacie poprawie ich wydajności katalitycznej.

Wyniki badań zebrane w formie publikacji naukowych przedstawionych w rozdziale 4 niniejszej pracy udowadniają postawione tezy. W pierwszym etapie przeprowadzona została synteza serii spineli $Mn_xCo_{3-x}O_4$, a badania wykazały, że najbardziej aktywna elektrokatalitycznie jest otrzymana dwufazowa struktura $MnCo_2O_4$. Dalsze prace przedstawiły możliwość optymalizacji stechiometrii spinelu $MnCo_2O_4$ oraz perowskitu $SrTiO_{3-d}$ poprzez podstawianie żelaza za kolejno kobalt lub tytan. Wprowadzenie żelaza do struktury spinelu lub perowskitu ma niebagatelny wpływ na modulację właściwości fizykochemicznych np. przewodności elektrycznej, rezystancji przeniesienia ładunku, ilości wakansów tlenowych, powierzchni właściwej czy rozkładu elektronów na orbitalach atomowych. Co ważniejsze zmiany tych własności znajdują odzwierciedlenie we wzroście wydajności katalizy reakcji utleniania tlenu w środowisku zasadowym, obserwowanej jako obniżenie nadpotencjału wymaganego do przebiegu reakcji.

Przedstawione wyniki dowodzą pierwszej tezy postawionej w niniejszej rozprawie.

W dalszej części zaproponowano zastosowanie obróbki cieplnej lub mechanicznej przygotowanych materiałów jako metody poprawy aktywności elektrokatalitycznej. Wykazano, że właściwości fizykochemiczne spineli $MnCo_2O_4$ oraz $MnCo_{1,5}Fe_{0,5}O_4$ mogą być modulowane bez zmiany ich składu chemicznego, poprzez zastosowanie posyntezowej obróbki zmieniającej morfologię oraz powierzchniową strukturę atomową, co ma bezpośredni wpływ na własności elektrokatalityczne.

Przedstawione wyniki dowodzą drugiej tezy postawionej w niniejszej rozprawie.

W szczególności, jako swoje osiągnięcia uważam:

- Opracowanie protokołów pomiarowych do wyznaczenia aktywności i stabilności elektrokatalitycznej katalizatorów proszkowych
- Syntezę złożonych materiałów tlenkowych metodą zol-żel
- Dopracowanie procesu polerowania elektrod roboczych oraz optymalizacja procesu nanoszenia warstw katalitycznych na podłoża piankowe oraz z węgla szklistego
- Zastosowanie metod elektrochemicznych i spektroskopowych do wyjaśnienia zmian aktywności elektrokatalitycznej materiałów wynikających z wprowadzenia nowych pierwiastków do struktury krystalicznej

Zaproponowane nanokrystaliczne materiały tlenkowe poddane odpowiedniej obróbce posyntezowej stanowią alternatywę dla stosowanych dotychczas, kosztownych materiałów elektrodowych. Zastosowane metody syntezy są osiągalne w typowym laboratorium technologicznym, co jest ważne z perspektywy produkcji katalizatorów w większej, przemysłowej skali.

Naturalnym kierunkiem rozwoju niniejszej pracy jest zastosowanie i przetestowanie przedstawionych materiałów jako elektrody w elektrolizerach dużej mocy. Ponadto dalsze badania skoncentrowane będą na poszukiwaniu nowych, bardziej przyjaznych środowisku katalizatorów pozbawionych w swojej strukturze kobaltu. Zastosowanie tego pierwiastka powinno być ograniczone ze względu na wiele aspektów, m.in. jego kancerogenność, wydobycie związane z łamaniem praw człowieka, czy rosnący popyt wynikający z rosnącej produkcji baterii do pojazdów elektrycznych, który w perspektywie 5 lat może przekroczyć podaż. Ciekawą alternatywą są spinele manganowo-kobaltowe, których aktywność elektrokatalityczna może być modyfikowana poprzez wprowadzenie domieszek lub podstawienie manganu lub miedzi poprzez inne metale przejściowe.

Niemniej, opublikowane artykuły stanowią kolejny krok w dążeniu do produkcji zielonego wodoru.

SPIS RYSUNKÓW

6. BIBLIOGRAFIA

[1] Platzer MF, Sarigul-Klijn N. The Green Energy Ship Concept. Renewable Energy from Wind Over Water. 2020.

[2] Kuo G. When Fossil Fuels Run Out, What Then? 2023. https://mahb.stanford.edu/library-item/fossil-fuels-run/.

[3] Uyar TS, Javani N. Renewable energy based solutions. 2022. https://doi.org/10.1007/978-3-031-05125-8.

[4] Godula-Jopek A, Millet P, Guillet N, Laurencin J, Mougin J, Bourasseau C, et al. Hydrogen Production by Electrolysis. Weinheim: Wiley-VCH Verlag GmbH & Co. KGaA,; 2015.

[5] Zhang L, Zhao H, Wilkinson DP, Sun X, Zhang J. Electrochemical Water Electrolysis. 2020.

[6] Detlef Stolten, Emonts B. Hydrogen Science and Engineering: Materials, Processes, Systems and Technology. vol. 1. Wiley-VCH; 2016.

[7] Häussinger P, Lohmüller R, Watson AM. Hydrogen, 6. Uses. Ullmann's Encycl. Ind. Chem., 2011. https://doi.org/10.1002/14356007.o13_o07.

[8] Kotowicz J, Szykowska K. Wodór i współczesne metody jego produkcji oraz wykorzystywania. Rynek Energii 2021;2:23–9.

[9] Yodwong B, Guilbert D, Phattanasak M, Kaewmanee W, Hinaje M, Vitale G. AC-DC converters for electrolyzer applications: State of the art and future challenges. Electron 2020;9:1–30. https://doi.org/10.3390/electronics9060912.

[10] Lewandowska M. Wytwarzanie materiałów nanokrystalicznych metodą wyciskania hydrostatycznego Fabrication of nanocrystalline materials by hydrostatic extrusion. Obróbka Plast Met 2006;XVII:9–14.

[11] Elektroliza Wody n.d. https://commons.wikimedia.org/wiki/File:Elektroliza_wody.svg.

[12] Adolf Kisza. Elektrochemia cz.2: Elektrodyka. Warszawa: WNT; 2001.

[13] Chakik F ezzahra, Kaddami M, Mikou M. Effect of operating parameters on hydrogen production by electrolysis of water. Int J Hydrogen Energy 2017;42:25550–7. https://doi.org/10.1016/j.ijhydene.2017.07.015.

[14] Zeng K, Zhang D. Recent progress in alkaline water electrolysis for hydrogen production and applications. Prog Energy Combust Sci 2010;36:307–26. https://doi.org/10.1016/j.pecs.2009.11.002.

[15] Burton NA, Padilla R V., Rose A, Habibullah H. Increasing the efficiency of hydrogen production from solar powered water electrolysis. Renew Sustain Energy Rev 2021;135:110255. https://doi.org/10.1016/j.rser.2020.110255.

[16] Jiao Y, Zheng Y, Jaroniec M, Qiao SZ. Design of electrocatalysts for oxygen- and hydrogen-involving energy conversion reactions. Chem Soc Rev 2015;44:2060–86. https://doi.org/10.1039/c4cs00470a.

[17] Godula-Jopek A, editor. Hydrogen Production. Weinheim, Germany: Wiley-VCH Verlag GmbH & Co. KGaA; 2015. https://doi.org/10.1002/9783527676507.

[18] Rashid MM, Mesfer MK Al, Naseem H, Danish M. Hydrogen Production by Water Electrolysis: A Review of Alkaline Water Electrolysis, PEM Water Electrolysis and High Temperature Water Electrolysis. Int J Eng Adv Technol 2015:2249–8958.

[19] Schematic of the basic operating principle of a polymer electrolyte membrane electrolysis cell n.d. https://commons.wikimedia.org/wiki/File:PEMelectrolysis.jpg.

[20] Yu ZY, Duan Y, Feng XY, Yu X, Gao MR, Yu SH. Clean and Affordable Hydrogen Fuel from Alkaline Water Splitting: Past, Recent Progress, and Future Prospects. Adv Mater 2021;33:1–35. https://doi.org/10.1002/adma.202007100.

[21] Carmo M, Fritz DL, Mergel J, Stolten D. A comprehensive review on PEM water electrolysis. Int J Hydrogen Energy 2013;38:4901–34. https://doi.org/10.1016/j.ijhydene.2013.01.151.

[22] Bodner M, Hofer A, Hacker V. H<inf>2</inf> generation from alkaline electrolyzer. Wiley Interdiscip Rev Energy Environ 2015;4:365–81. https://doi.org/10.1002/wene.150.

[23] Bieńkowski K, Gdula M. Krótkie wprowadzenie do tematyki ogniw fotoelektrochemicznych. Mater Elektron 2010;38:9–17.

[24] Grimes CA, Varghese OK, Ranjan S. Light, Water, Hydrogen The Solar Generation of Hydrogen by Water Photoelectrolysis. 2007. https://doi.org/10.1007/978-0-387-68238-9_1.

[25] Meyers RA. Encyclopedia ofSustainability Science and Technology: Hydrogen Production by Photoelectrochemical Water Splitting. vol. 27. Springer Science+Business Media LLC 2018; 2018. https://doi.org/10.5757/asct.2018.27.4.61.

[26] Pandiyan A, Uthayakumar A, Subrayan R, Cha SW, Moorthy SBK. Review of solid oxide electrolysis cells: A clean energy strategy for hydrogen generation. Nanomater Energy 2019;8:1–73. https://doi.org/10.1680/jnaen.18.00009.

[27] Scott K, Grigoriev SA, Fateev VN, Millet P, Bystron T, Paidar M, et al. Electrochemical Methods for Hydrogen Production. vol. 2020-Janua. 2020.

[28] Paidar M, Fateev V, Bouzek K. Membrane electrolysis—History, current status and perspective. Electrochim Acta 2016;209:737–56. https://doi.org/10.1016/j.electacta.2016.05.209.

[29] Vermeiren P, Adriansens W, Moreels JP, Leysen R. Evaluation of the zirfon® separator for use in alkaline water electrolysis and Ni-H2 batteries. Int J Hydrogen Energy 1998;23:321–4. https://doi.org/10.1016/s0360-3199(97)00069-4.

[30] Rakhshani S, Araneo R, Pucci A, Rinaldi A, Giuliani C, Pozio A. Synthesis and Characterization of a Composite Anion Exchange Membrane for Water Electrolyzers (AEMWE). Membranes (Basel) 2023;13. https://doi.org/10.3390/membranes13010109.

[31] Kaczur JJ, Yang H, Liu Z, Sajjad SD, Masel RI. Carbon dioxide and water electrolysis using new alkaline stable anion membranes. Front Chem 2018;6. https://doi.org/10.3389/fchem.2018.00263.

[32] Z. Liu, S. D. Sajjad, Yan Gao, J. J. Kaczur and RIM. An Alkaline Water Electrolyzer with Sustainion™ Membranes: 1 A/cm^2 at 1.9 V with Base Metal Catalysts. ECS Trans

2017;77:71–3.

[33] Dioxide Materials 2023. https://en.wikipedia.org/wiki/Dioxide_Materials.

[34] Sustainion® X37-50 Grade RT 2023. https://www.fuelcellstore.com/sustainion-x37-50-grade-rt-membrane.

[35] Santos DMF, Sequeira CAC, Figueiredo JL. Hydrogen production by alkaline water electrolysis. Quim Nova 2013;36:1176–93. https://doi.org/10.1590/S0100-40422013000800017.

[36] Karkoszka K, Wasilewski J. Przekształtniki i zasobniki energii – w kierunku wielonośnikowego systemu zaopatrzenia w energię n.d.:27–35.

[37] Phillips R, Dunnill CW. Zero gap alkaline electrolysis cell design for renewable energy storage as hydrogen gas. RSC Adv 2016;6:100643–51. https://doi.org/10.1039/c6ra22242k.

[38] Xu Q, Zhang L, Zhang J, Wang J, Hu Y, Jiang H, et al. Anion Exchange Membrane Water Electrolyzer: Electrode Design, Lab-Scaled Testing System and Performance Evaluation. EnergyChem 2022;4:100087. https://doi.org/10.1016/j.enchem.2022.100087.

[39] Park JE, Kang SY, Oh SH, Kim JK, Lim MS, Ahn CY, et al. High-performance anion-exchange membrane water electrolysis. Electrochim Acta 2019;295:99–106. https://doi.org/10.1016/j.electacta.2018.10.143.

[40] Ito H, Miyazaki N, Sugiyama S, Ishida M, Nakamura Y, Iwasaki S, et al. Investigations on electrode configurations for anion exchange membrane electrolysis. J Appl Electrochem 2018;48:305–16. https://doi.org/10.1007/s10800-018-1159-5.

[41] Fabbri E, Habereder A, Waltar K, Kötz R, Schmidt TJ. Developments and perspectives of oxide-based catalysts for the oxygen evolution reaction. Catal Sci Technol 2014;4:3800–21. https://doi.org/10.1039/c4cy00669k.

[42] Phillips R, Edwards A, Rome B, Jones DR, Dunnill CW. Minimising the ohmic resistance of an alkaline electrolysis cell through effective cell design. Int J Hydrogen Energy 2017;42:23986–94. https://doi.org/10.1016/j.ijhydene.2017.07.184.

[43] Raney M. Method of Preparing Catalytic Material (US Patent 1563587). Us1563587 1925:Patent US1563587.

[44] Plevová M, Hnát J, Bouzek K. Electrocatalysts for the oxygen evolution reaction in alkaline and neutral media. A comparative review. J Power Sources 2021. https://doi.org/10.1016/j.jpowsour.2021.230072.

[45] Esswein AJ, Mcmurdo MJ, Ross PN, Bell AT, Tilley TD. Size-dependent activity of Co3O4 nanoparticle anodes for alkaline water electrolysis. J Phys Chem C 2009;113:15068–72. https://doi.org/10.1021/jp904022e.

[46] Zhu YP, Liu YP, Ren TZ, Yuan ZY. Self-supported cobalt phosphide mesoporous nanorod arrays: A flexible and bifunctional electrode for highly active electrocatalytic water reduction and oxidation. Adv Funct Mater 2015;25:7337–47. https://doi.org/10.1002/adfm.201503666.

[47] Elkholy AE, El-Taib Heakal F, Allam NK. Nanostructured spinel manganese cobalt ferrite

for high-performance supercapacitors. RSC Adv 2017;7:51888–95. https://doi.org/10.1039/c7ra11020k.

[48] Chen C, Liu B, Ru Q, Ma S, An B, Hou X, et al. Fabrication of cubic spinel MnCo2O4 nanoparticles embedded in graphene sheets with their improved lithium-ion and sodium-ion storage properties. J Power Sources 2016;326:252–63. https://doi.org/10.1016/j.jpowsour.2016.06.131.

[49] Parida SK, Mohapatra J, Mishra DK. Structural and magnetic behavior of spinel CuMn2O4 synthesized by co-melting technique. Mater Lett 2016;181:116–8. https://doi.org/10.1016/j.matlet.2016.05.180.

[50] Fukushima J, Hayashi Y, Takizawa H. Structure and magnetic properties of FeAl 2 O 4 synthesized by microwave magnetic field irradiation. J Asian Ceram Soc 2013;1:41–5. https://doi.org/10.1016/j.jascer.2013.02.001.

[51] Garg N, Mishra M, Govind, Ganguli AK. Electrochemical and magnetic properties of nanostructured CoMn2O4and Co2MnO4. RSC Adv 2015;5:84988–98. https://doi.org/10.1039/c5ra16937b.

[52] Zhao Q, Yan Z, Chen C, Chen J. Spinels: Controlled Preparation, Oxygen Reduction/Evolution Reaction Application, and beyond. Chem Rev 2017;117:10121–211. https://doi.org/10.1021/acs.chemrev.7b00051.

[53] Lankauf K, Ostrowska K, Górnicka K, Karczewski J, Jasiński P, Molin S. Tetrahedrally modified MnMe0.1Co1.9O4 (Me = Zn, Mg, Li) spinels for non-enzymatic glucose sensing. Mater Lett 2022;323:132574. https://doi.org/10.1016/j.matlet.2022.132574.

[54] Bragg W. H. The Structure of Magnetite and Spinels. Nature 1915;95:561.

[55] Nishikawa S. Structure of Some Crystals of Spinel Group. Proc Tokyo Math Soc 2nd Ser 1915;8:199–209.

[56] Paji D. Superparamagnetic relaxation in Cu x Fe 3 À x O 4 2004;281:353–63. https://doi.org/10.1117/1.JPE.7.012009.Downloaded.

[57] Yokozaki R, Kobayashi H, Mandai T, Honma I. Effect of Al substitution on structure and cathode performance of MgMn2O4 spinel for magnesium rechargeable battery. J Alloys Compd 2021;872:159723. https://doi.org/10.1016/j.jallcom.2021.159723.

[58] Lankauf K, Cysewska K, Karczewski J, Mielewczyk-Gryń A, Górnicka K, Cempura G, et al. MnxCo3-xO4 spinel oxides as efficient oxygen evolution reaction catalysts in alkaline media. Int J Hydrogen Energy 2020;5. https://doi.org/10.1016/j.ijhydene.2020.03.188.

[59] Suen NT, Hung SF, Quan Q, Zhang N, Xu YJ, Chen HM. Electrocatalysis for the oxygen evolution reaction: Recent development and future perspectives. Chem Soc Rev 2017;46:337–65. https://doi.org/10.1039/c6cs00328a.

[60] Moure C, Peña O. Recent advances in perovskites: Processing and properties. Prog Solid State Chem 2015;43:123–48. https://doi.org/10.1016/j.progsolidstchem.2015.09.001.

[61] Hwang J, Rao RR, Giordano L, Katayama Y, Yu Y, Shao-Horn Y. Perovskites in catalysis and electrocatalysis. Science (80-) 2017;358:751–6. https://doi.org/10.1126/science.aam7092.

[62] Maiti T, Saxena M, Roy P. Double perovskite (Sr2B'B''O6) oxides for high-temperature thermoelectric power generation - A review. J Mater Res 2019;34:107–25. https://doi.org/10.1557/jmr.2018.376.

[63] Salunkhe RR, Kaneti Y V., Yamauchi Y. Metal-Organic Framework-Derived Nanoporous Metal Oxides toward Supercapacitor Applications: Progress and Prospects. ACS Nano 2017;11:5293–308. https://doi.org/10.1021/acsnano.7b02796.

[64] Danks AE, Hall SR, Schnepp Z. The evolution of "sol-gel" chemistry as a technique for materials synthesis. Mater Horizons 2016;3:91–112. https://doi.org/10.1039/c5mh00260e.

[65] Li T, Lv Y, Su J, Wang Y, Yang Q, Zhang Y, et al. Anchoring CoFe2O4 Nanoparticles on N-Doped Carbon Nanofibers for High-Performance Oxygen Evolution Reaction. Adv Sci 2017;4. https://doi.org/10.1002/advs.201700226.

[66] L.A. Dobrzański. Procesy nanoszenia powłok z fazy gazowej 2008:55–80.

[67] Tahir MB, Rafique M, Rafique MS, Nawaz T, Rizwan M, Tanveer M. Photocatalytic nanomaterials for degradation of organic pollutants and heavy metals. Elsevier Inc.; 2020. https://doi.org/10.1016/b978-0-12-821192-2.00008-5.

[68] Ziaja J. Cienkowarstwowe struktury metaliczne i tlenkowe. Właściwości, technologia, zastosowanie w elektrotechnice. Pr Nauk Inst Pod Elektrotechniki i Elektrotechnologii Politech Wrocławskiej 2012.

[69] Kellsal R., Hamley I. GM. Nanotechnologie. Warszawa: PWN; 2008.

[70] Wei C, Rao RR, Peng J, Huang B, Stephens IEL, Risch M, et al. Recommended Practices and Benchmark Activity for Hydrogen and Oxygen Electrocatalysis in Water Splitting and Fuel Cells. Adv Mater 2019;1806296:1–24. https://doi.org/10.1002/adma.201806296.

[71] Niu S, Li S, Du Y, Han X, Xu P. How to Reliably Report the Overpotential of an Electrocatalyst. ACS Energy Lett 2020;5:1083–7. https://doi.org/10.1021/acsenergylett.0c00321.

[72] Li G, Yang D, Chuang P-Y. Defining Nafion ionomer roles for enhancing alkaline oxygen evolution electrocatalysis. ACS Catal 2018:acscatal.8b02217. https://doi.org/10.1021/acscatal.8b02217.

[73] Garsany Y, Ge J, St-Pierre J, Rocheleau R, Swider-Lyons KE. Analytical procedure for accurate comparison of rotating disk electrode results for the oxygen reduction activity of Pt/C. J Electrochem Soc 2014;161:628–40. https://doi.org/10.1149/2.036405jes.

[74] McCrory CCL, Jung S, Peters JC, Jaramillo TF. Benchmarking heterogeneous electrocatalysts for the oxygen evolution reaction. J Am Chem Soc 2013;135:16977–87. https://doi.org/10.1021/ja407115p.

[75] VAN DER PAUW LJ. A method of measuring the resistivity and Hall coefficient on lamellae of arbitrary shape. Philips Tech Rev 1958;20:220–4.